

Development and performance studies of GEM based tracking detectors for the Compressed Baryonic Matter (CBM) experiment at FAIR

By

AJIT KUMAR

PHYS04201404005

Variable Energy Cyclotron Centre, Kolkata

A thesis submitted to

The Board of Studies in Physical Sciences

In partial fulfillment of requirements

for the Degree of

DOCTOR OF PHILOSOPHY

of

HOMI BHABHA NATIONAL INSTITUTE



November, 2021


Homi Bhabha National Institute¹

Recommendations of the Viva Voce Committee

As members of the Viva Voce Committee, we certify that we have read the dissertation prepared by **Ajit Kumar** entitled "**Development and performance studies of GEM based tracking detectors for the Compressed Baryonic Matter (CBM) experiment at FAIR**" and recommend that it may be accepted as fulfilling the thesis requirement for the award of Degree of Doctor of Philosophy.


Chairman - Prof. Subhasis Chattopadhyay

Date:

3/11/21 

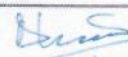
Guide / Convener - Dr. Anand Kumar Dubey

Date:


03/11/21

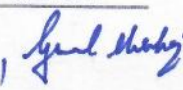
Examiner - Dr. Satyanarayana Bheesette

Date:


3/11/21

Member 1- Dr. Gopal Mukherjee

Date:

03/11/21 


Member 2 - Dr. Zubayer Ahammed

Date:


03/11/21

Member 3 - Dr. Basanta Kumar Nandi

Date:


03/11/2021

Final approval and acceptance of this thesis is contingent upon the candidate's submission of the final copies of the thesis to HBNI.

I/We hereby certify that I/we have read this thesis prepared under my/our direction and recommend that it may be accepted as fulfilling the thesis requirement.

Date: 03.11.2021

Place: Kolkata

Signature

Guide

¹ This page is to be included only for final submission after successful completion of viva voce.

STATEMENT BY AUTHOR

This dissertation has been submitted in partial fulfillment of requirements for an advanced degree at Homi Bhabha National Institute (HBNI) and is deposited in the Library to be made available to borrowers under rules of the HBNI.

Brief quotations from this dissertation are allowable without special permission, provided that accurate acknowledgement of source is made. Requests for permission for extended quotation from or reproduction of this manuscript in whole or in part may be granted by the Competent Authority of HBNI when in his or her judgment the proposed use of the material is in the interests of scholarship. In all other instances, however, permission must be obtained from the author.



Ajit Kumar

DECLARATION

I, hereby declare that the investigation presented in the thesis has been carried out by me. The work is original and has not been submitted earlier as a whole or in part for a degree / diploma at this or any other Institution / University.



Ajit Kumar

List of Publications arising from the thesis

Journal

1. “Operating large size GEM detectors using a novel optocoupler based biasing scheme for the Muon Chamber system of CBM experiment”
Ajit Kumar, et.al.,
Nucl. Inst. and Meth. A **958**, 162905 (2020)
2. “Commissioning and testing of pre-series triple GEM prototypes for CBM-MuCh in the mCBM experiment at SIS18 facility of GSI”
Ajit Kumar, et.al.,
JINST **16**, P09002 (2021).

Other

1. “Performance of a large size triple GEM detector at high particle rate for the CBM Experiment at FAIR”
R. P. Adak, Ajit Kumar, et.al.,
Nucl. Inst. and Meth. A **846**, 29-35 (2017)
2. “Challenges in QCD matter physics –The scientific programme of the Compressed Baryonic Matter experiment at FAIR”
T. Ablyazimov, ..., Ajit Kumar, ..., et.al.,
Eur. Phys. J. A **53**, 60 (2017)

Conferences/Symposiums

1. “Testing of triple GEM prototypes for the CBM Muon Chamber system in the mCBM experiment at the SIS18 facility of GSI”
Ajit Kumar, et.al.,
DOI:10.1088/1748-0221/15/10/C10020
JINST **15**, C10020 (2020).
2. “Testing large size triple GEM chambers with Pb+Pb collision at CERN SPS”

Ajit Kumar, et.al.,

XXIII DAE High Energy Physics Symposium. Springer Proceedings in Physics, vol 261. Springer, Singapore.

https://doi.org/10.1007/978-981-33-4408-2_98

3. **“Testing of 10×10 triple GEM detector using STS-XYTER for CBM experiment”**

C. Ghosh, Ajit Kumar, et.al.,

XXIII DAE High Energy Physics Symposium. Springer Proceedings in Physics, vol 261. Springer, Singapore.

https://doi.org/10.1007/978-981-33-4408-2_176

4. **“Design and Development of Various Cooling Arrangements for Muon Chamber Detector Electronics”**

C. Ghosh, A. K. Dubey, J. Kumar, Ajit Kumar, et.al.,

XXIII DAE High Energy Physics Symposium. Springer Proceedings in Physics, vol 261. Springer, Singapore.

https://doi.org/10.1007/978-981-33-4408-2_105

5. **“Systematic study of effect of setting parameters of n-XYTER self triggered electronics for CBM MUCH”**

Ajit Kumar, et.al.,

DAE Symp. Nucl. Phys. **60**, 1054 (2015).

6. **“Building and testing of the first real size prototype chamber of CBM MUCH”**

A. K. Dubey, J. Saini, Ajit Kumar, et.al.,

DAE Symp. Nucl. Phys. **60**, 1078 (2015).

7. **“Gain uniformity and gain dependence on T/P for real size prototype triple GEM for CBM experiment”** Ajit Kumar, et.al.,

DAE Symp. Nucl. Phys. **61**, 960 (2016).

8. **“High Voltage Distribution scheme for large size GEM detector”**

J. Saini, Ajit Kumar, et.al.,

DAE Symp. Nucl. Phys. **61**, 1004 (2016).

9. **“Design and fabrication of a water based cooling system for the CBM Muon Chamber”**

D. Nag, Ajit Kumar, et.al.,
DAE Symp. Nucl. Phys. **61**, 1096 (2016).

10. **“A lab setup for efficiency measurement of triple GEM detector using beta source”**

Ajit Kumar, et.al.,
DAE Symp. Nucl. Phys. **62**, 1104 (2017).

11. **“Study of basic characteristics of triple GEM detector”**

Ajit Kumar, et.al.,
DAE Symp. Nucl. Phys. **62**, 1116 (2017).

12. **“Testing of large size GEM detector with Pb+Pb collision at CERN-SPS”**

Ajit Kumar, et.al.,
DAE Symp. Nucl. Phys. **62**, 1006 (2017).

13. **“Real size triple GEM detector for mCBM experiment”**

Ajit Kumar, et.al.,
DAE Symp. Nucl. Phys. **63**, 1216 (2018).

14. **“Real size triple GEM detector for mCBM experiment”**

Ajit Kumar, et.al.,
DAE Symp. Nucl. Phys. **63**, 1216 (2018).

Technical Reports

1. **“Effect of parameter-settings of n-XYTER, self triggered electronics for CBM-MUCH”**

Ajit Kumar, et.al.,
CBM Prog. Rep. 71 (2015).

2. **“Study of triple GEM prototype characteristics at VECC”**

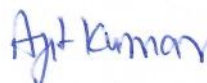
Ajit Kumar, et.al.,
CBM Prog. Rep. 86 (2016).

3. **“Beamtest of triple GEM prototypes with Pb+Pb collisions at CERN SPS”**

Ajit Kumar, et.al.,
CBM Prog. Rep. 88 (2016).

4. **“Study of triple GEM prototype characteristics at VECC”**
Ajit Kumar, et.al.,
 CBM Prog. Rep. 86 (2016).
5. **“High voltage distribution scheme for large size GEM detector”**
 J. Saini, Ajit Kumar, et.al.,
 CBM Prog. Rep. 95 (2016).
6. **“Testing of a triple GEM chamber with independent power supply”**
Ajit Kumar, et.al.,
 CBM Prog. Rep. 70 (2017).
7. **“Testing Pre-series prototype triple GEM chambers of CBM-MUCH with Pb+Pb collision at CERN SPS”**
Ajit Kumar, et.al.,
 CBM Prog. Rep. 75 (2017).
8. **“Testing Pre-series prototype triple GEM chambers of CBM-MUCH with Pb+Pb collision at CERN SPS”**
Ajit Kumar, et.al.,
 CBM Prog. Rep. 75 (2017).
9. **“Testing of Optocoupler based HV distribution for large size GEM detectors for CBM-MUCH”**
 J. Saini, Ajit Kumar, et.al.,
 CBM Prog. Rep. 78 (2017).
10. **“Installation, commissioning and testing of mMUCH modules in the mCBM experiment”**
Ajit Kumar, et.al.,
 CBM Prog. Rep. 51 (2018).
11. **“Fabrication of Mv2 module for mCBM experiment and first test with optocoupler based HV biasing”**
Ajit Kumar, et.al.,
 CBM Prog. Rep. 53 (2018).
12. **“QA of GEM foils: Measuring hole dimensions and pitch”**
 A. Agarwal, Ajit Kumar, et.al.,
 CBM Prog. Rep. 54 (2018).

13. **"First GEM detector tests using MUCH-XYTER"**
C. Ghosh, G. Sikder, Ajit Kumar, et.al.,
CBM Prog. Rep. 56 (2018).
14. **"Response of mMUCH modules in the mCBM campaign 2019"**
Ajit Kumar, et.al.,
CBM Prog. Rep. 71 (2019).
15. **"Study of 10 cm \times 10 cm GEM detector Characteristics using MUCH-XYTER v2.0 and v2.1 Asic"**
C. Ghosh, J. Saini, G. Sikder, Ajit Kumar, et.al.,
CBM Prog. Rep. 80 (2019).
16. **"Correlation between mMuCh hits and projected mTOF tracks in the miniCBM setup"**
E. Nandy, V. Singhal, A. Aggarwal, Ajit Kumar, et.al.,
CBM Prog. Rep. 105 (2019).
17. **"A Study of mMuCh Response at low and high intensity Pb+Au collisions at mCBM 2020"**
A. Agarwal, C. Ghosh, G. Sikder, S. Roy, S. Chatterjee, Ajit Kumar, et.al.,
CBM Prog. Rep. 73 (2019).
18. **"Update on mCBM data analysis of November/December 2019 beamtime"**
Ajit Kumar, et.al.,
CBM Prog. Rep. 86 (2020).
19. **"Studying effect of digitization parameters on omega (ω) reconstruction"**
Ajit Kumar, et.al.,
CBM Prog. Rep. 91 (2020).



Ajit Kumar

DEDICATION

Dedicated to my beloved family members:

My Grandfather - Anant Lal Maurya

My Father - Rajendra Prasad

My Mother - Urmila

My Brother - Veer Bahadur Maurya

ACKNOWLEDGEMENTS

Ph.D. is a long journey and it would not have been possible without the help and support of colleagues and friends to achieve all the work during my Ph.D. tenure. Therefore, I would like to express my sincere gratitude to all these people.

First of all, I would like to express my sincere gratitude to my thesis supervisor **Dr. Anand Kumar Dubey**, for his constant guidance, support, encouragement, and careful supervision throughout the research period. He has constantly been pushing me to work hard, and his expertise in detector physics and instrumentation helped me a lot to learn it quickly. Moreover, he has been supportive all the time whenever and whatever the help I needed, whether it is personal or official.

I am in debt to **Prof. Subhasis Chattopadhyay** for his constant support and guidance. He has helped me in many aspects like physics discussion, data analysis, etc., during my Ph.D. He has always been there for any help, either it is personal or official.

I also want to thank all my collaborators for their help and support. I have closely worked with wonderful people (Mr. J. Saini, Mr. V. Singal, Mr. V. Negi, Mr. C. Ghosh) of VECC. Without help from Dr. P. P. Bhaduri, E. Nandy, O. Singh, S. Chatterjee, it would not have been so easy to work on the CBM-MuCh simulation. I am very much thankful to all the GSI colleagues for their help during beamtime and during mCBM data analysis, mainly to Dr. C. Sturm, Dr. P.-A. Loizeau, Dr. F. Uhlig, Dr. D. Emschermann, Dr. N. Herrmann, Dr. I. Deppner (Heidelberg University), Dr. V. Fries, Dr. C. J. Schmidt. Special thanks to Dr. N. Herrmann for his help during SPS beamtime and in SPS data analysis. During my visit to Germany, Annette Zimbelius of GSI helped me with booking a guest house and other related works.

I am grateful to all my lab colleagues (G. Das, J. Kumar, S. Karmakar, Khokon Da, Sukumar Da, Tirthankar Da, Sanad Da) for their help during detector fabrication and tests.

I want to thank Dr. Jane-e-Alam (Ex. Dean Physical Sciences, VECC), Dr. Parnika Das (Dean Physical Sciences, VECC), and all my respected teachers who taught me in course

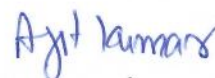
work.

I am thankful to Homi Bhabha National Institute for providing HBNI's student travel support and research fellowship. I would like to thank the CPDA lab group for providing a clean room during real-size chamber assembly. I want to express my thanks to my doctoral committee for the critical reviews and suggestions during the yearly renewal seminars.

I like to thank my friends from BHU, mainly U. Sonkar and Rajprince for their encouragement and support. During my Ph.D., I have met many friends, but the closest one is Homnath Luitel. He was the only one with whom I used to share every aspect of life. I am also fortunate to have some seniors who were and are more like brothers and good friends, mainly Anukul Dada, Ashif dada, Sushant dada. They have always supported me for everything whenever I was in need. I would also like to thank all people of the TT team, mainly, Homnath, Sushant da, Noor da, Santu da, Arindam Da, Ayan Da, Ashif da.

Special thanks go to all my batchmates and good friends (Safikul, Nachiketa, Ranabir, Dipak, Shabnam, and Ashik) also to my juniors (Apar, Mitali, Santanu, Shreyasi, Sumit, Sanchari, Soumen, Shabbir, Vivek, and many others) and seniors (Rajesh da, Argya da, Rajendra Da and many others) for their support and best wishes. I also like to thank VECC grid colleagues, mainly Prasun da, Abhishek, and Ashique, for their help during computer and software-related issues. I appreciate the support and co-operation of my friends O. Singh, S. Mehta, S. Khan, S. P. Rhode, K. Wadhwa, G. Sikdar, S. Chatterjee.

Finally, I want to thank my family members (especially my mother, father, and brothers) without whose support it would not have been possible to work patiently during the Ph.D. tenure. Also the soothing voice of kids (Shivansh, Shreya, Aryan, Rimjhim) makes me feel relax during stressful moments.



Ajit Kumar



Homi Bhabha National Institute

Synopsis of PhD Thesis

1. Name of the Student: Ajit Kumar
2. Name of the Constituent Institution: Variable Energy Cyclotron Centre, Kolkata
3. Enrolment No. : PHYS04201404005
4. Title of the Thesis: Development and performance studies of GEM based tracking detectors for the Compressed Baryonic Matter (CBM) experiment at FAIR
5. Board of Studies: Physical Sciences

SYNOPSIS

(Limited to 10 pages in double spacing)

The Compressed Baryonic Matter (CBM) [1] is a fixed target heavy-ion experiment designed to investigate properties of dense nuclear matter at Facility for Anti-Proton Ion Research (FAIR) [2] accelerator center, in GSI, Darmstadt, Germany. The primary goal of the CBM experiment is to explore Quantum Chromo Dynamics (QCD) phase diagram at moderate temperature and high net baryon densities by colliding heavy-ions beams in the energy range of 2-35 AGeV (in a SIS300 setup). The model calculation predicts that densities of $6-12\rho_0$ ($\rho_0 = 0.17\text{fm}^{-3}$ is normal nuclear matter density) can be achieved in the center of the reaction zone at these energies. This will open the possibility to understand the structure of the core of neutron star and hyperon-hyperon interactions. On the other hand, the RHIC and LHC experiments, complementary to CBM, are devoted to studying the QCD phase diagram for high temperature and nearly zero baryon densities.

Charmonium (J/ψ) and low mass vector mesons (ρ , ω , ϕ) are fundamental penetrating probes to understand the initial state of the collision system, which will indicate the occurrence of phase

transition from hadronic matter to the quark-gluon matter. The production cross-section of these particles is extremely small at FAIR energies. The main challenge is to measure these rare observables with high precision and statistics in heavy-ion collisions. The CBM experiment is designed to operate at an unprecedented interaction rate of ~ 10 MHz, enabling the measurement of these observables to the required precision. In such high interaction rates, the produced particle densities will be very high (400 kHz/cm^2 for central Au+Au collision at 10 AGeV), so we need fast and high rate detectors to handle such a high-rate environment.

A Muon Chamber (MuCh) [3] system being developed for CBM will be used for the detection of di-muon pairs [4] originating from the nucleus-nucleus collisions. Positioned downstream of the Silicon Tracking Station (STS), MuCh consists of alternating layers of segmented absorbers and detector stations. A triplet of tracking detectors called stations behind each absorber layer will be employed. This novel scheme of segmented absorbers allows the detection of muon tracks in a broad momentum range. In the first two stations, owing to high particle flux, high rate detectors based on Gas Electron Multiplier (GEM) technology would be used [5, 6]. The Resistive Plate Chamber (RPC) detectors will be used for 3rd and 4th stations where the particle densities are relatively lower. GEM detectors have been used for particle detection in many experiments [7, 8, 9, 10]. Likewise, large area GEM detectors of MuCh will carry out charged particle tracking to serve the goal towards muon identification. In any given layer, the particle densities per unit area change when going radially outwards in the transverse direction from the beam pipe. So, for the modules of the first station, the granularity of the GEM-MuCh module monotonically decreases from ~ 4 mm pads in the inner region to about ~ 17 mm in the outer region. The MuCh detectors will use self-triggered electronics as readout, which is a must for all the detector sub-system of the CBM.

The GEM detectors:

The GEM detector belongs to the family of Micro-Pattern Gas Detector (MPGD). It was first introduced by F. Sauli in 1997 [11]. The standard GEM foil consists of a thin dielectric polymer (polyimide) of $50 \text{ }\mu\text{m}$ thick and a metal (copper) layer of thickness $5 \text{ }\mu\text{m}$ coated on both sides of it. A regular hole of $70 \text{ }\mu\text{m}$ diameter and $140 \text{ }\mu\text{m}$ pitch is made in foils using the photolithographic technique. When a nominal voltage of $\sim 500\text{V}$ is applied across the two surfaces of the GEM foil, it creates a very high electric field ($\sim 100 \text{ kV/cm}$) inside the holes. When a charged particle passes through the gaseous medium, it creates an electron-ion pair. The electron drifts toward the GEM hole and is amplified by the high electric field inside the holes. These electrons, which form a signal, are collected at the readout electrode. The detector gain (ratio of output charge divided by the input charge (from pri-

mary ionization)) can be increased by inserting more layers of GEM foils between the drift and the readout electrode. In most of the experiments, triple GEM (three-layer of GEM foils) detectors are used. The advantage of using GEM detectors are its high rate handling capability, operation with high gas gain using multiple GEM, suppression of discharges during operation in intense particle beams, good spatial and time resolutions, and stable operation for the long run use.

As it has been mentioned that the large area triple GEM detectors will be used for muon detection in the CBM experiment, it becomes necessary to study and characterize their performance with regards to the design criteria for the final experiment. The work presented in this thesis is based on the development and performance of GEM detectors for their use in the CBM experiment. It is broadly divided into three parts. In the first part, the test of various prototype GEM detectors will be discussed. The second part will concentrate on the design, fabrication and assembly of real-size triple GEM prototypes and their test response. In view of this, a detailed investigation of these prototypes in N-N collisions of the mini-CBM experiment is discussed. The third part will focus on the physics performance simulation by implementing detector parameters such as gas gain and spot size.

Study of triple GEM detector prototypes:

A GEM detector consists of different regions: drift (active volume), GEM (amplification region), transfer, and induction. Triple GEM detector prototypes having sizes $10\text{ cm} \times 10\text{ cm}$ & $30\text{ cm} \times 30\text{ cm}$ were built and tested. A premixed gas of Ar/CO₂ in 70:30 proportion was used for all the tests described here. The HV bias was applied through the voltage divider resistive chain. The response of the detector was studied using X-ray (⁵⁵Fe) source, β -source (Sr90), and with cosmic muons. The corresponding pulse height spectra was analyzed and parameters like gain, energy resolution and its dependence on T/p studied. The measured effective gain of the detector was found to be $>10^3$, and energy resolution within $\sim 20\text{-}25\%$ at the operating conditions. A systematic study of the effect of drift field, transfer field, induction field, and GEM voltages on gain & energy resolution has been carried out using 5.9 keV X-ray (⁵⁵Fe) source.

The charged particle detection efficiency of the prototypes using self-triggered electronics was measured in the lab. A coincidence test-setup was built. Instead of cosmic muons, a β -source was used for sufficient statistics in a short time. The efficiency at the plateau region was observed to be $>95\%$. The time resolution, efficiency uniformity, etc., also have been measured. The efficiency varies within 3% throughout the active region of the detector of $10\text{ cm} \times 10\text{ cm}$ area. The maximum variation in time resolution measured at various regions of the detector was found to be $\sim 2\text{-}3\text{ ns}$.

Design, assembly, and test of large size prototype triple GEM detectors:

Large area GEM detectors will be used for the first two stations of the MuCh system in the CBM experiment. Building such large GEM modules (with a typical area of 2000 sq. cm. or more) is a challenge. Two versions of detector modules have been built at VECC, namely, Mv1 and Mv2. The gap configuration for Mv1 is 3-1-1-1.5 and for Mv2 is 3-2-2-2, where the number represents the drift, transfer, and induction gaps in mm, respectively. Large size trapezoidal-shaped single mask GEM foils were used. These were stretched using the no-glue or “NS-2” technique [12]. The top surface of each foil is segmented into 24 divisions. As part of the essential Quality Analysis (QA) of the GEM foils, the foils were selected only if they satisfied the no-short criteria and a low leakage current of <5 nA at ΔV_{GEM} of 550 V for every segment. The readout plane consists of trapezoidal-shaped pads with progressively increasing sizes from ~ 4 mm to ~ 17 mm. The Mv1 module was read out using 15 front end boards (FEBs), each connected to the pads in different detector regions, while Mv2 was read out using 18 FEBs.

The real-size module (Mv1) was tested with single-particle proton beams of momentum 2.36 GeV/c at COSY-Jülich Germany [6]. A charged particle detection efficiency higher than $\sim 95\%$ at $\Delta V_{GEM} = 1125$ V was achieved at COSY. The variation in efficiency with the rate of incoming protons was found to vary within 2% when tested up to a maximum rate of 2.8 MHz/cm². Two such modules were also tested with Pb+Pb collisions at beam momenta 30 AGeV/c and 150 AGeV/c at H4 beam-line of CERN-SPS [13]. The detector’s performance in a multi-particle environment was studied for the first time at SPS. A spray of particles produced from nucleus-nucleus collision passed through different detector regions, as the case would be in the actual CBM experiment. The detector was tested with CBM-like DAQ for the first time, which took data in a free streaming mode and almost full FEB coverage. With such a large number of working FEBs, an elaborate cooling [14] were implemented for the first time. Events were reconstructed using a diamond detector. A straight line track fitting has been performed to measure the track residuals using hit coordinates (x,y,z) in the common η - ϕ window for each detector plane.

In the case of Mv1, if any foil-segment becomes faulty during operation, we have to switch off the full detector, leading to a loss in acceptance. A novel optocoupler-based HV bias has been designed to take care of this issue in the Mv2. The details of the design can be found in [15].

A pre-cursor experiment of CBM consisting of all CBM detector subsystems has been set up at the SIS18 facility of GSI called mCBM [16] (“mini-CBM”), as a part of the “FAIR phase 0 program”. The mCBM experiment aims to test the real-size modules of each detector subsystem under realistic interaction rates in nucleus-nucleus collisions. Major tasks involve studying and optimizing the

DAQ and data transport to a computer farm, in particular, the timing-stability and data consistency of the subsystem data streams, investigating issues related to the operation of detectors in a high-rate environment, and developing and optimizing the software for online/offline data analysis. The reconstruction of rare events like Λ hyperon will be performed in nucleus-nucleus collisions at SIS18 energies.

In this regard, two real-size modules (Mv2), corresponding to the module sizes of station-1, were installed and commissioned in the mCBM experiment at GSI. A premixed gas mixture Ar/CO₂ (70/30) has been used for the fill gas. At mCBM, the goal is to study the simultaneous response from different detector regions and, in conjunction with those from other subsystems, when a multitude of particles originating from nucleus+nucleus collisions passes through them. The data at mCBM have been taken using the upgraded CBM-DAQ and realistic STS/MuCh-XYTER electronics.

Test with nucleus+nucleus collisions at a beam energy of 1-2 AGeV was carried out. Detector performance in terms of spill structure, time correlation, and time resolution has been studied. The events were reconstructed offline using time-stamps of the detector hits. Clustering and local hit reconstruction have been performed for the first time on the MuCh modules in the free streaming data set of mCBM. The cluster-size and cluster charge characteristics in different zones of the detector have been studied. The detector gain has been calculated using the reconstructed Hits' cluster charge, and its variation with GEM voltages studied. The gain was observed to be found >3500 . A time resolution of ~ 15 ns was measured for the GEM module. Uniformity of the detector response has been studied in terms of the relative gain plot using the Most Probable Value (MPV) of the cluster charge distribution zone-wise and the time resolutions measured for a large number of pads throughout the detector area. The average dispersion of the digis in time within a cluster has been studied. An excellent spatial correlation between GEM1 & GEM2 and between GEM & TOF modules have been observed, conveying an effective event reconstruction, also clearly demonstrate the time-synchronous behavior of two different detectors or, for that matter, even two different subsystems employing entirely different detector technologies and readout electronics. A straight line track fitting has been carried out using the TOF detectors and the GEM detectors. Track residuals have been measured at the different granularities of the GEM detectors.

Physics performance simulation studies:

The MuCh system at CBM aims to reconstruct di-muons originating from low mass vector meson (LMVM) and charmoniums, such as ρ , ω , ϕ , and J/ψ . The optimized design for the MuCh detector system at SIS100 energies consists of four absorbers. The first absorber composed of 30 cm low-

density graphite ($\rho = 1.7 \text{ g/cm}^3$) and 30 cm concrete. The rest three are made of iron with thickness 20, 20, and 30 cm, respectively. In the given setup, the reconstruction of ω meson, which decays to di-muons, has been performed. The yield of omega was calculated from the invariant mass distribution of di-muon pairs. The simulation has been performed for central Au+Au collision at 8 AGeV beam energy. The simulation chain involves the transport of particles through the detector sub-systems, followed by digitization, clustering and hit reconstruction, and finally, extraction of the di-muon signals. In the digitization step, we provide the detector parameters, namely the spot size and detector gain, for studying a realistic physics performance. The UrQMD event generator was used to generate background events, and PLUTO was used to generate the ω meson signal. Simulated data constituting embedded w-events were analyzed. From the reconstructed ω yield it has been observed that omega reconstruction efficiency saturates for gas gain 4000, and at any particular gain setting the efficiency is found to be independent of the spot-radius, studied in the range 250-1000 μm . The effect of these parameters on residuals, signal (S) to background (B) ratio, and significance ($S/\sqrt{S+B}$), has also been studied systematically.

References

- [1] The Cbm Experiment. <https://www.cbm.gsi.de/>.
- [2] The Fair Experiment. <https://fair-center.eu/>.
- [3] Subhasis Chattopadhyay et al., editors. *Technical Design Report for the CBM : Muon Chambers (MuCh)*. GSI, 2015.
- [4] Ablyazimov T et al. Challenges in QCD matter physics -- The scientific programme of the Compressed Baryonic Matter experiment at FAIR. *Eur. Phys. J. A*, 53(3):60, 2017.
- [5] A.K. Dubey et al. GEM detector development for CBM experiment at FAIR. *Nucl. Instrum. Meth. A*, 718:418 – 420, 2013.
- [6] Rama Prasad Adak et al. Performance of a large size triple GEM detector at high particle rate for the CBM Experiment at FAIR. *Nucl. Instrum. Meth. A*, 846:29 – 35, 2017.
- [7] The Phase-2 Upgrade of the CMS Muon Detectors. Technical Report CERN-LHCC-2017-012. CMS-TDR-016, CERN, Geneva, Sep 2017.

- [8] Upgrade of the ALICE Time Projection Chamber. Technical Report CERN-LHCC-2013-020. ALICE-TDR-016, Oct 2013.
- [9] Alessandro Cardini et al. The Operational Experience of the Triple-GEM Detectors of the LHCb Muon System: Summary of 2 Years of Data Taking. Technical report, CERN, Geneva, 2012.
- [10] W. Anderson et al. Design, construction, operation and performance of a Hadron Blind Detector for the PHENIX experiment. *Nucl. Instrum. Meth. A*, 646(1):35 – 58, 2011.
- [11] F. Sauli. Gem: A new concept for electron amplification in gas detectors. *Nucl. Instrum. Meth. A*, 386:531 – 534, 1997.
- [12] Andrey Marinov et al. Status of no-stretch no-spacer GEM assembly, the NS-2 technique method and experiment result. <https://indico.cern.ch/event/176664/contributions/1442160/>.
- [13] A. Kumar et al. Testing of large size GEM detector with Pb + Pb collision at CERN-SPS. *DAE Symp. Nucl. Phys.*, 62:1006–1007, 2017. <https://cds.cern.ch/record/2674709>.
- [14] S. K. Kundu et al. Performance study of the first two stations of CBM MuCh cooling system. *CBM Progress Report*, pages 102–103, 2020.
- [15] Ajit Kumar et al. Operating large size GEM detectors using a novel optocoupler based biasing scheme for the Muon Chamber system of CBM experiment. *Nucl. Instrum. Meth. A*, 958:162905, 2020.
- [16] The mCbm Experiment. <https://fair-center.eu/for-users/experiments/nuclear-matter-physics/cbm/projects/mcbm.html>.

Publications in Refereed Journals:

a. Published

1. **“Operating large size GEM detectors using a novel optocoupler based biasing scheme for the Muon Chamber system of CBM experiment”**
Ajit Kumar, et.al., Nucl. Inst. and Meth. A 958, 162905 (2020)
2. **“Performance of a large size triple GEM detector at high particle rate for the CBM Experiment at FAIR”**
R. P. Adak, Ajit Kumar, et.al., Nucl. Inst. and Meth. A 846, 29-35 (2017)
3. **“Challenges in QCD matter physics –The scientific programme of the Compressed Baryonic Matter experiment at FAIR”**
T. Ablyazimov, ..., A. Kumar, ..., et.al., Eur. Phys. J. A 53, 60 (2017)

b. Communicated

1. **“Commissioning and testing of pre-series triple GEM prototypes for CBM-MuCh in the mCBM experiment at SIS18 facility of GSI”**
Ajit Kumar, et.al., JINST Communicated.

Other publication

a. Conference/Symposium

1. **“Testing of triple GEM prototypes for the CBM Muon Chamber system in the mCBM experiment at the SIS18 facility of GSI”**
Ajit Kumar, et.al., DOI:10.1088/1748-0221/15/10/C10020, JINST 15, C10020 (2020).
2. **“Testing large size triple GEM chambers with Pb+Pb collision at CERN SPS”**
Ajit Kumar, et.al., XXII DAE High Energy Physics Symposium 2018.
3. **“Testing of 10 X 10 triple GEM detector using STS-XYTER for CBM experiment”**
C. Ghosh, Ajit Kumar, et.al., XXII DAE High Energy Physics Symposium 2018.

2. "Systematic study of effect of setting parameters of n-XYTER self triggered electronics for CBM MUCH"
Ajit Kumar, et.al., DAE Symp. Nucl. Phys. 60, 1054 (2015).
3. "Building and testing of the first real size prototype chamber of CBM MUCH"
A. K. Dubey, J. Saini, Ajit Kumar, S. Chattopadhyay and M.S. Ganti. DAE Symp. Nucl. Phys. 60, 1078 (2015).
4. "Gain uniformity and gain dependence on T/P for real size prototype triple GEM for CBM experiment" Ajit Kumar, et.al., DAE Symp. Nucl. Phys. 61, 960 (2016).
5. "High Voltage Distribution scheme for large size GEM detector"
J. Saini, Ajit Kumar, et.al., DAE Symp. Nucl. Phys. 61, 1004 (2016).
6. "Design and fabrication of a water based cooling system for the CBM Muon Chamber"
D. Nag, Ajit Kumar, et.al., DAE Symp. Nucl. Phys. 61, 1096 (2016).
7. "A lab setup for efficiency measurement of triple GEM detector using beta source"
Ajit Kumar, et.al., DAE Symp. Nucl. Phys. 62, 1104 (2017).
8. "Study of basic characteristics of triple GEM detector"
Ajit Kumar, et.al., DAE Symp. Nucl. Phys. 62, 1116 (2017).
9. "Testing of large size GEM detector with Pb+Pb collision at CERN-SPS"
Ajit Kumar, et.al., DAE Symp. Nucl. Phys. 62, 1006 (2017).
10. "Real size triple GEM detector for mCBM experiment"
Ajit Kumar, et.al., DAE Symp. Nucl. Phys. 63, 1216 (2018).
11. "Real size triple GEM detector for mCBM experiment"
Ajit Kumar, et.al., DAE Symp. Nucl. Phys. 63, 1216 (2018).


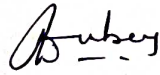
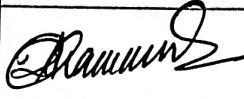
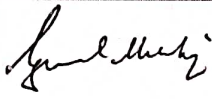

Signature of Student:

Ajit Kumar

Date:

20/01/2021

Doctoral Committee:

S. No.	Name	Designation	Signature	Date
1.	Prof. Subhasis Chattopdhyay	Chairman		20/1/21
2.	Dr. Anand Kumar Dubey	Guide/Convener		20.01.21
3.	Dr. Zubayer Ahammed	Member 1		20.01.21
4.	Prof. Gopal Mukherjee	Member 2		20/01/2021
3.	Prof. Basanta Kumar Nandi	Member 3		20.01.21

Contents

List of Figures	xxxiv
List of Tables	xxxv
Preface	xxxv
1 Introduction to Heavy Ion Physics	1
1.1 Phase diagram of strongly interacting medium and QGP	2
1.2 QGP in lab: Relativistic Heavy Ion Collisions	2
1.3 Signatures of phase transition	5
1.3.1 Lepton pairs	6
1.3.2 Quarkonium suppression	7
1.4 Summary	8
2 The Muon Chamber (MuCh) system of Compressed Baryonic Matter (CBM) experiment	9
2.1 The experiment at the Facility for Antiproton and Ion Research (FAIR)	10
2.1.1 Physics of Compressed Baryonic Matter (CBM) experiment	11
2.2 CBM Detector Sub-systems	12
2.3 Measurement of di-muons at FAIR	14
2.3.1 Low Mass Vector Mesons (LMVM)	14
2.3.2 Charmonium	15
2.3.3 Thermal Radiation	15
2.4 Muon Chamber (MuCh) of CBM	15
2.4.1 Conceptual layout of MuCh system	15
2.4.2 MuCh Setups	19

2.4.3	MuCh Simulation Steps	21
2.4.4	Track Reconstruction in MuCh	29
2.4.5	Muon identification and analysis	30
2.4.6	Integration of MuCh system in CBM	33
2.5	Technology options for MuCh	35
3	Detector performance studies in simulation	39
3.1	mCBM simulation	39
3.1.1	Results and discussion	40
3.1.2	Spatial correlation	42
3.1.3	Track reconstruction	42
3.2	Effect of detector parameters on ω reconstruction	43
3.2.1	MuCh setup	46
3.2.2	Results and Discussions	46
3.3	Summary	51
4	Gas Electron Multiplier Detector, Basic Characteristic Study	53
4.1	Particle interaction with matter	53
4.1.1	Interaction of charged particles with matter	53
4.1.2	Interaction of photon with matter	56
4.1.3	Drift and diffusion in gases	58
4.2	Gas detector, gas amplification and working principle	59
4.2.1	Operation modes of gas detectors	60
4.2.2	Choice of gas mixture	61
4.3	GEM detector	62
4.3.1	Working principle of GEM detector	62
4.3.2	Advantage of GEM detectors	63
4.3.3	Application of GEM detectors	63
4.4	Different readout chains used during the detector test	65
4.4.1	n-XYTER, ROC based readout chain	66
4.4.2	Conventional (NIM based) readout chain	68
4.5	Testing different GEM prototypes in lab	69
4.5.1	Effect of drift, transfer and induction on gain and energy resolution	69

4.5.2	Efficiency measurement of triple GEM in lab	73
4.5.3	Comparison with 3-2-2-2 gas gap configuration	79
5	Real Size Trapezoidal Chambers for MuCh	81
5.1	Assembly of real-size modules at VECC	82
5.1.1	Drift PCB	82
5.1.2	Readout PCB	83
5.1.3	Segmented GEM foils	84
5.1.4	Other components	85
5.1.5	Steps involved in the assembly and Quality Assurance (QA) of real-size triple GEM chambers	85
5.2	Test of first real-size module (“Mv1”)	88
5.2.1	Test in lab	88
5.2.2	Test with proton beam at COSY	92
5.2.3	Test with b+Pb collision at CERN-SPS	94
5.3	“Mv2” design, assembly and test	100
5.3.1	HV distribution design	102
5.3.2	Testing large size detector in mCBM experiment	111
5.4	Summary	112
6	Commissioning and testing of real-size GEM modules in mCBM experiment	113
6.1	mCBM experiment	114
6.2	mMuCh modules	115
6.3	Test setup at SIS18 facility of GSI (mCBM)	116
6.4	STS/MuCh-XYTER and Data Acquisition System (DAQ)	118
6.4.1	STS/MuCh-XYTER	118
6.4.2	Data Acquisition System (DAQ)	119
6.5	Results from the mCBM test	122
6.5.1	Results using STS/MuCh-XYTER v2.0:	122
6.5.2	Results using STS/MuCh-XYTER, v2.1	126
6.6	Event building	133
6.7	Spatial correlation and track reconstruction	141
6.8	Summary	146

7 Summary	149
Appendix A Systematic study of effect of setting parameters of n-XYTER self triggered electronics for CBM MuCh	153
Appendix B Effect of n-XYTER parameter (V_{th}, V_{bfb}) on detector characteristics	159
Appendix C Gain Comparison Between MCA and n-XYTER data	161
Appendix D Simulation result	163

List of Figures

1.1	Phase diagram of strongly interacting matter (QCD matter) [1]	3
1.2	Interaction rates for different experiments with the \sqrt{s} [2, 3, 4]. “STAR FXT” denotes fixed target operation of STAR experiment. NICA is fixed target experiment at JINR. CBM experiment at FAIR will be operated with highest interaction rate.	5
2.1	Yield of particles calculated from HSD transport [5] and statistical [6] models for central Au+Au collisions at 25 AGeV beam energy.	10
2.2	Layout of the FAIR experiment [7]	11
2.3	Total number of particles as a function of transverse length in Fe. The momentum were taken from the simulation of central Au+Au collisions at 25 AGeV.	17
2.4	Variation of particle multiplicity (primary + secondary) for central Au+Au collisions at 25 AGeV beam energy with thickness of iron absorber (left) and carbon absorber (right) event-by-event	18
2.5	Particle rate on detector stations of MuCh for Au+Au collision at 10 AGeV beam energy. The simulation has been performed using FLUKA	19
2.6	Schematic of MuCh setup	21
2.7	Schematic of MuCh setup for measurement of LMVM (left panel) and J/ψ in SIS100 facility	22
2.8	Schematic layout of the Muon Chambers (MuCh) with trapezoidal overlapping sectors.	23
2.9	Schematic of MuCh setup	24
2.10	Schematic picture of the segmentation of the modules. Entire area has been divided into projective pads of 1° angular regions in azimuth.	25
2.11	Schematic representation of the signal generation in GEM chambers	26

2.12	Illustration of digitization scheme for station 1(left panel) and station 2 (right panel)	27
2.13	Total charge created by the incident tracks inside the active volume of the detector. The gas depth is set to 3mm in simulation. The figure describes deposited charge versus particle kinetic energy for pions and protons. The black lines result from a Bethe-Block fit to the mean values.	27
2.14	Left: Charge deposition by a minimum ionization particle (MIP) in the gas volume of the detector. The mean gas gain has been set to to 10 ⁴ in simulation. Hence each MIP creates on the average about 33 primary electrons along its track inside the 3 mm gas volume. Right: Illustration of local maxima algorithm of hit finder.	28
2.15	Track visualization of one simulated central Au + Au collision at 25 AGeV	29
2.16	Mechanical layout of MuCh setup. Detector stations will be installed on super structure as shown. Cable carriers will be used for handling cables.	34
2.17	Three layers each stations are divided into two halves. Modules from each layer are attached on support structure. Half of the modules will be on one side of support and rest on other side.	35
2.18	Layout of the gas and water cooling system of MuCh. Left: One half portion of detector modules. Middle and Right: Schematic showing for gas, water connections.	36
2.19	Relative gain as function of rate for different detector technologies [8, 9]	37
3.1	Geometry of mCBM setup as implemented in the ROOT framework showing differ- ent detector subsystems at SIS18 facility of GSI. The beam enters from left	40
3.2	Left: Cluster size distribution for GEM1 plane in simulation. Right: Distribution of cluster charge for GEM1	40
3.3	Left: Distribution of number of hit per event (hit multiplicity) for GEM1 and GEM detector. Event-wise hit multiplicity correlation between GEM1 and GEM2.	41
3.4	X-Y distribution of GEM1 and GEM2 hits from simulation	41
3.5	Spatial correlation between GEM1 and GEM2 hit coordinates in X and Y from simulation	42
3.6	Spatial correlation between GEM1 and TOF hit coordinates in X and Y from sim- ulation	42

3.7	Track reconstructed using hits from 3 TOF planes and vertex ($z=0$). The distance between the nearest hit to the extrapolated track on GEM1 plane (left). Residuals in X (cm) (middle panel) and Y (cm) (right panel) at GEM1 plane with ~ 4 cm cut on distance.	43
3.8	2-D plot of residuals in X (cm) and Y (cm) at GEM1 plane with ~ 4 cm cut on distance.	43
3.9	Visualization of the spot size inside the detector	44
3.10	LMVM setup of CBM for SIS100. STS, MuCh, TRD and TOF subsystems are as indicated. 4 detector stations are used for MuCh	45
3.11	Closeup view of MuCh setup. 4 stations and 4 absorbers are used. First absorber is segmented in two parts as described in the main texts.	46
3.12	Distribution of residual of MuCh hits in x (cm) and y (cm)	46
3.13	Left: Variation of the residuals of MuCh hits in x (cm) with detector gain. Right: Variation of the residuals of MuCh hits in y (cm) with detector gain. The statistical errors are within point size.	47
3.14	Variation of the cluster size with gain. The statistical errors are within point size.	48
3.15	Left: Distribution of energy loss by charged particles from central Au+Au collisions at 8 AGeV beam energy for one module of station-I. Right: Multiplicity distribution of from set of data for one modules of station-I.	48
3.16	Momentum distribution (left) and transverse momentum (p_t) distribution (right) of input signal particles from Pluto generator. The statistical errors are within point size.	49
3.17	Left: Rapidity distribution of ω . The statistical errors are within marker size. Right: Y- P_t distribution of signal particles from Pluto generator.	50
3.18	Left: y- P_t distribution of signal particles after selection cut of STS+MuCh+TRD+TOF. Right: Invariant mass distribution spectra for omega meson.	50
3.19	Variation of ω reconstruction efficiency with gain for various spot size settings. The statistical errors are within marker size.	51
3.20	Left: Variation of S/N with gain for various spot size settings. Right: Variation of significance with gain for various spot size settings. The statistical errors are within marker size.	51

4.1	Stopping power for positive muons in copper as a function of $\gamma\beta$. Solid curves represents the total stopping power [10].	55
4.2	Energy loss of a MIP as a function of the atomic number of the medium [11]. The red line refers to the Argon (Z=18).	56
4.3	Absorption processes in photon interactions [9].	57
4.4	Gain-voltage characteristics for gaseous detectors showing the different operating modes [9]. The y-axis is refers to the collected charge in logarithmic scale.	60
4.5	Voltage divider schematic circuit for triple GEM detector.	64
4.6	Schematic of electron avalanche mechanism in triple GEM. The amplification happens primarily inside the GEM holes.	65
4.7	Schematic of the n-XYTER based readout system. The detector is connected directly to FEB which houses the n-XYTER ASIC and ADC. ROC as connected to the FEB is to control the data acquisition.	67
4.8	Left: n-XYTER calibration curve (taken from [12]). Middle: The gain vs ADC channel from n-XYTER in case the signal taken from ^{55}Fe . Middle: The gain vs ADC channel from n-XYTER in case the signal taken from charged particle (MIP). Statistical error bars are within the marker size.	67
4.9	Left: Schematic of the NIM-based readout chain.	68
4.10	Left: Calibration curve for NIM based DAQ. Error bars are within point size. Right: The gain vs ADC channel from MCA in case the signal taken from ^{55}Fe . Statistical error bars are within the marker size.	69
4.11	Photograph of experimental setup (left) and typical ^{55}Fe pulse height spectra (right).	69
4.12	Variation of Peak ADC channel with GEM voltage. Voltage of one GEM (say GEM1) varied keeping other (GEM2 and GEM3) fixed and vice-versa. Statistical error bars are within the marker size.	70
4.13	Left: Variation of photo-peak ADC channel and energy resolution as a function of combined GEM voltage (GEM1+GEM2+GEM3). Right: Variation of energy resolution with GEM voltage. Voltage of one GEM (say GEM1) varied keeping other (GEM2 and GEM3) fixed and vice-versa. Statistical error bars are within the marker size.	70
4.14	Variation of photo-peak ADC channel and energy resolution as a function of drift field (E_d). Statistical error bars are within the marker size.	71

4.15	Variation of Peak ADC channel and energy resolution with induction field. Statistical error bars are within the marker size.	72
4.16	Variation of Peak ADC channel and energy resolution with transfer field. Statistical error bars are within the marker size.	73
4.17	Schematic (left) and picture of test setup in lab.	73
4.18	Left: Distribution of time difference spectra between one scintillator to other scintillator, Middle: Distribution of time difference spectra between scintillator and GEM. Right: Variation of time resolution (σ) with high voltage. Statistical error bars are within the marker size.	74
4.19	Left: Pulse height distribution at GEM voltage ~ 1092 V for 3/2/2/2 gap configuration. Right: Channel hit distribution at GEM voltage ~ 1092 V for 3/2/2/2 gap configuration.	75
4.20	Variation of efficiency of GEM detector with GEM voltage ($\Delta V_{gem1+gem2+gem3}$). Statistical error bars are within the marker size.	76
4.21	Cluster size distribution at $\Delta V_{gem1+gem2+gem3} = \sim 1033$ V (left) and $\Delta V_{gem1+gem2+gem3} = \sim 1131$ V (middle). Right: Variation of cluster size with GEM voltage ($\Delta V_{gem1+gem2+gem3}$). Statistical error bars are within the marker size.	77
4.22	Event spread distribution at two different GEM voltage for 3/1/1/1.5 gap configuration. The left plot is for HV settings of 3000 V while middle one is for 3450 V. Right: Variation of average event spread with HV.	77
4.23	Left: Schematic of the uniformity scan measurement. Detector is divided in 16 zones. Right: Variation of efficiency over full active of the detector at GEM voltage 1102.7V.	78
4.24	Left: Variation of time resolution over full active of the detector at GEM voltage 1102.7V. Right: Variation of cluster size over full active of the detector at GEM voltage 1102.7V.	78
4.25	Left: Variation of efficiency with GEM voltage ($\Delta V_{gem1+gem2+gem3}$) for two gas gap configurations. Right: Variation of cluster size with GEM voltage ($\Delta V_{gem1+gem2+gem3}$) for two gas gap configurations. Statistical error bars are within the marker size.	79
5.1	Left: Gerber layout of real-size drift PCB with HV connections. Right: Picture of fabricated drift PCB with outer frame and spring contact soldered	83

5.2	Left: Gerber layout of real-size readout PCB with trapezoidal pads. Right: Photograph of the fabricated readout PCB.	84
5.3	Left: Large-size segmented GEM-top layer. Foil is divided in 24 segments Right: GEM-bottom layer. Divided in 4-segments	85
5.4	Left: Schematic of NS-2 stretching technique. A special screws mounted inside spacers for stretching the foils. Right: Schematic layout of assembly of different layers to build a final chamber	86
5.5	a) Part of the drift PCB showing spring contacts and brass support. b) Picture of leakage measurement setup in clean room. Leakage current measured for all 24 segments individually. c) Inner frames (spacers)	87
5.6	a) Placement of GEM foils and spacers. b) Cutting extra foil. c) Placement of three stack of GEM foils inside drift PCB for stretching and final assembly	88
5.7	a) Part of the chamber showing top screw and side screw. b) Tightening top screws. c) Stretching GEM foils by tightening side screws	89
5.8	a) Placement of outer frame (containing O-ring). b) Placement of readout PCB for final tightening of chamber. c) Final tightening chamber	90
5.9	Left: Experimental Setup in Lab. Middle: Typical ^{55}Fe with NIM based electronics. Right: Variation of photo-peak ADC channel with GEM voltage. Statistical error bars are within the marker size.	90
5.10	Left: Raw spectrum of ^{55}Fe . Middle: Baseline corrected spectrum of ^{55}Fe . Right: Variation of baseline corrected photo-peak ADC channel with GEM voltage. Statistical error bars are within the marker size.	91
5.11	Left: Variation of photo-peak with time. Middle: Variation of T/P(K/hPa) with time. Right: Variation of photo-peak with T/P(K/hPa). Statistical error bars are within the marker size.	91
5.12	Left: Variation of normalized photo-peak with time. Right: Variation of photo-peak at different position. Statistical error bars are within the marker size.	92
5.13	Left: Schematics of experimental setup at COSY, Jülich, Germany.	93
5.14	Left: Time correlation between triggered detector (hodoscope) and the GEM hits. Right: Variation of efficiency of the detector with time window (ns). Statistical error bars are within the marker size.	93

5.15	Left: Variation of detector gain with incident particle rate. Right: Variation of detector efficiency with incident particle rate. Statistical error bars are within the marker size.	94
5.16	Picture of test setup at H4 beamline of CERN-SPS.	95
5.17	Schematics of test setup (top) and DAQ (bottom)	96
5.18	Left: Picture of Fe absorber placed behind detector. Right: Spill structure seen on GEM2 plane	97
5.19	Results from the data. Left: Time difference spectra between GEM and diamond detector. Middle: Pulse height distribution with 3σ window of time correlation. Right: Hit multiplicity distribution	98
5.20	Left: Variation of σ with FEB number. Different FEBs are connected to different regions of the detector. Right: Variation of number of hit with time cut (see text). Statistical error bars are within the marker size.	99
5.21	Time difference spectra between one FEB with another FEB of same GEM plane before time-walk correction. Right: after time-walk correction.	100
5.22	a) Global X-Y distribution of detector hits. b) η - ϕ distribution of detector hits (Red-GEM1, Green-GEM2, Blue-GEM3).	101
5.23	Hit multiplicity correlation between GEM1 and GEM2 in same event (left) and in cross-events (right).	101
5.24	Residuals in X (mm) and Y (mm) at GEM1 plane	102
5.25	Left: Variation of cluster size with HV for the GEM2 plane. The pad size varies from $\sim 6.17\text{mm}$ to $\sim 6.72\text{mm}$ for this region. Right: Variation of the average hit with HV. Statistical error bars are within the marker size.	102
5.26	Spill structure showing noisy and non-noisy regions	103
5.27	Left: Distribution of number of digi/event. Right: Pulse height distribution	103
5.28	Hit distribution with and without 20 cm thick Fe absorber for GEM2 in data (left panel) and in simulation (middle panel). Right: Hit distribution with and without 20 cm thick Fe absorber data for GEM2, away from the absorber zone.	104
5.29	Schematic of HV layout on drift PCB	104
5.30	Picture of large size GEM foil with 24 segments	105
5.31	Schematic of voltage divider circuit for GEM with optocoupler for one half. Inset: Optocoupler schematic	106

5.32	Comparison of leakage currents of optocoupler before and after the irradiation. Statistical error bars are within the marker size.	107
5.33	Schematic (left) and picture (right) of the setup for spark tests with the optocoupler.	107
5.34	Comparison of leakage currents of optocoupler before and after the spark tests. Statistical error bars are within the marker size.	108
5.35	Comparison of peak pulse height at varying voltages with and without optocoupler. Statistical error bars are within the marker size.	109
5.36	Picture of the final drift PCB with optocouplers mounted on it	109
5.37	Schematic layout of assembly of different layers to build a final chamber	110
5.38	Left: ^{55}Fe pulse height spectrum from Mv2 module. Right: Variation of phot-peak ADC channel with HV. Statistical error bars are within the marker size.	111
5.39	Left: Schematic of chamber showing position numbers. Right: Photo-peak ADC at different regions of the detector. (without T/P corrected). Statistical error bars are within the marker size.	111
6.1	Conceptual sketch of the mCBM test setup. The detector subsystems are approximately positioned at 25° from the primary beam.	114
6.2	Left: Photograph of the experimental setup as of November 2019 showing the installed detector subsystems inside the mCBM cave at the SIS18 facility of GSI. Right: Closeup picture of two installed mMuCh modules.	116
6.3	Schematic picture of cooling plate. Circular drill for fitting copper tube. Water flows inside the copper tube.	117
6.4	Closeup photograph of the mMuCh setup along with other components. CROB, FEBs, LVDB is also shown.	118
6.5	Schematic setup of mCBM experiment as of November 2019 as per the realistic mCBM geometry implemented in ROOT. Detectors are placed at $\sim 25^\circ$ from the beam axis. The diamond detector (T0) is placed inside the target chamber. mSTS - mini-Silicon Tracking System, mMuCh - mini-Muon Chamber System, mTRD - mini-Transition Radiation Detector, mTOF - mini-Time Of Flight, mRICH - mini-Ring Imaging Cherenkov.	119
6.6	The block diagram of STS/MuCh-XYTER chip [13].	120

6.7	Schematic setup of the Data Acquisition System (DAQ) of the mCBM experiment [14].	120
6.8	Schematic setup of the Data Acquisition System (DAQ) of the mCBM experiment.	121
6.9	Schematic of data transport for CBM [15]	121
6.10	Top Left: Spill structure plot for all hits from one FEB (in 10 ms bins). Top Right: Variation of duplicate hits time with the channel number. Bottom Left: Spill structure after removing duplicate hits and noisy channels and the inset is for $1\mu\text{s}$ bin size. Bottom Right: Distribution of consecutive duplicate hits	122
6.11	Schematic of detectors showing pads row and col. numbers	123
6.12	Consecutive time difference spectra for several channels of GEM1. It is fitted with exponential function to extract the slope and finally the average rate.	124
6.13	Left: Variation of signal rate per unit area with sector number of pads for near (top-left) the beam pipe and away (bottom-left) from the beam pipe. Right: Variation of signal rate per unit area with sector number of pads for 0.25 mm (top-right) and 2.5 mm (top-right) target thickness.	125
6.14	Distribution of number of digis/TS for GEM1. Average signal and noise rate are calculated using this.	126
6.15	Distribution of number of Digi per TS for run numbers 162, 163, 165 and 166. . .	127
6.16	Digi correlation in time slice between T0 digi and GEM1 digi in a time slice. Top left panel is between GEM1 and T0 for low intensity, while bottom left is for high intensity. Top right panel is between GEM1 and GEM2 for low intensity, while bottom right is for high intensity	128
6.17	Left: Variation of digi counts with time, spill structure, for GEM1-raw (green), GEM1/GEM2 - noise subtracted and T0. Right: Channel hit distribution for one of the FEB's in beam-off condition. Black corresponds to the raw channel count, and red is after masking noisy channels. Only a few channels are found to be noisy.	129
6.18	Variation of ADC with the channel, off-spill (left) and on-spill (right), for GEM1 for 1100 time slices.	129
6.19	Left: Schematic of FEB numbering (detector slot number) for Mv2 module. Right: Variation of noise rate with detector slot number.	130

6.20	Left: Distribution of the number of digis per time-slice (Digi/TS) for GEM1 (red), GEM2 (blue) and T0 (black). Middle: Variation of the number of T0 Digi/TS with GEM1 Digi/TS (red) and the number of GEM2 Digi/TS with GEM1 Digi (blue). Right: Time difference distribution between one FEB of GEM1 with T0 before (blue) and after (red) offset correction (see text).	130
6.21	Left: Variation of the time difference between signals in GEM1 and one of the TOF modules (super module 0) with pulse height (in ADC unit) of GEM1. Middle: Variation of the mean (ns) of the time difference spectra with ADC before (upper triangle) and after (open circle) time-walk correction. The raw values are parameterized using a polynomial fit. Right: Variation of the time difference between GEM1 and one of TOF counter for different ADC values after time-walk correction.	131
6.22	Variation of σ with ADC bin. σ improves for higher charge signal as expected. . .	131
6.23	Left: Variation of the mean position (nano seconds) of time difference spectra for each ASIC before (open circle) and after (close circle) offset correction. Mean positions for a few ASICs are not shown here due to large offset value (which is in several μ s). Right: The variation of σ with ASIC number before (open circle) and after (close circle) time-walk correction. The ASIC Id for GEM1 is from 0 to 23, while those beyond belong to GEM2.	132
6.24	Mean and sigma of time correlation spectra of roughly 3000 channels measured from data.	133
6.25	Left: Time resolution map on GEM1 plane. The z-axis is the σ (ns) of each pad. Right: 1-D distribution of time resolution for all the pads before (Blue) and after (Black) time-walk correction.	134
6.26	Left: 2D scatter plot of mean ADC for each channels. The third axis is the ADC channel. Right: 1-D projection of mean ADC channel.	134
6.27	Left: Schematic of event reconstruction algorithm. Right: Variation of number of event reconstructed with the event time window at different selection condition. .	135
6.28	Variation of the number of T0 digi (top) and number of events reconstructed (middle) with TS number. The variation of the ratio of the number of reconstructed events to the number of T0 Digi/TS with TS (bottom).	136

6.29	Left: 1-D distribution of the ratio of the number of reconstructed events to the number of T0 Digi/TS. Right: Distribution of the number events reconstructed per TS.	137
6.30	Distribution of the event-size (number of Digi/event) (left) and time separation between the last Digi to the first Digi in the event (right).	137
6.31	Left: Distribution of the number of T0 Digi / event. Middle: Distribution of the number of Digi (black), Cluster (red) and Hits (blue) per event. Right: Time difference distribution between the hits of GEM1 with that of T0 digi in the event.	138
6.32	Time difference distribution between the hits of GEM1 with that of T0 digi (left panel) and between the hits of GEM2 with that of T0 digi (right panel) in the event.	138
6.33	X (cm)-Y (cm) distribution of hits for GEM1 (left) and GEM2 (right) after hit reconstruction	139
6.34	Left: Cluster size distribution for the entire GEM1 plane. Middle: Cluster charge (ADC) distribution for GEM1. The distribution is fitted with a Landau distribution. Right: Time separation of digis within clusters. The standard deviation yields to ~ 19 ns.	139
6.35	Cluster charge (ADC unit) distribution for all clusters (left panel) and for the cluster with single digi (right panel).	140
6.36	Left: Variation of relative regions of detector. Statistical error bars are within the marker size. Right: The schematic of different regions.	140
6.37	Left: Variation of cluster size at different granularity regions. Statistical error bars are within the marker size. Right: Table for granularity regions and their respective pad sizes.	141
6.38	Variation of cluster size with voltage (left). Variation of average Hit/event with GEM voltage. Statistical error bars are within the marker size.	141
6.39	The variation of gain (left) and time resolution (right) of the detector with the GEM voltages. Statistical error bars are within the marker size.	142
6.40	Spatial correlation in X (cm) and Y (cm) between GEM1 and GEM2 hits	142
6.41	Spatial correlation in X (cm) and Y (cm) between GEM1 and TOF hits.	143
6.42	Schematic picture of track fitting	143

6.43	Left: χ^2 distribution of track reconstructed using 3 TOF plane and GEM1 plane. Middle: The extrapolated Y (cm) vs X (cm) of the tracks at $z=0$ plane. Right: Residuals in X (cm) and Y (cm) at vertex ($z=0$).	144
6.44	Track reconstructed using hits from 3 TOF planes and vertex ($z=0$). The distance between the nearest hit to the extrapolated track on GEM1 plane (left). Right: Residuals in X (cm) and Y (cm) at GEM1 plane with ~ 4 cm cut on distance. . . .	144
6.45	Residual distribution at different granularities of GEM detector.	145
6.46	Hit coordinates of GEM detector for efficiency measurement. Black point represents the actual hit coordinate, red is for the extrapolated tracks, blue is for the hits nearest to the extrapolated track and green is for the nearest hit with 4 cm cut. . .	146
A.1	Threshold calibration of n-XYTER chip. Taken from [16]	154
A.2	Left: Experimental Setup in at VECC. Middle: Raw spectrum of ^{55}Fe . Right: Baseline corrected spectrum of ^{55}Fe	155
A.3	Left: Variation of baseline with V_{th} at different V_{bfb} . Right: Variation of MPV of the pulse height spectra with V_{th}	155
A.4	Left: Variation of baseline with V_{biasS} . Right: Variation of peak pulse height with V_{biasS} at different ΔV_{gem}	156
A.5	Variation of peak pulse height with ΔV_{gem}	157
B.1	Left: Variation of detector efficiency with V_{th} . Middle: Variation of average cluster size with V_{th}	159
B.2	Left: Variation of detector efficiency with V_{bfb} . Middle: Variation of average cluster size with V_{bfb}	160
C.1	^{55}Fe spectrum from MCA and n-XYTER	161
C.2	ADC and Gain variation with GEM voltage from MCA	162
C.3	ADC and Gain variation with GEM voltage from n-XYTER	162
D.1	Ratio of average particle rate on mMuCh in FLUKA simulation [17]	163

List of Tables

2.1	Table for particle rates on the detector stations for Au+Au collision at 10 AGeV beam energy using FLUKA	20
2.2	Table for the specification of absorber specifications for SIS100 LMVM. LD stands for Low Density	20
2.3	Table for the specification of absorber specifications for SIS100 J/ψ . LD stands for Low Density	21
2.4	Table for the specification of modules of the first two stations.	22
2.5	Comparison of rate handling capacity of various micro-pattern gas detectors	38
3.1	Optimized design of MuCh setup for SIS100 energy	45
3.2	Track selection cuts	49
5.1	Specification of two versions of real-size prototype triple GEM detectors	82
5.2	Table for sparks test of opto-coupler	108
6.1	Information about the beam in different beamtimes	115
6.2	Effect of beam intensity on average hit rate.	124
6.3	Effect of target thickness on average hit rate	125
6.4	Table for noise for different detector slot numbers	128

Preface

The understanding of physics is built on the interrelationship between theory and experiment. One needs experimental evidence to validate a theory, and the theory, in turn, helps to provide an explanation to the experimental results and helps in guiding new experimental ideas and techniques. One of the physics problems in HEP² is to understand the phase diagram (temperature vs baryon chemical potential) of QCD³ matter. Large-scale experiments are needed to explore the different phases of this QCD matter. In these large and complex experiments, where heavy ions collide at high energies (\sim GeV), various types of particles are generated. Different kinds of particle detectors are needed to identify and extract information from these particles.

This thesis was conducted in the framework of detector development based on GEM⁴ technology for the MuCh⁵ system of CBM⁶ experiment at FAIR⁷ facility of GSI, Germany. The aim of MuCh in the CBM experiment is to measure di-muon signals originating from nucleus+nucleus collisions. The work is mainly focused on building and testing large-size GEM detectors. The goal is to implement suitable detectors which can carry out the desired physics measurements in a high interaction rate and harsh radiation environment of the CBM.

The present thesis is divided into 8 chapters. In chapter 1, a general introduction to the research in heavy-ion physics and Quark-Gluon Plasma (QGP) has been discussed. It is expected that the QGP medium will be formed at moderate temperatures and high net-baryon densities achieved in the heavy-ion collision of the CBM experiment.

In chapter 2, the design of the CBM experiment at FAIR has been described. A brief description of the different detector subsystems of the CBM, MuCh system in detail, has been given. The GEM-based detector technology has been chosen for the first two stations of MuCh, which is

²High Energy Physics

³Quantum Chromo Dynamics

⁴Gas Electron Multiplier

⁵Muon Chamber

⁶Compressed Baryonic Matter

⁷Facility for Antiproton and Ion Research

discussed in the last section of chapter 2.

The performance of detectors in the simulation was studied with varying detector parameters and details are described in chapter 3.

The discussion on the gaseous detector, which is the preferred option for the CBM-MuCh, has been included in chapter 4. In this chapter, the general operation of gaseous detectors followed by laboratory test results of some of the detector prototypes have been discussed.

During the R&D process, we have tested several triple GEM detectors using radioactive sources (β and X-rays) in the laboratory and using particle beams at different accelerator facilities. A dedicated experiment, called mCBM⁸ as a part of the FAIR phase 0 program, has been set up at the SIS18 facility of GSI to test different detectors at high interaction rates as would be the case in the main CBM experiment. Real-size modules, as part of mMuCh⁹, have been installed and commissioned in the mCBM experiment. The discussion about the design, assembly and test of the real-size triple GEM prototype of MuCh has been given in chapter 5. The design of a novel optocoupler-based HV¹⁰ biasing scheme for the GEM modules has been presented in the second part of this chapter. Simulation using mCBM setup has been performed and details are given in chapter 3. The rigorous test results from mMuCh modules are described in chapter 6. In free-streaming data, for the first time in the mCBM experiment involving different detector subsystems, event building algorithm has been carried out. The spatial correction between the hits of different detector modules followed by track reconstruction has also been studied.

Chapter 7 summarizes the work that has been discussed in this thesis.

⁸mini-CBM

⁹mini-MuCh

¹⁰High Voltage

Chapter 1

Introduction to Heavy Ion Physics

The matter around us is composed of constituents whose properties, in thermal equilibrium, are described by certain macroscopic observables such as temperature, pressure, etc. For example, at STP¹, the gold is solid, water is liquid, and nitrogen is gas. The properties of matter change with these observables (control parameters) and can have different “phases” with the transition from one phase to another. The different phases of matter in thermodynamics are described in a graphical representation called a “phase diagram”. The phase diagram of water is the most common example. It exhibits mainly in three phases, namely, ice (solid), water (liquid), and steam (gas). More details about the phase diagram of water can be found in many standard books.

Similarly, nuclear matter, governed by the strong interaction, can have different phases depending on the temperature and the net-baryon density. Different phases of the strongly interacting matter can be created either by heating nucleons to extremely high temperatures or by compressing them to extremely high densities [18, 19, 20, 21, 22, 23, 24]. The framework of the relativistic quantum field theory, known as Quantum Chromo Dynamics (QCD) [25], describes the strong interaction in the standard model. QCD is formulated by demanding local gauge invariance under SU(3) gauge transformations in the color space of quarks [26, 27]. Quarks and gluons are the elementary degrees of freedom in QCD and exist in six flavors: up, down, charm, strange, top, and bottom. Quarks are bound together inside the hadrons (baryons and mesons) due to color confinement, and they are essentially free inside the hadrons due to the phenomenon of asymptotic freedom [28, 29]. Let us understand these phenomena qualitatively. The normal thermalized nuclear matter is made of nucleons of finite size (~ 1 fm) with density $\rho = \rho_0 = 0.16/\text{fm}^3$ and at a temperature of the order of few MeV. If the temperature of the system is increased at a constant

¹Standard Temperature and Pressure

volume by supplying heat to the system, new hadrons are created. Beyond a certain temperature, due to large energy density, the large number of hadrons so formed begin to overlap so that the quarks and gluons that were confined to single hadrons can move freely in a larger volume. Due to the overlap of the hadronic wave functions, the system can no longer be described in terms of nucleonic degrees of freedom, and the relevant degrees of freedom become quarks and gluons. This new state of matter is known as the Quark-Gluon Plasma (QGP). Similarly, the QGP can be formed by compressing the nucleons to a very high density.

1.1 Phase diagram of strongly interacting medium and QGP

Scientists over the world are involved in exploring the extreme conditions (high temperature and high net-baryon density) of the QCD phase diagram for the past few decades. The phase diagram of QCD matter i.e., temperature (T) vs. baryon chemical potential (μ_B), is shown in Figure 1.1. At high temperatures, where the net-baryon density is approximately zero, as per QCD calculations, the quarks are no longer bound, and the hadrons dissolve into quarks and gluons above a temperature of about 155 MeV [30, 31]. It is believed that this type of situation happened few microseconds after the Big Bang. In this region of the diagram, we expect a smooth crossover between the hadronic matter to a partonic matter [32]. At relatively large baryonic chemical potential, model calculations suggest a critical end point [33]. For higher μ_B and low temperature, we expect a first-order transition between hadronic and partonic phases. At moderate T and large μ_B , a new phase called quarkyonic matter exists beyond the first-order phase transition [34]. At very high net-baryon densities (rightmost portion of the figure), other types of transitions may occur with the formation of bosonic di-quarks, which is known as color superconductor [35, 36]. It is not easy to form a color superconductor in the laboratory at significant compression without heating. However, a strongly interacting high-density cold matter is expected to exist in the core of a neutron star. The primary goal of the heavy-ion experiment at intermediate energies is to explore the regions of high net-baryon densities.

1.2 QGP in lab: Relativistic Heavy Ion Collisions

One can create energy densities far above that of the normal nuclear matter by colliding relativistically two heavy ions. In an experiment, the idea is to accelerate heavy-ions to high speed (close to the velocity of light) and then collide them. After the collision, a fraction of kinetic energy is

goal of the upcoming NICA⁶ [44] (a heavy-ion collider project) at JINR⁷ Dubna is to search for the co-existence of the phases of nuclear matter.

However, beam energy is not the only parameter for investigating the dense nuclear matter. The beam intensity plays a crucial role in measuring the bulk observables and the particles for which the cross-section are extremely small, commonly known as rare probes. The global properties of the medium can be studied with the measurement of soft hadrons (bulk observables). The term “bulk” means that they directly characterize the global properties of the medium produced in the collision. The capability of handling the interaction rates for existing and planned heavy-ion experiments as a function of collision energy (\sqrt{s}) is shown in Figure 1.2. The CBM at SIS100 will be operated at unprecedented collision rates up to 10 MHz. The rate capability of other experiments is also shown in the figure.

The rare probes like ρ , ω , J/ψ , D likely to be produced early carry the information of the early phase of the collision systems. Moreover, the measurement of multi-differential observables such as the flow of the identified particles as a function of transverse momentum (p_t) of particles, mass distribution of di-leptons, and of heavy quark particles will provide information about the dense phase of the fireball evolution.

Measurement of rare probes with good statistics requires high collision rates, fast detection of particles, and a high-speed data acquisition system. The collider experiments are limited by their beam luminosity, while the detector rate capabilities are the main limitation of the fixed-target experiments. In a fixed-target experiment, one gets significantly high statistics of data due to higher interaction rates.

The program of the CBM⁸ experiment at FAIR⁹ [45] is dedicated to the measurement of both the rare probes and bulk properties with unprecedented statistics. This will be achieved using high-intensity beams along with a high-rate detector system.

The CBM [46, 47, 48] is a fixed target heavy-ion experiment designed to investigate the properties of dense nuclear matter at FAIR [49] accelerator center in GSI, Darmstadt, Germany. The primary goal of the CBM experiment is to explore the QCD phase diagram at low temperature and high net baryon densities by colliding heavy-ions beams in the energy range of 2-14 AGeV (SIS100 setup). The model calculation predicts that a density of $4\text{--}5\rho_0$ can be achieved in the center of the

⁶Nuclotron-based Ion Collider fAcility

⁷Joint Institute for Nuclear Research

⁸Compressed Baryonic Matter

⁹Facility for Antiproton and Ion Research

reaction zone at these energies. This will open up the possibility to understand the properties of the core of neutron stars. On the other hand, the RHIC and LHC experiments, complementary to CBM, are devoted to studying the QCD phase diagram for high temperature and nearly zero baryon densities.

A precursor experiment called mini-CBM has been set up at the SIS18 facility of GSI to test different detector subsystems of CBM at high interaction rate along with data transport to long-distance, online/offline data analysis, data acquisition system, etc. This will be helpful at the time of the final commissioning of detector subsystems in the main CBM experiment. In this regard, real-size GEM modules have been installed and commissioned in the mCBM experiment. The simulation response of mMuCh modules has been discussed in chapter 3 and the detailed test of these modules in nucleus+nucleus collisions has been described in chapter 6.

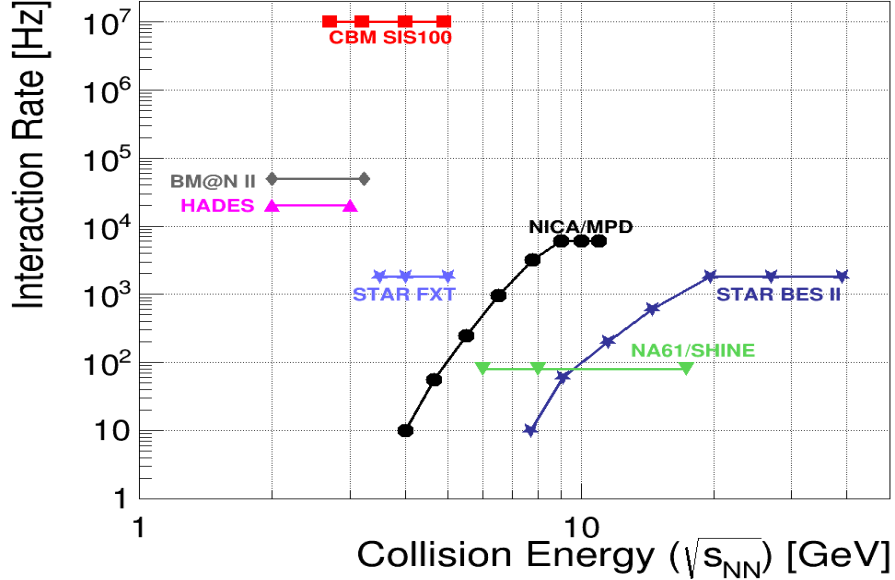


Figure 1.2: Interaction rates for different experiments with the \sqrt{s} [2, 3, 4]. “STAR FXT” denotes fixed target operation of STAR experiment. NICA is fixed target experiment at JINR. CBM experiment at FAIR will be operated with highest interaction rate.

1.3 Signatures of phase transition

In this section, various experimental signatures which would indicate the formation of QGP are described. One cannot detect QGP directly due to the very short life time of the fireball but can be indirectly studied by looking at the signals which are linked to the evidence of QGP. Different probes for the QGP have been proposed over the past decades [50, 51, 52, 53, 54, 55, 56, 57], which

we believe carry experimental signatures for de-confined transition.

The main signatures describing the properties of the medium produced in A-A collision are:

- Strangeness enhancement as compared to pp collisions [58, 59, 60, 61, 62, 63, 64]
- Quarkonium suppression, Jet Quenching [65, 66, 67, 68, 69, 70, 71]
- High values of the anisotropic flow coefficient [72, 73, 74, 75, 76, 77],
- Characteristic correlation and fluctuations [78, 79, 80, 81, 82, 83, 84] measured for produced particles
- Emission of photons & di-leptons from thermal —

The MuCh system aims to measure di-muons, so the main focus in thesis is given on the di-leptons and quarkonium physics as described in the subsections below.

1.3.1 Lepton pairs

Di-leptons created in high-energy heavy-ion collisions offer a unique opportunity to understand the properties of the strongly interacting matter. The electromagnetic radiation (virtual photons) is emitted in nuclear collisions during the whole time evolution of the system [85, 86]. These photons, once produced, decay into di-electron or di-muon channels. Hence, the study of these leptonic decay channels can provide information about the fireball at high temperatures and density. The mean free path of photons (10^2 - 10^4 fm) at the highest temperature and density is much larger than the fireball size (~ 10 fm), thereby they do not suffer any further interaction, thus carrying the information about the initial state of the system. They (di-leptons and photons) are known as “penetrating” probes of hot and dense matter. Measurement of photons and di-leptons provides information about the average temperature of the system created in the collision. They can also give information about the other aspects of the collisions, like (i) formation of QGP [87] using the measured elliptic flow of photons as well as momentum anisotropy of the initial partons, (ii) system size, among others.

Di-leptons are emitted at every stage of the heavy-ion collisions and from different sources [48]. The two parameters, namely the invariant mass (M) and the transverse momentum (p_T) of the di-leptons, can be used for investigating the different stages of the fireball. High p_T and large invariant mass di-leptons are created at the early phase of the collision system, where the temperature of the system is large. On the other side, low invariant mass lepton pairs come from the stage where the temperature is relatively smaller. Annihilation of quark-antiquark pair ($q + \bar{q} \rightarrow l^+ + l^-$, q

$+ \bar{q} \rightarrow g + l^+ + l^-$) and Compton scattering ($q(\bar{q}) + g \rightarrow q(\bar{q}) + l^+ + l^-$) phenomena are the most significant sources of the di-leptons. Direct decay of hadronic resonances likes ρ , ω , ϕ , J/ψ , ψ' etc. and Drell-Yan processes also produce di-leptons pairs. There are also contributions from the Dalitz decays like $\pi^0 \rightarrow e^+ + e^- + \gamma$, $\omega \rightarrow \pi^0 + e^+ + e^-$, $\eta \rightarrow e^+ + e^- + \gamma$.

The di-lepton spectrum is divided into three regions depending on the invariant mass, namely, a) Low Mass Region (LMR): $M \leq M_\phi$ ($=1.024$ GeV), b) Intermediate Mass Region (IMR): $M_\phi < M < M_{J/\psi}$ ($= 3.1$ GeV) and c) High Mass Region (HMR) : $M \geq M_{J/\psi}$.

Till now, no di-lepton data are available for beam energies between 2-40 AGeV. The CBM experiment will perform the multi-differential measurement of di-leptons over the full range of invariant mass emitted from the fireball. The invariant mass spectra will have a contribution from the various processes [88], as per the model calculations [48]. The thermal radiation includes radiation from the QGP [89], broadened in-medium ρ meson [90, 91, 92, 93, 94], and lepton pairs from multi-pion annihilation processes [95, 96]. The di-leptons from multi-pion annihilation reflect ρ -a1 chiral mixing and directly linked to chiral symmetry restoration. The experimental challenge in measuring these are the very low signal cross-section, decay probabilities are of the order of 10^{-4} , and the large combinatorial background.

1.3.2 Quarkonium suppression

The quarkonium is a bound state of heavy quarks and its anti-quarks. They are collectively known as quarkonia. Bound state of charm and anti-charm is known as charmonia and bottomonia for the bottom quarks and anti-bottom quarks. The properties of the quarkonia state are determined by the strong force, which is analogous to the positronium (bound state of e^+ and e^-) states governed by the electrostatic Coulomb force. J/ψ and Y are the vector mesons (spin-one) particles whose ground states belong to the family of the charmonium and bottomonium, respectively [97, 98, 99].

Matsui and Satz argued in their paper [100] that the QGP medium would suppress the production of J/ψ and other resonances of the quarkonium due to the Debye screening from the free color charges. Depending on the binding energy of the different quarkonium states, the magnitude of the suppression will be different. The strongly bound states (such as Y) will have less or no modification [101]. Suppression of J/ψ yield would be either due to $c\bar{c}$ pair fails to form a J/ψ or due to produced J/ψ dissolves in its subsequent interaction with the medium.

Charmonium (J/ψ) and low mass vector mesons (ρ , ω , ϕ) are one of the fundamental penetrating probes to understand the initial state of the collision system, which will indicate the

occurrence of de-confinement phase transition from hadronic to the quark-gluon degree of freedom. The production cross-section of these particles is extremely small at FAIR energies. So, the main challenge is to identify these penetrating probes in heavy-ion collisions. In CBM, the unprecedented interaction rate of ~ 10 MHz will open the possibility to measure these particles with high precision. The produced particle densities will be very high at such high interaction rates, so we need high rate detectors to handle such a harsh environment. The detectors of Muon Chamber (MuCh) systems are being developed at VECC¹⁰, which will be used for the detection of di-muon pairs [48] originating from these nucleus-nucleus collisions. More details about the physics of CBM and MuCh system are described in chapter 2 and also can be found in [46, 102]

1.4 Summary

The basic physics of the QGP formation and its signatures are described. The main emphasis is given mainly on di-lepton physics. However, one can find more details about these in the given references. In chapter 2, the CBM experiment and the MuCh system have been described in detail.

¹⁰Variable Energy Cyclotron Centre

Chapter 2

The Muon Chamber (MuCh) system of Compressed Baryonic Matter (CBM) experiment

In chapter 1, we have discussed the theoretical understanding of strongly interacting matter and how we can create this in the laboratory. We also discussed the signatures of QGP, mainly the di-lepton and quarkonia suppression. In this chapter, the details about the CBM experiment and the conceptual layout of the full setup, including other detector subsystems, are described. The goal of the CBM is to measure charged-particle multiplicities, phase-space distributions and flow of protons, pions, kaons, hyperons, hadronic resonances, light vector mesons, charmonium, and open charm, including their correlations and event-by-event fluctuations in heavy-ion collisions [48]. The technical challenge is to identify both hadrons and leptons and filter out rare probes at unprecedented reaction rates of up to 10 MHz. Measurements at such a high rate can not be performed with slow detectors like the Time-Projection Chambers (TPC) but rather require extremely fast and radiation hard detector (and electronic) components. Moreover, the experiment has to measure leptons, high-resolution secondary vertex, and requires a high-speed trigger and data acquisition system. The CBM detector system will have the capability to measure both electrons and muons. This approach combines the advantages of both methods and guarantees reliable results. In the end, both data sets should agree with each other despite the very different background sources.

The main experimental difficulty is to measure multi-differential observables and the particles having very low production cross-sections such as particles with charm quark, multi-strange (anti-)

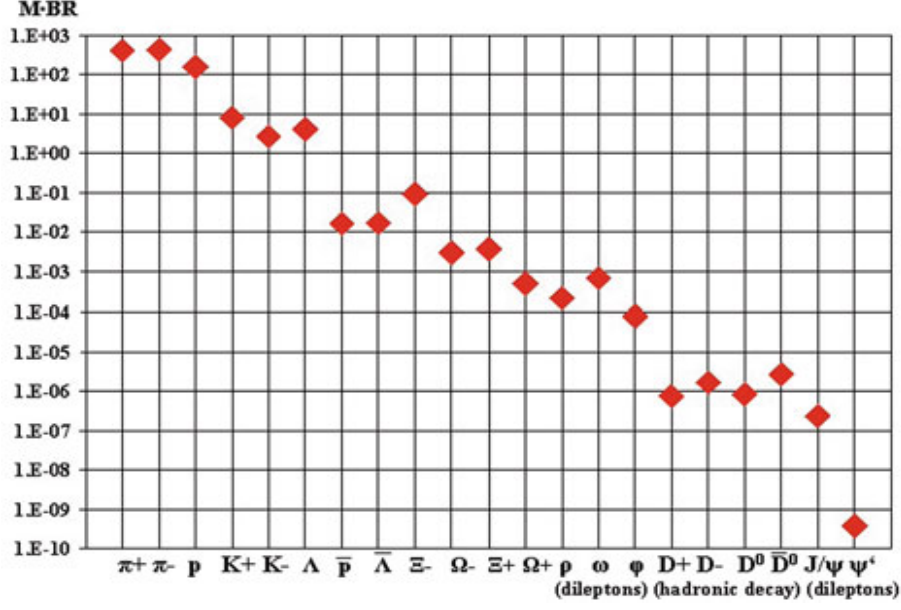


Figure 2.1: Yield of particles calculated from HSD transport [5] and statistical [6] models for central Au+Au collisions at 25 AGeV beam energy.

hyperons, and di-leptons with high precision. The yield of particles are calculated by multiplying the multiplicity and branching ratio. The yield for various particles for central Au+Au collisions at 25 AGeV beam energy is shown in Figure 2.1.

The data points are obtained using HSD transport code [103] and thermal model with corresponding temperature and baryon-chemical potential [5]. The yields of charmed mesons are lower by about nine orders of magnitude than that of pions (except for the ψ' meson, which is suppressed even more). The di-lepton yield is six orders of magnitude lower than that of pion, similar to the yield of multi-strange anti-hyperons.

2.1 The experiment at the Facility for Antiproton and Ion Research (FAIR)

The FAIR facility comprises of synchrotron with a magnetic rigidity of 100 Tm (SIS100). This facility includes four experiments, namely, the CBM experiment, the PANDA detector for hadron physics experiments, the NUSTAR for nuclear astrophysics &, and Plasma Physics & Atomic Physics experiments. The available kinetic beam energy per nucleon depends essentially on the bending power $B \cdot r$ provided by the dipole magnets:

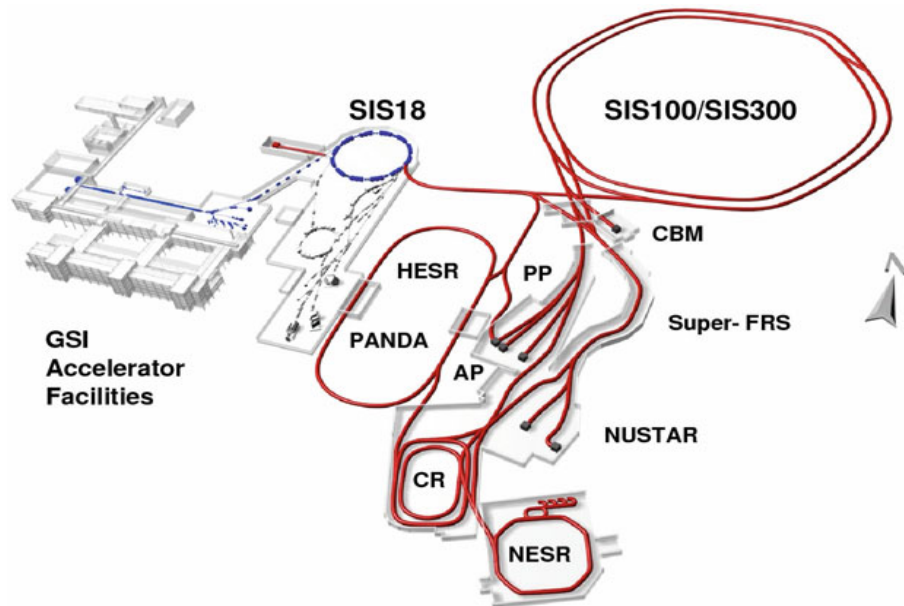


Figure 2.2: Layout of the FAIR experiment [7]

$$E/A = \sqrt{(0.3 \cdot B \cdot r \cdot Z/A)^2 + m^2} - m \quad (2.1)$$

With Z and A being the charge and the atomic number of the ion, and m being the mass of the nucleon. The minimal available ion beam energy is about 2 AGeV. The layout of the FAIR facility along with the experimental sites is shown in Figure 2.2.

2.1.1 Physics of Compressed Baryonic Matter (CBM) experiment

CBM SIS100 setup

The SIS100 accelerator ring will provide different beams of kinetic energy up to 11 AGeV for Au, 14 AGeV for Ca, and 29 GeV for protons. The energy densities up to 2.5 GeV fm^{-3} and a baryon density of 2-7 times normal nuclear matter density is expected at the center of the reaction zone according to the transport model calculations. Such situations are likely to happen in the core-collapse supernovae and at the core of neutron star. Measurement at SIS100 will provide information on the transition region of the QCD phase diagram. In this setup, the following important investigations of the QCD phase diagram at high net baryon density will be performed, like the first-order phase transition and the critical endpoint, equation-of-state of high dense baryonic matter, and the search for modifications of hadronic properties in the dense medium as the likely signature of chiral symmetry restoration.

2.2 CBM Detector Sub-systems

We discuss here the different detector subsystems of the CBM experiment.

Dipole Magnet

The dipole magnet of CBM has a large aperture of 25° polar angle in both positive and negative directions. It will provide a magnetic field of 1 Tm and will be superconducting in order to reduce operating costs. More details can be found in [104].

Micro-Vertex Detector (MVD)

The MVD detector system is needed to measure the secondary vertices of the short-lived particles like D mesons with high spatial resolution. It comprises of two layers of ultra-thin and highly-granulated Monolithic Active silicon Pixel Sensors (MAPS) located at 10 cm and 20 cm downstream to the target.

The lifetime of D mesons are $\tau = 123 \mu\text{m}/c$ for D^0 and $\tau = 314 \mu\text{m}/c$ for D^\pm and it decays into pions and kaons via weak hadronic decay. The measurement of these short-lived particles requires detectors with outstanding position resolution and low material budget (to reduce multiple scattering). The MAPS technology fulfills these requirements. One can achieve a position resolution of $\sigma = 3 \mu\text{m}$ using these sensors of size $40 \times 40 \mu\text{m}^2$. The total material budget in this, including support structure, will be of the order of 300 μm silicon equivalent. More details about MVD can be found in yearly CBM progress reports [105, 106, 107, 108, 109].

Silicon Tracking System (STS)

The STS system is at the heart of the CBM experiment, which will be installed inside the large acceptance dipole magnet. It consists of low-mass silicon micro-strip detectors. The aim of the STS system is to measure the momentum of the charged particles by reconstructing tracks. This system allows the track reconstruction in the momentum range of 100 MeV/c up to 10 GeV/c. The current design of the STS has 8 tracking layers, and they will be placed downstream the target, roughly at a distance of 30 cm for the first layer and 100 cm for the last layer. Momentum resolution ($\Delta p/p$) is of the order $\sim 1\%$ is required for good track & momentum resolution.

The STS will use silicon micro-strip detectors which will be read out using micro-cables with fast and radiation hard electronics at the periphery of the stations. These micro-strip sensors will be double-sided with a stereo angle of 15° , the pitch of 60 μm , the length between 20 and 60 mm, and thickness of 250-300 μm . The material budget of the detector, including the support structure about 800 μm silicon equivalent. More details can be found in [110].

Ring Imaging Cherenkov Detector (RICH)

The identification of electrons will be performed using the RICH detector in the momentum range below 8 GeV/c. It comprises of a 2.9 m long gas vessel filled with N₂ as a radiator material and two photo-detector planes. Each consists of Hamamatsu multi-anode photomultipliers with size $1.7 \times 0.7 \text{ m}^2$. More details can be found in [111].

Muon Chamber (MuCh) System

The MuCh systems will be used to measure di-muons, and they will be placed downstream to the STS at the position of RICH. MuCh consists of segmented absorbers, and the triplet of the detector layers will be placed in between these absorbers. This novel scheme allows momentum-dependent muon identification. The challenge in the muon measurement at FAIR is to identify low-momentum muons in high particle density environment.

The absorber and detector system should be as compact as possible to reduce the meson decays into muons. The MuCh system for the SIS100 setup consists of 4 absorbers and 4 detector stations (12 tracking layers) behind each absorber.

The large particle density imposes a challenge for the MuCh setup and for the track reconstruction algorithms. For the first two stations, which face a high radiation environment, have a peak particle density of 400 kHz/cm² (maximum for the inner segments of the first station) for Au+Au minimum bias collisions at 10 AGeV beam energy. Therefore, a high rate detector based on Gas Electron Multiplier (GEM) technology will be used for the first two stations. More details about the MuCh system are described in this chapter and also can be found in [112].

Transition Radiation Detector (TRD)

The TRD detector subsystem will be used for the identification of electrons and positrons with momentum $> 1.5 \text{ GeV}/c$ ($\gamma > 1,000$). It consists of 3-4 detector layers, positioned at 5 m, 7.2 m, and 9.5 m downstream to the target, respectively. The approximate active area of the TRD systems is about 1100 m². More details about the TRD system can be found in [113].

Time-of-Flight (TOF)

An array of Multi-gap Resistive Plate Chambers (MRPC) will be used for hadron identification via time-of-flight (TOF) measurements. The active area of the TOF detectors will be about 120 m², which will be located downstream to the target by about 10 m. The time resolution requirement for the TOF is of the order of 80 ps. The detector has to handle particle rates up to 20 kHz/cm² for the 10 MHz minimum bias Au+Au collisions in the innermost regions. The details about the TOF system can be found in [114].

Electromagnetic Calorimeter (ECAL)

The ECAL detector system will be used to measure direct photons and photons that decay from neutral mesons (such as π , θ , η). The module of ECAL consists of 140 layers of 1 mm lead and 1 mm scintillator, having a cell size of $3 \times 3 \text{ cm}^2$, $6 \times 6 \text{ cm}^2$, and $12 \times 12 \text{ cm}^2$. More about the ECAL system can be found in the yearly CBM progress reports [105, 106, 107, 108, 109].

Projectile Spectator Detector (PSD)

As the name suggests, this detector will be used to measure the number of non-interacting nucleons from a projectile nucleus in nucleus-nucleus collisions. These measurements will provide information about the orientation of the reaction plane and determine the collision centrality. The analysis of event-by-event observables requires very precise characterization of event class, and the study of collective flow desires a well-defined reaction plane. It consists of 60 lead/scintillator layers with a surface area of $10 \times 10 \text{ cm}^2$. The details about the PSD system can be found in [115].

Online event selection and data acquisition

High statistics measurements of rare probes require high reaction rates. The CBM detectors, the online event selection systems and the data acquisition will be designed for an event rate of 10 MHz, corresponding to a beam intensity of 10^9 ions/s and a 1% interaction target. For example, assuming an archiving rate of 1 Gb/s and an event volume of about 40 kB for minimum bias Au+Au collisions, an event rate of 25 kHz can be accepted by the data acquisition. Therefore, measurements with event rates of 10 MHz require online event selection algorithms (and hardware) which reject the background events (which contain no signal) by a factor of 400 or more.

2.3 Measurement of di-muons at FAIR

One of the sensitive diagnostic probes of the medium formed inside the fireball is the di-leptons emitted from the N-N collisions. The following are the most interesting source of the di-leptons.

2.3.1 Low Mass Vector Mesons (LMVM)

The ρ^0 , ω , and ϕ particles are known as the LMVM. The ρ^0 meson, in particular, has a short lifetime, and it decays inside the fireball. The properties of the ρ^0 meson changes in this hot and dense medium. This type of in-medium modification is expected when chiral symmetry is restored.

The NA60 collaboration has measured the di-muon spectra for In+In collision at 158 AGeV beam energy and the results can be found in [116, 117]. Calculations of R. Rapp [118] suggests

that, for low mass region ($< 0.8\text{GeV}/c^2$), the ρ^0 resonance is theoretically compatible with the chiral symmetry restoration [119].

2.3.2 Charmonium

Heavy quarks, produced predominately in the hard scattering in the initial phase, are one of the distinctive probes to explore the properties of the QGP produced in the heavy-ion collisions. Charmonium (bound state of $c\bar{c}$) is exposed to the highest temperature and density. The dissociation of charmonium (predicted to occur due to color screening in de-confined medium) can be studied to extract information about the medium formed [100].

The suppression of charmonium was studied by the NA50/NA60 collaborations for Pb+Pb and In+In collisions [120]. They observed an anomalous suppression of the order of 20-30% for central Pb+Pb collisions.

The challenging task is to measure charmonium at FAIR energies due to the very low charm production cross-section. The charm production cross-section has been calculated by Frawley and can be found in [121]. There is no charmonium data at FAIR energies ($\sqrt{s_{NN}} < 8\text{ GeV}$). Precision data at these energies are needed to clarify the production mechanism of charm at an energy close to the production threshold energy.

2.3.3 Thermal Radiation

The thermal EM radiation, which gets converted into lepton pairs, provides the temperature of the fireball medium. This type of radiation is emitted at every stage of the collision dynamics and gives integrated information on the temperature evolution. One can find the theoretical basis in more detail in [118] also in [122, 123].

2.4 Muon Chamber (MuCh) of CBM

2.4.1 Conceptual layout of MuCh system

The detection of muons in any HEP experiment uses the following general philosophy. A thick absorber material with high Z value is used to absorb hadron backgrounds and it is placed before the detector tracking stations. The idea is that all the other particles get absorbed inside the absorber, and the muons pass through it due to their highly non-interacting nature. How we decide which kind of absorbers and what will be the thicknesses of the material used, depend on

the hadron interaction length (λ_I) of the material. λ_I depends on the total inelastic cross-section for hadron nucleus interaction and the density of material [124]. One can calculate empirically the hadronic interaction length as: $\lambda_I \sim 35 A^{1/3} \text{ gm cm}^{-2}$.

The muon setup of the CBM experiment is designed to cope up with huge background radiation produced in heavy-ion collisions. The following design considerations have been taken for the detection of di-muons in such an environment, a) the total space should be as minimum as possible in order to minimize the combinatorial background, and the λ_I should be as low as possible. b) the mass resolution should be as good as possible so that one can resolve between ψ' and J/ψ as well as ϕ and $\rho+\omega$. c) In such a high interaction rate, it is demanded to have detectors that can handle such rates, particularly for the first two stations of MuCh (which are closest to the target).

As discussed in chapter 1 and also in the previous section of this chapter, the main experimental challenge for the muon measurement in CBM experiment at FAIR energies is the identification of low momentum muons, which originates from the LMVM in a very high particle density environment. The novelty of muon measurement in the CBM experiment from the other experiment is the following. The total absorbers in the CBM muon system will be sliced, and the detector stations will be placed in between the absorber stations. However, in muon systems of other HEP experiments, the absorbers are not sliced, and the detectors stations are placed at the end of the absorber. This novel feature of the MuCh system facilitates momentum-dependent track identification. This way, one can improve the measurement of low momentum muons, which the single thick absorber would have otherwise stopped.

The MuCh system layout, like the number of detector layers/stations, the thickness of the absorbers material, and the granularity of the detector modules has been optimized from the response simulation in the CBM setups. The simulation has been performed for Au+Au collisions at different beam energies. The UrQMD [125] event generator was used for the input particle, and the GEANT3 [126] transport engine is used for the transport of particles through the setup. We have chosen Fe as the principal component for hadron absorbers such that they can be absorbed before their decay into muons. The main contribution of the background muons comes from the weak decays of pions and kaons.

In addition to λ_I , the multiple scattering suffered by the muons should be small to reduce the fake matches of tracks. The mass resolution is directly related to the multiple scattering. We have to compromise between the interaction length and radiation length ($X_0 \propto A/Z^2$). λ_I should be as small as possible to absorb hadrons, and X_0 should be as large as possible to reduce the multiple

scattering.

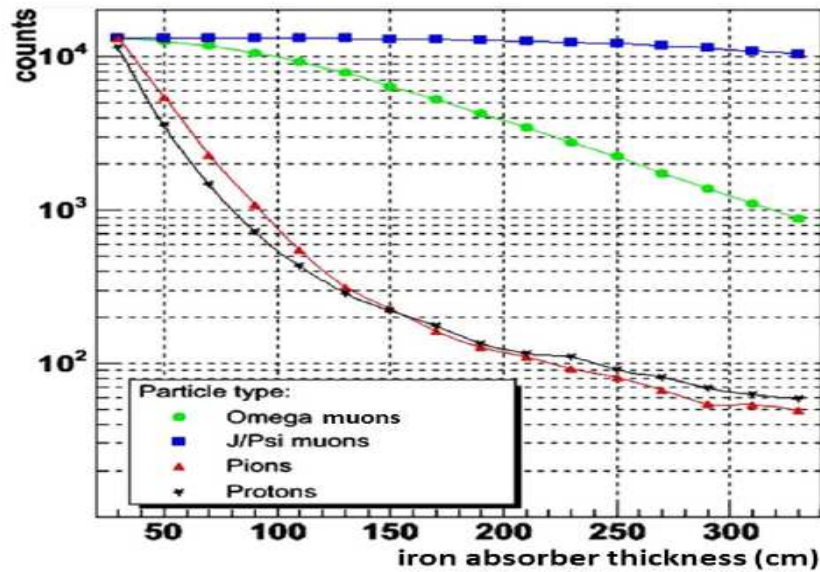


Figure 2.3: Total number of particles as a function of transverse length in Fe. The momentum were taken from the simulation of central Au+Au collisions at 25 AGeV.

The multiple scattering is inversely proportional to β , momentum (p) and X_0 . Fe has been found to be the optimum material for the absorber if we compare different materials for their interaction length and radiation length. Figure 2.3 shows the total number of the particles as a function of the thickness of the Fe absorber. One can estimate the required thickness of the hadron absorbers for the measurement of LMVM and charmonia from this figure. As can be seen from the figure, the muons from the J/ψ can go up to a distance of 250 cm in Fe absorber without a significant suppression, while the muons from ω particle gets absorbed in such thick absorber by a factor of about 10. It can also be seen that beyond thickness of 1.5 m, muons from ω get absorbed as pions and protons. This implies that the “signal-to-background ratio” (S/B) will not improve further if we add extra material beyond 1.5 m. So, for efficient measurement of LMVM’s, the Fe absorber thickness should not exceed 1.5 m. However, for the J/ψ detection, one should add an extra Fe absorber of ~ 1 m thickness in conjunction with the number of detector layers.

In addition to total absorber thickness, one also has to optimize the thicknesses of individual absorber layers in MuCh, where a compromise between hadron absorption and multiple scattering is needed, in particular for the first absorber. A thick absorber helps in reducing the hadron background. On the other hand, a thick absorber increases the probability of multiple scattering, and for a given thickness, multiple scattering increases with Z , hence, the number of mismatched

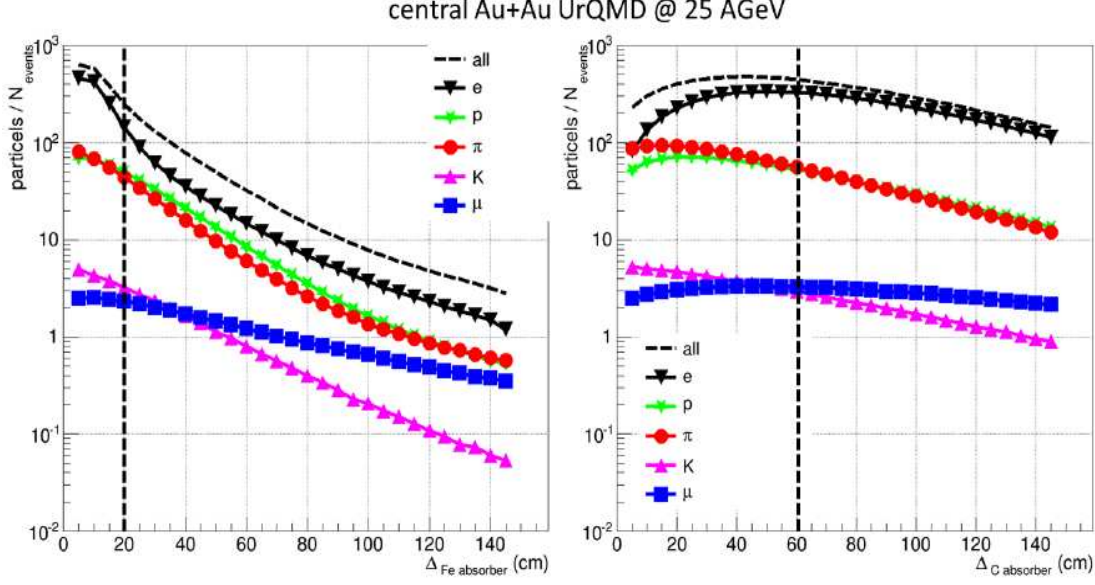


Figure 2.4: Variation of particle multiplicity (primary + secondary) for central Au+Au collisions at 25 AGeV beam energy with thickness of iron absorber (left) and carbon absorber (right) event-by-event

tracks.

From the simulation, it was optimized that a 20 cm thick Fe absorber will be good for the first station of the MuCh system. The other option for the first station absorber can be carbon (graphite block). The 60 cm of carbon is equivalent to 20 cm Fe in terms of interaction length. Figure 2.4 shows the particle multiplicity for Au+Au collision at 25 AGeV beam energy as a function of carbon and iron absorber thickness. We can observe from the figure that the Fe of 20 cm thickness has similar hit multiplicity as compared to that due to the carbon of 60 cm thickness [127]. As per the recent design of CBM, the first absorber will be placed slightly inside the magnetic field. Hence, taking these considerations along with the aspect of mechanical integration, carbon is preferred over Fe. The other advantage of carbon is the large radiation length, and the multiple scattering will be less. The rest of the absorbers (other than station-I) will be made of slices of Fe to maintain the compactness of the total detector system, which will reduce the meson decays.

Due to the manufacturing constraint, availability, and practical considerations, the first absorber is divided into two pieces. The first absorber will be made of a combination of low density (LD) graphite and concrete blocks. The 28 cm LD graphite will be placed inside the magnet, and 30 cm of concrete will be placed outside the magnet. As discussed, the Fe absorbers will be outside the magnet, but they will be made of stainless steel (which is non-magnetic in nature) instead of soft iron to avoid any residual magnetic field.

2.4.2 MuCh Setups

As already discussed, the MuCh system in CBM will have a segmented absorber with detector stations placed in between the absorbers. The absorber material, its thickness, etc., has been optimized by performing simulation in a CBMROOT environment. The schematics of the MuCh setup for heavy-ion collisions at SIS100 energies is shown in Figure 2.6. It consists of 5 absorbers and 4 detector tracking stations. The specification of the absorbers and detector stations are given in table 2.2 and in table 2.3. Each tracking station consists of three detector layers which are located in the air gap after each absorber. The air gap between two successive absorbers has been optimized to 30 cm. The total number of detector layers is 12 (3 in each station) for the SIS100 setup. A 30 cm gap between the absorbers is required to accommodate the total detector profile, including detector electronics, cooling arrangement, and mechanical structure. The total absorber length for SIS100 setup is ~ 240 cm ((28 cm LD graphite + 30 cm concrete) + 20 cm Fe + 30 cm Fe + 30 cm Fe + 100 cm Fe). The angular acceptance of the detector is from $\pm 5^\circ$ to $\pm 25^\circ$.

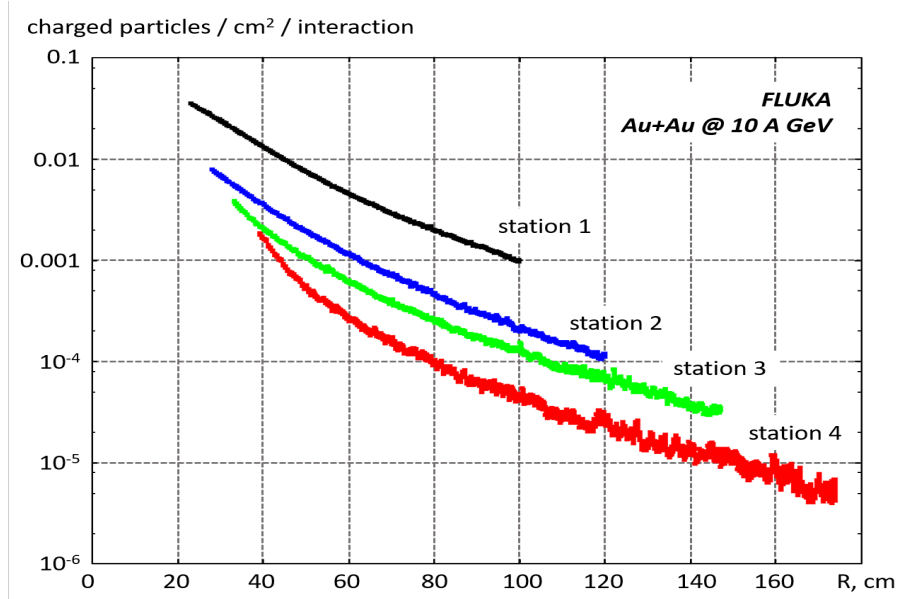


Figure 2.5: Particle rate on detector stations of MuCh for Au+Au collision at 10 AGeV beam energy. The simulation has been performed using FLUKA

Simulation has been performed to measure the particle rates falling on the detectors stations using FLUKA for Au+Au collisions at 10 AGeV beam energy. The particle rate distribution as a function of radial distance shown in Figure 2.5. As expected, the particle rates on the first two stations are higher compared to that for other stations. The maximum rates for each station are summarized in table 2.1. The radiation dose level has been calculated using FLUKA simulation

and it has been that the expected neutron dose is $\sim 10^{12}$ n_{eq} /cm² and Gamma dose is about 30 krad equivalent to ten years of operation in CBM.

In the current design of MuCh, the Gas Electron Multiplier (GEM) detector technology will be used for the first two stations due to high particle rates. A detector based on Resistive Plate Chamber (RPC) detector technology would be employed for the 3rd and 4th stations. The detailed discussions about the MuCh simulation and optimization of the absorbers and detectors can be found in the Technical Design Report (TDR) of MuCh [112] and in the MuCh section of the annual CBM progress report [105, 106, 107, 108, 109]. The active gas-thickness of 3 mm has been used in the simulation for GEM detectors. The cables, electronic components, are yet to be included in the simulation. The distance between the detector layers is 10 cm, and the space of 5 cm is given between the end of the absorber to the nearest detector layer. A realistic detector geometry such as the PCBs (drift and readout) has been implemented. Each module consists of a trapezium and has sector shape geometry.

Table 2.1: Table for particle rates on the detector stations for Au+Au collision at 10 AGeV beam energy using FLUKA

Station Number	Max. Particle Rate (kHz/cm ²)
1	~ 380
2	~ 80
3	~ 36
4	~ 18

Table 2.2: Table for the specification of absorber specifications for SIS100 LMVM. LD stands for Low Density

Station Number	Absorber material	Absorber Thickness (cm)	Number of detector layers	Number of modules per layer
1	LD Graphite+Concrete	(28+30 = 58)	3	16
2	Fe	20	3	18
3	Fe	20	3	20
4	Fe	30	3	22

SIS100 Setup

The SIS100 LMVM (left panel) and J/ ψ (right panel) setup are shown in Figure 2.7. The setup consists of 4 absorbers and four tracking stations. As usual, each tracking station has three circular

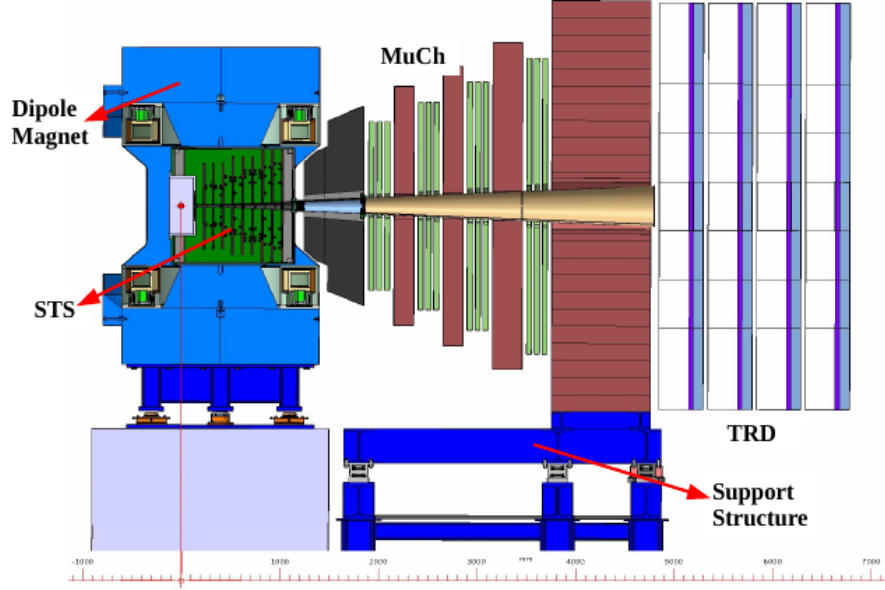


Figure 2.6: Schematic of MuCh setup

Table 2.3: Table for the specification of absorber specifications for SIS100 J/ψ . LD stands for Low Density

Station Number	Absorber material	Absorber Thickness (cm)	Number of detector layers	Number of modules per layer
1	LD Graphite+Concrete	(28+30 = 58)	3	16
2	Fe	20	3	18
3	Fe	20	3	20
4	Fe	30	3	22
4	Fe	100	TRD	TRD

layers of modules, and in each layer, there will be 16 modules (8 on the front side of the support structure and eight on the backside) for the first station. In the J/ψ setup, one iron thick absorber of 1 m thickness (fifth absorber) will be placed just before the TRD detector station.

2.4.3 MuCh Simulation Steps

Simulation framework

The block diagram shown in Figure 2.9 describes the basic steps involved in performance simulation using the UrQMD event generator and GEANT3 transport engine. The simulation chain is divided in to mainly following blocks: a) Geometry implementation and transport, b) segmentation of readout pads and digitization, c) Local hit reconstruction, d) Track reconstruction and propagations, and e) selection of tracks as muon candidate. Finally, identification of di-muons is

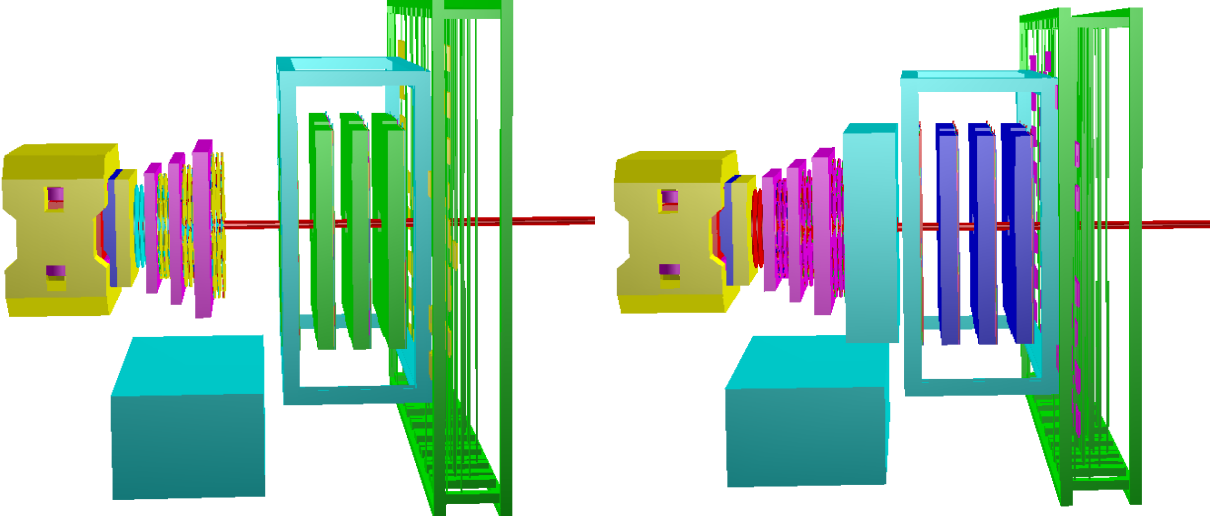


Figure 2.7: Schematic of MuCh setup for measurement of LMVM (left panel) and J/ψ in SIS100 facility

Table 2.4: Table for the specification of modules of the first two stations.

Station number	Number of layers	Total # of modules	Total # of readout channels	Total # of FEBs	Typical dimension of one module (cm) (active area)	Granularity (mm)
1	3	48	$\sim 107k$	864	Inner ~ 7.5 Outer ~ 40.0 Length ~ 80.0	Min. ~ 3.2 Max. ~ 17
2	3	60	$\sim 109k$	900	Inner ~ 7.9 Outer ~ 41.5 Length ~ 100.5	Min. ~ 4.5 Max. ~ 21.5

performed, which is a part of the analysis chain.

- Geometry implementation and transport:** The aim of MuCh is to identify the tracks which pass through the detector stations. We first need to make geometry setups (for every subsystem) in ROOT by implementing the actual material budget. Each station of MuCh consists of 3 layers of detectors, as can be seen in Figure 2.7. Then, the particles (from UrQMD) are transported through these absorbers and detector geometries for realistic performance simulation using GEANT3 transport engine. These particles, when they pass through active volume, generate respective signals. The detector commonly contains active and passive volumes.
- Segmentation and digitization:** The GEANT provides the position of energy deposition of particles inside the detector active volume. These positions (containing coordinates x , y , z) along with energy deposition are called MuCh points. The readout plane of the detector

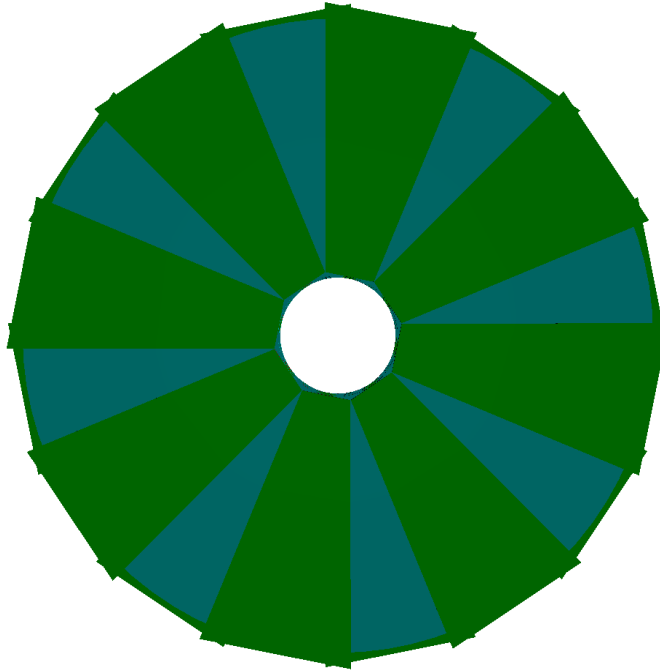


Figure 2.8: Schematic layout of the Muon Chambers (MuCh) with trapezoidal overlapping sectors.

modules is segmented into pads for collecting a final detectable signals. The primary charges from these MuCh points get multiplied by the detector gain and are distributed to the readout pads. This procedure is called digitization, which requires the detailed implementation of the detector response to the energy deposition inside the modules. In this scheme, MuCh points are subjected to create primary ionizations, charge multiplication, and the generation of signal inside the gas volume.

- **Clustering and Local Hit Finder:** Each particle track that produces a signal in the detector may affect one or more pads. The digitized signals from pads are grouped together using a suitable cluster finding algorithm to form hits. The large clusters are divided into sub-clusters and treated as hits. The centre of gravity method provides the hit coordinates in both cases, which will be used for tracking.
- **Track propagation:** The propagation of reconstructed STS tracks through the MuCh layers are done using the Kalman Filter technique. The MuCh detector hits, which are closest to the extrapolated track points, are taken as track candidate. In the final analysis of MuCh, the number of STS and MuCh hits, χ^2 associated with the tracks are taken as the track parameters.

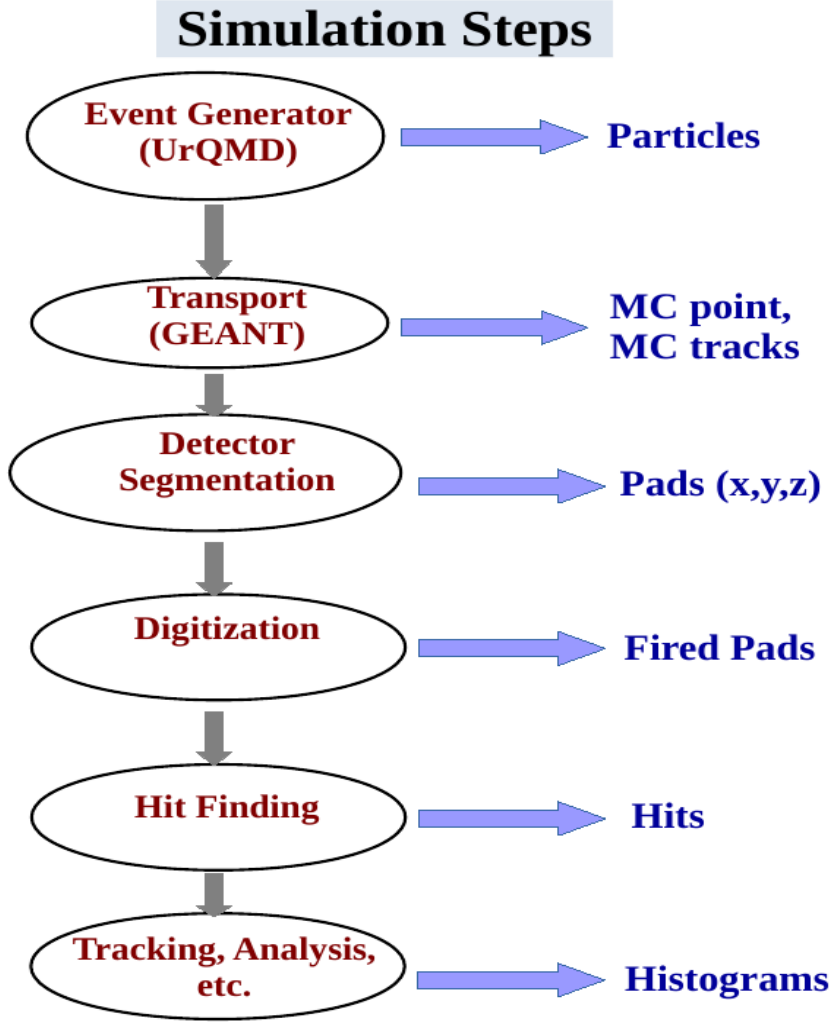


Figure 2.9: Schematic of MuCh setup

Detector segmentation, digitization, cluster finding and hit formation

The MuCh system has to handle high particle density. The segmentation study aims to find the realistic and optimized detector layout for physics measurements. The particle density varies with radial distance from the beam pipe ($\propto 1/r$), the readout of MuCh is segmented in various annular regions with pads of appropriate size which increases progressively with radius. The sizes are optimized to achieve the desired detector occupancy ($\lesssim 5\%$). The spatial resolution, apart from occupancy, is another constraint that limits the maximal pad size.

For the sector shape geometry, projective pads of increasing pad size are implemented in the segmentation scheme, as can be seen from Figure 2.10. The pad dimensions are determined by angular separation on the transverse plane. The present segmentation algorithm determines the

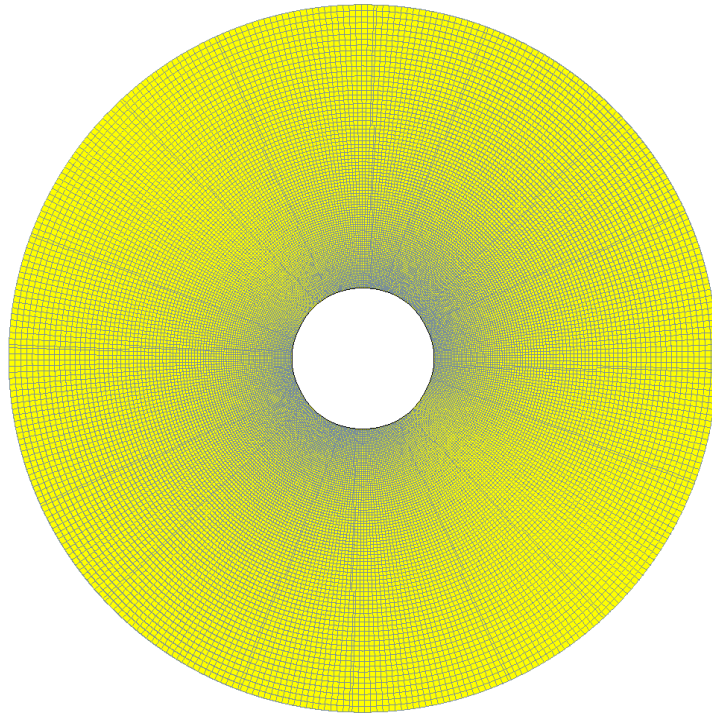


Figure 2.10: Schematic picture of the segmentation of the modules. Entire area has been divided into projective pads of 1° angular regions in azimuth.

angular dimensions and positions of each pad depending on the radius in such a way that the radial dimension of each pad is kept equal to the azimuthal dimension ($\Delta r \sim r\Delta\phi$) at the given radius. We have used a 1-degree separation at an azimuthal angle. The total number of the readout pads/channels for the first two stations of MuCh are given in table 2.4. The other two stations, 5 and 6-degree segmentation's, have been implemented due to lower particle rates in these stations as compared to the first two.

The response simulation of the GEM detector is shown schematically in Figure 2.11. In the simulation, the active gas volume is divided into drift and avalanche regions, and the triple GEM structure is ignored in the simulation. Primary ionization happens in the drift volume, and it is then multiplied by the detector gain. The digitization process can be understood in several steps:

- When a particle interacts with the gas volume, it creates primary ionization. The determination of number of primary electrons for every MuCh points is based on Landau distribution for Argon-based gas mixture, length of track in gas volume, type and energy of the particle. The HEED [128] package is used to determine the parameters of the Landau distribution, namely expectation value, and variance. The primary electrons are then distributed ran-

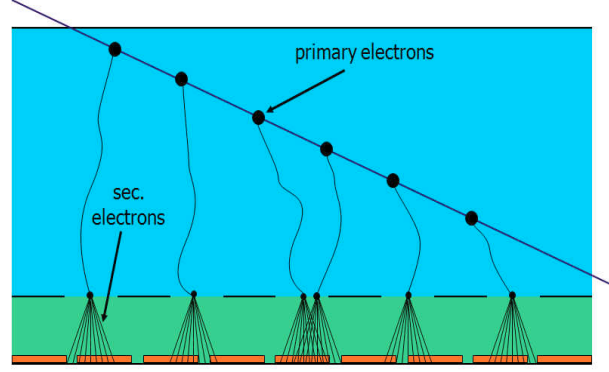


Figure 2.11: Schematic representation of the signal generation in GEM chambers

domly according to the Poisson law along the incident track direction.

- In the process of avalanche, the primary electrons get multiplied. The determination of these secondary electrons is done using an exponential gas gain distribution with a mean gain of 5k. The transverse diffusion of the avalanche is assumed to be constant, which gives the measure of spot size.
- Find the number of signals arriving at each pad and the charge of each signal. The standard spot radius of 500 μm is used in the simulation (found from the literature survey). The arrival time of charge is calculated from the time of MuCh points plus the primary electron drift time ($t = d/v$), where d is the distance traveled by the primary electrons from the point of its first interaction to the last interaction inside the 3 mm drift gap, and v is the drift velocity of primary electrons ($v = 100 \mu\text{m/ns}$).
- The signal charge information is converted into ADC channels using formula:

$$ADC = \frac{Q_{signal} - Q_{th}}{Q_{max} - Q_{th}} \times nADC \quad (2.2)$$

where Q_{signal} is charge of signal, Q_{max} is the maximum charge a pad can collect, Q_{th} is charge threshold, and $nADC$ is the number of ADC channels (for our case it is 5-bit ADC so in total 32 channels) for the pads.

- The ADC and timestamp of signal is decoded into 32-bit and stored in the array of Cbm-MuChDigi objects.

The illustration of the digitization algorithm for a reconstructed charge on pads is shown in Figure 2.12. This is a visual demonstration of the fired pads, but in addition to this, quality assurance is performed by looking at the charge from the track as a function of energy and particle

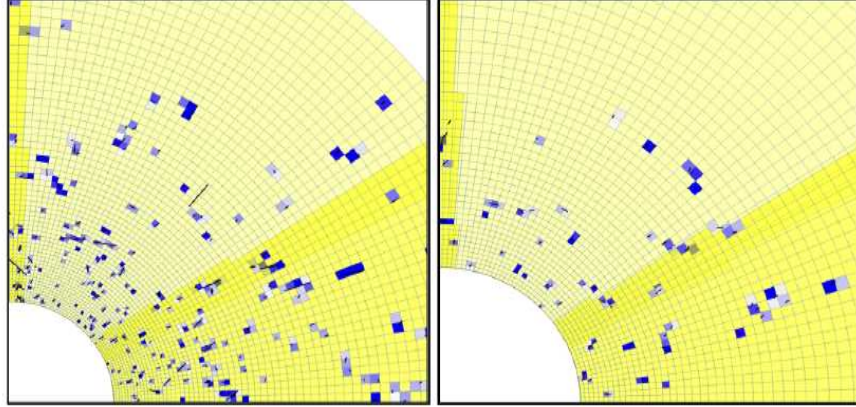


Figure 2.12: Illustration of digitization scheme for station 1 (left panel) and station 2 (right panel)

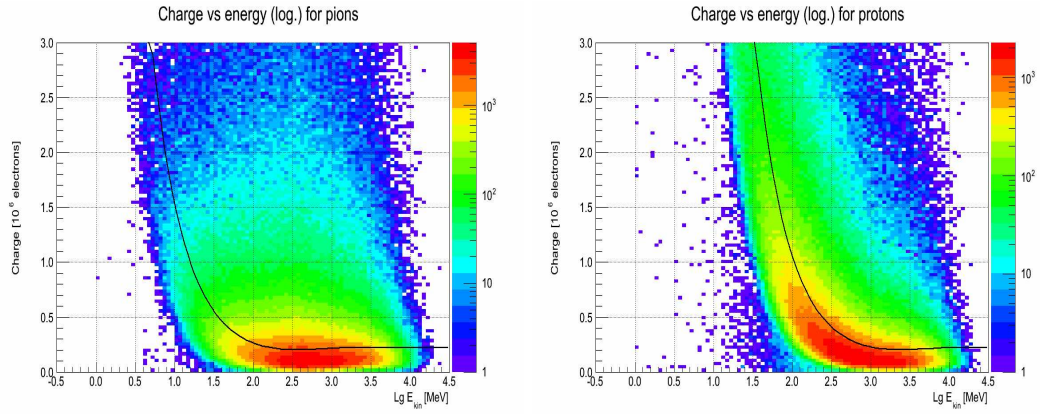


Figure 2.13: Total charge created by the incident tracks inside the active volume of the detector. The gas depth is set to 3mm in simulation. The figure describes deposited charge versus particle kinetic energy for pions and protons. The black lines result from a Bethe-Bloch fit to the mean values.

type. One example of charge vs. energy distribution is shown in Figure 2.13. The black line shown in the figure is from Bethe-Bloch's calculation. The charge deposition by a minimum ionizing particle (MIP) is shown in the left panel of Figure 2.14, and it follows the Landau distribution as expected.

The parameters of the detector are tunable and could take values depending on the technology of detector, such as spot radius. The avalanche for each primary electron is extrapolated to the pad plane, and the total charges at each pad is calculated. The other tunable parameters are total number of ADC channels, the maximum charge (Q_{max}) that a pad can collect, and the threshold charge (Q_{th}). The $Q_{max} - Q_{th}$ defines the dynamic range of the readout ASIC. If the corresponding energy deposition goes beyond the specified dynamic range for a particular channel, the channel gets saturated. The threshold charge is set above the expected noise level. However,

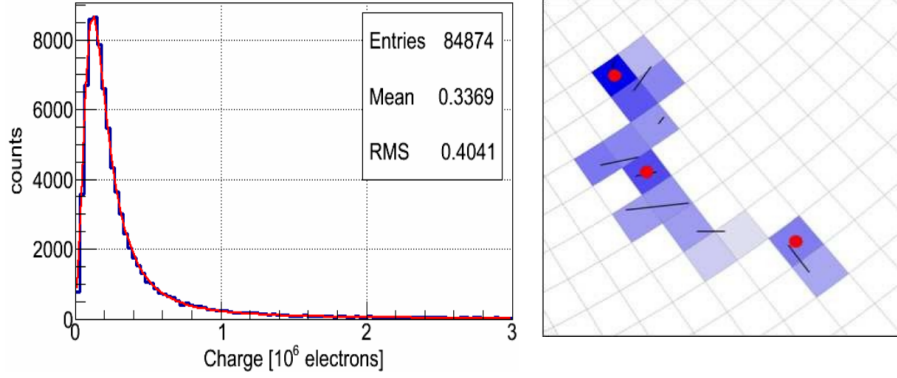


Figure 2.14: Left: Charge deposition by a minimum ionization particle (MIP) in the gas volume of the detector. The mean gas gain has been set to 10 4 in simulation. Hence each MIP creates on the average about 33 primary electrons along its track inside the 3 mm gas volume. Right: Illustration of local maxima algorithm of hit finder.

in the simulation performed in the chapter 3, no additional noise has been introduced. The noise threshold has therefore been kept at a reasonably low level. There are following parameters which need to be set before performing full simulation: (i) Total number of ADC Channels: 32, (ii) Q_{max} : 80 fC, (iii) Q_{th} : 2.0 fC, (iv) spot radius: 500 μm . Within an Argon-filled drift volume, a MIP typically produces 100 - 120 primary electrons per cm. Hence, for a drift gap of 3 mm, the number of primary electrons would be approximately 30 - 40. For an average gain of 5k, the total number of electrons created by an incident muon track will be $\sim 15 \times 10^4$ which is equivalent to a deposited charge of 25 fC (1 fC = 6,250 electrons). Hence setting up a noise threshold of $Q_{th} = 2$ fC is not likely to significantly affect the signal.

The digis are clubbed together to form clusters. These cluster are then deconvoluted to form hits. A search for local maxima algorithm has been used for clustering. The hit coordinates are assigned to the centers of the pads, corresponding to the local maxima. If dimension of the clusters are 2×1 pads (2 digis per clusters), one hit is created. The advantage of this method being that it works for large clusters and one can find single-track hits that contributed to the mother cluster (see right panel of Fig 2.14). Nevertheless, in the case of large clusters (produced due to inclined low-energy electrons), local maxima may arise due to random fluctuations of charges on pads. This may lead to the creation of fake hits. Also some tracks may still could remain unresolved by this algorithm.

This cluster and hit finding algorithm can be used for simulation purposes as well as for the reconstruction of real data. We have used this algorithm for analyzing data of the mCBM experiment. The results from this experiment is described in chapter 6.

2.4.4 Track Reconstruction in MuCh

One of the major challenges in the CBM-MuCh detector is to reconstruct tracks from the high particle multiplicity in A+A collisions. At CBM energies, about thousands charged particles are produced in central Au + Au collisions, which results into a high track and hit density in the MuCh detector, particularly, on the first station (see Figure 2.15).

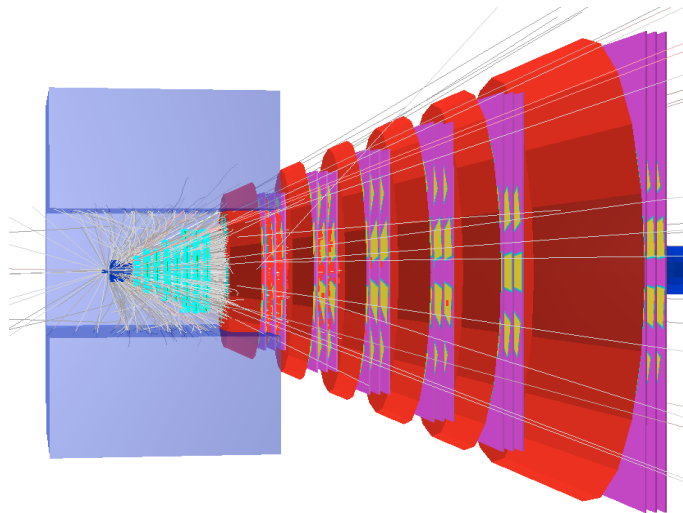


Figure 2.15: Track visualization of one simulated central Au + Au collision at 25 AGeV

The track reconstruction algorithm in MuCh is based on track following using reconstructed tracks in the STS as seeds. The track reconstruction in STS is based on the cellular automation (CA) method [129], and the its track parameters are used as starting point for the subsequent track prolongation. This track following is based on the standard Kalman filter (KF) technique [130] and is used for the evaluation of track parameters [131] and trajectory recognition. The main components in tracking are track propagation, track finding, track fitting, and finally, a selection of good tracks.

The trajectories and its errors in a covariance matrix are estimated by track propagation algorithm. This considers three physics processes that influence the trajectory, i.e., energy loss, multiple scattering, and the influence of a magnetic field. The influence of the material on the track momentum is taken into account by calculating the expected average energy loss due to ionization (Bethe-Bloch formula) and Bremsstrahlung (Bethe-Heitler formula) [132]. A Gaussian approximation using the Highland formula [132] is used to estimate the average scattering angle. The propagation of the trajectory is done according to the equation of motion in magnetic field and it is solved by applying 4th order Runge-Kutta method [133]. In case of the tracks that passes

through field-free region, a straight line track fitting algorithm is used for propagation and the transport matrix calculation. The transport matrix is calculated by integrating the derivatives along the so-called zero trajectory [134]. A detailed description of the developed track propagation can be found in [135].

After track propagation, we use a track-finding algorithm. In this algorithm, hits are attached to the propagated track at each detector station using two different methods, namely, *nearest-neighbor* and *branching*. In the former method, just the nearest hit is attached to the track, while all hits within a certain environment are included in the branching method. For the first method, only one track is further propagated, and the second method allows for several track branches to be followed, one for each attached hit.

Assignment of new hits is done step by step at each detector station. After the track propagation to the next station, possible hits are attached, and the KF updates track parameters.

The clone tracks (made from a very similar set of hits) and ghost tracks (made from a random set of hits) must be rejected while keeping correctly found tracks with high efficiency. The selection algorithm works in two steps. First, tracks are sorted by their quality which is defined by the track length and χ^2 . Then, starting from the highest quality tracks, all hits belonging to a track are checked. In particular, the number of hits shared with other tracks is calculated and the track is rejected if more than 15% of the hits are shared.

MuCh simulations are performed using input particles which generated from UrQMD event generator [136]. To enhance statistics and investigate the MuCh response to primary muons, one signal (LMVM, J/ψ , etc.) particles decaying into muon pairs ($\mu^+ \mu^-$) were embedded into each UrQMD event.

The performance of the algorithms was obtained using information from the Monte Carlo input. A track is defined as correctly found if it has more than 70% of hits from one Monte-Carlo track, and the rest is defined as a ghost track. The track reconstruction efficiency is defined as $v_{track} = N_{reconstructed}/N_{accepted}$. $N_{reconstructed}$ is the number of correctly found tracks after reconstruction, $N_{accepted}$ is the number of reconstructable tracks in the MuCh acceptance.

2.4.5 Muon identification and analysis

We apply a set of cuts at the analysis level from the global reconstructed tracks to identify muon tracks originated from signals (LMVM, J/ψ , etc.). Our aim is to reject background due to non-muonic tracks and muons from weak decays (of pions and kaons). The cuts which are used for the

selection of muon tracks are (a) from STS: number of hits in STS and χ^2 of STS track and (b) from MuCh: number of much hits, χ^2 of the MuCh track. In addition to that, a cut on χ^2_{vertex} is also applied. For the selection of muons from low-mass vector mesons and charmonia, the numbers of MuCh hits in a track are taken to be different. The muon tracks coming from LMVM's are softer, and they are expected to stop inside the last thick iron block (100 cm), and the required number of MuCh hits does not exceed 12.

Each reconstructed muon track satisfying the above set of cuts is now selected for di-muon invariant mass analysis. Each selected track is represented by its 4-momentum vector:

$$P_\mu = (E_\mu, \vec{p}_\mu) \quad (2.3)$$

Using the energy-momentum conservation, we can write invariant mass (m_{inv}) of the di-muon pairs as:

$$m_{inv}^2 = 2m_\mu^2 + 2(E_{\mu 1}E_{\mu 2} - \vec{p}_{\mu 1} \cdot \vec{p}_{\mu 2}) \quad (2.4)$$

where the rest mass (m_μ) of muon is 105 MeV. m_{inv} is invariant under Lorentz transformation. The other di-muon kinematic variables are the pair p_T , pair rapidity (Y), and the opening/decay angle ($\theta_{\mu 1 \mu 2}$) defined as the angle between $\vec{p}_{\mu 1}$ and $\vec{p}_{\mu 2}$. The above equation can be written as (neglecting the muon mass):

$$m_{inv} \simeq \sqrt{2p_1 p_2 [1 - \cos\theta_1 \cos\theta_2 - \sin\theta_1 \sin\theta_2 \cos(\phi_1 - \phi_2)]} \quad (2.5)$$

where p_i , θ_i and ϕ_i are the magnitude of 3-momentum, polar and azimuthal angles of the single muon tracks.

The pair p_T can be written as:

$$p_{T, \mu 1 \mu 2} = \sqrt{p_{x, \mu 1 \mu 2}^2 + p_{y, \mu 1 \mu 2}^2} \quad (2.6)$$

where

$$p_{i, \mu 1 \mu 2} = \sqrt{p_{i, \mu 1}^2 + p_{i, \mu 2}^2}; (i = x, y, z) \quad (2.7)$$

The pair rapidity in lab frame is given by

$$Y_L = \frac{1}{2} \log\left(\frac{E + p_z}{E - p_z}\right) \quad (2.8)$$

where E and p_z denote the pair energy and longitudinal momentum in the laboratory frame. Pair rapidity in laboratory systems is given by

$$Y_L = Y^* + Y_{CM} \quad (2.9)$$

where Y_{CM} is the rapidity of the centre of mass (CM) system and can be expressed as

$$Y_{CM} = \frac{1}{2} \log\left(\frac{1 + \beta_c}{1 - \beta_c}\right) \quad (2.10)$$

where β_c is the velocity of the center of mass of the collision system in the laboratory and can be calculated as

$$\beta_c = \frac{|\vec{P}_{lab}|}{E_{lab}} = \frac{|\vec{P}_{beam}|}{E_{beam} + m_{target}} \quad (2.11)$$

where \vec{p}_{beam} and E_{beam} are projectile momentum and energy and m_{target} is the mass of the target. For 25 AGeV Au+Au collisions, $Y_{beam} = 3.99$ and $Y_{CM} = 1.99$.

Kinematics Resolution:

In general the kinematic resolutions the di-muon experiments are governed by three factors: a) the multiple scattering of the muons in the target and the hadron absorber, b) the energy loss of the muons in the hadron absorber, and c) the proper error of the measurement in the tracking chambers.

The last one is negligible compared with the previous two. One novel feature of the CBM experiment compared to the previous and existing experiments is that the full tracking will be performed in the STS detector system upstream to the absorber. Hence the momentum measurements will not affect the multiple scattering or energy loss effects inside the absorber. Also, the target thickness of CBM is much smaller ($1\% \lambda_I$) compared to the other experiment (for example, the target thickness in the NA50 experiment was varied between $7-30\% \lambda_I$), which also helps to reduce the multiple scattering and thus improve upon the momentum resolution. Under such conditions, the momentum resolution will be considerably affected by the magnetic field only. Note that for a dipole magnetic field of strength B and extended over a length L , the momentum resolution of a track having momentum p can be written as:

$$\frac{\Delta p}{p} \propto \frac{p}{BL^2} \quad (2.12)$$

With the existing dipole magnet designed for tracking, the momentum resolution of the muon tracks are $\Delta p/p \sim 1\%$. So far as di-muon mass resolution is concerned, note that from Eq. 2.4, neglecting the muon mass, we can write

$$m_{inv}^2 = 2p_{\mu 1}p_{\mu 2}(1 - \cos(\theta_{\mu 1\mu 2})) \quad (2.13)$$

where the symbols carry their usual meanings. As the average signal momentum strongly increases with mass, the multiple scattering which contributes to the angular resolution ($\Delta\theta_{\mu 1\mu 2}$) is more important at low masses (e.g., ρ , ω , etc.) and has a negligible effect in the high mass (e.g., J/ψ , ψ') regime. Neglecting the angular resolution, we can estimate the expected mass resolution as:

$$\frac{\Delta m_{inv}}{m_{inv}} = \frac{\Delta p_{\mu}}{\sqrt{2}p_{\mu}} \quad (2.14)$$

2.4.6 Integration of MuCh system in CBM

The details of integration aspects of the MuCh system of CBM experiment are itemized below:

- **Mechanical integration:** The cave of the CBM will have different floors in the building for housing different services like electronics, gas, etc. The CBM setup will be placed in the main hall just after the HADES setup, mainly in SIS100 running scenario. The STS system, which is the main tracking system of CBM, will be placed inside magnet, and will occupy the space up to 120 cm. The RICH detector will be placed just outside the magnet in the di-electron mode of operation, while the MuCh needs to be as closely located to the target as possible to avoid the pions decaying to muons in the di-muon mode of operation. A small portion of the first absorber will be inside the magnet, as discussed in the previous section. The detector stations, three layers of each, are housed in a 30 cm space between two consecutive absorbers are to be installed. This will have a provision to move the system in transverse directions. All the services are to be mounted with the main platform. The system of absorber layers and detector stations are to be mounted on main platform that can have a possibility of moving to a parking position for operation in di-electron mode.

- **Electronics Integration:** The readout electronics (Front End Board (FEB)) of MuCh will be mounted on the chambers directly. One Application-Specific Integrated Circuit (ASIC) will be used in the FEB, which will process the analog signals from the detectors. The digitized signals (called as digis) from a group of FEBs will be transported to the GBTx data concentrator ASICs which forward the data over optical links to FPGA-based data processing boards (DPBs), which will be placed outside the CBM cave. A Common Readout Board (CROB) will be used to hold the GBTx and associated optics components. The data will be transported to the first level event selector (FLES) of CBM. The electronic components at each of these stages will face different radiation dose levels and that is why these hardware needs to be radiation resistant accordingly. The maximum radiation level will be handled by the FEBs and need to be suitably placed to reduce the effect.

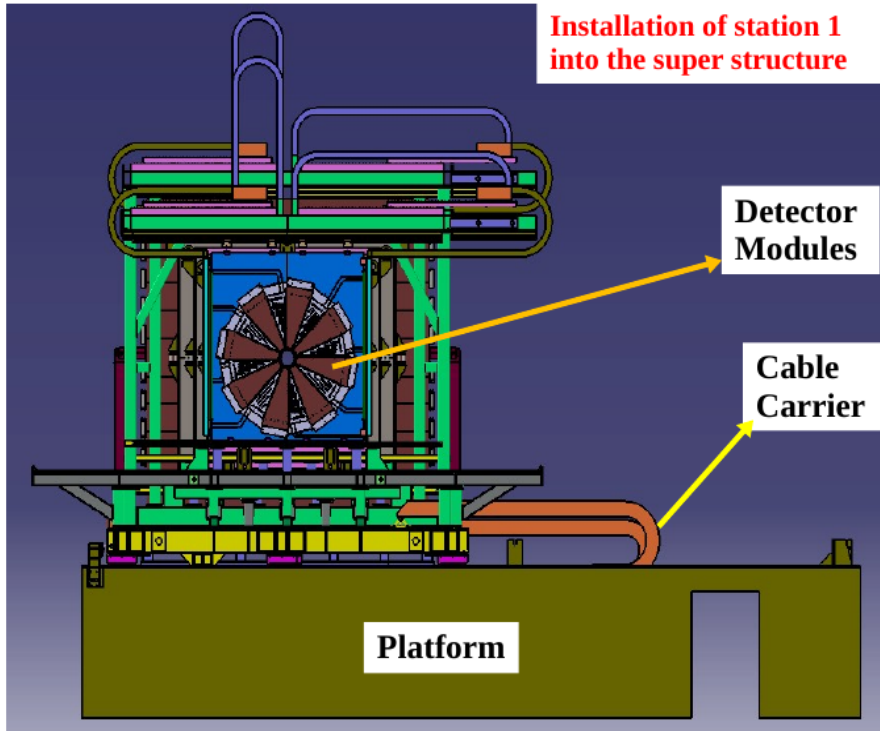


Figure 2.16: Mechanical layout of MuCh setup. Detector stations will be installed on super structure as shown. Cable carriers will be used for handling cables.

Mechanical layout of MuCh system

The major assembly components of MuCh system are (a) MuCh absorbers assembly in the CBM setup and (b) assembly of individual chambers (discussed in detail in chapter 5). The following

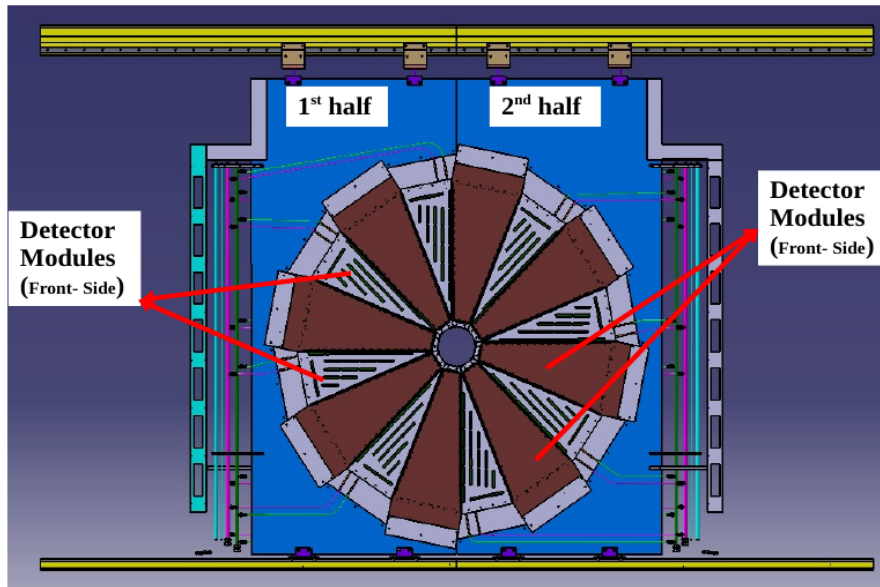


Figure 2.17: Three layers each stations are divided into two halves. Modules from each layer are attached on support structure. Half of the modules will be on one side of support and rest on other side.

points are to be taken into consideration while designing the system,

- MuCh will take data only in the di-muon setup, so there should be provision that the detectors of the di-electron setup could be placed in a short time interval and with minimum intervention as and when required.
- Proper care to be taken to assemble the first MuCh absorber that is likely to be placed inside the magnet.
- Provisions of mounting and dismounting of other detectors in the setup should be made.
- The choice of materials should take care of the magnetic field whenever present in the setup.

Only the mechanical layout of the full MuCh system is briefly discussed here. The entire MuCh system, including platform along with different components like detector layers, absorbers, cable layouts, among others, is shown in Figure 2.16. The zoomed picture of one layer of detector modules is shown in Figure 2.17.

2.5 Technology options for MuCh

The choice of the detector technology is governed by the following criteria apart from the requirements of high resolution and high efficiency.

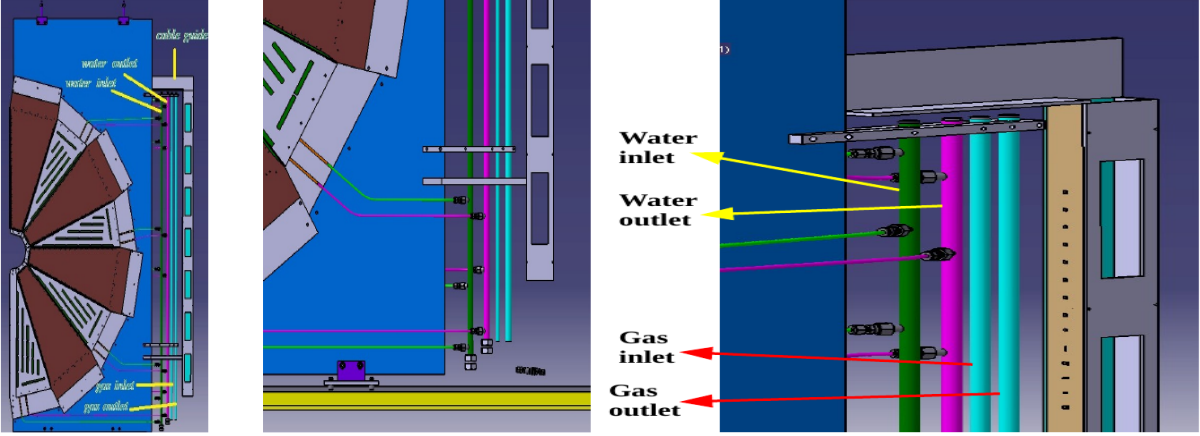


Figure 2.18: Layout of the gas and water cooling system of MuCh. Left: One half portion of detector modules. Middle and Right: Schematic showing for gas, water connections.

- **Particle density:** Depending on the location of the station and of the layer, the density of incident detectable particles may vary from $\sim 0.04 \text{ cm}^{-2}$ to 10^{-4} cm^{-2} . The particle density is governed by the profile of incident particles coupled to the total absorber thickness it passes through. The particle density determines the profile and segmentation of the detectors.
- **Particle rate:** CBM is to operate at a 10 MHz collision rate. The interaction rate and the particle density together determine the particle rate a detector needs to handle. It has been found by simulation, as discussed in the section 2.4, that for SIS-100 setup, the maximum required rate is 0.38 MHz/cm^2 at the innermost part of the layer located immediately after the first absorber.
- **Detector area:** The layers located at the end of the MuCh setup need to be considerably larger in size compared to the stations located close to the magnet. The ability to build large-area detectors using a particular technology governs the selection of technology at those locations.
- **Radiation hardness:** One specific challenge that the MuCh detectors face is the large number of secondaries produced inside the absorber, which reach the detector stations unabsorbed. Neutrons are the most significant contributors. It has been estimated that the first station is to face about $10^{11} n_{eq}$ (for the 10-year operation of CBM). The detector must not produce hits due to these neutrons; otherwise, they will add to the hit density. In addition to that, the detector materials must be resistant to the huge neutron flux both in long and short duration. Even though the detectors face mostly minimum ionizing particles, however, at the CBM energy range, slow-moving ionizing particles might deposit a relatively larger

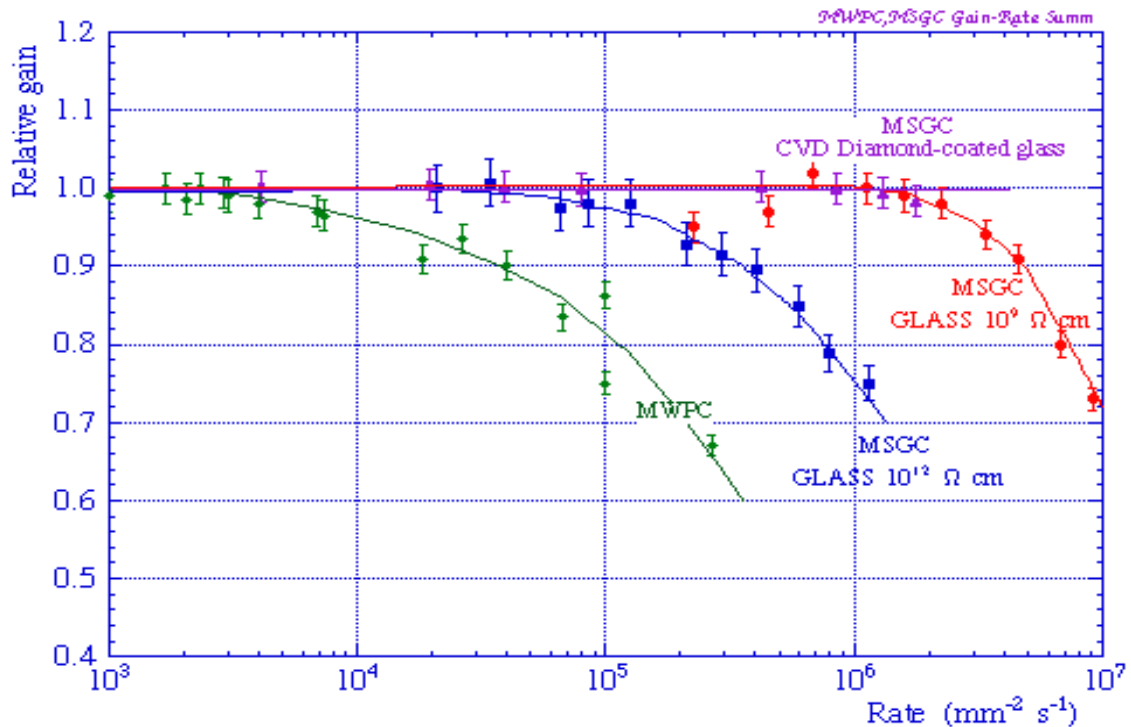


Figure 2.19: Relative gain as function of rate for different detector technologies [8, 9]

amount of energy, and the detector must be able to withstand this large energy deposition. The criticality of radiation hardness applies to the detectors in the first two stations only. Even though they need to be of large size, the detectors located in most downstream stations need to be of large size and handle very low particle density.

Keeping the above factors in mind, simulations have been performed to optimize MuCh geometry, as discussed in this chapter and also can be found in MuCh-TDR [112]. The decision on detector technology has been taken by looking at the requirements at different stations separately. The first two stations face high particle rate & harsh radiation environments and require specialized technology, and the later stations can use conventional detector technology that can be built in a large area. The three layers of a station will use one particular technology.

For the first two stations, which face high particle rates and harsh radiation environments, we considered gaseous detector options based on GEM, MICROMEGAS, and MWPC. So far, MWPC is the most widely used type of gaseous detector for HEP experiments. However, the use of MWPC in MUCH is constrained by its rate handling capability. Figure 2.19 shows the relative gain of different detectors as a function of rate [8, 9]. The gain starts falling sharply after about 10^4 Hz/mm² of incident particle rate for MWPC. The qualifying parameters of these three detector

Table 2.5: Comparison of rate handling capacity of various micro-pattern gas detectors

Parameters	MWPC	GEM	Micromegas
Rate capability (Hz/mm ²)	$\sim 10^4$	$\sim 5 \times 10^5$	$\sim 10^6$
Gain	High (10^6)	Single GEM (10^3) Triple GEM (10^5)	10^5
Position resolution	$< 200 \mu\text{m}$	$\sim 200 \mu\text{m}$	$< 50 \mu\text{m}$
Time resolution	$\sim 100 \text{ns}$	$\sim 50 \text{ns}$	$\sim 50 \text{ns}$
Mag. Field Effect	High	Low	Low
Cost	Expensive	Expensive	Cheap, robust but sparks can be catastrophic to FEE.

technologies as per the literature survey are compared in Table 2.5. It is clear that MWPC will not be able to cope with the required rate at the first stations of MuCh. Out of the two other options, GEM has been taken as the baseline option for the first two stations of both SIS100 and SIS300 after performing detailed R&D on GEM. The performance study of GEM detectors in a CBM-like environment is being done in the mCBM experiment [137] at GSI. (refer to chapter 6).

Chapter 3

Detector performance studies in simulation

In this chapter, we have studied the simulation response of the GEM chambers. We have basically dealt with two categories of simulation work. As discussed in detail in chapter 6, two GEM modules, referred to as mMuCh subsystem, were installed in mini-CBM (mCBM) experiment at GSI. So in the first part of this chapter (section 3.1) we have studied the simulated response of the GEM chambers in mCBM environment. In the second portion (section 3.2), as a part of physics performance, we have investigated the impact of the digitization parameters of MuCh detectors on omega reconstruction.

3.1 mCBM simulation

The mCBM experiment at GSI is a precursor experiment of CBM, consisting of all CBM detector subsystems, setup at the SIS18 facility of GSI. The detailed description of this experiment is given in chapter 6. Figure 3.1 shows the layout the mCBM setup. The actual geometries and configurations of different subsystems participating in mCBM experiment, are implemented in CBMROOT framework. Two mMuCh modules (described in detail in chapter 6) are also implemented as shown in the same figure.

For studying the mMuCh response, we have considered detector acceptance identical to the configuration with which data was taken in mCBM campaign 2019. As part of detector parameters, we have considered a mean gain of 5.5 k (as observed from data) and an electronic threshold of 6 fC on the charge collected at each readout pad, corresponding to actual case. Pads that were

masked in data were also masked for the simulation studies. Input particles were generated for Ar+Au collisions at beam kinetic energy of 1.70 AGeV using UrQMD event generator.

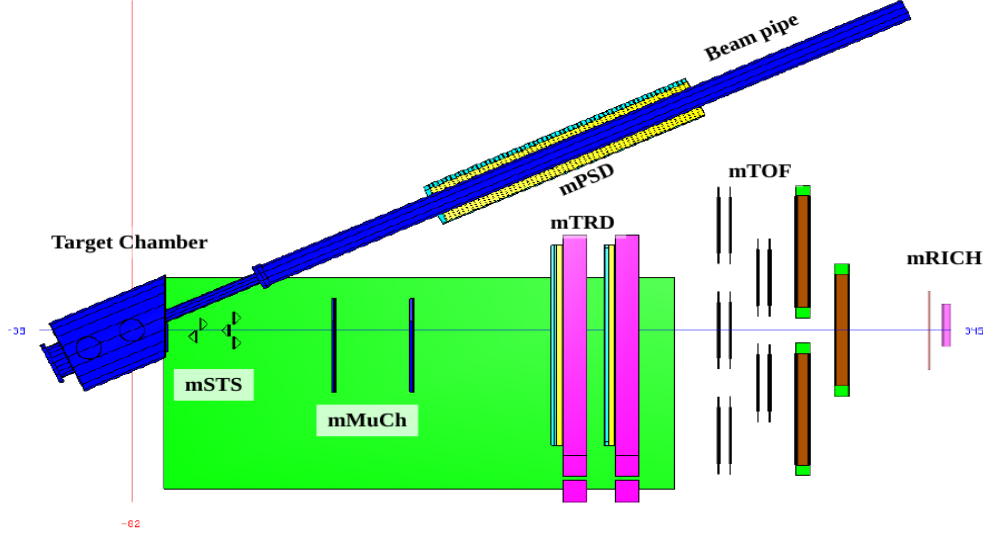


Figure 3.1: Geometry of mCBM setup as implemented in the ROOT framework showing different detector subsystems at SIS18 facility of GSI. The beam enters from left

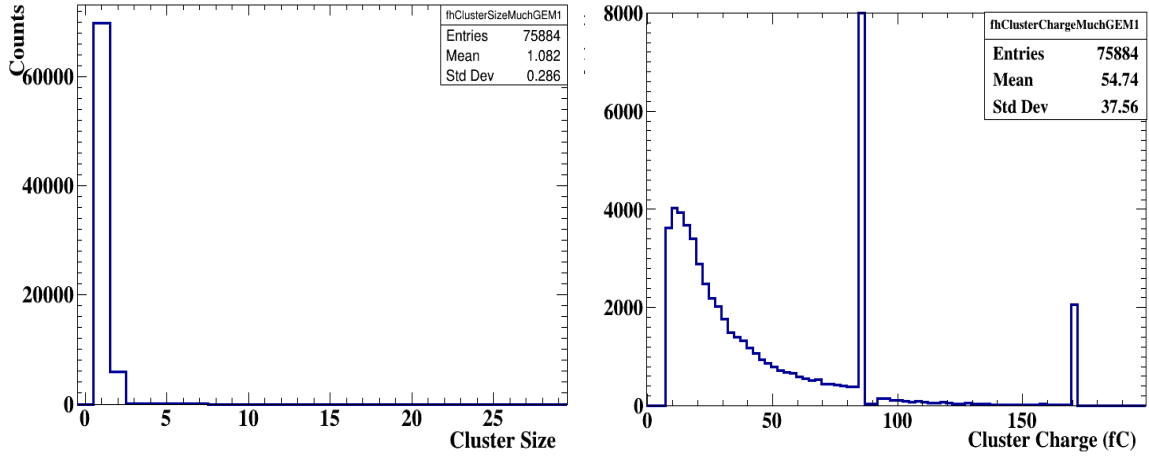


Figure 3.2: Left: Cluster size distribution for GEM1 plane in simulation. Right: Distribution of cluster charge for GEM1

3.1.1 Results and discussion

The cluster characteristics from simulation has been studied. The cluster size distribution for GEM1 detector is shown in the left panel of Figure 3.2. The average cluster size is about 1.1. The corresponding cluster charge (in fC) is shown in the right panel of Figure 3.2. Cluster charge

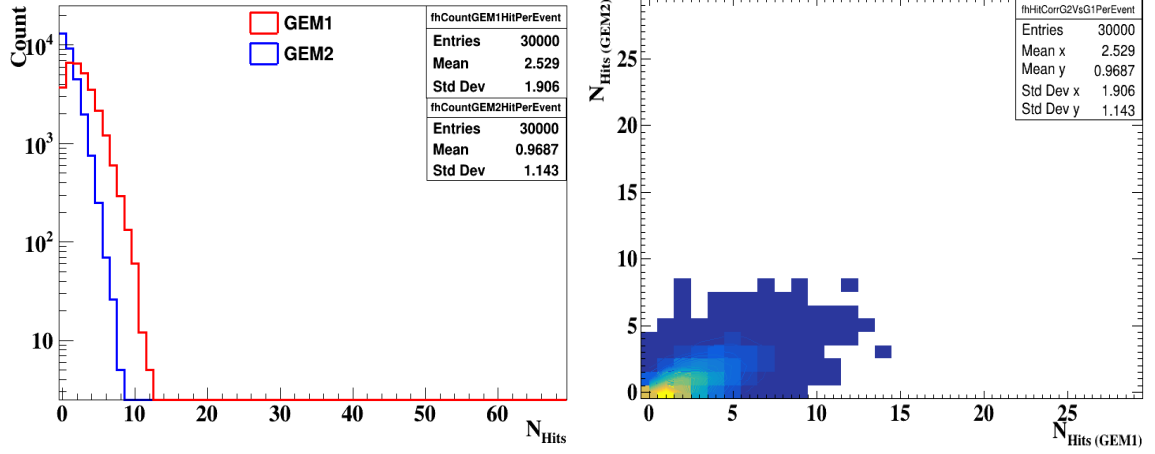


Figure 3.3: Left: Distribution of number of hit per event (hit multiplicity) for GEM1 and GEM2 detector. Event-wise hit multiplicity correlation between GEM1 and GEM2.

distribution in data and simulation matches closely. The sharp peak at about 81 fC is due to saturation feature of electronics at this value of charge. This is discussed in details in chapter 6.

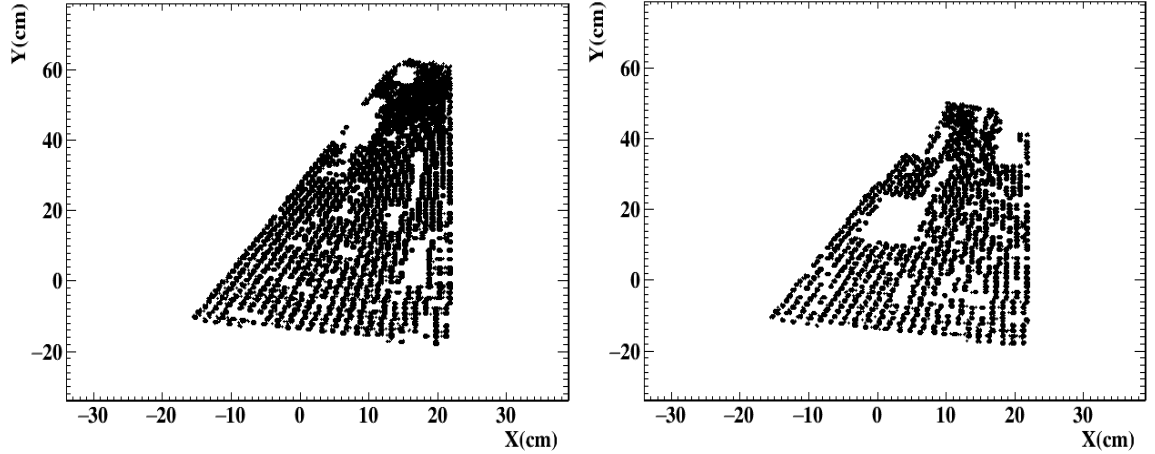


Figure 3.4: X-Y distribution of GEM1 and GEM2 hits from simulation

Actual detector acceptance, as it is in data, was implemented in the simulation and hit multiplicity was studied. The distribution of the number of hits per event for GEM1 (red) and GEM2 (blue) plane is shown in the left panel of Figure 3.3. An average hit of about 2.5 for GEM1 plane is observed from the figure. The same for 100% detector acceptance for the given collision system comes out to be ~ 3 . Hit multiplicity correlation between these two detectors is shown in the right panel of same figure. The centroid of the scatter plot is tilted more towards GEM1 due to its greater acceptance compared to GEM2.

The distribution of hit coordinates for GEM1 and GEM2 planes are shown Figure 3.4. The blank spaces correspond to the masked pads.

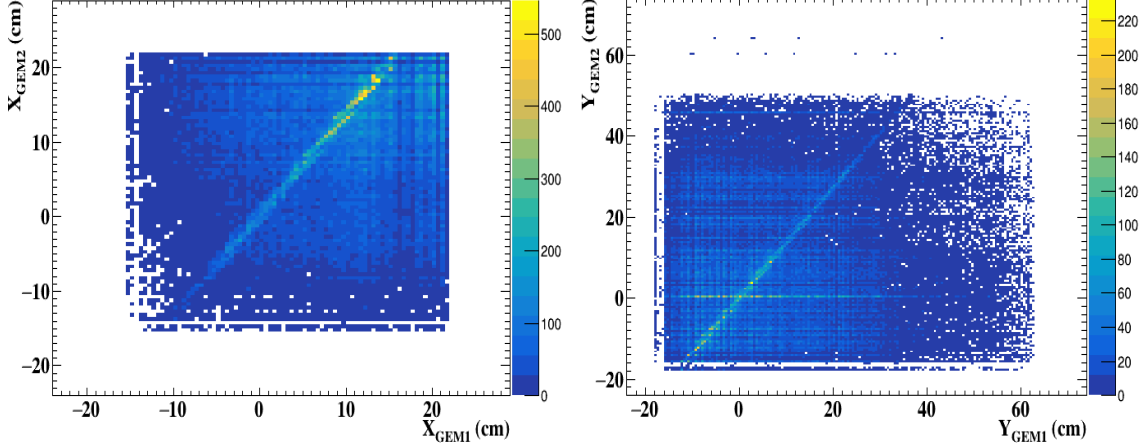


Figure 3.5: Spatial correlation between GEM1 and GEM2 hit coordinates in X and Y from simulation

3.1.2 Spatial correlation

A look at spatial correlation between hit coordinates of detector in simulation serves as useful guidance while analyzing data. Shown in Figure 3.5 is spatial correlation between hit coordinates of GEM1 and GEM2 in X and Y, while that between TOF and GEM1 detector is shown in Figure 3.6. A clean correlation line is observed in both the cases.

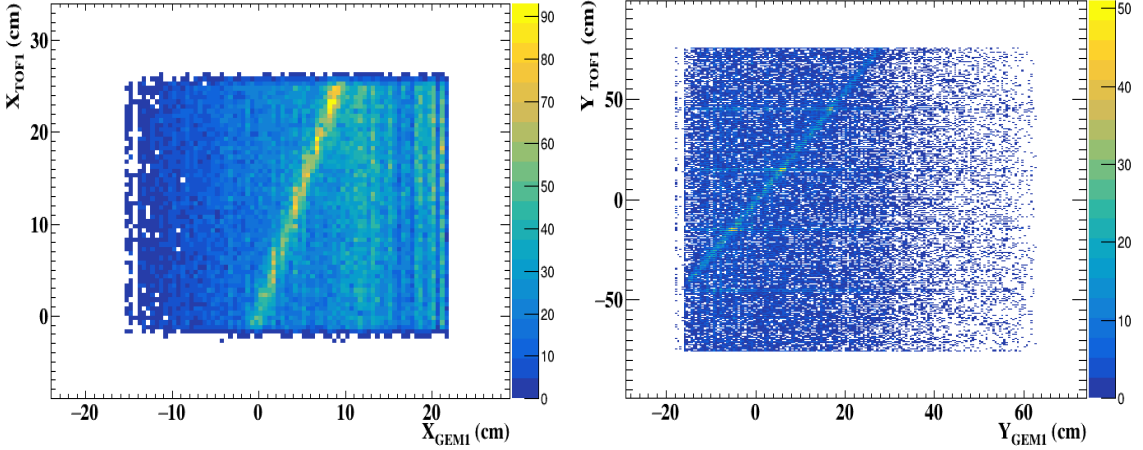


Figure 3.6: Spatial correlation between GEM1 and TOF hit coordinates in X and Y from simulation

3.1.3 Track reconstruction

Track reconstruction using 3 TOF modules (placed at different z-positions) and the vertex ($z=0$) was performed. The details about the track reconstruction algorithm is given in section 6.7. The distance between the extrapolated hits and the actual nearest hits on GEM1 plane was calculated. The distribution of this distance is shown in the left panel of Figure 3.7. The reason for the long

tail can be because of the noise hits and some non-real tracks. With a 4 cm cut on distance (which covers full peak), we have measured track residuals in X as well as in Y, which is shown in the middle and the right panel of Figure 3.7. A $\sigma_x \sim 0.77$ cm and $\sigma_y \sim 0.72$ cm is observed from the figure. 2-D scatter plot of residuals in X and Y is shown in Figure 3.8, which is centered at (0,0) as expected.

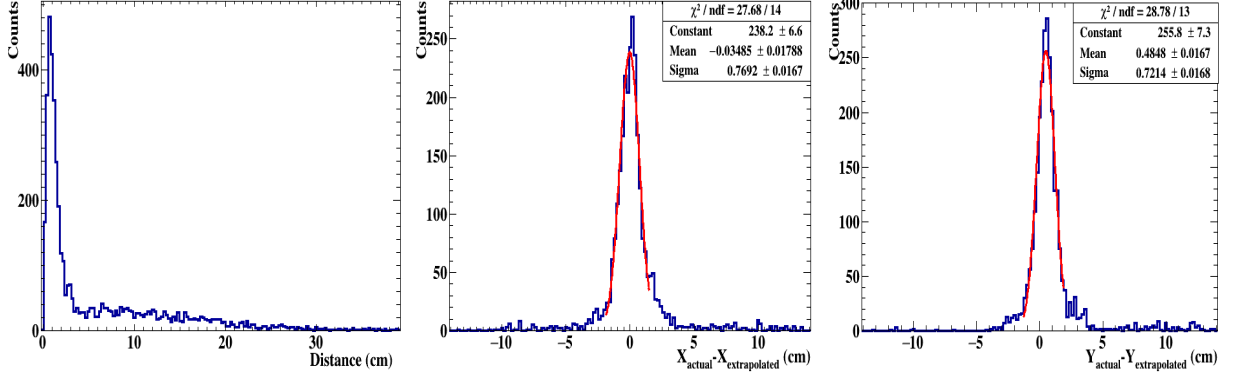


Figure 3.7: Track reconstructed using hits from 3 TOF planes and vertex ($z=0$). The distance between the nearest hit to the extrapolated track on GEM1 plane (left). Residuals in X (cm) (middle panel) and Y (cm) (right panel) at GEM1 plane with ~ 4 cm cut on distance.

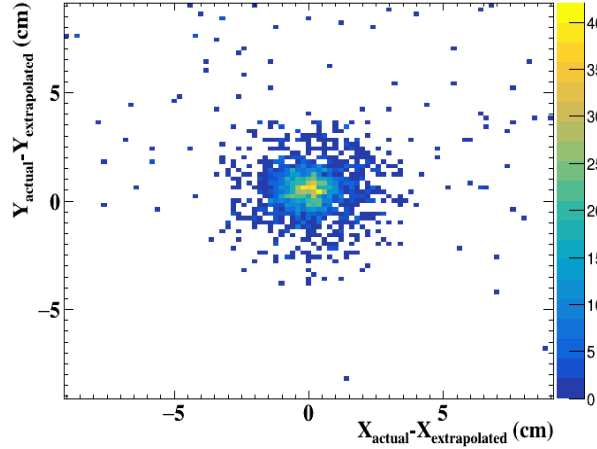


Figure 3.8: 2-D plot of residuals in X (cm) and Y (cm) at GEM1 plane with ~ 4 cm cut on distance.

3.2 Effect of detector parameters on ω reconstruction

This section describes the simulation response of GEM detectors, which has been carried out by implementing the actual acceptance and incorporating the layout of MuCh in CBM framework. The detector dimensions, their acceptance and the thickness of the instrumented absorbers considered are as per latest MuCh configuration. A detailed introduction to the MuCh system has

been presented in chapter 2. The optimized design for the MuCh setup for identifying muons at SIS100 energies consist of the 1st absorber made of a 30 cm thick low-density graphite ($\rho = 1.7 \text{ g/cm}^3$) and a 30 cm thick concrete attached back to back. The rest three absorbers are made of iron (Fe) with thicknesses 20, 20, and 30 cm respectively. These values are given in table 3.1. A triplet of tracking detectors called stations behind each absorber layer will be employed. The performance simulations of MuCh have been carried out with GEM-like detectors in stations 1 and 2 and RPC-like detectors in stations 3 and 4 [106] (page 76-77). The detector modules in each layer are trapezoidal for both detector types. A one-degree segmentation in azimuth has been implemented for the first two stations, and for the 3rd and 4th stations, five and six-degree segmentation were used. A 35 μm thick Copper layer of size similar to the detector's size have been implemented on the side of the 3 mm thick G10 sheets to incorporate a realistic material budget for all the stations. The active volume consists of a 3 mm thick gas mixture of Ar/CO₂ (70:30) for the GEM detectors and 2 mm thick RPC gas (R134a (95%) + isobutane (4.5%) + SF₆ (0.5%)) for the RPC detectors. Also, 1 cm thick aluminum plates have been implemented along with detector geometry as a support structure and which will be required for cooling to the detector electronics.

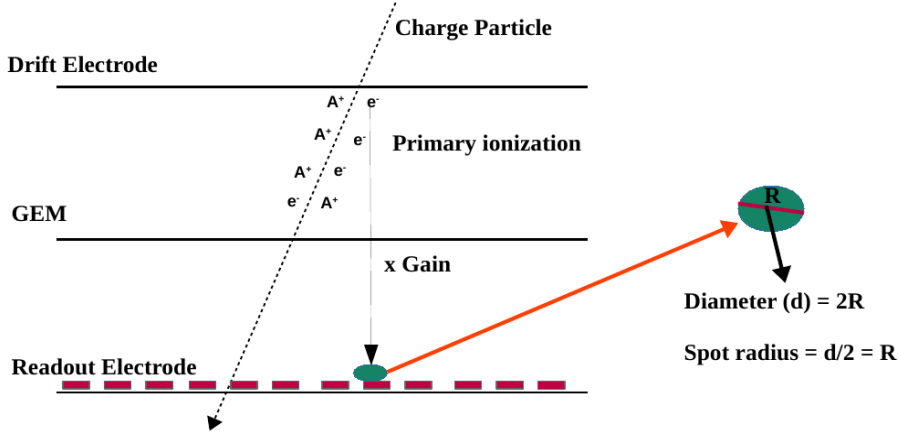


Figure 3.9: Visualization of the spot size inside the detector

The simulation chain consists of the following steps (more details are given in chapter 2):

- Generation of particle in A-A collision using the event generators like UrQMD to represent the background events and PLUTO for signal events.
- Transport of particles through the detector setup using GEANT3 transport engine.
- Digitization of points (generated by incident particles on the detector) to form digitized signal.
- Clustering and local hit reconstruction.

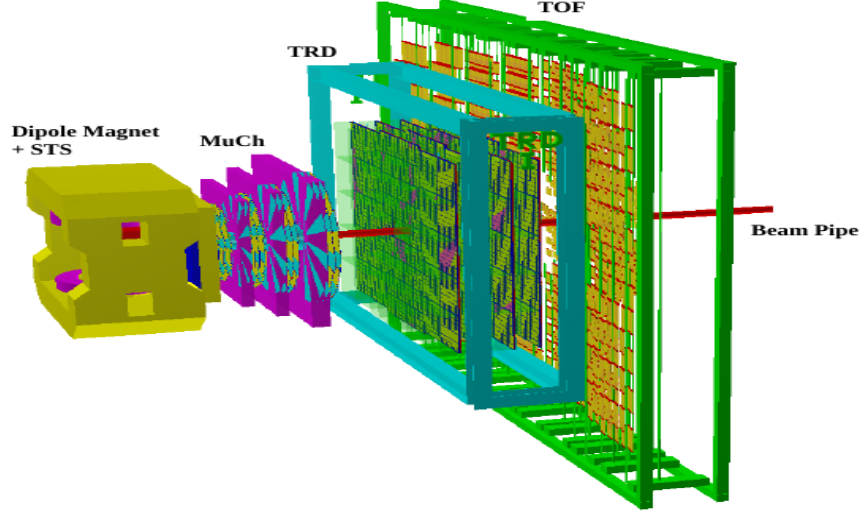


Figure 3.10: LMVM setup of CBM for SIS100. STS, MuCh, TRD and TOF subsystems are as indicated. 4 detector stations are used for MuCh

Table 3.1: Optimized design of MuCh setup for SIS100 energy

Station No.	Absorber Type	Absorber Thickness	Detector Type
1	Graphite ($\rho = 1.7 \text{ g/cm}^3$) + Concrete	30 cm+28 cm	GEM
2	Fe	20 cm	GEM
3	Fe	20 cm	RPC
3	Fe	30 cm	RPC

- Analysis of di-muon reconstruction.

In the third step, we provide the detector parameters, such as spot size and mean gas gain as informed, for studying the realistic performance. The spot radius is defined as the radius of the avalanche on the readout plane due to the single primary electrons (generated in gas medium by incident particle). The visualization of the spot size is shown in Figure 3.9. The primary electrons get multiplied as per the detector gain (equivalent to triple GEM). In this chapter, the effect of these parameters on the reconstruction of ω particles and on the track residuals have been systematically studied. The UrQMD [125] event generator was used to generate background events, while the ω meson signals were generated using the PLUTO [138] event generator. One ω decaying into $\mu^+\mu^-$ was embedded per event into the background event. The simulation has been performed for central Au+Au collision at 8 AGeV beam energy. CBMROOT release version of APR20 has been used for the simulation.

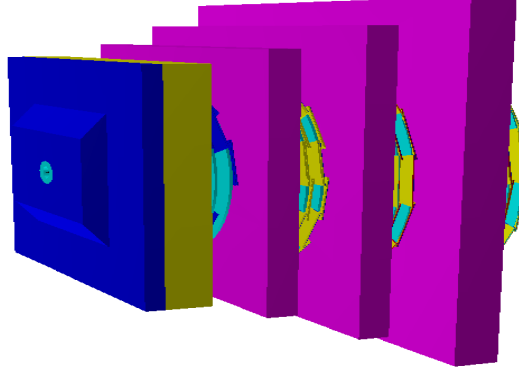


Figure 3.11: Closeup view of MuCh setup. 4 stations and 4 absorbers are used. First absorber is segmented in two parts as described in the main texts.

3.2.1 MuCh setup

The LMVM setup of CBM in di-muon mode for SIS100 consists of the dipole magnet, STS, MuCh, TRD and TOF subsystems, respectively, and is shown in Figure 3.10. The zoomed view of MuCh setup (4 absorbers + 4 stations) is shown in Figure 3.11. The latest version of detector geometry (v20c) for GEMs has been used. The realistic material budget of detectors has been implemented in this version of geometry, which includes two 3 mm thick G10 material for drift and readout PCBs, 35 μm copper (which is a part of these PCBs), support structure, etc.

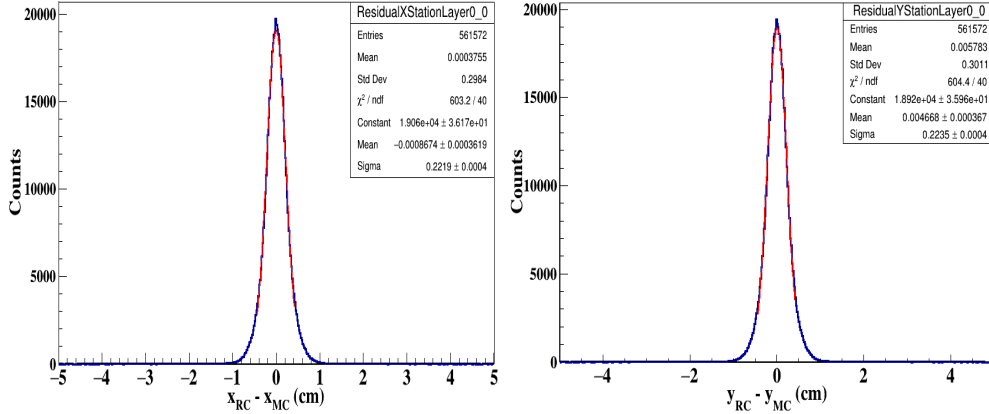


Figure 3.12: Distribution of residual of MuCh hits in x (cm) and y (cm)

3.2.2 Results and Discussions

Track residuals

Due to the scattering of charged particles with materials used in the setup, the original position of the tracks can be shifted. Also, the detector parameters (mean gas gain and spot size) can affect

the σ of the track residuals. The effect of these parameters has been studied systematically.

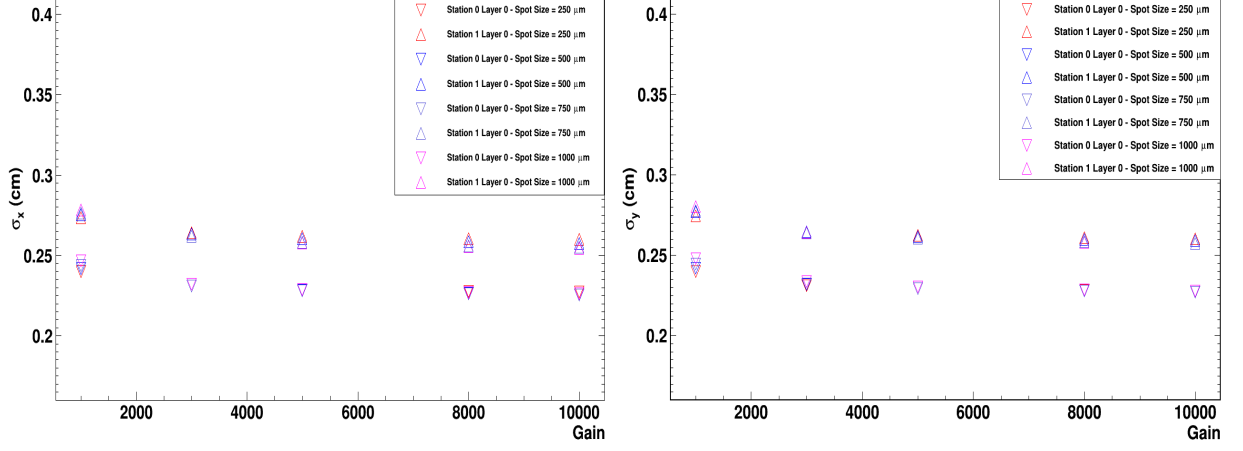


Figure 3.13: Left: Variation of the residuals of MuCh hits in x (cm) with detector gain. Right: Variation of the residuals of MuCh hits in y (cm) with detector gain. The statistical errors are within point size.

The track residual is defined as the difference between the reconstructed (RC) hit coordinates with Monte Carlo (MC) hit coordinates. The distribution of the residuals in X and Y-coordinates are shown in the left and right panels of Figure 3.12, respectively. The σ of the distributions are related to the spatial (pad) resolution, which can vary by changing the digitization parameters. The variation of σ_x with mean gas gain at different spot size is shown in Figure 3.13 (left). The resolution improves by increasing gain and is observed to saturate after a gain of about 3.5k. At a particular gain, the effect of spot size is insignificant on track resolution. This means that the change in spot size from 250-1000 μm does not affect the track resolution significantly. While, at a particular spot size, an improvement in σ is observed with increasing gain. This improvement is of the order of $\sim 10\%$. It can also be seen from the same figure that the 1st station has a smaller value of σ as compared to that with 2nd station. The increase in σ for the second station can occur due to multiple scattering of charged particles inside the absorbers. The same observation can also be seen in σ_y , shown in Figure 3.13 (right).

The variation of cluster size (number of the fired pads per hit) with mean gas gain at different spot size settings is shown in Figure 3.14. It increases by increasing the gain as expected. The percentage increase in cluster size due to the increase in gain is small ($\sim 12\%$) at a smaller value of the spot size and increases (by up to 15%) at the highest spot size value.

The distribution of energy deposition by charged particles from central Au+Au collisions at 8 AGeV beam energy (generated from UrQMD events) for one detector module of station-I is

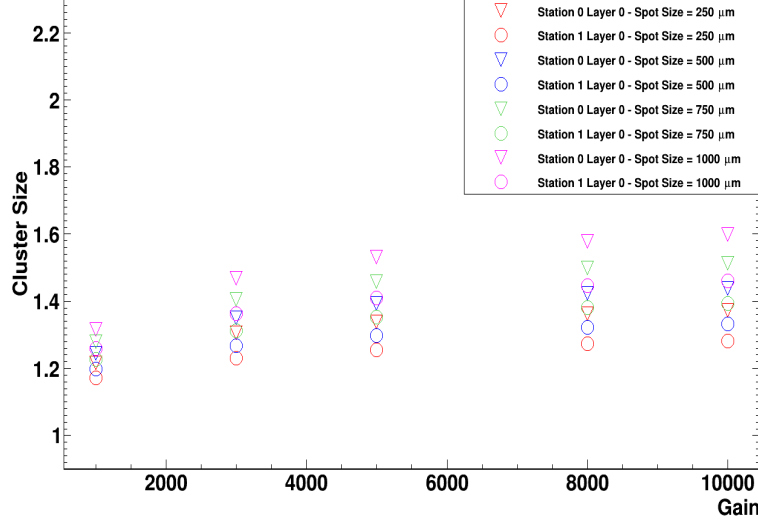


Figure 3.14: Variation of the cluster size with gain. The statistical errors are within point size.

shown in the left panel of Figure 3.15. The average energy loss of about 550 keV per event is observed. The corresponding multiplicity distribution for one module of station-I is shown in the right panel of same figure. On an average, we observed about 48 particles per event per module. By taking in to account the detector area and interaction rate (10 MHz) of CBM, the average particle rate comes out to be 250 kHz/cm² for central collisions. For minimum bias (1/4th of the central), it comes out to be about 62 kHz/cm².

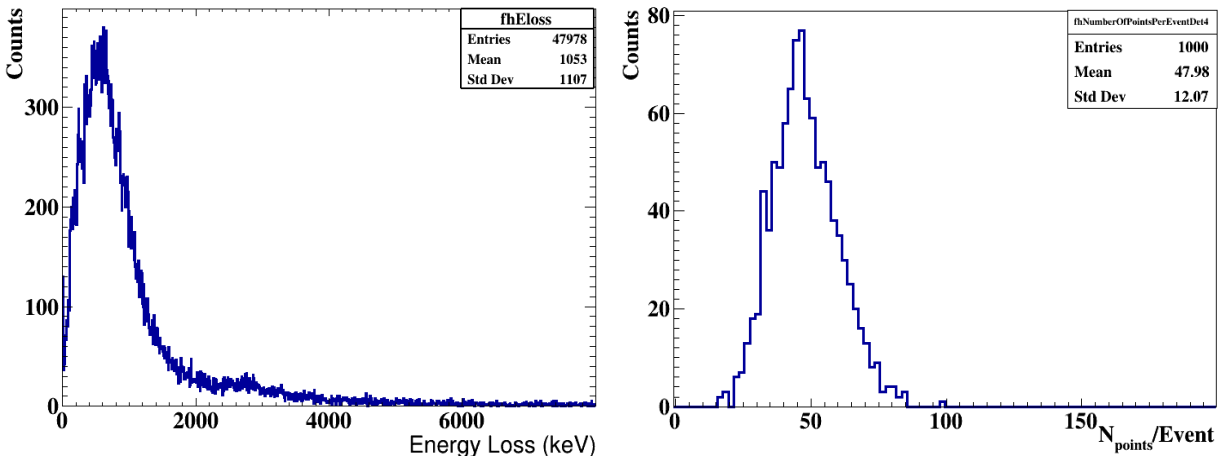


Figure 3.15: Left: Distribution of energy loss by charged particles from central Au+Au collisions at 8 AGeV beam energy for one module of station-I. Right: Multiplicity distribution of from set of data for one modules of station-I.

Table 3.2: Track selection cuts

N_{STS}	≥ 7
N_{MuCh}	≥ 11
N_{TRD}	≥ 1
χ^2_{Vertex}	≤ 2.0
χ^2_{STS}	≤ 2.0
χ^2_{MuCh}	≤ 2.0

Reconstruction of ω in CBM by the di-muon channel

Pluto is a Monte-Carlo event generator designed for hadronic interactions from Pion production threshold to intermediate beam energies. The momentum (p) and transverse momentum (p_t) distribution of ω meson, generated from PLUTO, is shown in Figure 3.16. The rapidity (y) and y - p_t distribution of the input signal particles is shown in Figure 3.17.

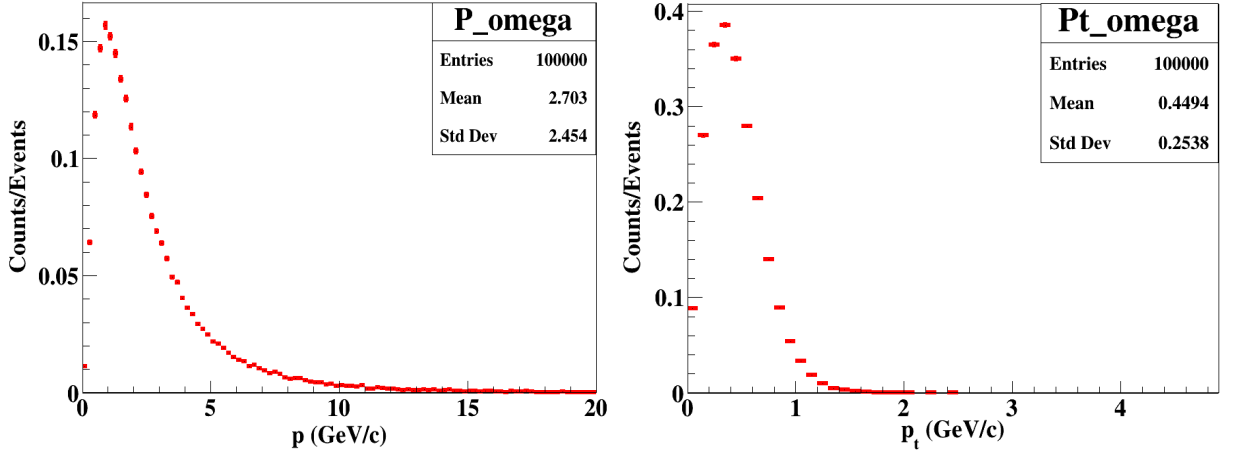


Figure 3.16: Momentum distribution (left) and transverse momentum (p_t) distribution (right) of input signal particles from Pluto generator. The statistical errors are within point size.

The invariant mass of the ω meson has been calculated after full simulation and reconstruction. A set of track quality cuts are applied to every reconstructed global track to identify them as muon track candidates. The cuts used on reconstructed global tracks for selecting valid muon track in the present simulation are given in Table 3.2. The contribution of the non-muonic tracks can be further reduced by applying a 2σ cut on the reconstructed TOF mass. The y - p_t phase-space distribution of accepted ω signal meson is shown in the left panel of Figure 3.18. The signal is extracted from the embedded set of events by selecting oppositely charged muon candidate tracks on track-by-track basis per event. The background is calculated using the super event (SE) technique, where a pair is made using muon candidates from a large number of events and one muon candidate track is combined with all the other oppositely charged muon candidate tracks to calculate the

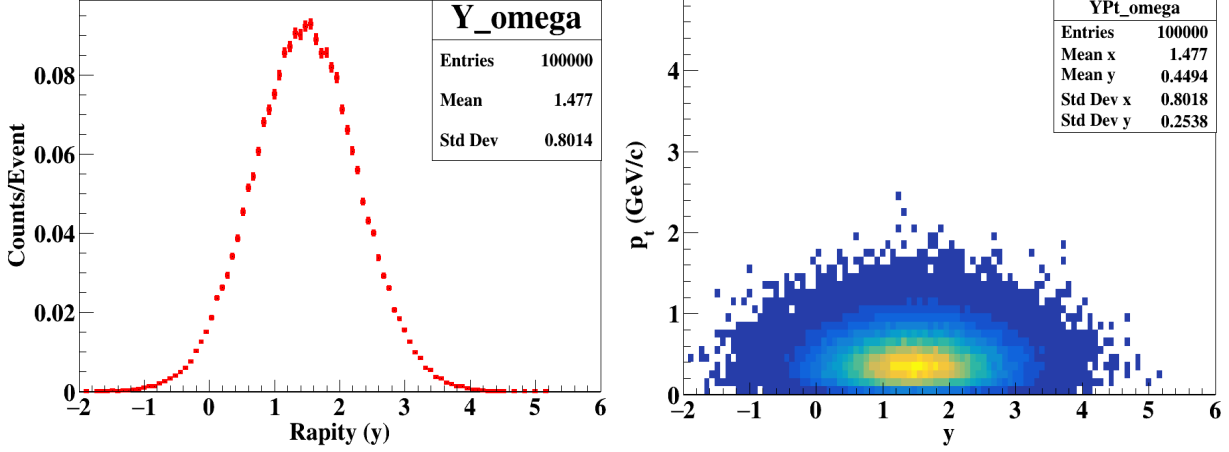


Figure 3.17: Left: Rapidity distribution of ω . The statistical errors are within marker size. Right: Y- P_t distribution of signal particles from Pluto generator.

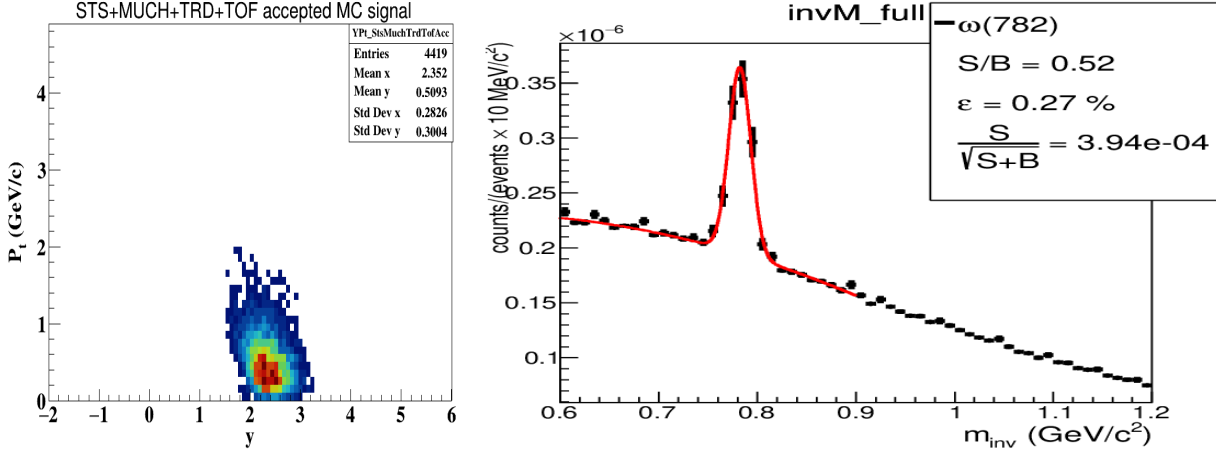


Figure 3.18: Left: y - P_t distribution of signal particles after selection cut of STS+MuCh+TRD+TOF. Right: Invariant mass distribution spectra for omega meson.

combinatorial background. The invariant mass distribution for the ω meson at mean gas gain of 5 k and spot radius of 500 μm is shown in Figure 3.18 (right).

The variation of the reconstructed efficiency with mean gas gain at various spot size settings is shown in Figure 3.19. It increases by increasing the gain, as expected, and saturates after a gain of about 3.5 k. At a particular gain, the effect of the spot radius on the efficiency is less and remains almost constant. As observed, if the gain of the detector is higher than 3.5 k, reconstruction efficiency of ω meson does not vary further and becomes constant. The S/B ratio for each of these settings has been calculated and shown in Figure 3.20. The S/B decreases by increasing gain. We cannot conclude from this study whether the signal is affecting the S/B ratio or the background or this is an effect of both. So, we look at significance ($S/\sqrt{S+B}$) variation, which is shown in Figure 3.20. The trend is entirely similar to what we saw in the efficiency plot.

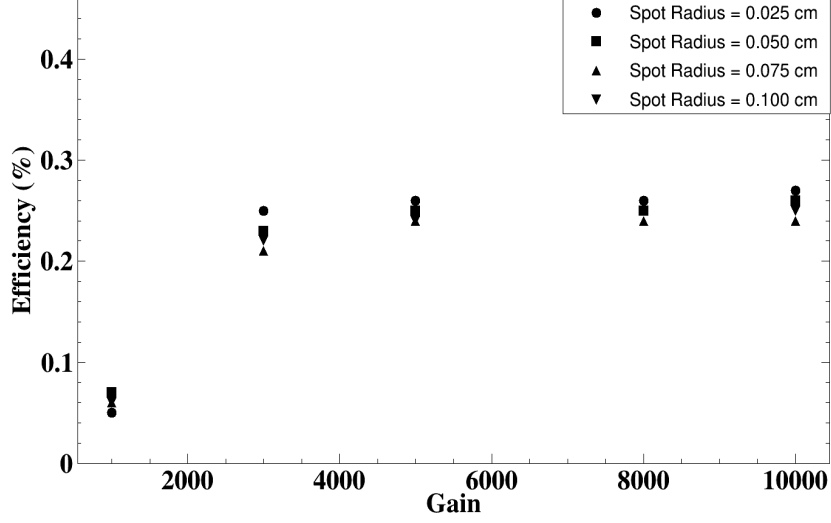


Figure 3.19: Variation of ω reconstruction efficiency with gain for various spot size settings. The statistical errors are within marker size.

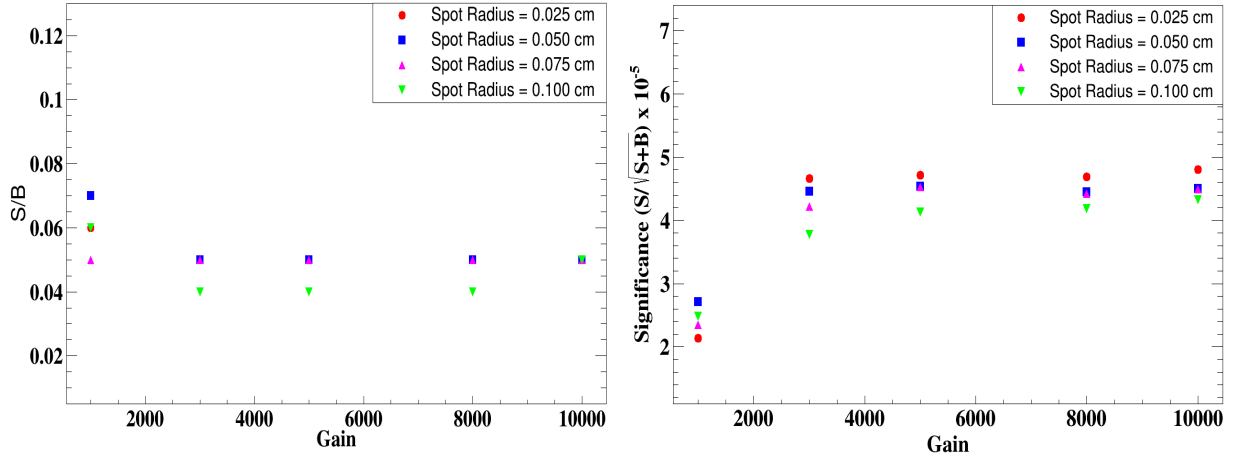


Figure 3.20: Left: Variation of S/N with gain for various spot size settings. Right: Variation of significance with gain for various spot size settings. The statistical errors are within marker size.

3.3 Summary

In summary, we conclude that the efficiency of finally detecting ω meson does not vary with spot radius. It however increases with gain and saturates after a gain of about 3.5k. So, if our detector modules in the final CBM experiment run at a gas gain of higher than 3.5k, we will be able to reconstruct ω without any loss in the detection efficiency. From this study, the optimized value of mean gas is about 3.5 k or greater than that, and spot radius can be between 250 μm -1000 μm .

Chapter 4

Gas Electron Multiplier Detector, Basic Characteristic Study

The discussion on CBM and MuCh systems are given in chapter 2. Understanding the main physics behind the working of a detector, i.e., the interaction of radiation with matter, is a must before building and testing. So, in the first part of this chapter, we discuss particle interactions with matter. In the second part, working principle of GEM detectors, its advantage, and applications are discussed. The test of different prototype detectors in the lab with radioactive sources (such as X-ray, β -source, etc.) is discussed in the third part of this chapter.

4.1 Particle interaction with matter

The interaction of charged particles, photons, and neutrons with matter will be the main processes that will be important in the CBM environment and during the test of detectors in the lab and the beams. However, the interaction of neutron with matter is not discussed here, but one can find in references [139, 140].

4.1.1 Interaction of charged particles with matter

A fast charged particle that passes through the detector medium (in the form of gas, solid, or liquid) can interact via three different processes: i) Electromagnetic (EM), ii) Strong and iii) Weak interactions. Of all these interactions, only the electromagnetic one is the dominant process. The weak interactions are negligible (except for the neutrinos) for all the particles, and the typical range of strong interactions is 10^8 to 10^{10} orders of magnitude lower than that of the atomic scale.

Coulomb interaction is one of the main processes via which interaction takes place. In this process of interaction, the excitation and/or ionization of the medium happens. As a result, a free charge is released, which can be used to generate electronic signals.

Energy loss

A heavy charged particle ($m \gg m_e$ = mass of electron) interacts with the atomic electrons of the matter and transfer part of its energy, which results in the ionization and/or excitation of the medium. In the ionization process, the atomic electrons from the atom gets ejected. In some cases, the atoms get excited by the incoming particles, and in the process of de-excitation, the electrons are ejected. The average energy loss ($-dE/dx$) of the incoming charged particles in the medium is given by the Bethe-Bloch formula:

$$\langle -\frac{dE}{dx} \rangle = \frac{0.3071}{A} \frac{z^2 Z}{\beta^2} \left(\frac{1}{2} \ln \left(\frac{2m_e \beta^2 \gamma^2 T_e^{max}}{I^2} \right) - \beta^2 - \frac{\delta(\gamma\beta)}{2} - \frac{C_e}{Z} \right) \quad (4.1)$$

where A is Avogadro number, z and $\beta=v/c$ is the charge and velocity of the incoming particles, Z is the atomic number of medium and I is the mean excitation energy, $\delta(\gamma\beta)/2$ is the density effect correction term at high energy, C_e/Z is atomic shell correction term at lower energy, etc. T_e^{max} represents the maximal kinetic energy transferred to an ionized electron

$$T_e^{max} = \frac{2m_e c^2 \beta^2}{1 - \beta^2} \quad (4.2)$$

The Bethe-Bloch equation is only valid for $0.1 \lesssim \gamma\beta \lesssim 1000$. Equation 4.1 gives the mass stopping power and its unit is $\text{MeV g}^{-1} \text{ cm}^2$. On multiplying it with corresponding ρ (density - g/cm^3) of the medium we get the linear stopping power $\rho(dE/dx)$ (MeV/cm).

The projectile velocity becomes comparable to the velocities of atomic electrons for $\gamma\beta \sim 0.1$, and the radiative loss effect starts at $\gamma\beta \sim 1000$. These two limits are Z -dependent. The T_e^{max} depends slightly on the incident particle mass at high energies, but for all practical purposes, the stopping power is a function of β alone for a given material. The stopping power first decreases as a function $1/\beta^\alpha$ where $\alpha \approx 1.4$ - 1.7 , and it depends slightly on the incident particle mass and decreases with Z , and reaches a minimum at $\beta\gamma \approx 3.5$ - 3.0 . It then begins to rise due to logarithmic terms. More detailed discussion about this can be found in [10].

In the case of the HEP experiments, most of the relativistic particles have a mean energy loss close to the minimum. They are identified as “Minimum Ionizing Particles” (MIP).

The GEM detectors of the MuCh system will operate in an Argon-based gas mixture. The

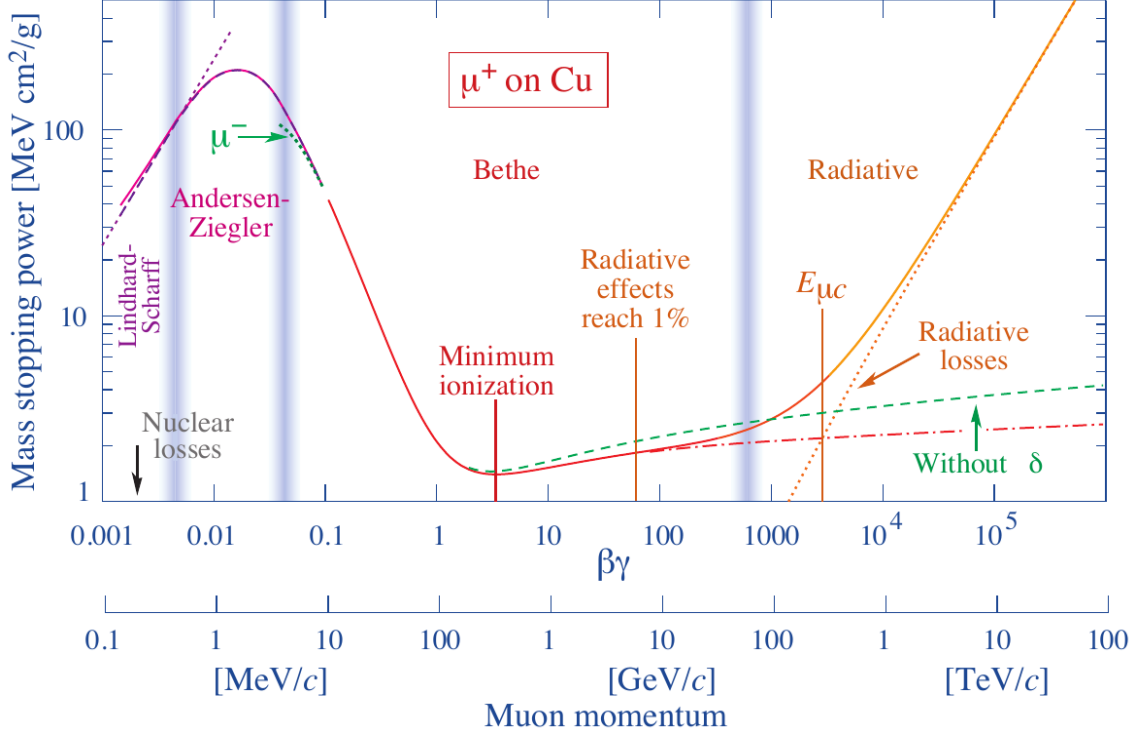


Figure 4.1: Stopping power for positive muons in copper as a function of $\gamma\beta$. Solid curves represents the total stopping power [10].

average energy loss in Argon at MIP is close to 1.53 MeV/g/cm^2 as can be seen in Figure 4.2. Energy loss per unit length in Argon gas ($\rho = 1.78 \times 10^{-3} \text{ gm cm}^3$) of thickness 1 cm is

$$\Delta E_{\text{argon}} = -\left\langle \frac{dE}{dx} \right\rangle \times \rho \times d = 1.53 \times 1.78 \times 10^{-3} \times 1 = 2.72 \text{ keV/cm} \quad (4.3)$$

We can estimate the total number of electron-ion pair (n_T) produced by both the primary and secondary ionization using the following equation:

$$n_T = \frac{\Delta E}{W_i} \quad (4.4)$$

where ΔE is the total energy transferred to the given volume and W_i is the effective average energy to produce one ion-electron pair. We can calculate the total number of primary electrons produced by MIPs in the MuCh detector for Ar/CO₂ (70:30) gas mixture. For 3 mm gas thickness the $\Delta E = 861 \text{ eV}$ (calculated using equation 4.3). Therefore, the number of primary ionization for Ar/CO₂ gas mixture

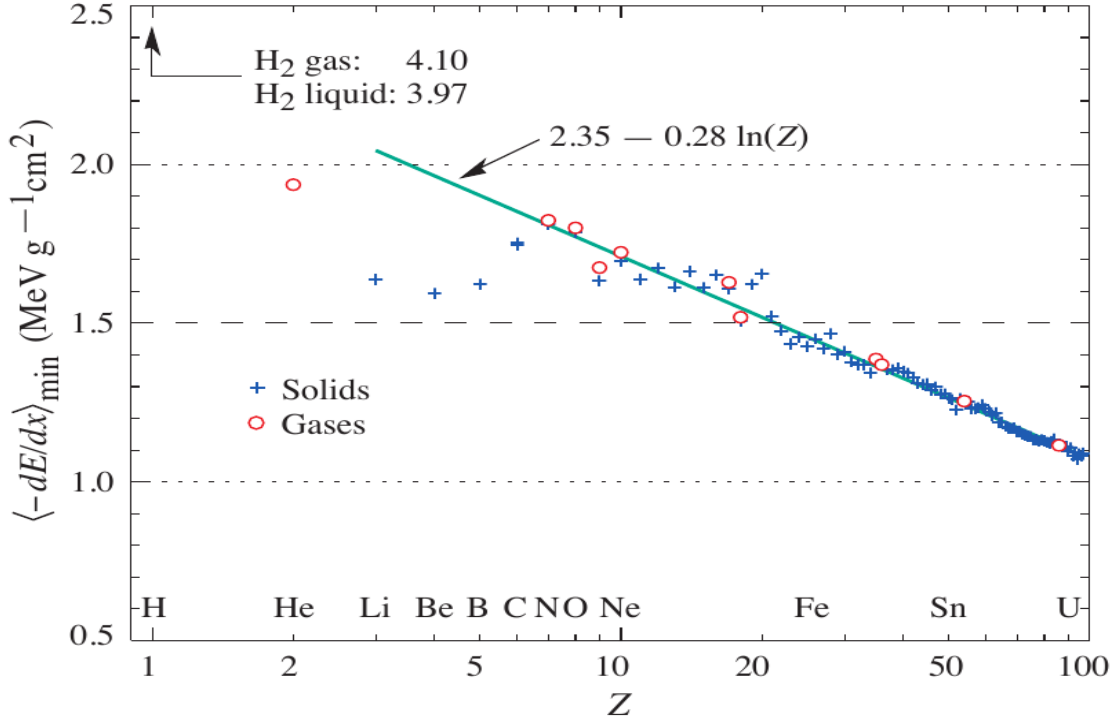


Figure 4.2: Energy loss of a MIP as a function of the atomic number of the medium [11]. The red line refers to the Argon ($Z=18$).

$$n_T = \Delta E \left[\frac{0.7}{W_i(Ar)} + \frac{0.3}{W_i(CO_2)} \right] \approx 31 \text{ pairs} \quad (4.5)$$

4.1.2 Interaction of photon with matter

As we test our detectors in the lab with X-rays, we remind ourselves about the photon interactions with matter briefly.

The photon interacts with matter mainly via three processes, namely photo-electric effect, Compton scattering, and pair production. The photon interaction in the matter is localized, and it loses energy in a single event while it is gradual in the case of charged particles. If we consider a beam of photons with energy E and intensity I passes through the medium of thickness x ; then the intensity loss is given by:

$$dI = -N\sigma(E, Z)I dx \quad (4.6)$$

where σ is the total cross-section of interaction for a given material of atomic number Z and atomic density N . Considering the initial intensity of beam I_0 , the total attenuation is:

$$\frac{I}{I_0} = e^{-N\sigma(E,Z)x} = e^{-(\mu/\rho)X} = e^{-\mu_m X} \quad (4.7)$$

where $\mu_m = \mu/\rho$ is the mass attenuation coefficient, and $X=\rho x$ is the reduced thickness of the medium.

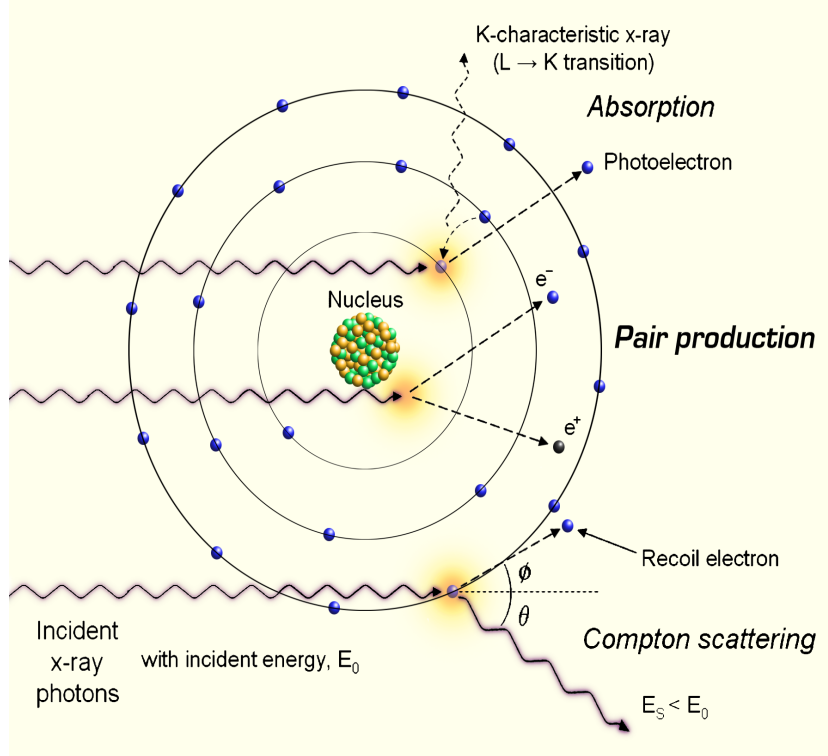


Figure 4.3: Absorption processes in photon interactions [9].

The several absorption processes of photon interactions are shown in Figure 4.3. The total μ_m is simply defined as the sum of all the partial coefficients:

$$(\mu_m)_{total} = (\mu_m)_{photoelectric} + (\mu_m)_{Compton} + (\mu_m)_{pair} \quad (4.8)$$

Interaction of X-rays from ^{55}Fe source with gas:

As discussed in section 4.2.2, Ar/CO₂ (70:30) gas mixture will be used for GEM detectors. We test our detector in lab with mono-energetic X-ray source, mainly with ^{55}Fe . It produce photons of an average energy 5.9 keV (5900 eV). The total number of primary ionization can be calculated using equation 4.3:

$$n_T = \Delta E \left[\frac{0.7}{W_i(\text{Ar})} + \frac{0.3}{W_i(\text{CO}_2)} \right] = 5900 \times \left[\frac{0.7}{26} + \frac{0.3}{33} \right] \approx 212 \text{ pairs} \quad (4.9)$$

4.1.3 Drift and diffusion in gases

The moving charged particle interacts with the gaseous medium and creates electron-ion pair, called primary ionization. These ionized electrons generate a signal in the electronics. However, these electrons encounter other gas atoms in their path before they get collected at the readout. So, understanding these interactions is necessary for selecting gas mixtures.

The energy loss due to the interaction of primary electrons with the gas medium is gradual, and it is described by Maxwell distribution.

The displacement of the charges at the distance x from the origin after time t can be calculated by Gaussian distribution:

$$\frac{dN}{N} = \frac{1}{\sqrt{4\pi Dt}} e^{-\frac{x^2}{4Dt}} dx \quad (4.10)$$

where D - coefficient of diffusion which depends on nature of charge and the medium, N - number of charge, T - Temperature, and k - Boltzmann constant. The mean free path (λ) is defined as average distance between two collisions is given by:

$$\lambda = \frac{1}{n\sigma_{collision}} \quad (4.11)$$

where σ - interaction cross-section, n - number of atoms per unit volume.

Free charges move along the field when it is placed in a uniform electric (E) field. The mobility of the charge is:

$$\mu = \frac{v_d}{E} \quad (4.12)$$

The above equation can be written as (using Einstein's relation):

$$\mu = \frac{e}{kT} D \quad (4.13)$$

The drift velocity and mobility of the electrons are not constant when it moves in an electric field. The simple expression for the drift velocity of electron is given by Townsend as:

$$v_d^e = \frac{e}{2m_e} E\tau \quad (4.14)$$

where τ is the mean time between collisions. Using ideal gas approximations, the drift velocity

becomes proportional to the E/P and T , where T is the temperature of the medium and P is the pressure of the gas:

$$v_d^e \propto \frac{ET}{P} \quad (4.15)$$

4.2 Gas detector, gas amplification and working principle

Understanding the physical phenomena requires a powerful detector to measure infinitesimal objects and their properties. There exist many types of particle detectors. In all these detectors, the most commonly used are gaseous detectors, which are very light and provide a high level of flexibility in terms of composition and geometry. The gas detectors are used in many HEP experiments for these reasons. The amount of primary charge produced is much less compared to that in other technologies due to a very low density of the detection medium. That is why these kinds of detectors require an amplification stage to measure the signal. In this section, the basic operation of the gas detectors is discussed.

The primary electrons generated via incoming particles get enough kinetic energy in the electric field to ionize other gaseous atoms. This chain of the process is responsible for the amplification of the electrons in gas detectors. The mean free path is defined as the average distance between successive collisions. The first Townsend coefficient (α) is the inverse of the mean free path and given by:

$$\frac{\alpha}{P} = Ae^{-BP/E} \quad (4.16)$$

where A and B are parameters that depend on the type of gas and electric field (E), and P is the pressure of the gas. Consider n as the number of electrons at a given particular position x , and after a path of dx along the drift direction, the number of electrons after amplification can be calculated using the following formula

$$dn = n\alpha dx \quad (4.17)$$

The amplification factor (M) is given by:

$$M = n/n_0 = e^{\alpha x} \quad (4.18)$$

The above equation is for a uniform electric field, and it depends on the distance x . The M between x_1 and x_2 can be expressed as:

$$M = \exp\left[\int_{x_1}^{x_2} \alpha(x) dx\right] \quad (4.19)$$

The M increases exponentially with the electric field. However, it shows a limit around $M=10^8$ due to space charge influence on electric field and because of the spread of avalanche by photon emission. This is known as the Raether limit, which corresponds to $\alpha x \sim 20$.

4.2.1 Operation modes of gas detectors

The operation of gas detectors can be understood by assuming a parallel plate geometry. The signal in the form of charge generated from this detector is dependent on the applied voltage across the two electrodes. There are mainly four modes of operation, namely ionization, proportional, Geiger, and streamer, respectively, in the gas detector operation. These regions are shown in Figure 4.4.

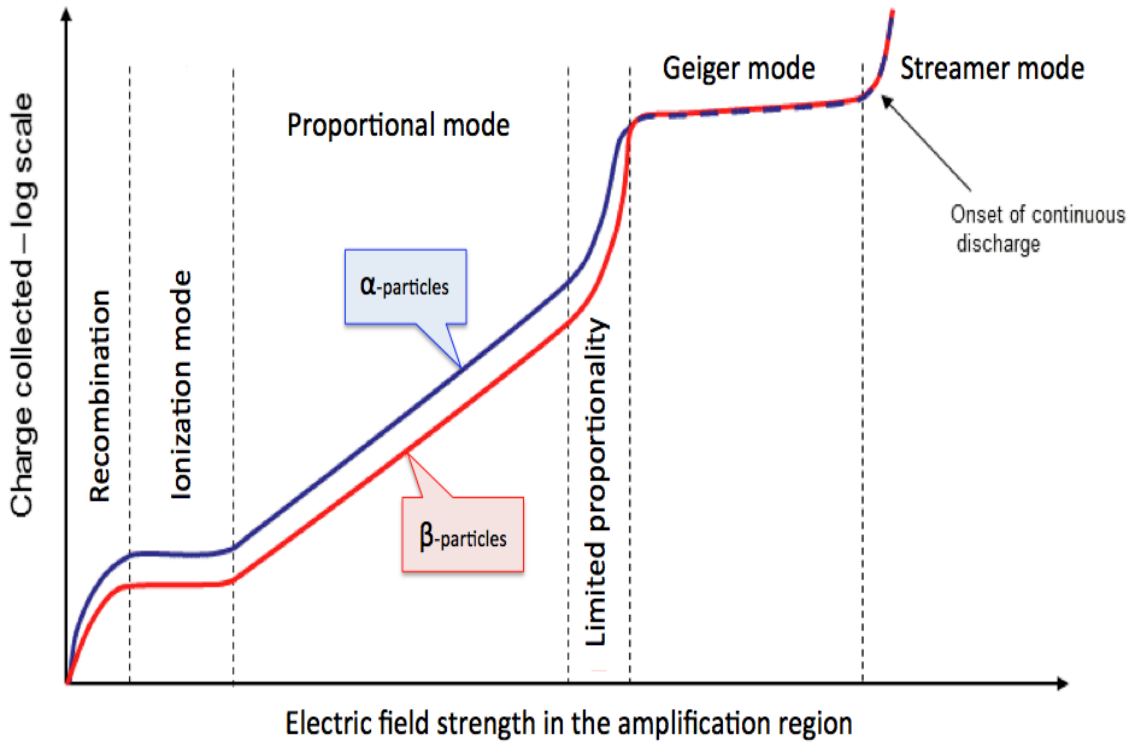


Figure 4.4: Gain-voltage characteristics for gaseous detectors showing the different operating modes [9]. The y-axis is refers to the collected charge in logarithmic scale.

At the start of Figure 4.4, where the electric field is too low, and the generated primary charges recombine. This region is known as the recombination region.

Ionization Mode: The recombination process starts to decrease by increasing the applied field, and a plateau is reached where all the primary charges get collected at the readout. This region is known as the ionization region. In this mode, it is not necessary to amplify the primary charge before collection.

Proportional Mode: In the HEP experiment, detectors are used to detect the high-energy charged particles and/or photons. The primary charges produced in ionization are not enough to generate signals. So, we need to amplify it. One can achieve this by increasing the applied electric field. The number of electrons after amplification is proportional to the primary charges and hence proportional to the energy of the incoming particles. If we increase the electric field further, the secondary ionization is no longer proportional to the primary, and this region is known as limited proportional.

The gas detectors, such as proportional counters, multi-wire chambers, and micro-pattern gas detectors, are widely used in many HEP experiments. The triple GEM detectors, discussed in this thesis, are operated in this proportional region.

Geiger Mode: At relatively higher electric fields, the multiple secondary avalanches are generated by the primary avalanche mostly because of the emissions of the UV photons. The total charge in this case after amplification is independent of the primary charges. This kind of detector is generally used for counting the number of particles since the primary charge information is lost.

Streamer Mode: If we further increase the applied voltage across the electrodes, the space charge density becomes comparable to the surface charge density of the electrode. The secondary electrons generated due to photo-electrons in the GM region can drift along the field and induce additional avalanche. In this region, a thin plasma filament is produced in the medium, also known as a streamer. The streamer can propagate towards the electrode and can trigger a discharge.

4.2.2 Choice of gas mixture

Good operation of the detectors imposes a condition on the choice of the gas. The primary charges of the amplification strongly depend on the properties of the gas. In addition, different experiments have their own requirements, such as high rate capability, maximum longevity, good spatial and time resolutions, or low discharge probability. The gas mixture proposed for MuCh-GEM detectors is Ar/CO₂ (70:30).

Most of the poly-atomic molecules de-excite via non-ionizing processes, but noble gases are preferred for the detection of MIPs at low electric fields. Argon gas is widely used because it

gives an acceptable number of electron-ion pairs and is relatively cheaper than Krypton or Xenon. However, photon emissions of energies greater than 11.6 eV happen when an Argon gas de-excites from the excited state to the ground state. These photons can induce a secondary avalanche. Therefore, we need to remove these photons, and this is done using “quenching” gas, which absorbs these photons and dissipates energy through a non-ionizing process. The CO₂ gas is mainly used as a quencher because of its very high absorption of photons. – sudden end

Several triple GEM detectors have been built of various sizes within the dimension ranges of 10 cm × 10 cm to 50 cm × 40 cm, and their characteristics have been studied using both conventional and self-triggered electronics. The final version of self-triggered ASIC (STS/MuCh-XYTER) [141, 142, 143] has also been used for the detector tests. However, before this final version, n-XYTER [144, 145] ASIC has been used, as it was the only self-triggered electronics available at that time. Test of small size chambers is discussed in this chapter, and the test of real-size modules has been discussed in chapter 5 and chapter 6

4.3 GEM detector

The Gas Electron Multiplier (GEM) detector belongs to the family of the gaseous detector, and it was first introduced by F. Sauli in 1997 [146]. The detector has three main components, drift electrode, GEM foil, and readout electrode. Of all these components, GEM foil is the primary component, which acts as a gas amplifier, if the nominal voltage is applied across the electrodes of the foil. The standard GEM foil consists of a thin dielectric polymer (polyimide) of 50 μm thick and a metal (copper) layer of thickness of 5 μm coated on both sides of it. Regular holes of 70 μm diameter and 140 μm pitch are made in the foils using the photolithographic technique. A nominal voltage of $\sim 500\text{V}$ is applied across the two electrodes of the GEM foil, which creates a very high electric field ($\sim 50 \text{ kV/cm}$) inside the holes.

4.3.1 Working principle of GEM detector

When a charged particle passes through the gaseous medium (active volume), it creates an electron-ion pair. The electron drifts toward the GEM hole and gets amplified by the high electric field inside the holes. These electrons are collected at the readout electrode, forming a signal. The detector gain is defined as the ratio of output charge divided by the input charge. The input charge is calculated using primary ionization (refer equations 4.5 and 4.9), while the output charge

is calculated using electronic signal. The detector gain can be increased by increasing GEM voltage or also by inserting more GEM foils between the drift and the readout electrode. In most of the HEP experiments, triple GEM (three-layer of GEM foils) detectors are used/chosen for their advantages given below:

4.3.2 Advantage of GEM detectors

- large gas gain in multistage operation
- low discharge probability
- handling high particle rates
- good spatial and time resolutions
- high degree of granulation of GEM amplification cells, allows imaging of highly resolved events during readout etc.

4.3.3 Application of GEM detectors

The main application of the GEM detectors are given below and one can find more details about this in the review article [147]. The GEM detectors can be used for:

- ◇ charge particle tracking
- ◇ fast detectors for trigger systems
- ◇ end-cap detectors for time-projection chambers
- ◇ gas photo-detectors
- ◇ cryogenic detectors for detecting neutrinos
- ◇ dark matter detectors for detecting coherent neutrino scattering by nuclei
- ◇ X-ray detectors etc.

The triple GEM detectors are used in many HEP experiments like, TOTEM¹ [148], COMPASS² [149], LHCb³ [150], CMS⁴ [151, 152, 153], ALICE⁵ [154, 155], and PHENIX⁶ experiment [156] etc. As already discussed, a triple GEM detector will also be used for the first two stations of MuCh. It consists of drift (active volume), GEM (amplification region), transfer, and

¹TOTAL cross-section, Elastic scattering and diffraction dissociation Measurement at the LHC

²Common Muon and Proton Apparatus for Structure and Spectroscopy

³Large Hadron Collider beauty experiment

⁴Compact Muon Solenoid

⁵A Large Ion Collider Experiment

⁶Pioneering High Energy Nuclear Interaction eXperiment

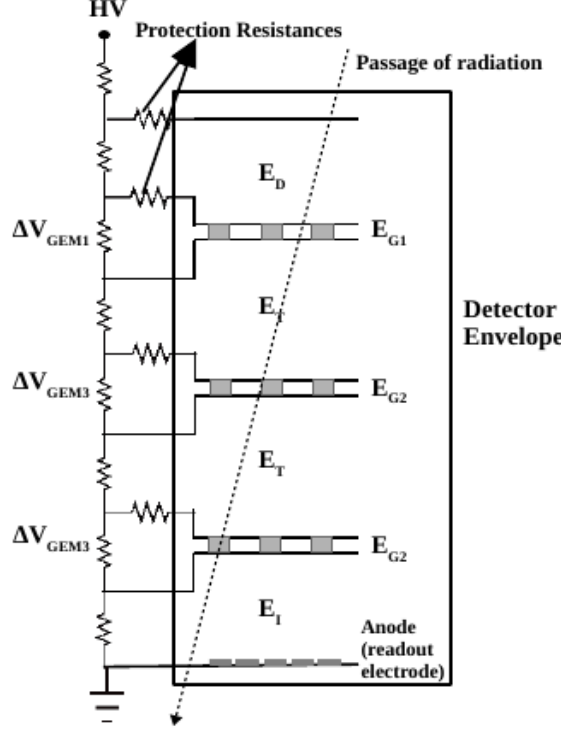


Figure 4.5: Voltage divider schematuc circuit for triple GEM detector.

induction regions. The electric field or voltage symbols for different regions are E_d (drift field), E_i (induction field), E_t (transfer field), E_{G1} (field for top/first GEM foil), E_{G2} (field for middle/second GEM foil), E_{G3} (field for bottom/third GEM foil) and E_G (sum of all GEM fields = $E_{G1} + E_{G2} + E_{G3}$). In the case of GEM foils, sometimes we will use voltage (V) instead of electric field (E). We have used two schemes to power the triple GEM detector: (1) through a resistive divider chain. (2) through independent power supply to each electrode. The advantage of the first method is that we need only one voltage supply for powering the different electrodes. However, at high rate, the latter configuration may be more suited. At higher rates, the pulsed current due to charged particles increases and this can lead to an increase in the overall branch current of the divider circuit, which would result in a decrease in effective GEM voltage. In the case of an independent power supply, the GEM voltages would remain constant. However, the independent power supply is a much expensive option, as compared to using a simple resistive chain circuit. As per calculations at a branch current of $750\mu\text{A}$, the change in GEM3 voltage due to expected pulsed current is of the order of few Volts, which will not affect detector gain. In view of the above arguments, in the final design, the cost-effective option of using a resistive divider circuit will be used for powering GEMs. A schematic picture of the divider chain for triple GEM is shown in

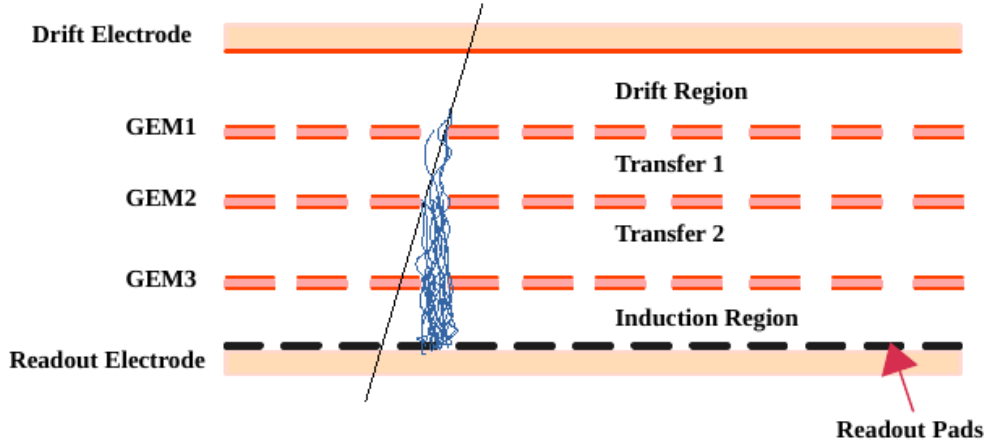


Figure 4.6: Schematic of electron avalanche mechanism in triple GEM. The amplification happens primarily inside the GEM holes.

Figure 4.5. The gaps of 3 mm (drift gap), 2 mm (transfer gaps), and 2 mm (induction gap) between different layers will be used in the final experiment. So, the gap configuration becomes 3/2/2/2. However, in the lab and the test beams, we have also used the gap configuration of 3/1/1/1.5.

When radiation passes through the detector (as shown in the figure 4.6), it ionizes the gas medium and creates ion-electron pair. The electrons then focused on GEM holes due to the drift field and get multiplied in the holes (due to the large electric field). The same process happens for the other two GEM foils and, finally, the signal is collected at the readout electrode. The schematic of avalanche process in triple GEM is shown in Figure 4.6.

4.4 Different readout chains used during the detector test

During the R & D of GEM detectors, we have used mainly two types of readout chains: conventional (NIM-based) electronics and self-triggered (n-XYTER, and STS/MuCh-XYTER based) electronics. As already discussed in the previous chapters, the main goal of CBM is to measure rare probes with good statistics. In order to do that, the data will be collected in self-triggered mode and the signals from the detectors will be read out using self-triggered electronics. The n-XYTER and STS/MuCh-XYTER has similar working principle except for a few differences. The n-XYTER was the first such chip available for the test. The conventional electronics are used for the detector test in the lab. The description of the conventional and n-XYTER (rev-D) based readout chains is discussed in this section, while the STS/MuCh-XYTER is discussed separately in chapter 6.

4.4.1 n-XYTER, ROC based readout chain

In the lab and test beams, we have used n-XYTER ASIC [145] based front-end-boards (FEB) for reading a signal from the GEM detectors. This ASIC is no longer produced or used, and a new ASIC called STS/MuCh-XYTER [141, 142, 143] is currently under use, which is the final ASIC for the STS and the MuCh detector systems. n-XYTER is a 128 channel self-triggered readout ASIC, which can measure both the amplitude and time of the hits. Architecture and its basic working principle can be found in the manual [144] and in [145]. Each channel of this chip has two shapers, namely, the slow shaper with a rise time of 130 ns for the measurement of signal amplitude and the fast shaper of rise time 19 ns for the time measurement. The key features of this chip are given below:

- It is based on CMOS technology
- It has 128 channels
- It is a self-triggered and can read signals up to 32 MHz
- It has a 12-bit ADC
- Its dynamic range is 25 fC
- Slow shaper with a rise time of 130 ns and it has 600 enc at 30 pF
- Fast shaper with a rise time of 19 ns and it has 850 enc for positive signal and 1000 enc for negative signal at 30 pF
- Timing resolution $\sim 2\text{-}3$ ns, time stamp resolution 1 ns
- Power dissipation of 12 mW/channel

There are certain registers (bias) settings of n-XYTER, which can affect signals. The detailed discussion on the study of these bias settings is described in appendix A. The schematic picture of the n-XYTER based readout chain is shown in Figure 4.7. The FEBs are connected to the readout connectors of the detector. The signal from FEBs are then transferred to the ROC⁷ board and then finally to the PC.

Charge calibration:

The charge calibration curve for the n-XYTER chip is shown in the left panel of Figure 4.8. The calibration equation, ADC to charge (fC) conversion, for the n-XYTER chip is given below, and it is taken from [12]:

⁷Read Out Controller

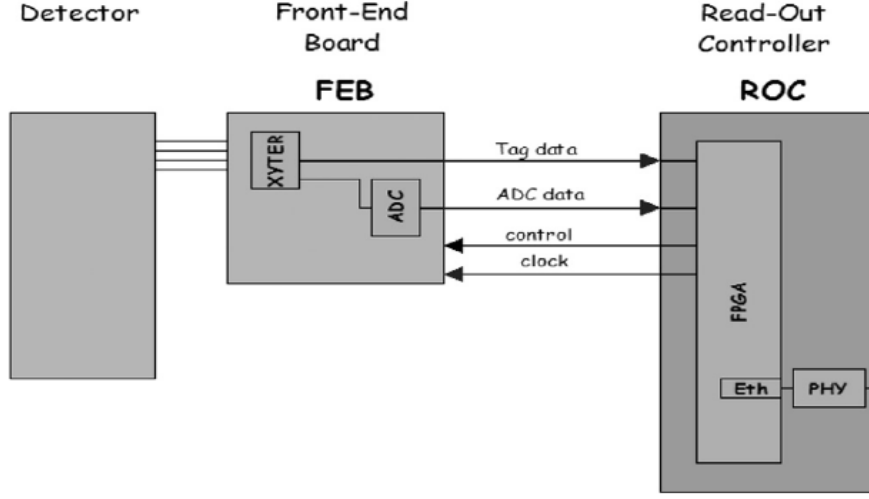


Figure 4.7: Schematic of the n-XYTER based readout system. The detector is connected directly to FEB which houses the n-XYTER ASIC and ADC. ROC as connected to the FEB is to control the data acquisition.

$$Q_{n-XYTER}(fC) = 0.2025 + 20.53 \times 10^{-3} \cdot A - 6.733 \times 10^{-6} \cdot A^2 + 13.24 \times 10^{-9} \cdot A^3 - 3.556 \times 10^{-12} \cdot A^4. \quad (4.20)$$

The ADC of the chip is linear up to 700 ADC and it has non-linear behavior after that. This is the characteristics of the chip itself.

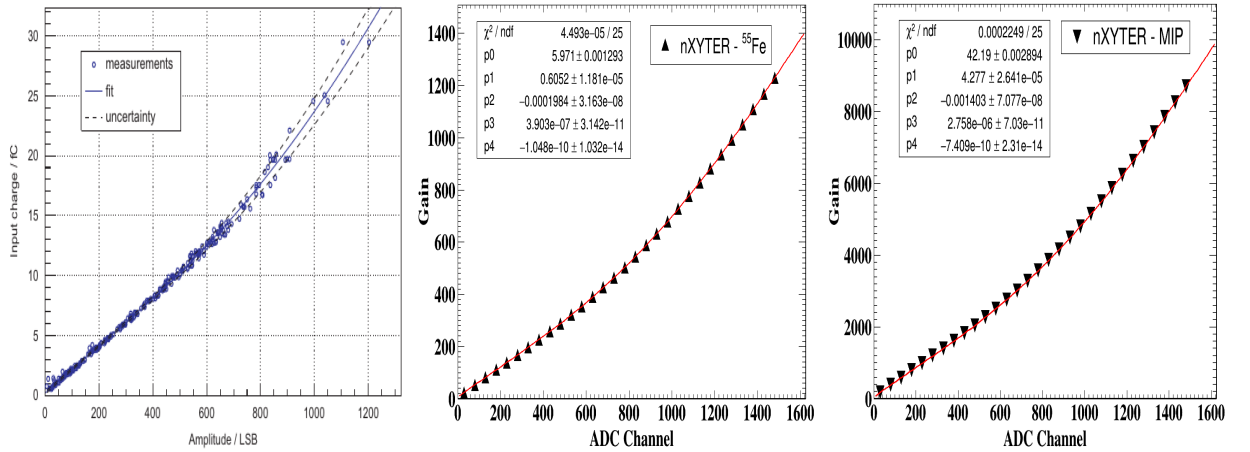


Figure 4.8: Left: n-XYTER calibration curve (taken from [12]). Middle: The gain vs ADC channel from n-XYTER in case the signal taken from ⁵⁵Fe. Middle: The gain vs ADC channel from n-XYTER in case the signal taken from charged particle (MIP). Statistical error bars are within the marker size.

where A is the ADC channel. The ADC channels are then converted to obtain the gain value

using the number of primary electrons and the charge value ($Q_{n-XYTER}$). For calculation of the number of primary ionization's, please refer to equations 4.5 and 4.9, respectively. The gain value can be different for ^{55}Fe and charged particle due to the difference in number of primary electrons. The gain variation with ADC value for n-XYTER in case of ^{55}Fe is shown in Figure 4.8 (middle panel), and in the case of MIP is shown in Figure 4.8 (right panel).

4.4.2 Conventional (NIM based) readout chain

The block diagram of the NIM-based setup for detector test is shown in Figure 4.9. The signal from the detector is fed first to the pre-amplifier, which accepts a negative charge pulse. The output of this pre-amp is a positive voltage pulse that is transferred to the amplifier and then to ADC⁸, which is a part of MCA⁹. The data is then stored in a computer for offline analysis.

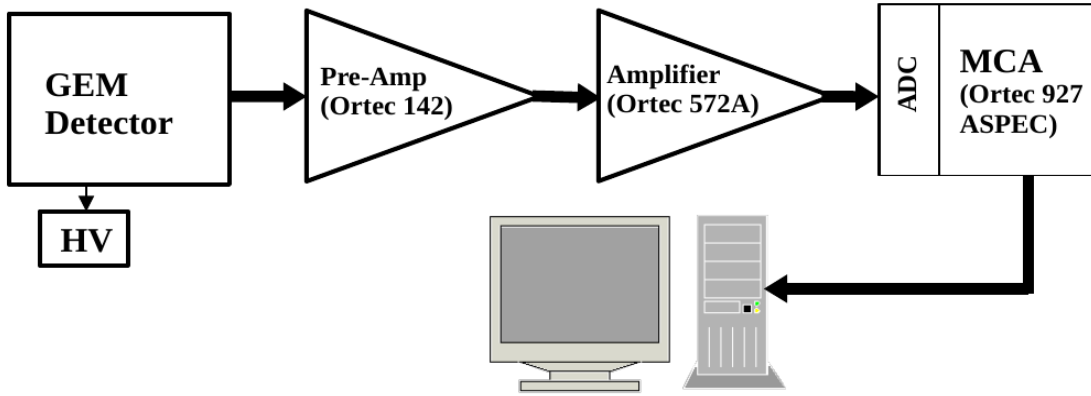


Figure 4.9: Left: Schematic of the NIM-based readout chain.

The charge calibration curve for NIM based readout chain is shown in the left panel of Figure 4.10. The calibration equation is given by:

$$Q_{NIM} (fC) = -0.7288 + 0.4513 \times A. \quad (4.21)$$

where A is the ADC channel. The same calculation for gain is done in the case of MCA data as it was done for the n-XYTER ASIC. The variation of gain with the ADC value for MCA in case of ^{55}Fe is shown in Figure 4.10 (right panel).

As mentioned, the triple GEM detectors will be used for muon detection in the CBM experiment. Therefore, it is necessary to characterize and study the GEM detectors' performance before their use in the final experiments.

⁸Analog to Digital Converter

⁹Multi Channel Analyzer

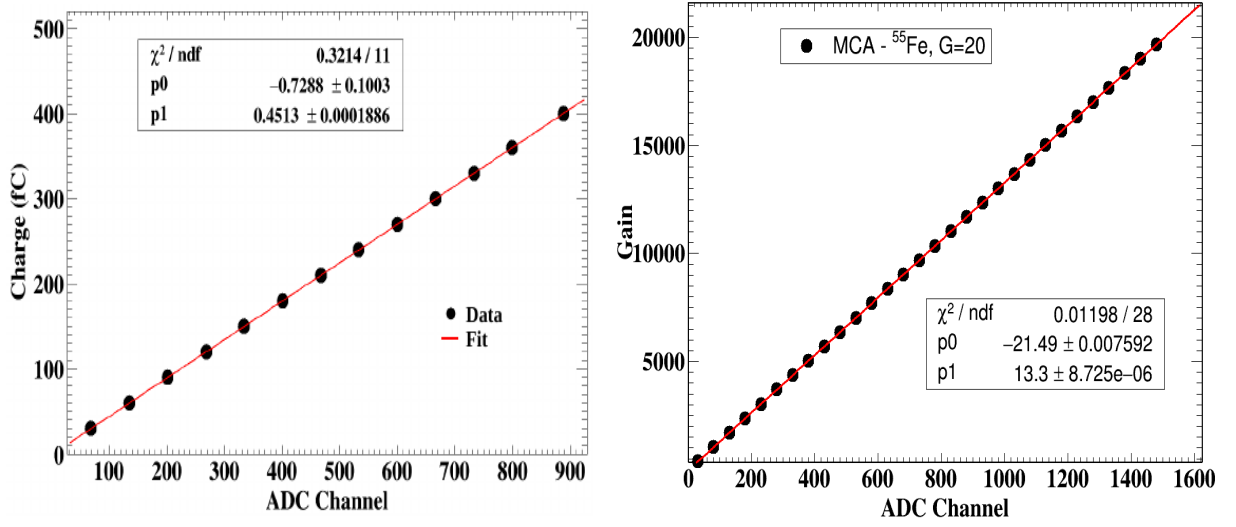


Figure 4.10: Left: Calibration curve for NIM based DAQ. Error bars are within point size. Right: The gain vs ADC channel from MCA in case the signal taken from ^{55}Fe . Statistical error bars are within the marker size.

4.5 Testing different GEM prototypes in lab

4.5.1 Effect of drift, transfer and induction on gain and energy resolution

A $31 \text{ cm} \times 31 \text{ cm}$ triple GEM has been used for this test. The description of the triple GEM and resistive divider chain is discussed in section 4.3. The systematic effect of individual voltage (like drift, transfer, induction, and GEM) on detector gain, energy resolution, time resolution, etc., has been studied using an independent power supply [157, 158].

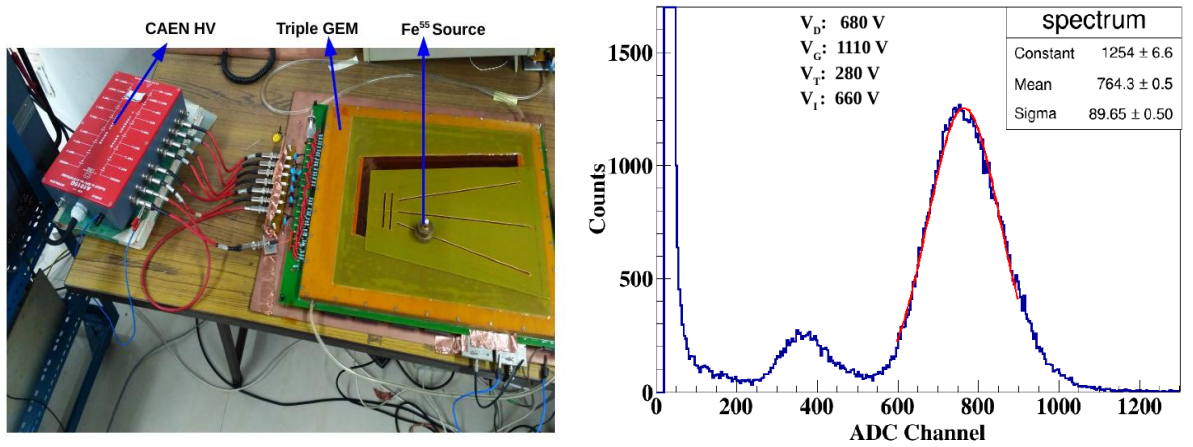


Figure 4.11: Photograph of experimental setup (left) and typical ^{55}Fe pulse height spectra (right).

Experimental setup

The block diagram of the experimental setup is shown in Figure 4.9. The detector has a gap configuration of 3 mm / 1 mm / 1 mm / 1.5 mm, and the readout consists of pads with varying sizes from $\sim 3 \text{ mm} \times \sim 3 \text{ mm}$ to $\sim 10 \text{ mm} \times \sim 10 \text{ mm}$. ^{55}Fe (X-ray source) has been used for this test. The photograph of the test setup in the lab is shown in Figure 4.11 (left panel). A CAEN-built [157, 158] independent power supply has been used for biasing the GEM detector.

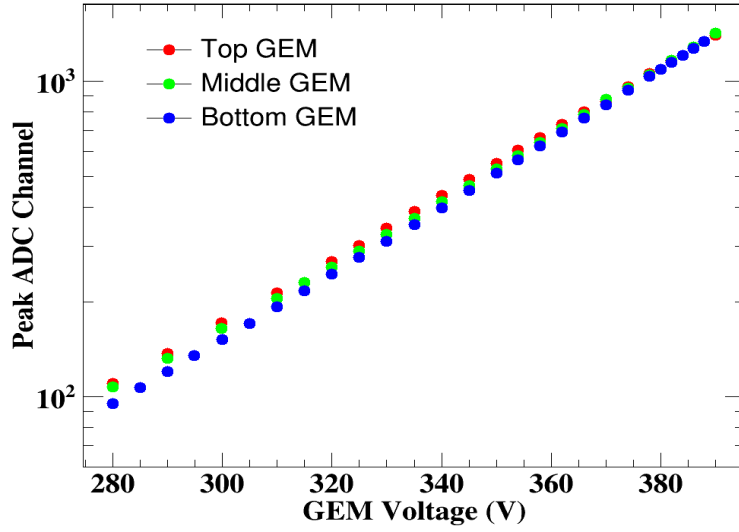


Figure 4.12: Variation of Peak ADC channel with GEM voltage. Voltage of one GEM (say GEM1) varied keeping other (GEM2 and GEM3) fixed and vice-versa. Statistical error bars are within the marker size.

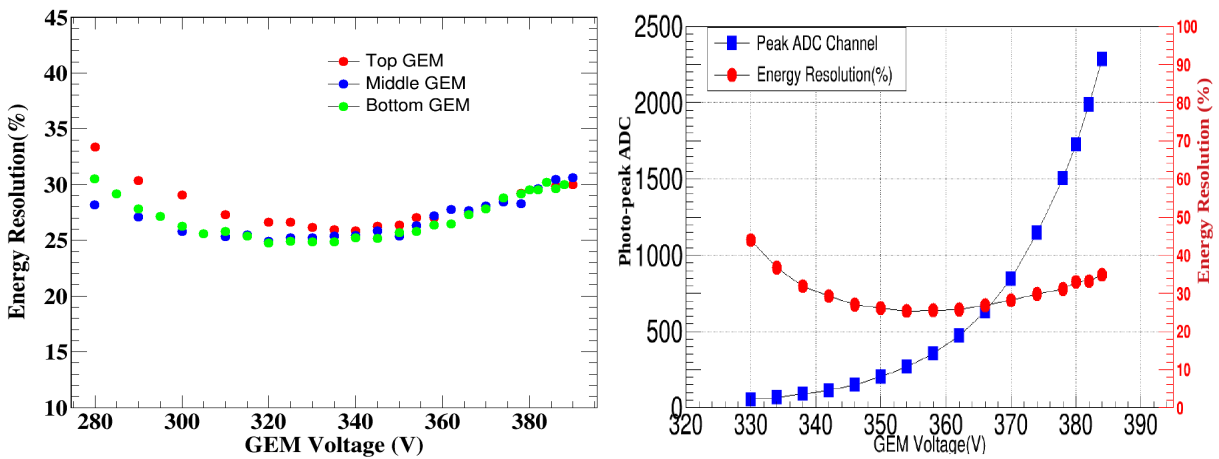


Figure 4.13: Left: Variation of photo-peak ADC channel and energy resolution as a function of combined GEM voltage (GEM1+GEM2+GEM3). Right: Variation of energy resolution with GEM voltage. Voltage of one GEM (say GEM1) varied keeping other (GEM2 and GEM3) fixed and vice-versa. Statistical error bars are within the marker size.

Analysis and Results

The effect of drift, induction, transfer, and GEM voltages on gain (ADC channel) and energy resolution of triple GEM detector has been studied. This test was performed by varying one voltage setting and keeping the other voltages fixed. A typical ^{55}Fe pulse height spectra from the detector is shown in the right panel of Figure 4.11. The energy spectrum is fitted by the Gaussian distribution to extract the mean and sigma. The energy resolution is given by:

$$R(\%) = \frac{FWHM}{\text{Peak ADC Channel}} \quad (4.22)$$

where FWHM is Full Width at Half Maximum and Peak ADC channel is mean of Gaussian fit.

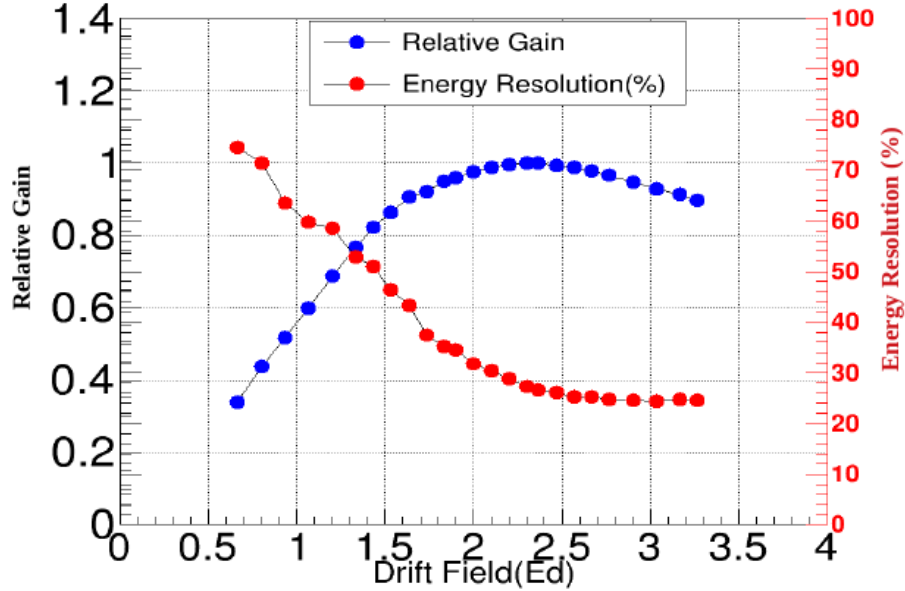


Figure 4.14: Variation of photo-peak ADC channel and energy resolution as a function of drift field (E_d). Statistical error bars are within the marker size.

Effect of GEM voltage: Figure 4.12 shows the variation of gain (in ADC unit) with GEM voltage by keeping other voltages fixed ($V_d=680\text{V}$, $V_t=280\text{V}$, $V_i=660\text{V}$). The different colors in the legends are for different GEMs. Here, we increase the voltage of one GEM foil (say GEM1) from $\sim 280\text{ V}$ to $\sim 385\text{ V}$ keeping GEM2 and GEM3 fixed at 370 V , and vice-versa. Photo-peak ADC increases exponentially by increasing GEM voltage as expected. The gain from the three GEM foils shows similar behavior, as can be inferred from the figure. Variation of energy resolution (%) with GEM voltage is shown in the left panel of Figure 4.13. It first decreases and then increases with voltage. The first decrease of resolution is due to the increase in the number of multiplication,

but the increase is due to the UV emission, which leads to more fluctuations in charges. The effect of the combined GEM voltage (voltages of three GEM foils increased simultaneously) on peak ADC and energy resolution has also been studied by keeping other voltage (V_d , V_i , V_t) fixed, and shown in Figure 4.13.

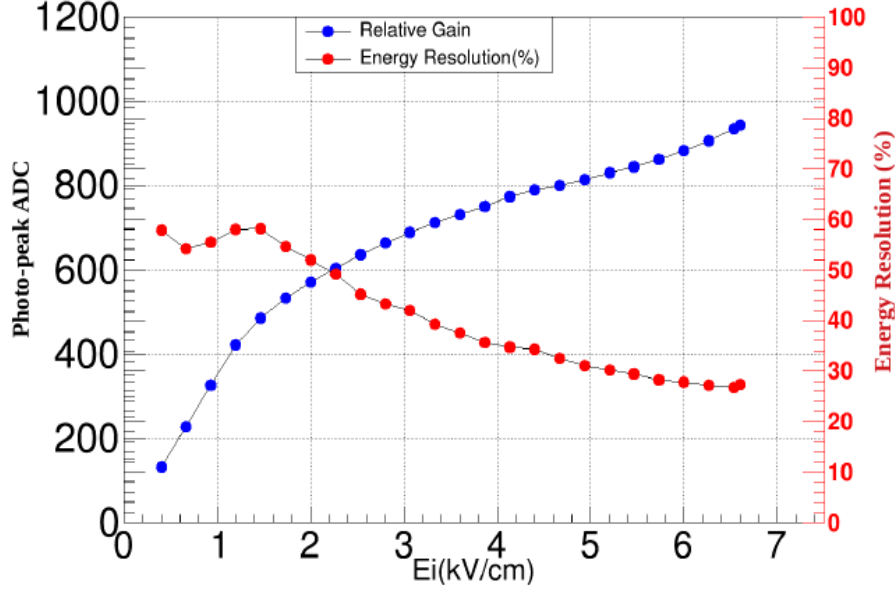


Figure 4.15: Variation of Peak ADC channel and energy resolution with induction field. Statistical error bars are within the marker size.

Effect of drift voltage: Effect of drift field on detector gain and energy resolution is shown in Figure 4.14, keeping other voltages fixed ($V_t=280V$, $V_i=660V$, $V_{G1}=V_{G2}=V_{G3}=370V$). By increasing the drift field, the relative gain increases and then decrease as expected. The first increase is due to less recombination, and the decrease is due to the loss of primary electrons on top of GEM1 foil. Similarly, the % resolution is larger at lower drift voltage and decreases at higher drift voltage.

Effect of induction voltage: The effect of induction voltage on the gain and energy resolution of the detector is shown in Figure 4.15. keeping other voltages fixed ($V_d=680V$, $V_t=280V$, $V_i=660V$, $V_{G1}=V_{G2}=V_{G3}=370V$). If we increase the induction voltage, we collect more and more charges, so gain increases. Resolution is large at lower induction and decreases as we increase the induction field.

Effect of transfer voltage: The effect of transfer (transfer voltage varied equally, $V_{t1}=V_{t2}$) on gain and resolution is shown in Figure 4.16, keeping $V_d=680V$, $V_i=660V$ and $V_i=660V$, $V_{G1}=V_{G2}=V_{G3}=370V$ fixed. Gain increases with V_t as can be expected. The decrease in rel-

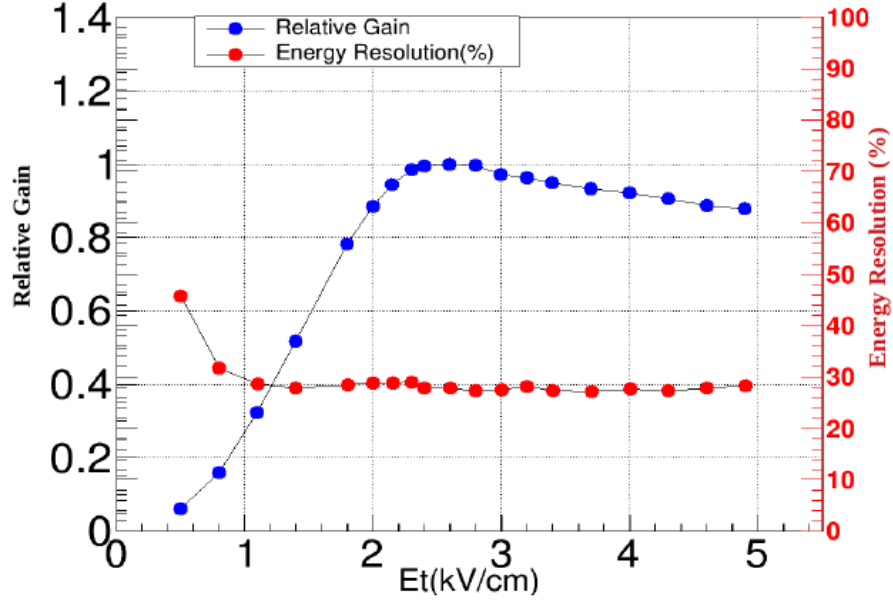


Figure 4.16: Variation of Peak ADC channel and energy resolution with transfer field. Statistical error bars are within the marker size.

ative gain at higher V_t could be because of the losses of an avalanche in the transfer region as well as on top of GEM2 and GEM3 foils. Resolution at lower transfer is larger and decreases for high transfer.

4.5.2 Efficiency measurement of triple GEM in lab

The measurement of time resolution, efficiency, etc., has been performed for the triple GEM chamber in lab using a β -source. Study of these parameters have also been performed with two different detector gap configurations, 3/1/1/1.5 and 3/2/2/2.

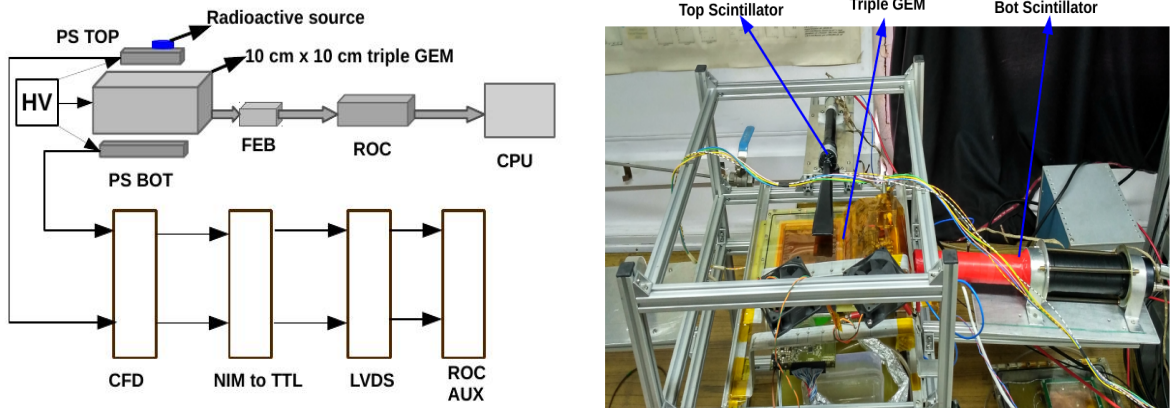


Figure 4.17: Schematic (left) and picture of test setup in lab.

Experimental setup

The block diagram of the experimental setup is shown in Figure 4.17 (left). A $10\text{ cm} \times 10\text{ cm}$ triple GEM detector with a 1-dimensional strip readout was used for the test. The readout consists of 128 strips of width 0.5 mm and pitch 0.2 mm. A resistive divider circuit has been used to provide bias to the GEM detector. One FEB with the n-XYTER chip was used for reading out the signals from the GEM detector. Two scintillator detectors, one (having a dimension of $3\text{ cm} \times 3\text{ cm}$) on the top and another one (having dimension $6\text{ cm} \times 6\text{ cm}$ in size) at the bottom of the GEM was used for trigger selection. The analog signal from the scintillators is first discriminated for noise by Constant Fraction Discriminator (Canberra QUAD CFD 454). CFD delivers a fast negative NIM digital signal. Since the LVDS (Low Voltage Differential Signal) accepts a signal greater than -1.8V, we used a NIM-to-TTL converter to increase the CFD output signal voltage. The signal from LVDS was then given to the auxiliary channels of ROC, which stores the timestamps of the scintillator's signal. We keep ^{90}Sr (β -source) on the surface of the top scintillator and acquire data for different high voltage (HV) settings. A collimation of 3 mm in diameter was used for the source. The photograph of the test setup along with the detectors (GEM and scintillators) is shown in Figure 4.17 (right). We made an arrangement using Al profiles such that we can move the detectors (scintillators as well as GEM) to any position in the frame. In this way, we will be able to test the GEM detector over the full area.

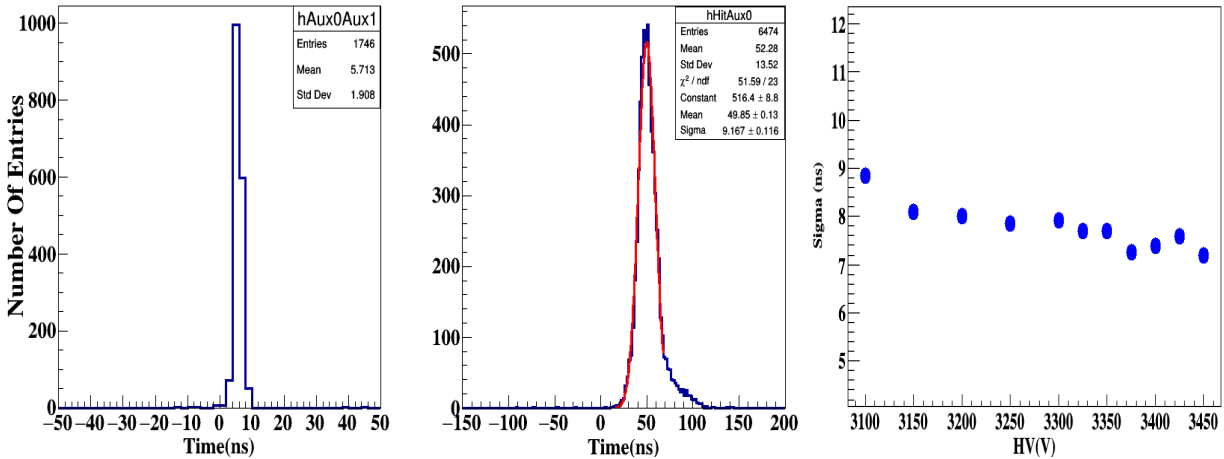


Figure 4.18: Left: Distribution of time difference spectra between one scintillator to other scintillator, Middle: Distribution of time difference spectra between scintillator and GEM. Right: Variation of time resolution (σ) with high voltage. Statistical error bars are within the marker size.

Results and Discussions

Figure 4.18 (left) shows the time difference spectra between the top and the bottom scintillators. This shows that the signal from the top scintillator is correlated with that of the bottom one with standard deviation of about 1.5 ns. We choose time window of $\text{mean} \pm 3\sigma$ from the time correlation, and select the GEM hits which lies within this window. The middle panel of the same figure shows the distribution of time difference spectra between one of the scintillators with GEM detector within a time window of two scintillators. The peak position is shifted from zero due to the delays in the cables and the electronics. The σ of the time correlation spectra provides a measure of the time resolution of the GEM detector. The variation of this sigma with high voltage is shown in the right panel of Figure 4.18. σ improves with voltage as expected. The signal from n-XYTER is inverted, so we need to correct the signal from baseline. The detailed discussion is given in appendix A. The pulse height histogram within the GEM scintillator time correlation window ($\text{mean} \pm 3\sigma$) is shown in the left panel of Figure 4.19, which shows a clear Landau distribution. The distribution of the affected channels in the n-XYTER (total 128 channels) within same window is shown in the right panel of the same figure, which is Gaussian in nature as expected from the source profile.

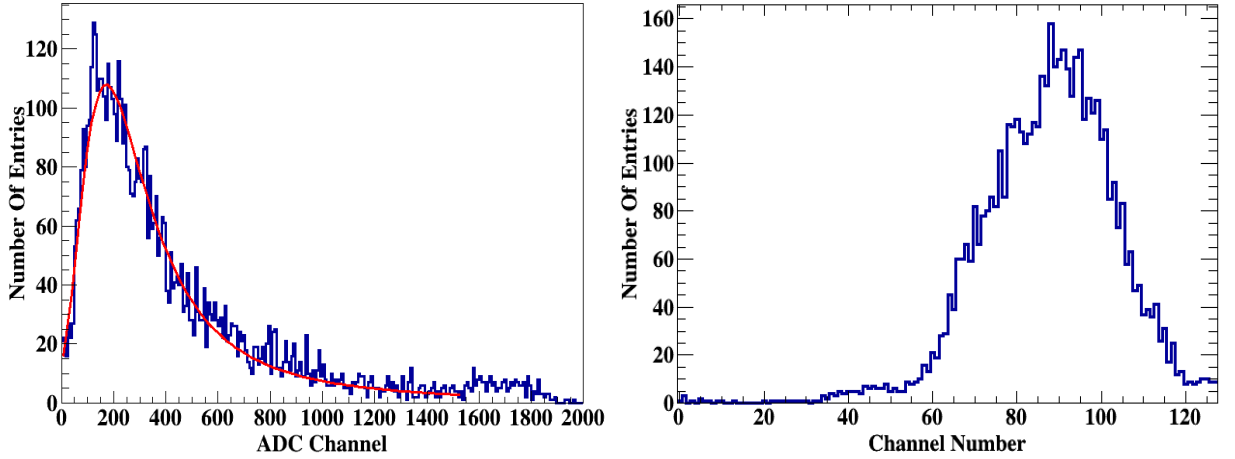


Figure 4.19: Left: Pulse height distribution at GEM voltage ~ 1092 V for 3/2/2/2 gap configuration. Right: Channel hit distribution at GEM voltage ~ 1092 V for 3/2/2/2 gap configuration.

The efficiency of the detector under test is defined as follows

$$Efficiency(\%) = \frac{Three\ Fold\ Count}{Two\ Fold\ Count} \times 100.0 \quad (4.23)$$

The integral of the time difference distribution of two trigger scintillators within the 3σ window gives the number of trigger (two-fold count). For each trigger, the number of GEM hits are

measured. The three-fold-count is given by the condition of minimum one GEM hits within 3σ time window. The variation of detector efficiency with a sum of GEM voltage is shown in Figure 4.20. The plateau starts at GEM voltage ~ 1060 V.

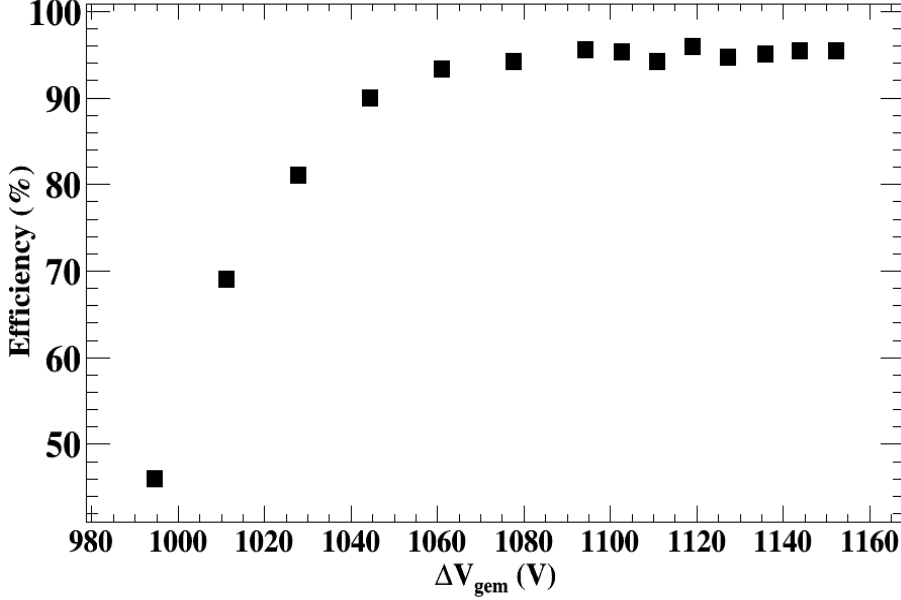


Figure 4.20: Variation of efficiency of GEM detector with GEM voltage ($\Delta V_{\text{gem}1+\text{gem}2+\text{gem}3}$). Statistical error bars are within the marker size.

The cluster size is defined as the number of fired strips per event/trigger. The cluster size distributions for two voltage settings (one at ~ 1033 V and the other at ~ 1131 V) are shown in the left and middle panel of Figure 4.21. One can observe from the figure that, for lower voltage settings, the average cluster size is small (~ 1.5), and it increases to ~ 2.7 for higher voltage, as expected. The variation of average cluster size with GEM voltage is shown in Figure 4.21 (right panel), which increases with GEM voltage as expected.

The event length is defined as the time spread between the first signal to the last signal in an event. The event spread distribution for two voltage settings is shown in the left and right panel of Figure 4.22. At a lower voltage, the spread is much less compared to a higher voltage. In any event, the hits are spread in time. But we expect that this spread should be within time correlation window ($2 \times 3\sigma$). At lower voltage, the number of hits in a event is less (order of 1 or 2 in most of the cases). That is why the time difference between these digis are small. The variation of average time spread (mean of the 1-D distribution) with varying HV is shown in the right panel of same figure. The average value increase and then saturates.

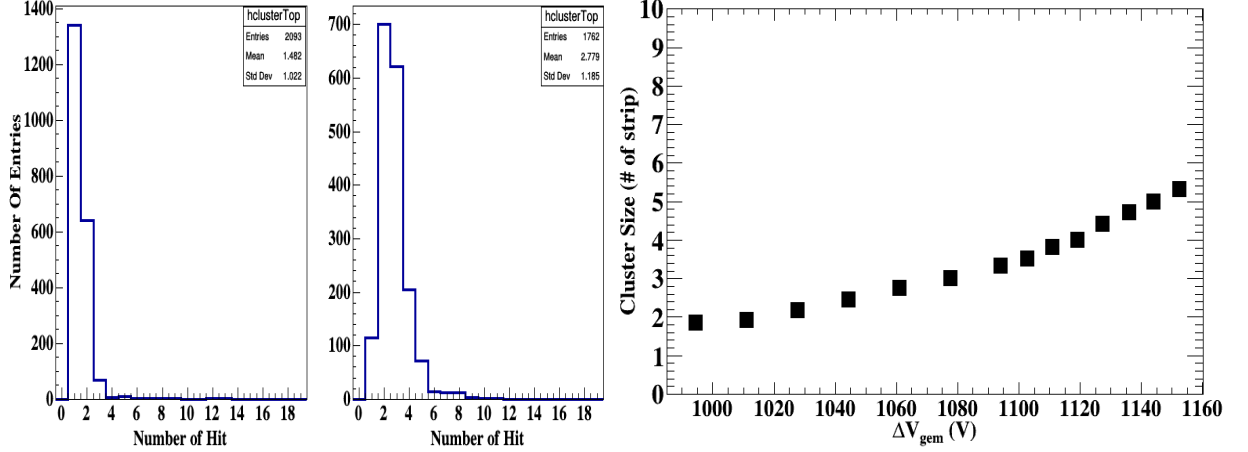


Figure 4.21: Cluster size distribution at $\Delta V_{gem1+gem2+gem3} \approx 1033$ V (left) and $\Delta V_{gem1+gem2+gem3} \approx 1131$ V (middle). Right: Variation of cluster size with GEM voltage ($\Delta V_{gem1+gem2+gem3}$). Statistical error bars are within the marker size.

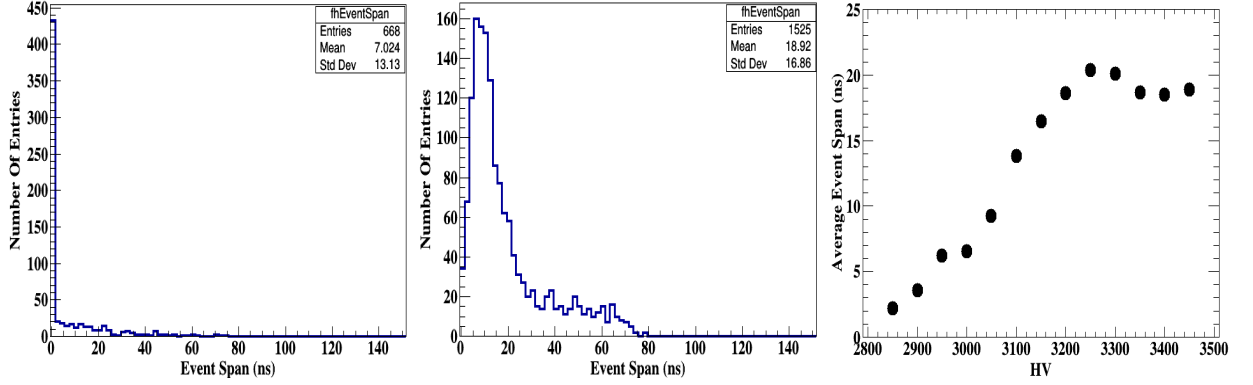


Figure 4.22: Event spread distribution at two different GEM voltage for 3/1/1/1.5 gap configuration. The left plot is for HV settings of 3000 V while middle one is for 3450 V. Right: Variation of average event spread with HV.

Uniformity of 10 cm \times 10 cm prototype

The whole active area of the detector is divided roughly into 16-zones for uniformity measurements. The uniformity in terms of efficiency, cluster size, and time resolution has been studied, and the results are described here. The voltage of detector was kept fixed at $\Delta V_{GEM(sum)} \approx 1102$ V for this test. The schematic picture is shown in Figure 4.23 (left panel).

Efficiency: The uniformity of the efficiency over the whole active area of the detector has been studied. In an ideal case, the detector's efficiency should be uniform over the whole region of the detector. However, in the actual case, it is not uniform and has variations. This non-uniform behavior may be because of the GEM foil geometry (amplification will be different at different regions of foil), distortion in the electric field (sagging), etc. The 2-D plot of efficiency over the

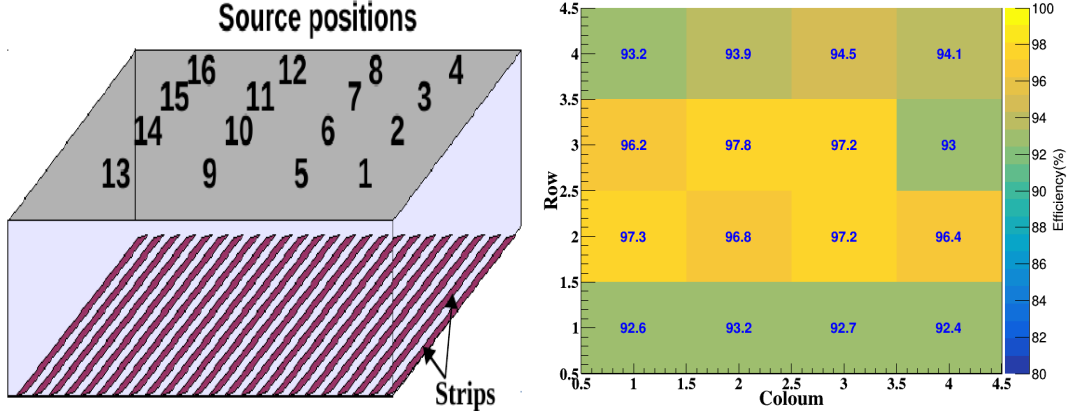


Figure 4.23: Left: Schematic of the uniformity scan measurement. Detector is divided in 16 zones. Right: Variation of efficiency over full active of the detector at GEM voltage 1102.7V.

entire active area of the detector is shown in the right panel of Figure 4.23. The efficiency is relatively uniform with a maximum variation of $\sim 3\%$ from the mean value.

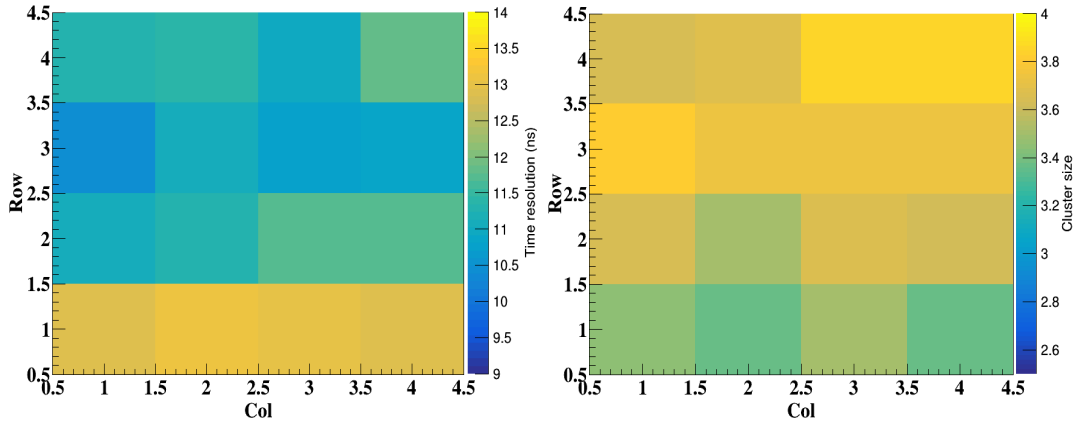


Figure 4.24: Left: Variation of time resolution over full active of the detector at GEM voltage 1102.7V. Right: Variation of cluster size over full active of the detector at GEM voltage 1102.7V.

Time resolution: Ideally, different detector regions should respond uniformly, but it shows variation from the average value in actual cases. The variation of time resolution of the detector over the whole active area is shown in Figure 4.24 (left panel). As can be observed from the figure, the time response varies within ~ 2 ns.

Cluster size: Similarly, the average cluster size over the full active area of the detector was measured, and its 2-D scatter plot is shown in Figure 4.24 (right). The cluster size is quite uniform and varies within $\sim 5\%$.

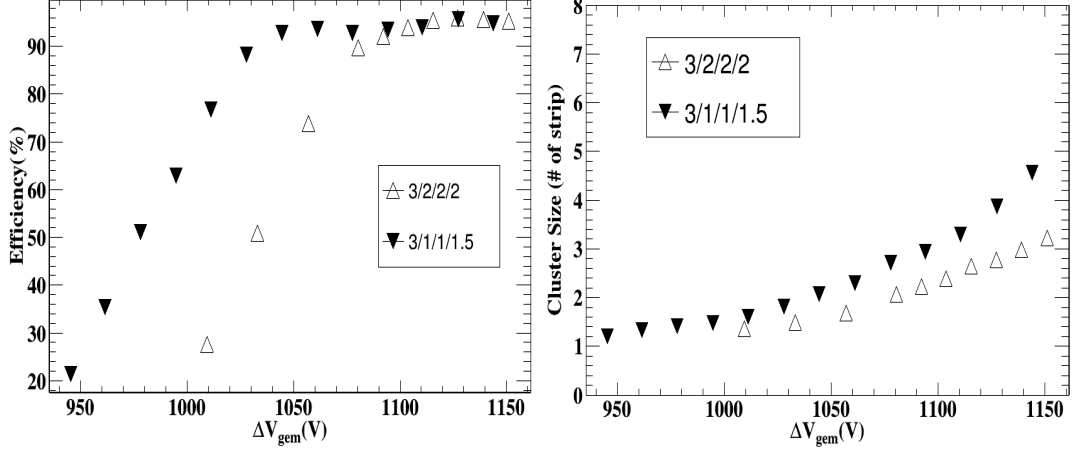


Figure 4.25: Left: Variation of efficiency with GEM voltage ($\Delta V_{\text{gem}1+\text{gem}2+\text{gem}3}$) for two gas gap configurations. Right: Variation of cluster size with GEM voltage ($\Delta V_{\text{gem}1+\text{gem}2+\text{gem}3}$) for two gas gap configurations. Statistical error bars are within the marker size.

4.5.3 Comparison with 3-2-2-2 gas gap configuration

The performance of the detector in two gap-configurations has also been studied. Only efficiency and cluster are shown here. The variation of efficiencies for two gas gap configurations with the sum of GEM voltage is shown in Figure 4.25 (left panel). For the 3/2/2/2 gap configuration, asymmetric voltages to the GEM electrode have been given. The discrepancy at lower GEM voltage can be due to different transfer and induction fields at the same HV settings (because of the divider configuration).

Chapter 5

Real Size Trapezoidal Chambers for MuCh

Test of small size ($10\text{ cm} \times 10\text{ cm}$) and moderate size ($30\text{ cm} \times 30\text{ cm}$) triple GEM detectors has been discussed in chapter 4. In this chapter, the design, assembly, and test of the real-size modules for the first station of MuCh are discussed in detail. The detailed specifications of the detector modules for the first two stations of MuCh are given in chapter 2. As already mentioned, large area triple GEM detectors will be used for the first two stations of the MuCh. In this regard, during the R & D phase, two versions of the real-size prototype detectors were built at VECC, namely, “Mv1” and “Mv2”. The comparison between these versions are given in table 5.1. The “Mv2” modules are designed for the first station of MuCh. The no-glue, “NS-2” technique has been used for the assembly of these modules, where NS-2 means no-stretch and no-spacer. This is one of the standard techniques for building large area triple GEM detectors. Detailed design and fabrication procedures of the large-size modules are discussed in section 5.1. The test of the “Mv1” module in the lab is discussed in section 5.2. These modules were also tested with proton beam at COSY, Germany, and with particles from nucleus-nucleus collisions at CERN-SPS. The results from these tests are discussed in section 5.2. The detailed design of “Mv2” modules, which has dimensions similar to that to be now in station-I, and its test with the radioactive source in the lab is discussed in section 5.3. The test of this module with N-N collision in the mCBM experiment will be discussed in the next chapter.

Table 5.1: Specification of two versions of real-size prototype triple GEM detectors

Variables	Module Versions	
	Real-size (Mv1)	Real-size (Mv2)
Size of Active Area	Inner ~ 9.8 cm Outer ~ 38.5 cm Length ~ 72 cm (Not exactly station-1 size)	Inner ~ 7.5 cm Outer ~ 40 cm Length ~ 80 cm (Exactly station-1 size)
Gap Configurations (mm)	3/1/1/1.5	3/2/2/2
HV Design	Voltage Divider	Voltage Divider + Optocouplers
Pad dimensions (mm)	~ 4 - ~ 17	~ 3.2 - ~ 17
FEB requirement	15	18
Number of readout pads	1817	2231

5.1 Assembly of real-size modules at VECC

Building large-size triple GEM modules requires special treatments. The main challenges are (a) design and fabrication of large-area Printed-Circuit-Board (PCBs). (b) fabrication of large-size GEM foil (c) stretching large foils, and (d) proper layout of the PCB tracks to accommodate the variation in occupancy.

The design of the readout PCBs was done at VECC. The foils were procured from the RD51 lab, CERN. The PCBs were fabricated in India by an Indian Industry. The Assembly procedure for both the versions of the chamber (“Mv1” or “Mv2”) is the same. The main difference between these two versions is given in table 5.1.

5.1.1 Drift PCB

The Gerber layout of the drift PCB is shown in Figure 5.1 (left). The HV connection layout for powering the drift and GEM foil segments is shown on the top of the PCB. The picture of the fabricated drift PCB is shown in Figure 5.1 (right). The active layer of the PCB is segmented into two halves. Spring contacts are soldered on the PCB, which provide bias to the GEM foil segments. The outer frame and brass support are also shown in the same figure. The drift plane is a 3.2 mm thick plane with copper-clad on a single side, which acts as drift electrode. The drift plane was extended laterally by 5 mm in order to accommodate the High Voltage (HV) lines for connections to the spring contacts. Fourteen holes, each of 1 mm diameter, are made on PCB at appropriate positions to allow X-rays to pass through during test validation of the chamber. The holes are covered with Mylar foils to make the chamber gas-tight.



Figure 5.1: Left: Gerber layout of real-size drift PCB with HV connections. Right: Picture of fabricated drift PCB with outer frame and spring contact soldered

5.1.2 Readout PCB

The Gerber layout of the readout PCB from the pad side and the photograph of the fabricated PCB is shown in the left and right of Figure 5.2, respectively. Due to the high flux in the inner region (near the beam pipe) and relatively lower rate radially outwards (away from the beam pipe), progressive pad geometry was chosen for the GEM chambers. There will be a relatively higher density of pads in the inner ring due to progressive pad geometry, and hence the design required an 8-layered PCB. This makes the fabrication procedure difficult. The tracks are drawn beneath the pads to reduce the noise, and the bottom plane is used as a ground plane. Although this extra ground plane adds the capacitance simultaneously, additional shielding is not required to achieve the acceptable noise levels. The maximum track lengths are approximately 30 cms at the outer zone where pads are more scattered.

To fit in the sector geometry and have the lowest dead area, each pad is a trapezoid where two larger angles of the trapezoid are of 0.5° each. For the PCB discussed here, the pad size varies from ~ 4 mm to ~ 17 mm. Each GEM chamber is designed to have a coverage of 22.5° , which makes 16 chambers cover the entire layer of the 1st station. To cover the full azimuthal region, alternate chambers are planned to be put in different planes with active area overlap to avoid the dead areas due to the mechanical structure of the chamber. This design is made with 23° coverage

so as to overlap half a degree with the consecutive sectors to reduce the dead space. With 23° , the PCB has 23 pads in the annular ring and 79 pads in a radial direction, giving a total number of pads to be 1817 (23×79) for the given detector module. This PCB is divided into 15 readout zones amongst 15 FEE boards, each having 128 channels.

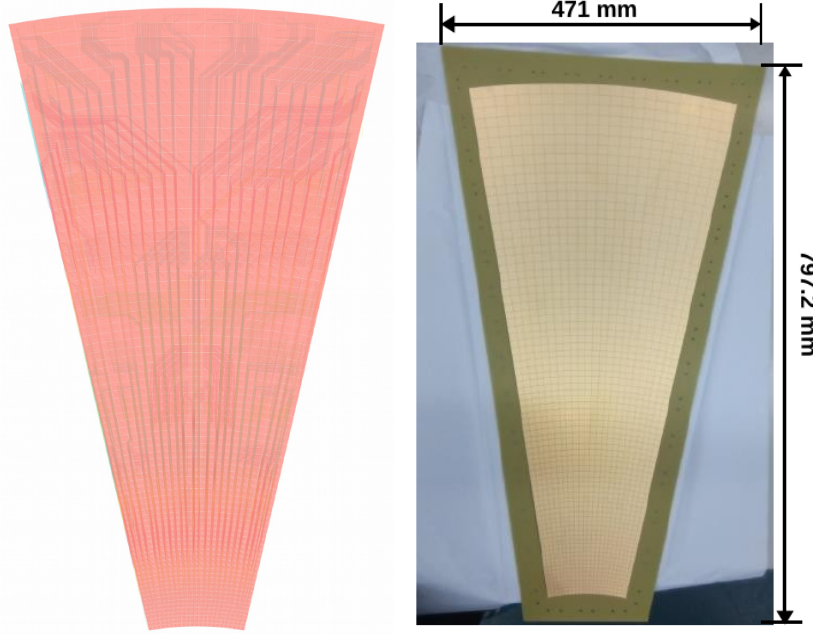


Figure 5.2: Left: Gerber layout of real-size readout PCB with trapezoidal pads. Right: Photograph of the fabricated readout PCB.

5.1.3 Segmented GEM foils

The large size GEM foil for the prototype chamber was procured from RD51 lab at CERN. Each of the GEM foils have provision for stretching it by NS-2 technique. The Gerber layout of GEM foil showing segmentation on top is shown in Figure 5.3. The segmentation is made based on the occupancy of the chambers in Au+Au collisions at SIS-300 energy. It is therefore expected that the chamber will be able to handle particle rate at SIS100 quite comfortably. We have decided to use the NS-2 [159] technique developed at CERN, which has the advantages that (i) foils can be easily replaced, (ii) no permanent gluing is done. This way the assembly procedure becomes faster than the thermal stretching technique. We show the basic principle of the NS-2 technique in Figure 5.4. The specially designed side screws will be used for stretching three GEM foils together.

Each GEM foil is segmented into two halves. Each half further segmented into 12 sections, so a total of 24 sections of the foil per layer. A HV divider circuit will be used for powering the GEM foil segments and will be placed on the top portion of the drift PCB as shown in the right panel of

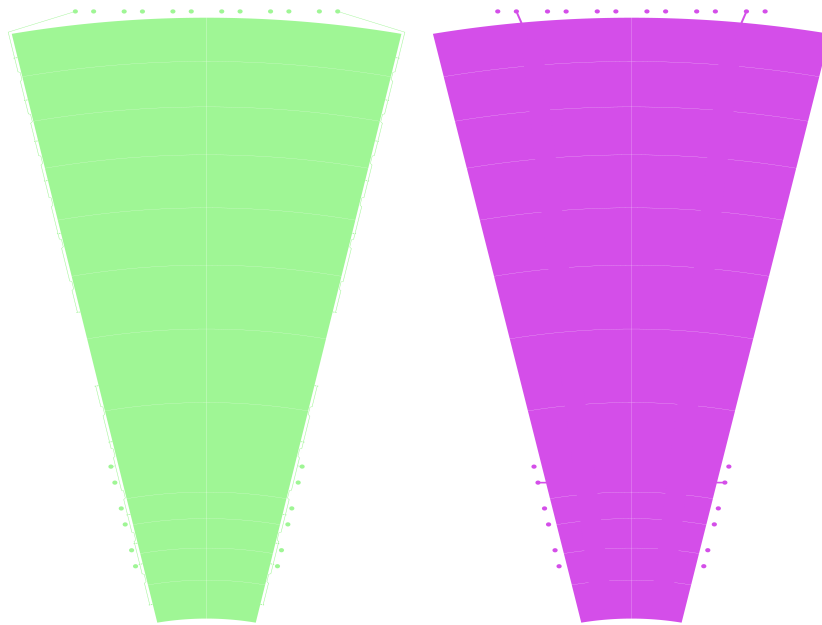


Figure 5.3: Left: Large-size segmented GEM-top layer. Foil is divided in 24 segments Right: GEM-bottom layer. Divided in 4-segments

Figure 5.1. The active area of the drift PCB is divided into four zones, and each zone has separate connections to the HV divider.

5.1.4 Other components

The other component like, inner frame (spacers), outer frame, O-ring, etc. are discussed along with the assembly process.

5.1.5 Steps involved in the assembly and Quality Assurance (QA) of real-size triple GEM chambers

The basic steps involved in the assembly and QA test of the chamber are described below.

- Physical inspection of the readout plane and the drift plane. This involves pad/tracks connectivity, the dimension measurement, spring contact soldering on drift PCB.
- Physical inspection of the holes of each GEM foils - hole size measurement.
- Leakage current test of the foils - segment by segment
- Inspection of the stretching frames and their alignment
- Mounting and stretching of the GEMs using NS2 stretching technique sandwiched between drift plane and readout plane

- Gas tightness check - the volume will be sealed mechanically via O-rings. NS2 technique does not involve any gluing process
- Soldering of protection resistances and resistive chain
- Test of the chambers in the lab using either β or cosmic rays
- Gain uniformity measurement in the lab using X-rays.

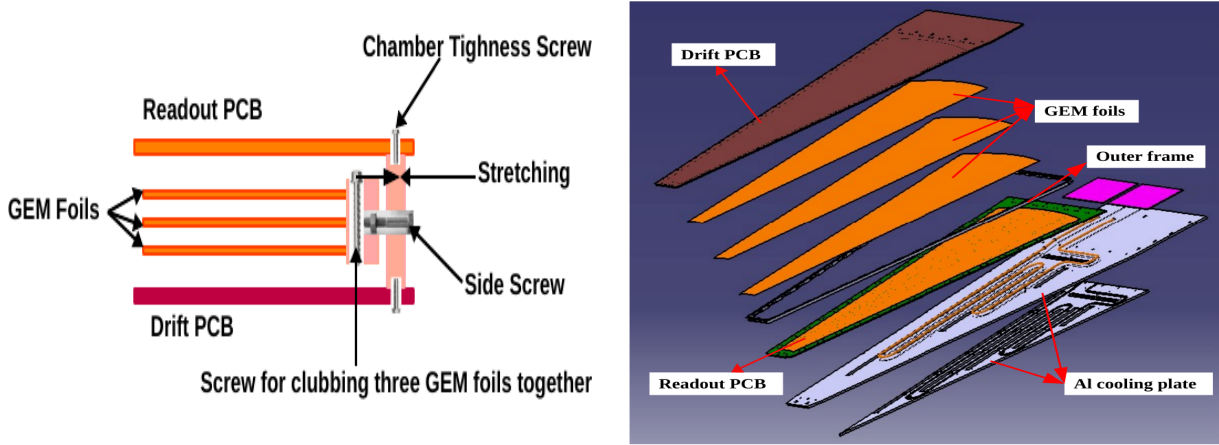


Figure 5.4: Left: Schematic of NS-2 stretching technique. A special screws mounted inside spacers for stretching the foils. Right: Schematic layout of assembly of different layers to build a final chamber

The schematic of “NS-2” technique is shown in Figure 5.4 (left). Side screws are used to stretch the GEM foils. The split view of different layers of triple GEM detectors are shown in Figure 5.4 (right).

The assembly procedure of the large-size GEM chambers is described in Figures 5.5, 5.6, 5.7 and 5.8 respectively. The assembly was done in clean room of VECC-CPDA lab (class 100,000).

Figure 5.5 (a) shows the closeup view of the drift PCB, where brass support, spring contact, and the active layer can also be seen. These spring contacts provide bias to the GEM foil segments. Leakage current measurement of GEM foils is shown in Figures 5.5 (b). Measurement was done in the air where room temperature was 23°C, and RH was 45-50%. HV bias is applied to the two electrodes of the GEM foils for the leakage current measurement. The surface conductivity of the Polyimide mostly drives the observed leakage current, and this conductivity strongly depends on the quality of the GEM foils and also on the cleanliness. The presence of dust, contamination, or defects will act as an electrical bridge between the electrodes and increase the leakage current. Therefore, we ensure the quality of the GEM foil by measuring the current. To be on the safe side, we apply voltage on the GEM electrode higher than the real operation voltage. However, this

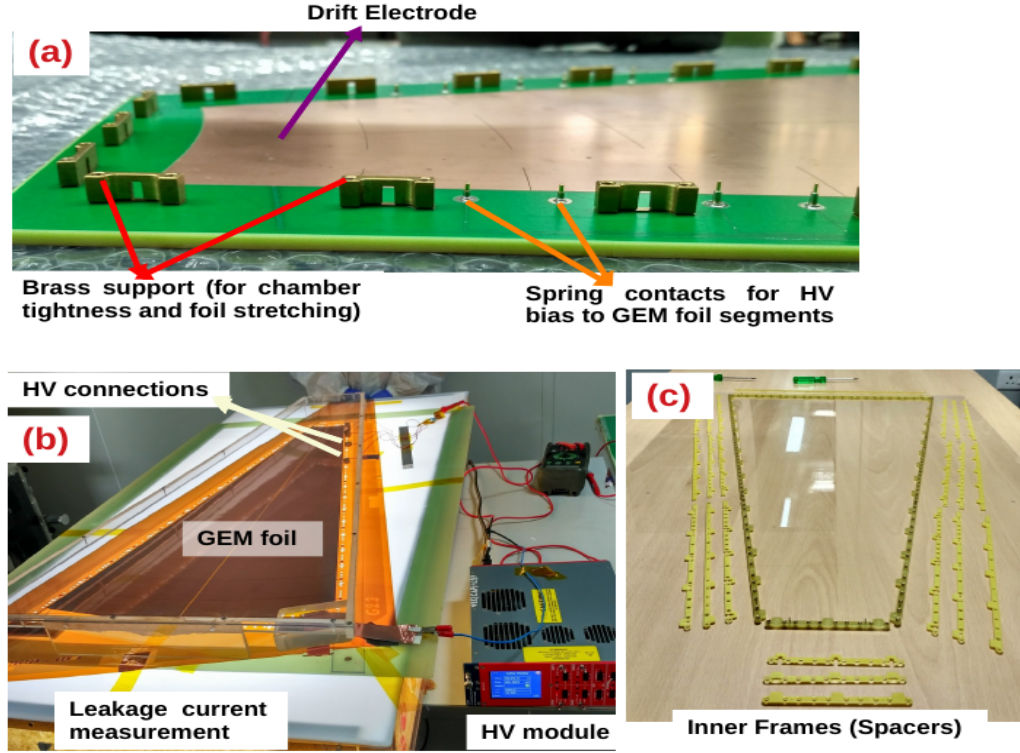


Figure 5.5: a) Part of the drift PCB showing spring contacts and brass support. b) Picture of leakage measurement setup in clean room. Leakage current measured for all 24 segments individually. c) Inner frames (spacers)

should not be higher than the breakdown voltage (V_b) of the medium under which the measurement is performed. The V_b depends on the medium (gas, air, etc.), the distance between two electrodes, and pressure, etc. The breakdown voltage of air at 30% RH is ~ 650 V. In our case, it will be less than 650 V, because the humidity is higher (45-50%). We have done leakage current measurement up to 580 V. The foils were selected only when they satisfied the criteria of no-short along with a low leakage current of < 3 nA at ΔV_{GEM} of 580 V for every segment. The picture of inner frames is shown in Figure 5.5 (c). The thicknesses of each spacer were measured, which was within $< 5\%$ tolerance.

After a successful leakage test, the selected foils were placed one by one along with the spacers on the support frame as shown in Figure 5.6 (a). The all three GEM foils were tighten slightly from top screws, such that they become interconnected to each other. Some part of foils are going outside of the frame, as can be seen from the same figure. This extra portions are then removed as shown in Figure 5.6 (b). The stack of three GEM foils is then placed inside the drift board for stretching and final assembly. This is shown in Figure 5.6 (c).

The top screws are used to tighten the three GEM foils, and side screws are used to stretch the

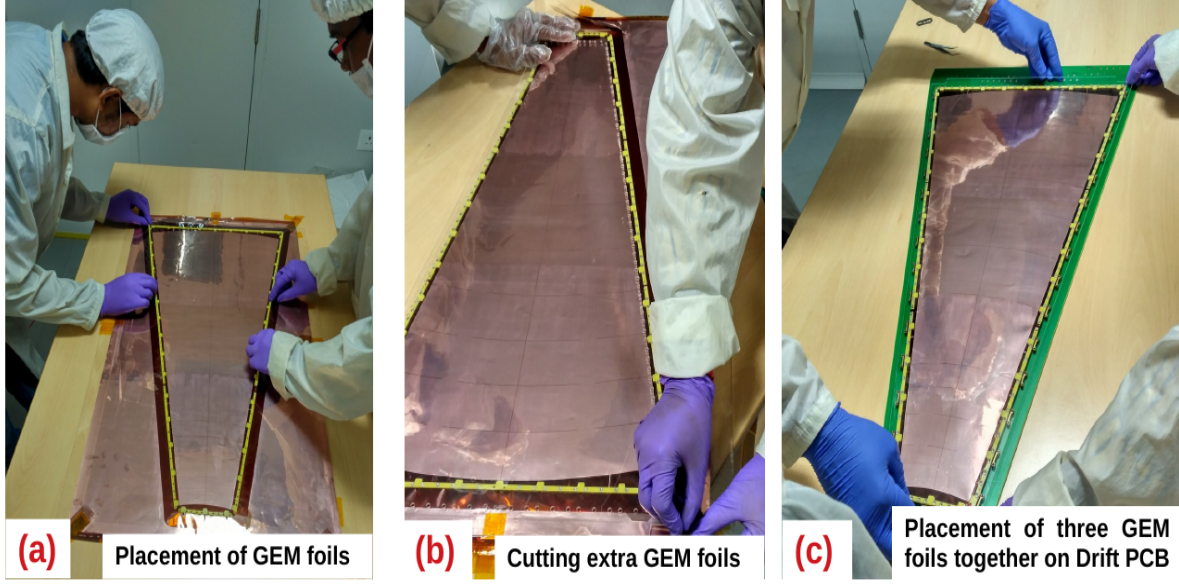


Figure 5.6: a) Placement of GEM foils and spacers. b) Cutting extra foil. c) Placement of three stack of GEM foils inside drift PCB for stretching and final assembly

GEM foils as shown in Figure 5.7 (a). Tightening of the GEM foils from the top and stretching it from the side is shown in Figure 5.7 (b) and Figure 5.7 (c) respectively. The stretching was done pitch-by-pitch, and the over-stretching was monitored by visual inspection.

After successful stretching of foils, we then place outer frames (Figure 5.8 (a)), and then the readout board is placed on drift PCB. Both the PCBs are screwed together for gas tightness. The placement and tightening of the readout PCB are shown in Figure 5.8 (b) and Figure 5.8 (c), respectively. This completes our final chamber assembly. The chamber is then flushed in gas for 8-10 hours.

5.2 Test of first real-size module (“Mv1”)

5.2.1 Test in lab

The assembled module was tested with ^{55}Fe (5.9 keV X-ray) in the lab. The experimental setup is shown in Figure 5.9 (left). The top visible side in the same figure is the drift board, while the FEBs are connected at the bottom. The FEBs are cooled with simple computer fans. We place the source on the holes of the detector for testing. A premixed gas mixture of Ar/CO₂ (70:30) was used. A typical ^{55}Fe energy spectrum from the detector under test is shown in Figure 5.9 (middle) at total HV=3100 V. The variation of photo-peak ADC with GEM voltage (summed

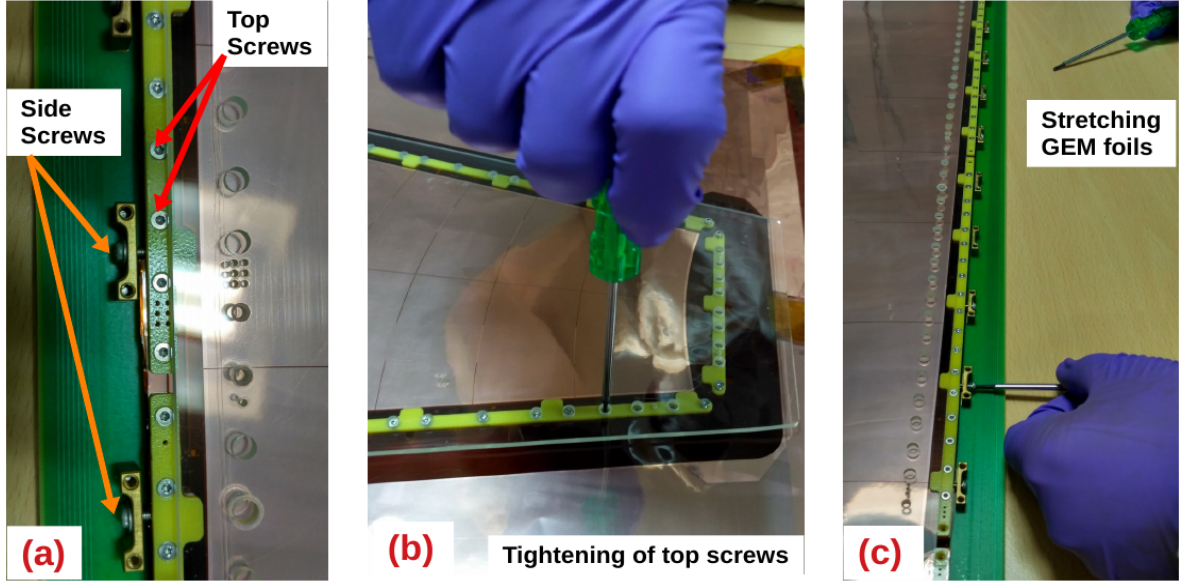


Figure 5.7: a) Part of the chamber showing top screw and side screw. b) Tightening top screws. c) Stretching GEM foils by tightening side screws

voltage = $3 \times$ value in x-axis) is shown 5.9 (right). It is always required that the gain has to be stable and uniform over different regions of the detector. So the study of gain stability in terms of environmental parameters (such as Temperature and Pressure) and gain uniformity are essential. We have done gain measurements at different positions and studied gain dependence on T/P for a real-size prototype triple GEM detector at VECC Lab and using n-XYTER FEBs.

For Temperature (T) and Pressure(P) monitoring, we have used a data logger (Extech SD700) [160], which records the T and P values, and the data were acquired using DABC software developed at GSI [161, 162]. For gain dependence with time, we have kept the ^{55}Fe source fixed at one of the hole positions and measured the photo-peak position at regular time intervals lasting up to several hours. For the measurement of gain uniformity over the surface, we have varied the position of the source and measured the photo-peak at each of these positions. At each position, we wait for ~ 30 minutes for gain stabilization.

The signal from n-XYTER is inverted, so we need to correct the signal from baseline (refer appendix A). The detailed discussion of the chip can be found in section 4.4 of chapter 4. The left and middle panels of Figure 5.10 show the raw and baseline corrected ^{55}Fe spectrum, respectively. The variation of photo-peak ADC channel with GEM voltage from n-XYTER is shown in Figure 5.10 (right).

The variation of photo-peak ADC and T/P (K/hPa) with time is shown in Figure 5.11 (left)

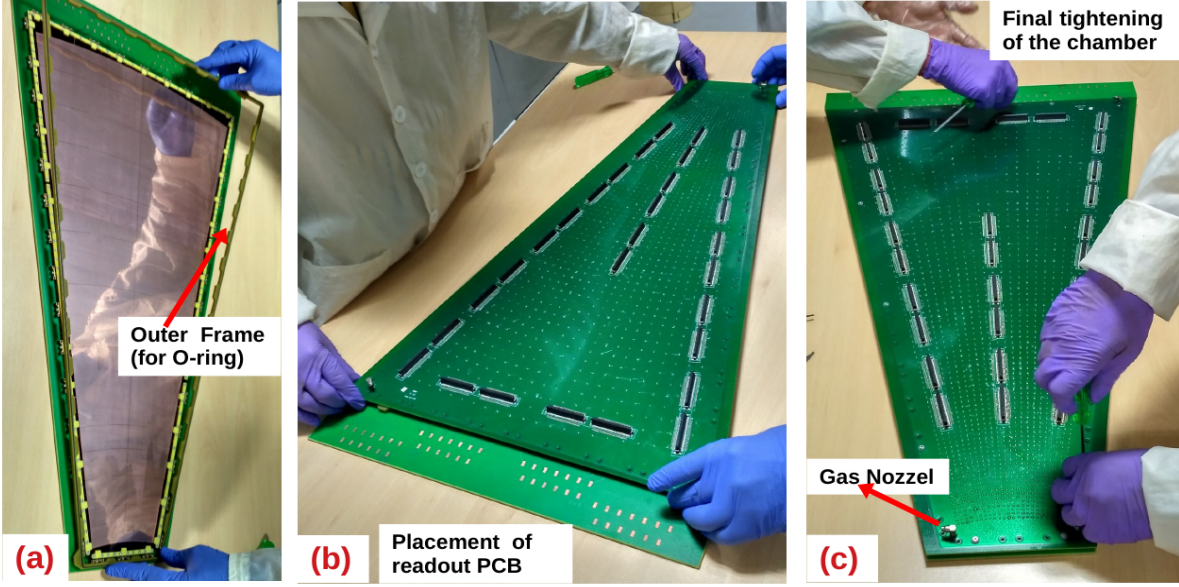


Figure 5.8: a) Placement of outer frame (containing O-ring). b) Placement of readout PCB for final tightening of chamber. c) Final tightening chamber

and Figure 5.11 (middle), respectively. There we can see a good correlation between the photo-peak ADC and T/P. Since the gain increases with an increase in T/P, both T/P and photo-peak follow the same trend. This correlation of photo-peak ADC with T/P is shown in Figure 5.11 (right). The data points are fitted with an exponential distribution indicating an exponential dependence of gain on T/P as per expression below,

$$G(T/P) = Ae^{B\frac{T}{P}} \quad (5.1)$$

where A and B are the fit parameters and T/P is in K/hPa unit, respectively. The normalized gain is expected to be independent of environmental parameters and can be computed as:

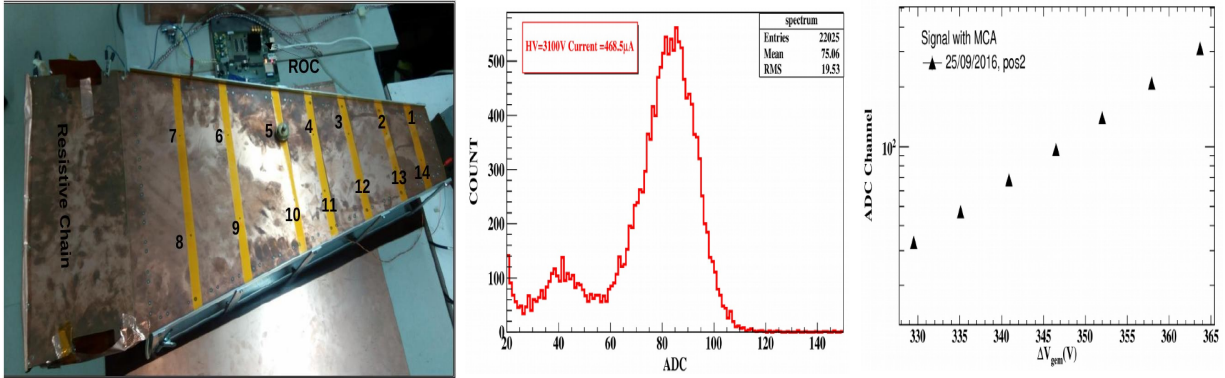


Figure 5.9: Left: Experimental Setup in Lab. Middle: Typical ^{55}Fe with NIM based electronics. Right: Variation of photo-peak ADC channel with GEM voltage. Statistical error bars are within the marker size.

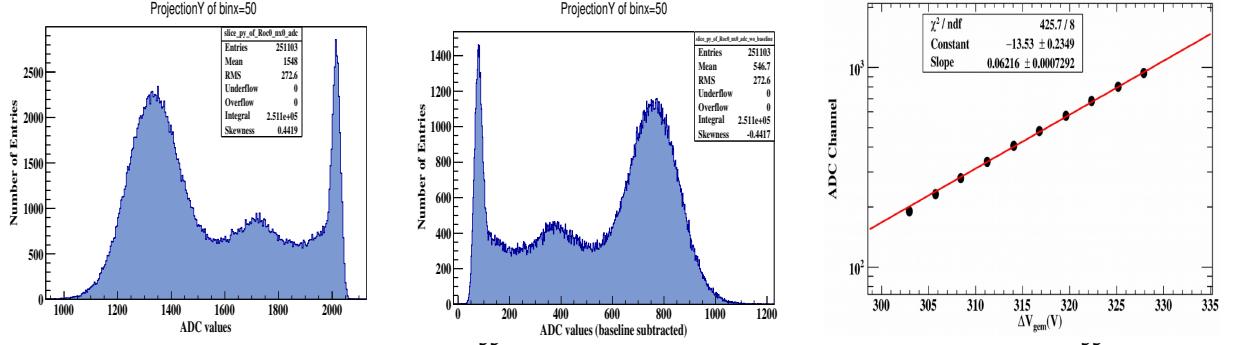


Figure 5.10: Left: Raw spectrum of ^{55}Fe . Middle: Baseline corrected spectrum of ^{55}Fe . Right: Variation of baseline corrected photo-peak ADC channel with GEM voltage. Statistical error bars are within the marker size.

$$G_{\text{Normalized}} = \frac{G_{\text{measured}}}{Ae^{B\frac{T}{P}}} \quad (5.2)$$

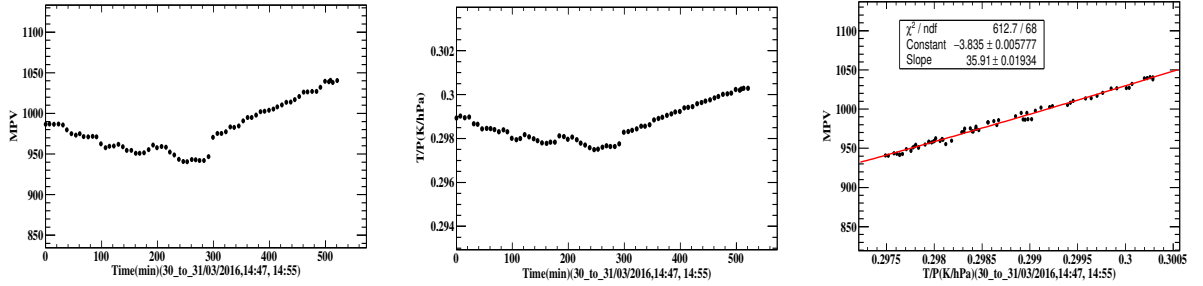


Figure 5.11: Left: Variation of photo-peak with time. Middle: Variation of T/P(K/hPa) with time. Right: Variation of photo-peak with T/P(K/hPa). Statistical error bars are within the marker size.

The variation of normalized photo-peak ADC with time is shown in Figure 5.12 (left). This reveals a very stable gain with time fluctuating within 4%. The variation of photo-peak at different positions is shown in Figure 5.12 (right). The gain after T/P correction seems to be vary by about 22%. These variations in the gains at various positions can arise due to the following reasons. (i) Local contamination: this is related to the chemical residue (e.g., from the GEM production process), (ii) poor stretching can induce the non-uniformity of the electric fields between the foils, which lead to the non-uniformity of the GEM transparency and therefore the effective gain. Over-stretching may reduce the thickness of the GEM foils locally and, therefore, the amplification field. There can be other reasons, like gas flow distribution, and environmental conditions during the test, etc. The geometry of the GEM foil (hole diameters, pitch, etc.) can also contribute to this non-uniformity. However, if we operate our detector in the middle of efficiency plateau region, a

small fluctuation in gain will not affect the efficiency of detector significantly.

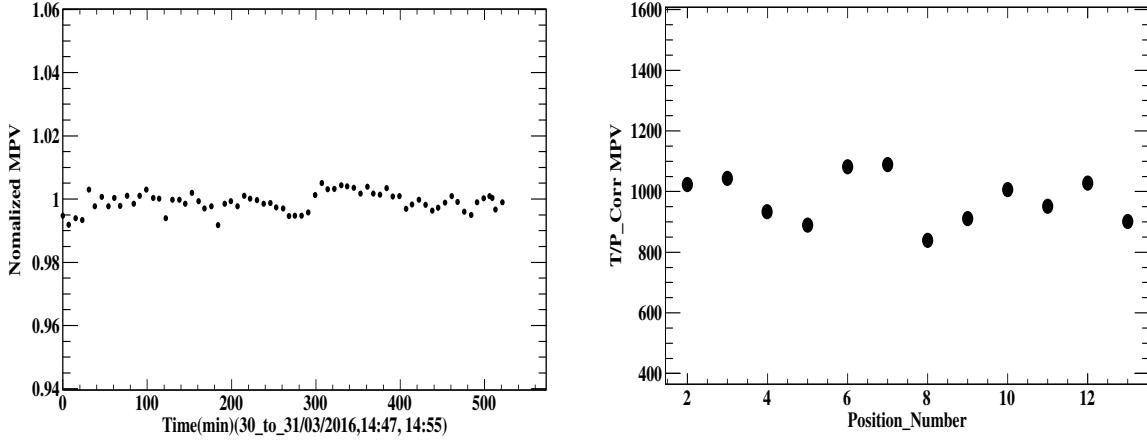


Figure 5.12: Left: Variation of normalized photo-peak with time. Right: Variation of photo-peak at different position. Statistical error bars are within the marker size.

5.2.2 Test with proton beam at COSY

The GEM chamber was tested along with three STS sensors at the Jessica cave of COSY, Jülich, Germany, using a proton beam of momentum 2.36 GeV/c. The schematic layout of the experimental setup for testing the chamber is shown in Figure 5.13. A pair of crossed optical fiber scintillator hodoscopes with an overlapping area of 6 cm \times 6 cm placed at the two ends of the setup have been used for the beam trigger. The coincidence signals from the front and rear hodoscope were connected to the auxiliary channels of ROC to record the timestamps of the beam particles. The detector was read out by the n-XYTER (see section 4.4) FEBs directly connected to the chamber followed by the ROC. One ROC can handle two FEE boards. Data were collected in self-triggering mode. The n-XYTER ASIC records the timestamps of each hit that crosses the predefined threshold. The timestamps of all the hits above the threshold are digitized and stored. Data were recorded for different beam intensities by adjusting the collimator windows. Data at different voltage settings across the GEM foils were taken for different regions of the detector where readout pads of different sizes were exposed to the beam. All GEM foils in the chamber were kept at the same voltage setting. A premixed gas mixture of Ar/CO₂, mixed in 70:30 ratio by mass, was used.

In a self-triggered readout system where all hits are stored along with their timestamps, the first step of data analysis would be to find hits that are correlated in time with the trigger time stamps. The distribution of the time difference between the coincidence trigger signal from the

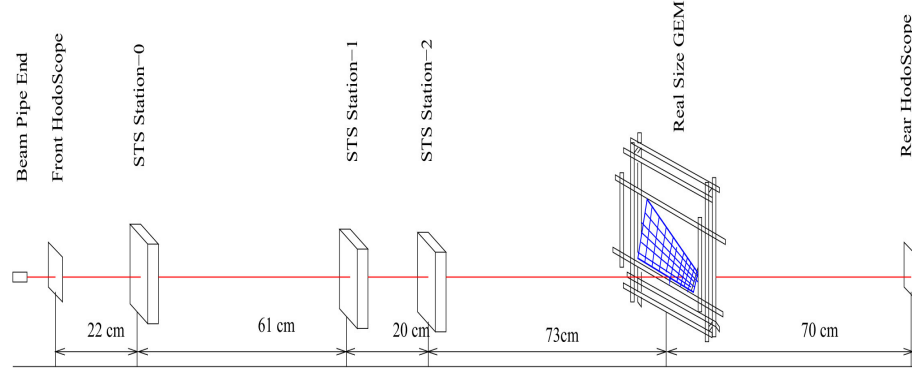


Figure 5.13: Left: Schematics of experimental setup at COSY, Jülich, Germany.

hodoscopes and those of the hits is shown in Figure 5.14 (left). The efficiency of the chamber was calculated using the two-fold and three-fold coincidence method as described in section 4.5.

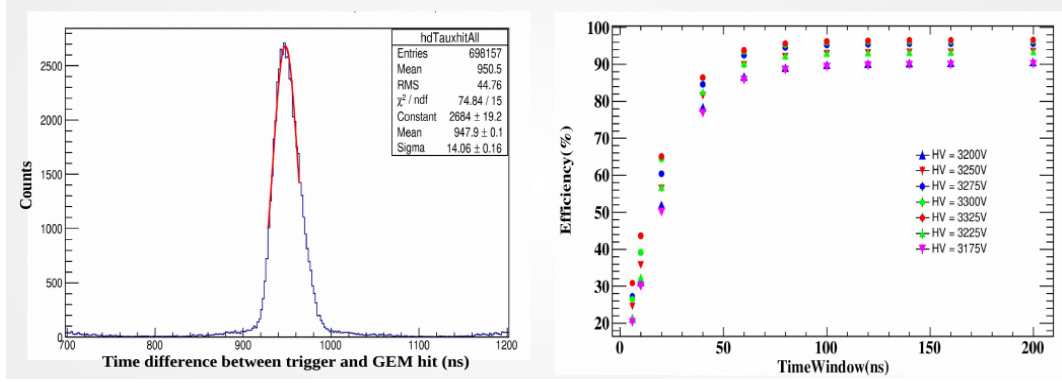


Figure 5.14: Left: Time correlation between triggered detector (hodoscope) and the GEM hits. Right: Variation of efficiency of the detector with time window (ns). Statistical error bars are within the marker size.

The GEM detector will be used to track muons in CBM, so to operate the GEM detector in CBM-MuCh at a high interaction rate, the detector's efficiency should be $>95\%$. As the GEM detector is aligned with the hodoscopes, the particles with correlated hits on both the front and rear hodoscopes are taken as the input particle into the GEM. Particles are said to be detected if they have at least one hit on the GEM chamber within the time correlation window. Thus, the ratio of the number of detected particles as defined above and the number of triggers in a given time interval gives the efficiency of the detector. The variation of detector efficiency with time window cut (from time correlation spectra) is shown in Figure 5.14 (right). As we increase the time window, the efficiency increases and reaches the plateau for a time window of 80-90 ns. This value of time cut is similar at several HV settings.

The gain is almost stable with a variation $\sim 9\%$ at the highest rate of 2.8 MHz/cm^2 as shown

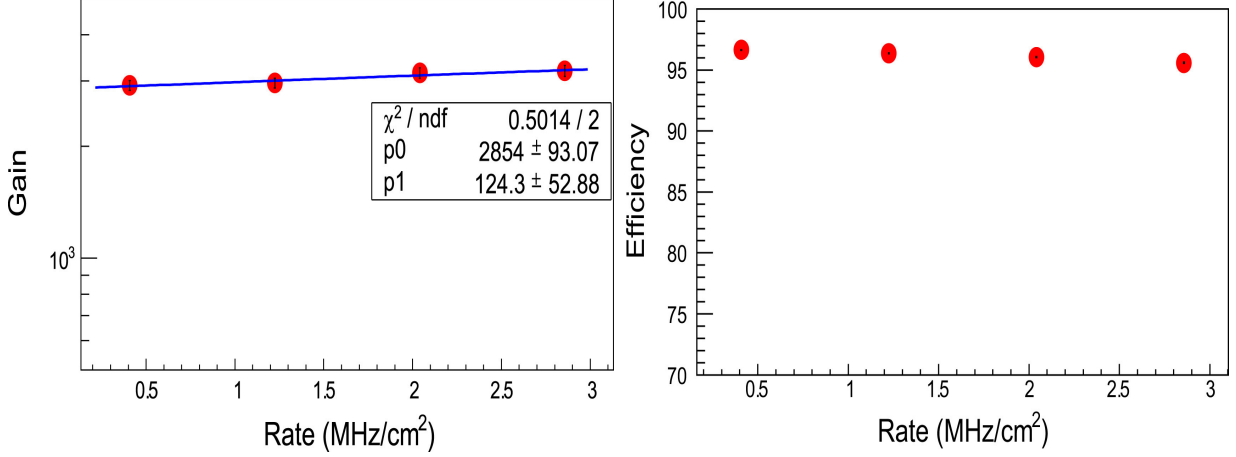


Figure 5.15: Left: Variation of detector gain with incident particle rate. Right: Variation of detector efficiency with incident particle rate. Statistical error bars are within the marker size.

in Figure 5.15 (left). The gain starts to increase slowly at a higher rate, probably due to space charge distortions. At an even higher rate, the gain will decrease [163, 164].

The variation of efficiency with the average rate of the incoming particles is shown in Figure 5.15 (right). The efficiency at a fixed $\Delta V_{GEM} = 375.2$ V is shown up to extracted beam rate of 2.8 MHz/cm^2 . The size of the beam is determined from its spot size on the hodoscopes. This rate is higher than the maximum particle rate that the 1st MuCh stations have to face. As the particle rate increases, efficiency decreases slightly. At a very high rate, the space charge effect starts to play role, which is why the efficiency decreases. However, in our case the decrease in the efficiency at a higher rate is insignificant [165]. The detection efficiency drops marginally ($\sim 2\%$) when operated at high rates.

5.2.3 Test with b+Pb collision at CERN-SPS

Tests of the large size “Mv1” prototype and a small chamber (10 cm x 10 cm) with single-particle beams have been reported in the previous section, and the details can be found in [166, 167, 167, 168, 168]. In this section, we present the response of the large size prototype to the Pb+Pb collisions at the H4 beamline of CERN-SPS, wherein a simultaneous response from the entire active area of the detector due to a spray of high energy particles originating from a nucleus-nucleus collision at 150 AGeV/c has been studied for the first time. The new CBM DAQ took data in free-streaming mode, involving a large number of FEBs for the first time. It was also the first prototype test employing a water-based cooling system. The GEM foils were powered using a resistive chain as shown in Figure 4.5. The schematics and picture of the test setup is shown in Figure 5.16 (a,b,c,d).

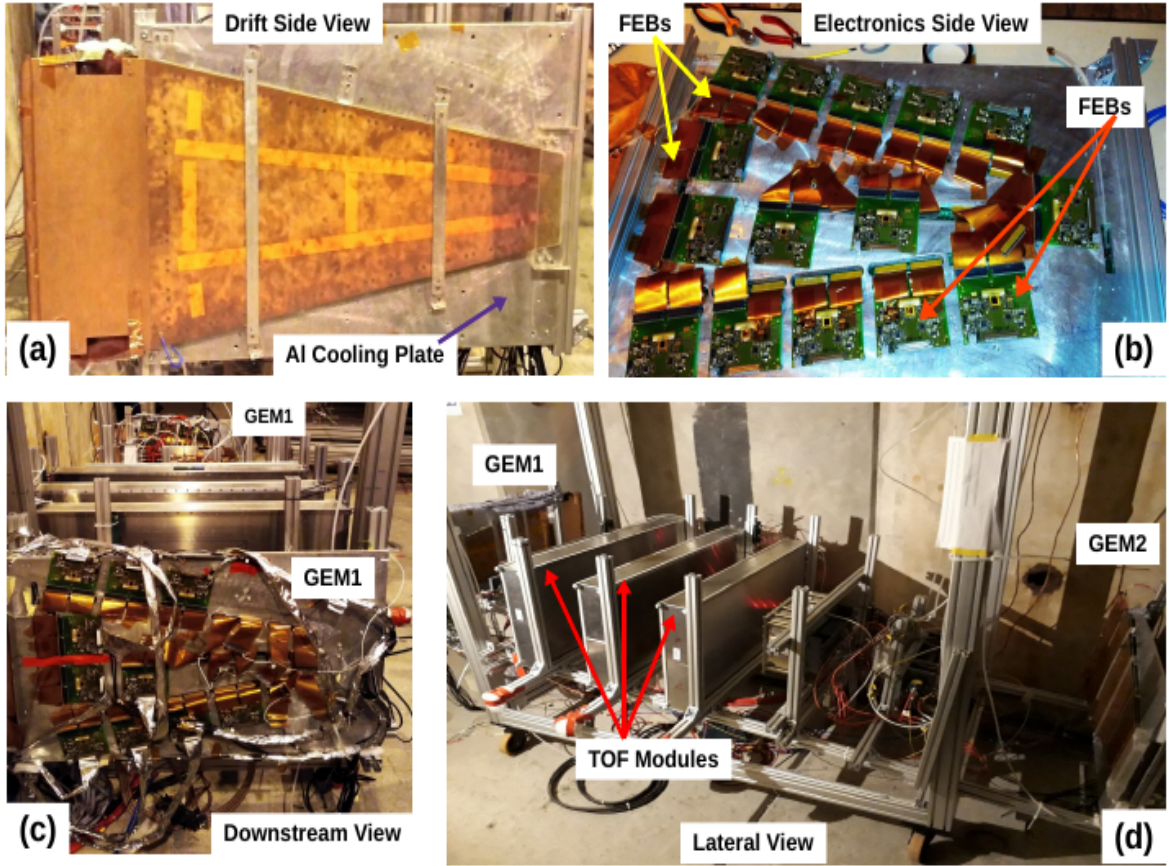


Figure 5.16: Picture of test setup at H4 beamline of CERN-SPS.

Data were taken with almost full FEB (n-XYTER rev-F) coverage. An elaborate cooling^[169] arrangement involving a ~ 12 mm Aluminum plate with controlled water flow through grooved channels in one chamber and through 6 mm Al pipe winding inside the plate volume in another one was used for the first time. The left panel of Figure 5.16 (b) shows the picture of the cooling plate with all the FEBs mounted on one side. Small, flat copper pieces of 3 mm thickness were thermal-glued below the FEBs, providing the metal contact with the plate. The detector is mounted on the other side of this plate. A 10 mm wide slots were machined at 15 readout connector positions. The FEBs were connected with these connectors via 10 cm long flexible Kapton cables, each carrying signals from 64 channels. A premixed gas mixture containing Ar/CO₂ in a ratio of 70/30 was used as the fill gas for all three GEM detectors.

The schematic of the experimental setup is shown in the right panel of Figure 5.17 (a). Pb beams of 150 GeV/c collided on a 1 mm thick Pb target having an area of 9 cm x 9 cm. A diamond detector was placed just before the target to provide beam information. The prototype detectors

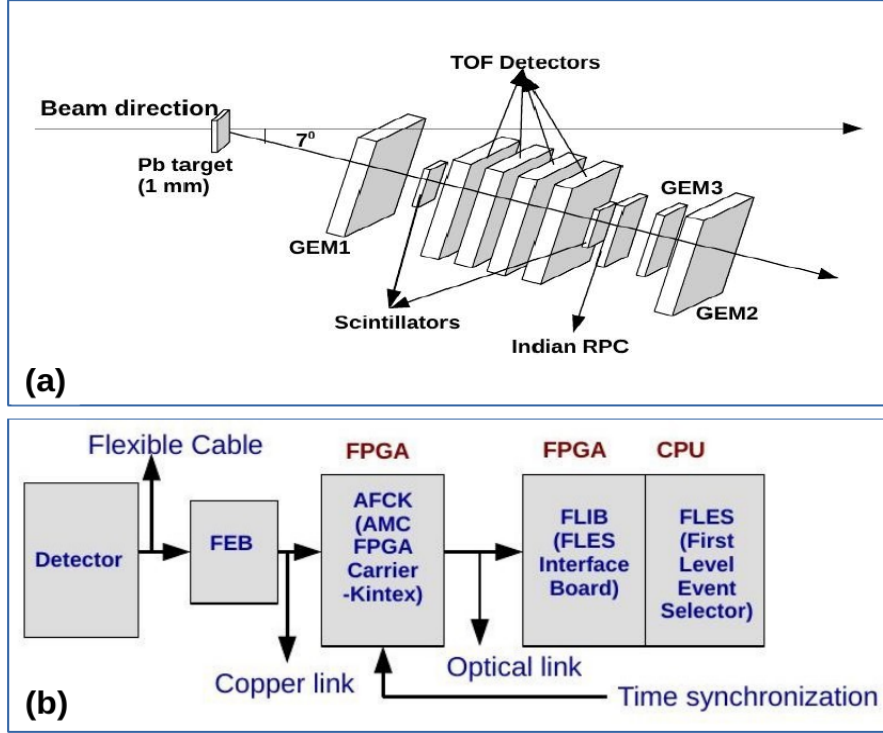


Figure 5.17: Schematics of test setup (top) and DAQ (bottom)

were placed on a common mounting frame, tilted at about $\sim 7^\circ$ from the beam axis, considering the target positioned at (0,0,0). Two “Mv1” modules, one in the front and the other at the back of the setup, were placed as shown in the figure. The first GEM module (GEM-1) was placed at ~ 3 meters distance from the target and its upper boundary about ~ 20 cm below the beam axis. The second GEM module (GEM-2) was placed at ~ 6 m from the target position. A third triple GEM chamber of size 10 cm x 10 cm, GEM-3 (built at GSI), was also put in at a later stage to provide an additional hit-point for tracking.

The block diagram of the data acquisition system is shown in Figure 5.17 (b). Data from different detectors (TOF, MuCh) were processed by the FPGA-based Data Processing Board (DPB)[170, 171]. These DPBs were configured on AFCK board, and it was mounted on a μ TCA crate. Twisted pair LVDS flat ribbon cables, ~ 6 meters in length, were used as signal cables from the back-end of FEBs to the front-end of AFCK boards. An optical cable of ~ 50 meters in length was used from the back-end of the AFCK to the FLIB (FLES Interface Board) board which was mounted on FLIB-PC. Time-synchronization for combining the detector hits in the two subsystems was carried out via two dedicated AFCK (master and slave) boards placed in the same crate.

Pb-Pb collision data taken for $E_{lab}=150$ GeV/c have been analyzed. Individual channel hits in

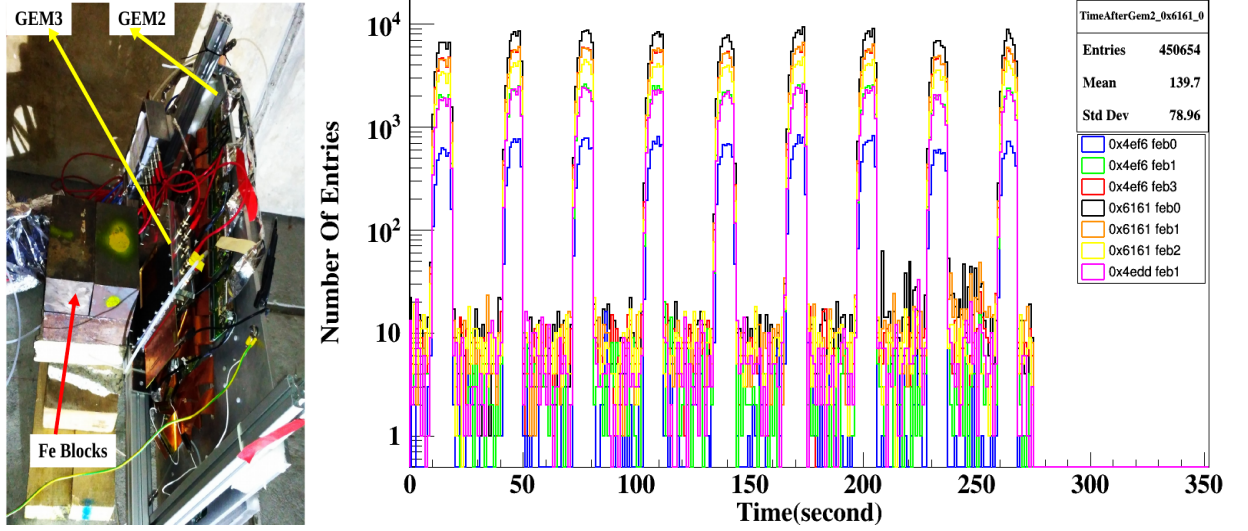


Figure 5.18: Left: Picture of Fe absorber placed behind detector. Right: Spill structure seen on GEM2 plane

the detector prototypes due to particles were recorded along with the corresponding time-stamps and amplitude. This free-streaming data was stored in time slices of 10 ms interval. Data were taken for different GEM voltages and also for different noise thresholds. The unsorted raw data was sorted within every time slice during unpacking and later corrected for time offsets.

The incident Pb beam for collisions was delivered in spills. The right panel of Figure 5.18 shows this spill structure as observed from the hits in the GEM2 detector. A spill frequency of ~ 30 s and spill width of ~ 9 s can be noted. The various colors in the figure represent different FEBs connected to pads in different regions. Constructing single events from the collection of hits with time-stamp becomes a challenging task. A diamond detector (placed just before the target) was selected as a reference detector for building an event. A simple algorithm wherein all the GEM hits which lie between two consecutive diamond hits was taken to be one event. The time difference spectra of hits in GEM2 and Diamond, event by event, is shown in Figure 5.19 (left). The σ of these spectra is the order of ~ 14 ns, which is a measure of the time resolution of the detector. The pulse height spectra fitted to the Landau distribution for GEM2 within 3σ window of time correlation spectra are shown in Fig. 5.19 (middle). The distribution of number hits per event (hit multiplicity) for GEM2 detector event-by-event is shown in Fig. 5.19 (right).

The variation of σ (ns) of time correlation spectra for different FEB board is shown in Figure 5.20 (left). We observed a maximum variation in time resolution of 4-5 ns. The variation of the average number of hits for GEM with time cut (ns) (from diamond reference) is shown in Figure 5.20 (right). We observed that the number of hits first increase and then saturates as expected.

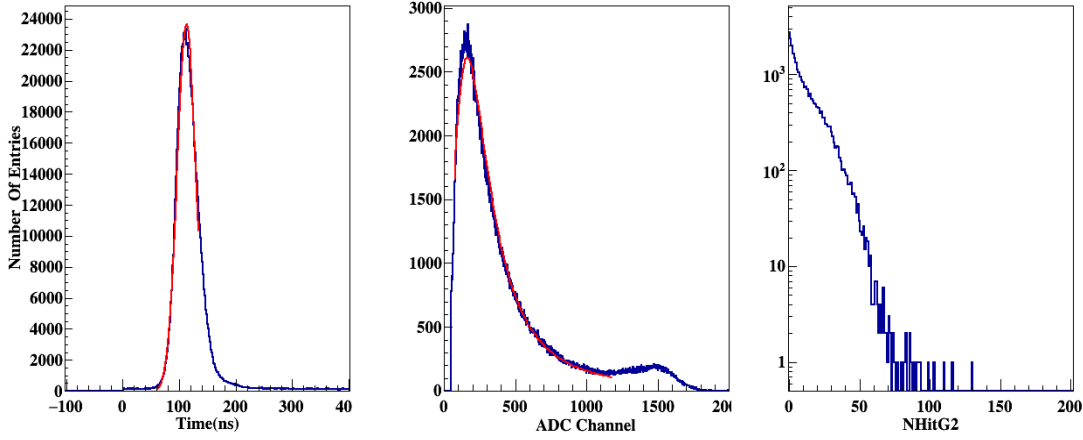


Figure 5.19: Results from the data. Left: Time difference spectra between GEM and diamond detector. Middle: Pulse height distribution with 3σ window of time correlation. Right: Hit multiplicity distribution

Figure 5.21 (top) shows the time correlation spectra between hits of one FEB with another in the GEM2 plane. The spectra peaks at ~ 14 ns with σ of ~ 23 ns, and after walk correction, a reduction of ~ 3 ns was observed, as shown in Figure 5.21 (bottom). Detector resolutions add up in quadrature. The value after walk correction is found to be consistent with this theoretical deduction considering a value of 14 ns from Figure 5.19 (left).

The global X (mm)-Y (mm) distribution of hit-coordinates for the three GEM detectors is shown in Figure 5.22 (left panel) and the corresponding η - ϕ coordinates is shown in Figure 5.22 (right panel).

The hit multiplicity correction between GEM1 and GEM2 hits in same event is shown in Figure 5.23 (left), while for the cross-event is shown right panel of same figure. They seemed to be correlated to each other.

A track-fit was carried out using hit-coordinates in different detector planes. Considering the origin (0,0,0) and two GEM hits in detectors GEM2 and GEM3 lying in a common window of $1.39 < \eta < 1.42$ & $262 < \phi < 264$, a straight-line fit was carried out, and the extrapolated hit-coordinates in GEM1 plane was calculated based on the fit parameters. The detailed schematics and algorithm of track fitting is discussed in the next chapter (section 6.7). The distribution of residuals thus obtained for GEM1 hits in X and Y is shown in Figure 5.24. The overlapping area between these three detectors is minimal (due to $10 \text{ cm} \times 10 \text{ cm}$ detector). However, in the mCBM experiment (chapter 6), the overlapping area is relatively larger, and one can study track resolutions at various pad-granularity.

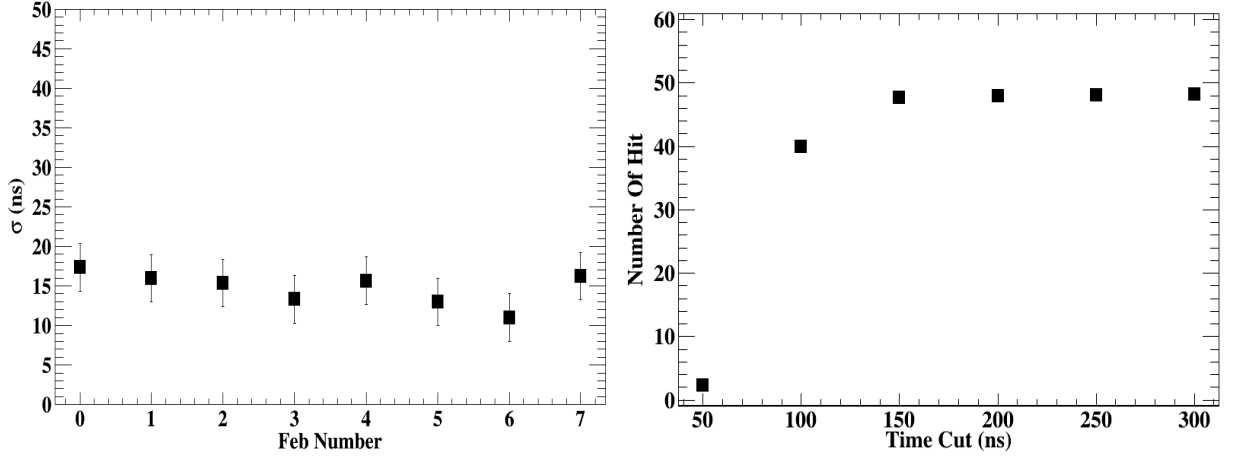


Figure 5.20: Left: Variation of σ with FEB number. Different FEBs are connected to different regions of the detector. Right: Variation of number of hit with time cut (see text). Statistical error bars are within the marker size.

Effect of GEM voltage on cluster size and hit multiplicity

Cluster size (the number of fired pads in a cluster) should increase with bias voltage. Figure 5.25 (left) shows the variation of cluster size with HV. The pad size varies from ~ 6.17 mm to ~ 6.72 mm for this region. The number of hits falling on the detector per event depends on the bias voltage, and it should increase by increasing the bias because of the increase in efficiencies. The variation of an average hit/event with HV is shown in Figure 5.25 (right).

Comparison of noisy and non-noisy data

In between the runs, we observed a sudden increase in the noise rate, as can be seen in Figure 5.26. The noisy region and the non-noisy regions are divided to study the effect of noisy data on detector hits. Event reconstruction in both regions has been performed. The distribution of the number of hits per event and pulse height spectra for both the regions is shown in the left and right panel of Figure 5.27. We can observe that after event reconstruction, the number of hits per event in both the case looks similar and also for the pulse height spectra. (The gain of the detector was about 1.5 k)

Effect of absorber on detector hits

In the last few runs, a 20 cm thick Fe absorber of size $20 \text{ cm} \times 20 \text{ cm} \times 20 \text{ cm}$ was placed behind GEM2 and GEM3 detectors to study the effect of absorbers on the detector hits. The picture of the Fe absorber behind the GEM2 detector is shown in Figure 5.18 (left). The distribution

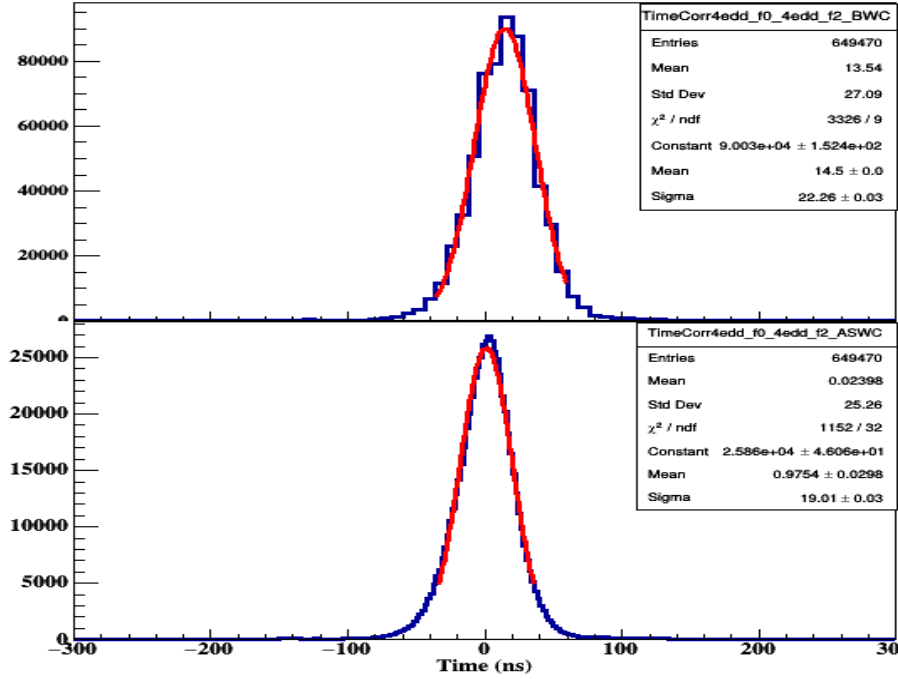


Figure 5.21: Time difference spectra between one FEB with another FEB of same GEM plane before time-walk correction. Right: after time-walk correction.

of the number of hits per event with and without absorber from data is shown in the left panel of Figure 5.28. Simulation has been performed for this setup in CBMROOT, and the number of hits/event is shown in the middle panel of Figure 5.28. We can observe that, the trend from data and simulation is similar. For quality assurance, same distribution has plotted for the GEM hits which are away from the absorber region, and it is shown in right panel of same figure. No effect in number of hits are observed, as expected.

In summary, we have tested for the first time large-size GEM detectors in a multi-particle environment coupled to self-triggered electronics and studied their response in terms of time correlation spectra, hit-correlation, and event reconstruction. A straight line fit was carried out using the hits in the three GEM planes and the diamond. The corresponding residual distributions were also studied.

5.3 “Mv2” design, assembly and test

The test of a real-size triple GEM chamber prototype for CBM-MuCh with X-ray source and particle beams has been discussed in the previous sections. This was the first real-size prototype having appropriate GEM foil segmentation, as discussed in the section. However, owing to the

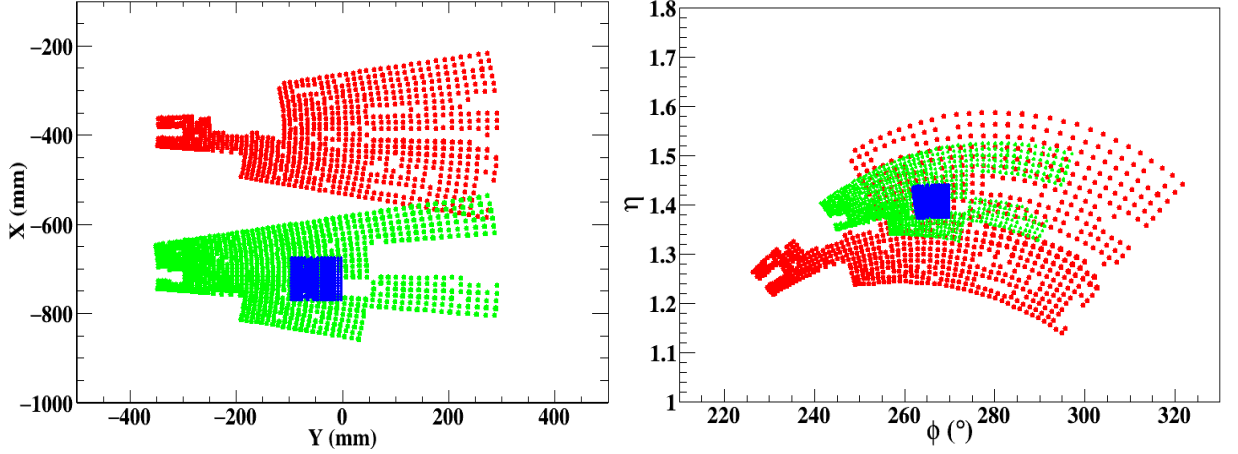


Figure 5.22: a) Global X-Y distribution of detector hits. b) η - ϕ distribution of detector hits (Red-GEM1, Green-GEM2, Blue-GEM3).

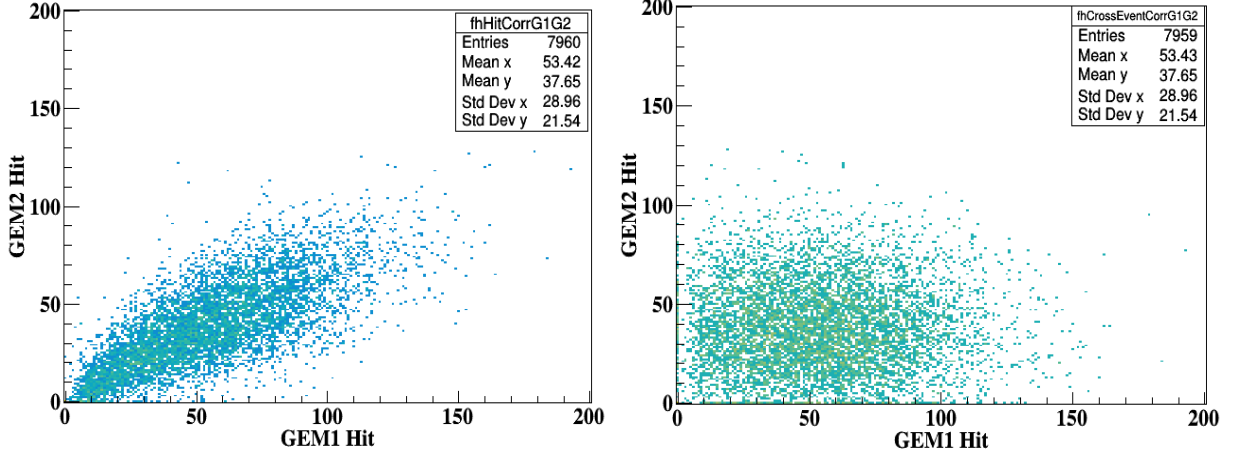


Figure 5.23: Hit multiplicity correlation between GEM1 and GEM2 in same event (left) and in cross-events (right).

absence of any clear scheme of HV biasing, these prototypes were operated with a single resistive divider, i.e., without any individual-segment control. For the final CBM configuration, we have to make ourselves ready to handle foil-segments, which may suddenly go bad during long-term operation due to some unforeseen reasons, such as large discharges. This issue has been taken care of in the present prototype being discussed in this section. The top surface of each foil segment is connected to the respective point in the divider chain via optocouplers, as explained in the next section. One resistive divider has been used for each half of the module. During the operation, if any segment develops some serious fault, this will lead to an increased branch current, which will trigger an alarm in monitoring. In a sequential iterative approach, one would be able to identify & isolate the particular faulty segment, restoring the operating condition and, most importantly, losing only a part of the module acceptance. Handling a faulty segment is one of the issues on

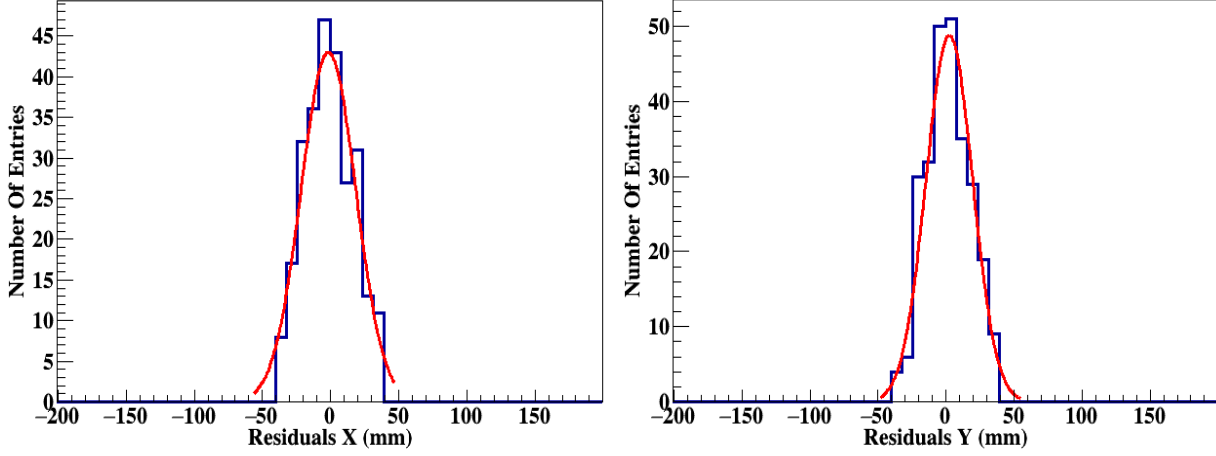
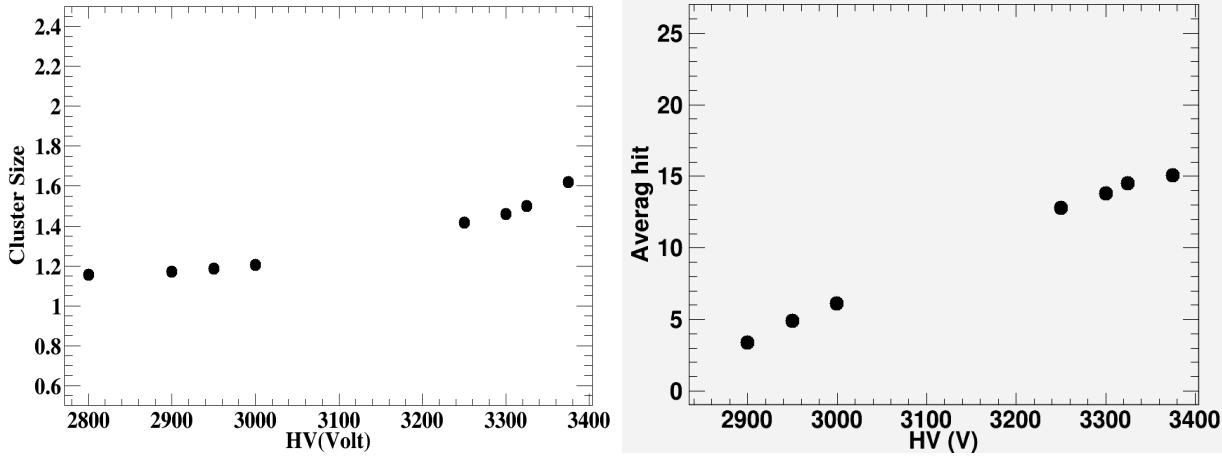


Figure 5.24: Residuals in X (mm) and Y (mm) at GEM1 plane

Figure 5.25: Left: Variation of cluster size with HV for the GEM2 plane. The pad size varies from $\sim 6.17\text{mm}$ to $\sim 6.72\text{mm}$ for this region. Right: Variation of the average hit with HV. Statistical error bars are within the marker size.

which R & D is still going on. The main advantage of the optocoupler approach is that it is cost-effective as compared to other options [152, 153] and easy to implement, along with its capability to handle multiple shorts.

5.3.1 HV distribution design

The HV layout on a drift PCB is shown in Figure 5.29. HV track lines of different lengths, totaling 78 in number (72 for the top GEM-surfaces and 6 for the bottom ones), are etched on the outer side of the drift PCB, and as many numbers of spring contacts are carefully soldered in the inner plane of the drift PCB to draw out the connections from all the GEM foil segments. These pins passing through the spacers have different lengths depending upon whether they are for the top, middle, or bottom foil. All the HV tracks are routed towards the broad top portion of the trapezoid,

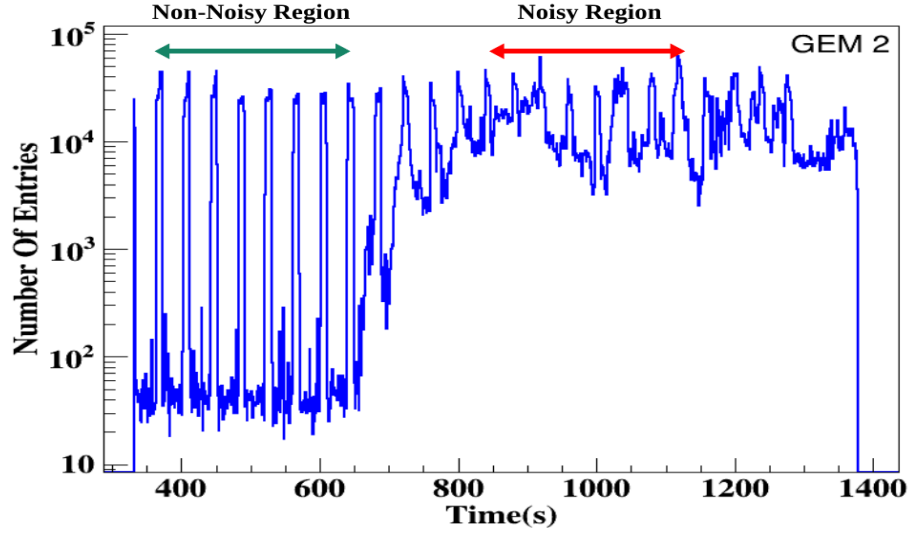


Figure 5.26: Spill structure showing noisy and non-noisy regions

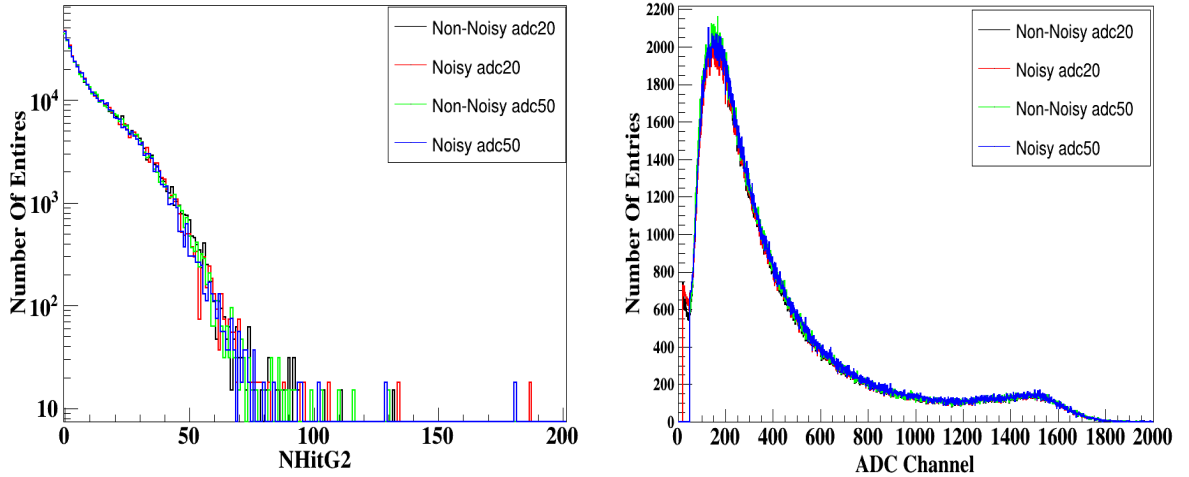


Figure 5.27: Left: Distribution of number of digi/event. Right: Pulse height distribution

where each of them is finally connected to the corresponding points in the divider chain for the respective half. The tracks for the segments of each GEM layer are connected via optocouplers to the respective point in the divider chain. A manual switch has been provided for controlling the ON/OFF operation of the optocouplers. An FPGA-based control port has also been provided for controlling it remotely. The $1\text{ M}\Omega$ protection resistances for the foils are soldered on the top of the drift board close to the optocoupler region, outside the gas volume. A commercially available ceramic divider customized to 3-2-2-2 mm gap configuration has been used as the resistive chain for each half. The resistances across the top, middle & bottom GEM layers are 0.55M , 0.50M , 0.45M , respectively, and the typical operating branch current is $\sim 750\mu\text{A}$. Figure 5.30 shows a picture of

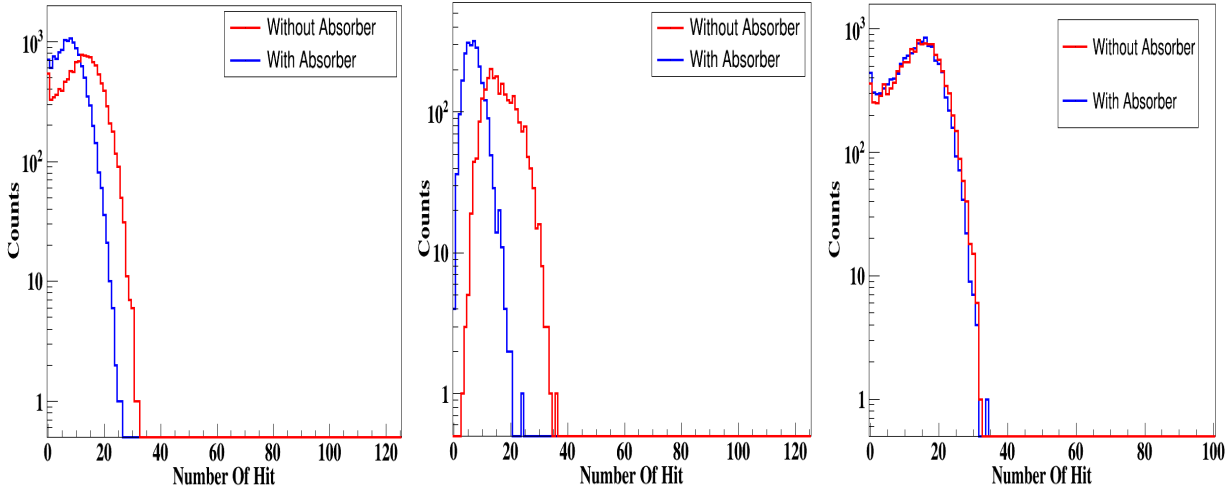


Figure 5.28: Hit distribution with and without 20 cm thick Fe absorber for GEM2 in data (left panel) and in simulation (middle panel). Right: Hit distribution with and without 20 cm thick Fe absorber data for GEM2, away from the absorber zone.

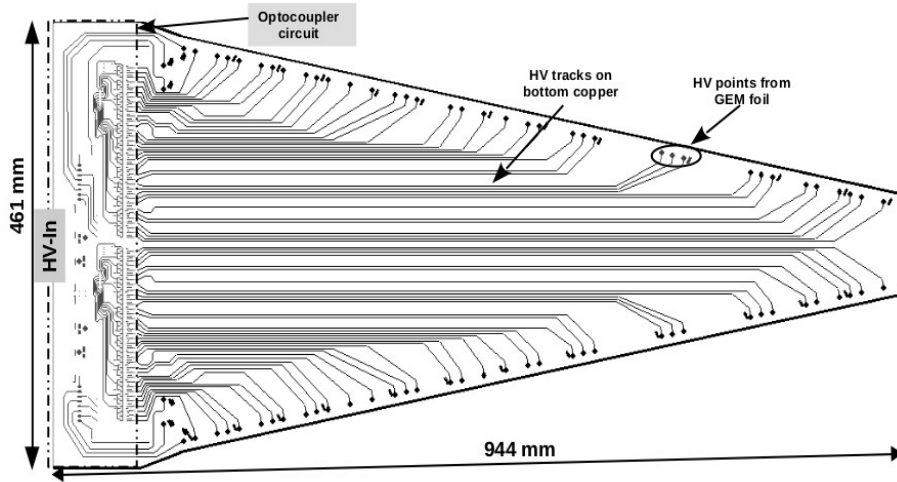


Figure 5.29: Schematic of HV layout on drift PCB

the large size GEM foil for station-1 modules. The HV points for spring contacts, the two halves (each divided into 12 segments) of the foil, and numerous slots for side-screw nuts are also shown.

A) Novel optocoupler based HV design

Optocoupler: An optocoupler is a device that transfers a signal between two isolated points. It is also known as Solid State Relay as well as OptoMOS relay. The relay output is constructed with efficient MOSFET switches. The input in these devices consists of a highly efficient infrared LED that controls the optically coupled output, which means a short optical path or link is coupled to the signal from one electrical circuit to another while providing electrical isolation. Hence, these are thus also commonly referred to as optocouplers or optoisolators. Based on the high voltage

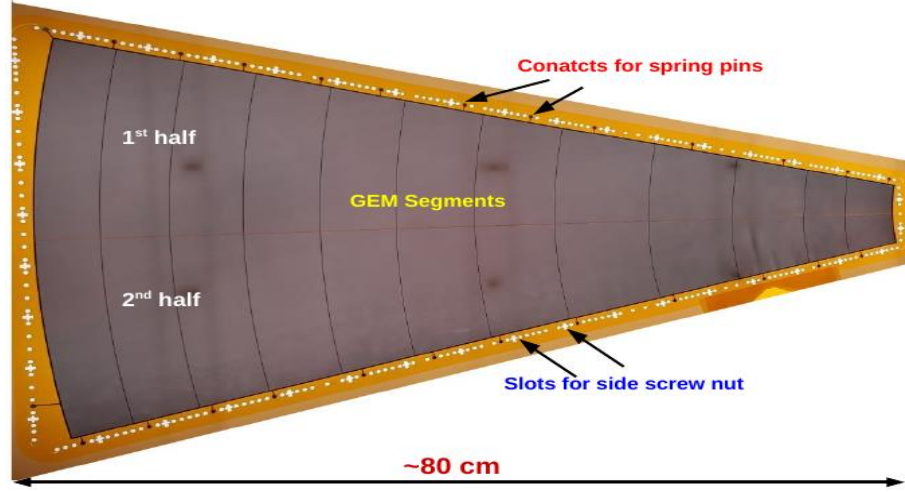


Figure 5.30: Picture of large size GEM foil with 24 segments

and GEM voltage requirements associated with the GEM-MuCh biasing, we have used a single pole optocoupler device [172] for our tests. This device has high I/O isolation & blocking voltage. Also, it has an MSL (Moisture sensitivity level) rating of 1, implying that it remains unaffected by humidity variations, which is a desired property for long-term operation. The schematic picture of the voltage divider circuit with these devices is shown in Figure 5.31. In this four-pin device, one pair of pins (1&2 in the figure) is connected to the control side (LV side) and the other two to the load side (GEM foil side). In the normal operating condition, the optocoupler is in ON state, the junctions 3 and 4 start conducting, and the actual voltage from the resistive chain is transmitted to point 4, representing the direct connection to the foil. In OFF condition, there will be no conduction between pin 3 and pin 4.

B) Test of optocouplers

For its intended use in CBM, one needs to study the characteristics of these devices in terms of 1. Radiation hardness as per the requirement of CBM. 2. Effect of sparks on their operation. 3. Effect on detector gain, and 4. Handling short segments.

a) Radiation hardness test: All components of MuCh detector subsystem should withstand the expected radiation dose in the CBM environment [112], which for neutron is $\sim 10^{12} n_{eq}/cm^2$ and for Gamma is ~ 30 krad. These numbers are equivalent to ten years of operation in CBM. The optocouplers were subjected to neutron irradiation up to $4.46 \times 10^{12} n_{eq}/cm^2$ and no noticeable increase in the leakage current was observed. These were then subjected to a Gamma dose up to 60 krad (using ^{60}Co source). Leakage currents have been measured for both before and after irradiation by applying appropriate voltages across the load terminals 3 & 4 (see Figure 5.31) in

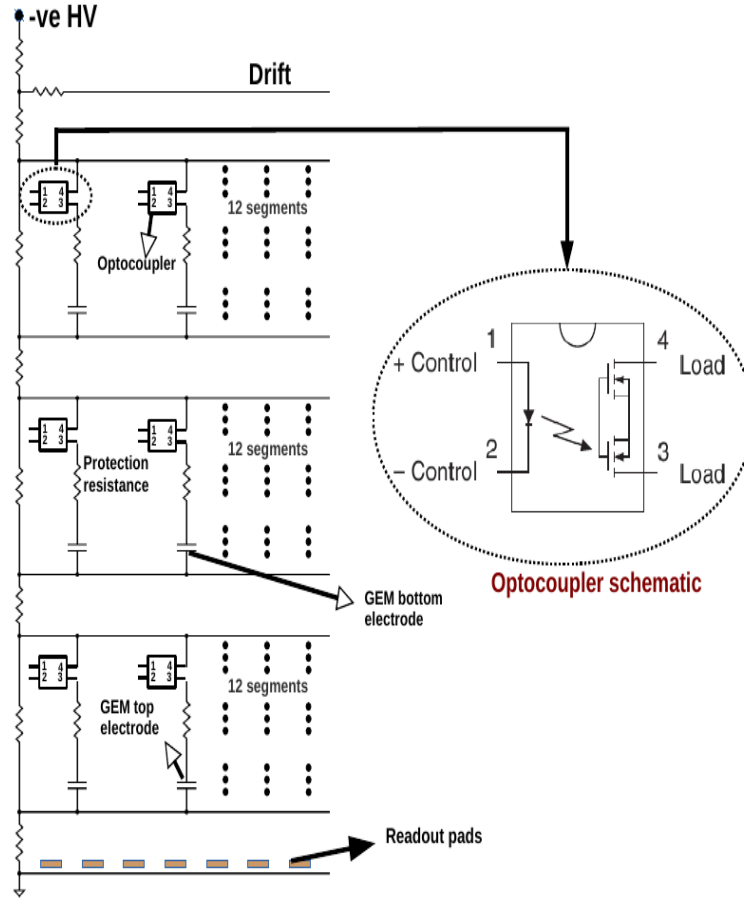


Figure 5.31: Schematic of voltage divider circuit for GEM with optocoupler for one half. Inset: Optocoupler schematic

the "OFF" ("open") state of the device. A comparison of the measured currents for the two cases is shown in Figure 5.32. The slight increase in leakage current from its normal value after irradiation can easily be explained by charge deposition of Gamma radiation, and this extra $\sim 14\text{nA}$ current does not give any substantial voltage drop across the optocouplers in OFF condition. This test validates the radiation hardness requirements.

b) Spark test: The optocouplers should be resilient to high current surges, and one of the potential sources for this is the occasionally occurring sparks in any gas detector. So it becomes essential to test the spark-stability of these optocouplers. The schematic and picture of the test setup in the lab are shown in Figure 5.33. This being a destructive test, a single $10\text{ cm} \times 10\text{ cm}$ GEM foil having poor voltage characteristics was used. The voltages across the GEM surfaces were applied via an optocoupler, as shown. The test was conducted in the air. Table 1 shows a summary of this test. The number of sparks observed for different time duration against different GEM voltage settings was counted. This way, the optocoupler was subjected to many sparks for a

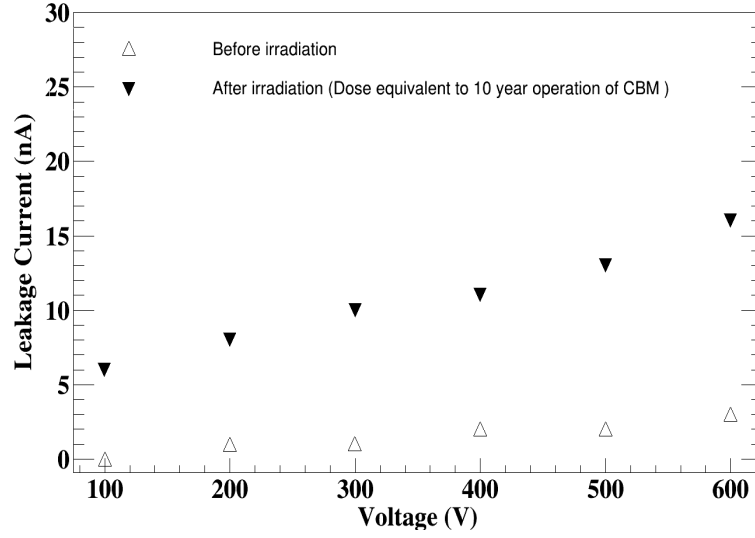


Figure 5.32: Comparison of leakage currents of optocoupler before and after the irradiation. Statistical error bars are within the marker size.

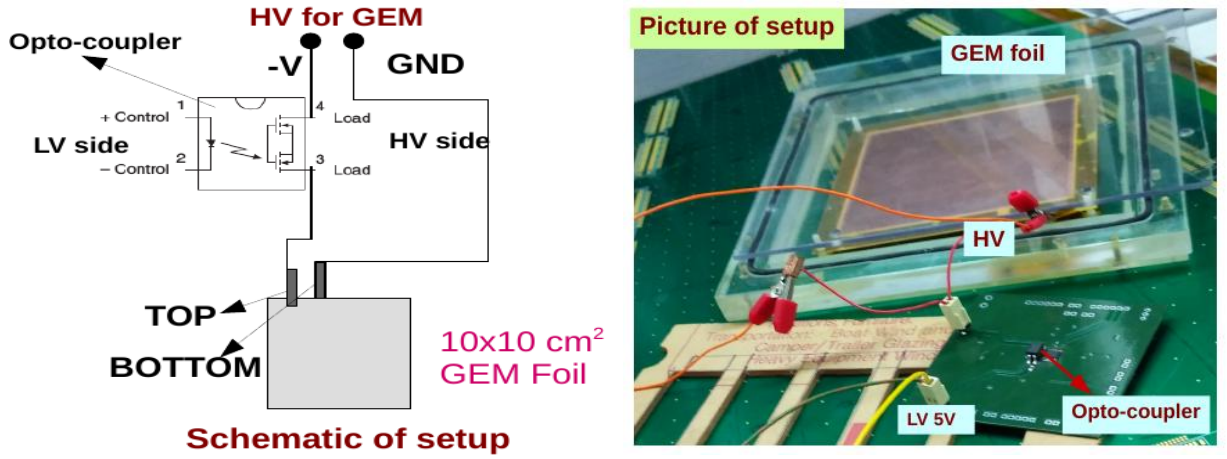


Figure 5.33: Schematic (left) and picture (right) of the setup for spark tests with the optocoupler.

time duration going up to ~ 3 hours. The leakage current of the optocoupler measured before and after the spark test shows identical values as observed from Figure 5.34. The maximum current in GEM foil at 500V due to intermittent sparks, as noted in the tests, was found to be ~ 3 to ~ 4 μA , while the device can sustain a load current up to 90mA, revealing its robustness towards sparks.

c) Effect on gain of detector: The gain of the detector depends on the voltage applied, and placing an optocoupler in the path should not alter the settings. However, this has to be verified. A 10 cm x 10 cm triple GEM detector was used to test this effect. The gas mixture and the data acquisition system are the same as explained in section 4. The photo-peak ADC channel with and without optocoupler has been measured at different high voltages as shown in Figure 5.35. We observe that the photo-peak positions are similar in both cases.

Table 5.2: Table for sparks test of opto-coupler

$\Delta V_{GEM}(V)$	Time (min)	Number of sparks
530	35	22
550	178	48
570	200	45
590	153	260

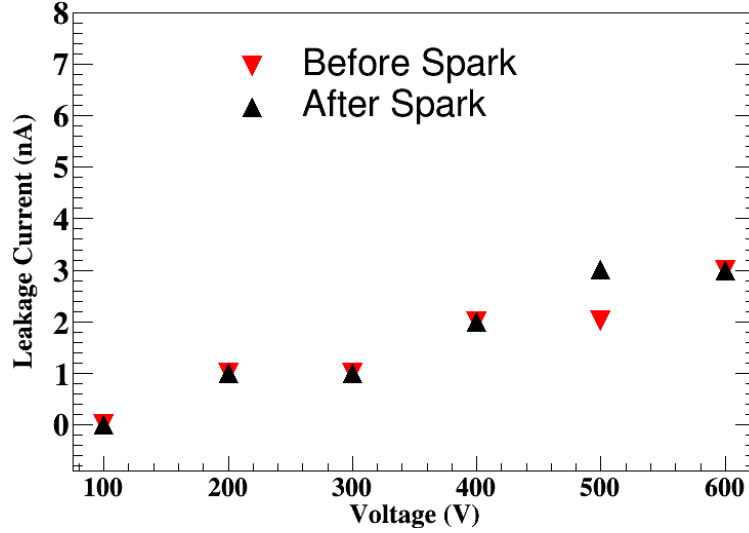


Figure 5.34: Comparison of leakage currents of optocoupler before and after the spark tests. Statistical error bars are within the marker size.

d) Short segment test: What happens to the detector in case there suddenly occurs a short in the GEMs? As per calculations, in such a case, less than $300\mu A$ of current flows through the corresponding optocouplers, which is well within the limiting value of 90 mA. As a simple exercise, we tested this by manually shorting one of the segments. A large size GEM chamber was used for this purpose; refer to Figure 5.36. The high voltage was set to 4600V, and the divider current ($688\mu A$) was noted. We then manually shorted one of the segments and observed a significant increase in the branch current, as expected. Then the optocoupler corresponding to that segment was manually switched off, and the current was found to restore to its normal value ($688\mu A$) as before.

The picture of the fabricated drift PCB with HV lines and optocouplers mounted on it is shown in Figure 5.36. In total, 72 such devices (36 for each half) are used, and a group consisting of top electrodes of the top, middle, and bottom foils of one triple GEM segment is controlled by one LV switch. The large size triple GEM detector was thus built, having a realistic readout and drift PCB.

C) Calculations on the maximal current in spark and short circuit configuration

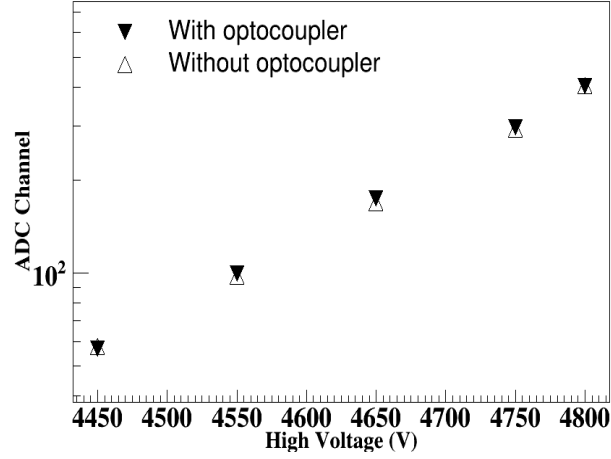


Figure 5.35: Comparison of peak pulse height at varying voltages with and without optocoupler. Statistical error bars are within the marker size.

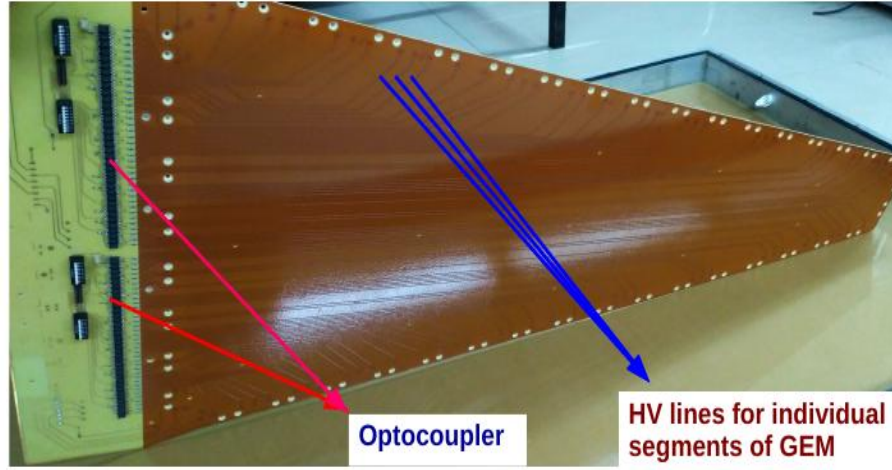


Figure 5.36: Picture of the final drift PCB with optocouplers mounted on it

1. *In the case of sparks:* The maximum current in GEM foil at $\sim 500\text{V}$ due to intermittent sparks, as observed in the tests, was found to be ~ 3 to $\sim 4 \mu\text{A}$ (on a full scale of $21 \mu\text{A}$), while this device can sustain a load current up to 90 mA . Thus the performed spark-tests reveal that the device is robust to sparks.

2. *In the case of segment short circuit:* Consider the schematic in Figure 5.37 (which is an equivalent divider circuit), where the optocoupler circuit for a particular segment of the top GEM layer is shown.

The resistance values for this equivalent circuit are as follows.

$R_1 = 2 \text{ M}\Omega$, $R_2 = 0.55 \text{ M}\Omega$, R_3 (protection resistance) $= 1 \text{ M}\Omega$, $R_4 = 3.95 \text{ M}\Omega$,

R_{opto} (under “ON” condition $\sim 50 \Omega$).

In case a segment gets short, the equivalent resistance of the divider chain will be

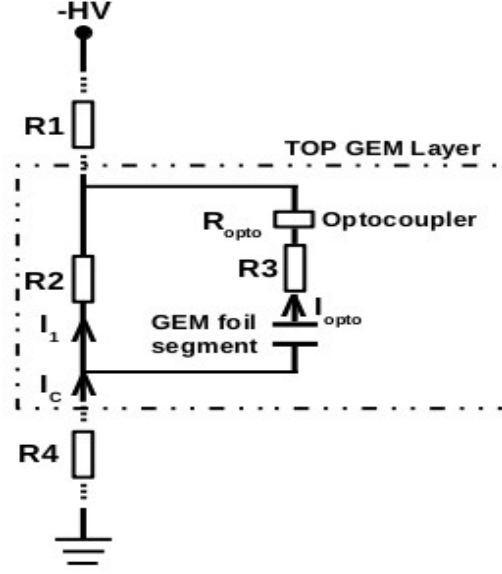


Figure 5.37: Schematic layout of assembly of different layers to build a final chamber

$R_{eq} = 6.305 \text{ M}\Omega$ (In normal case the divider resistance is $6.5 \text{ M}\Omega$).

Total chain current, $I_C = 5000 \text{ V} / R_{eq} = 793.03 \text{ }\mu\text{A}$ (for $HV = 5000\text{V}$)

Thus $I_C = I_1 + I_{opto}$ and, $I_1 R_2 = I_{opto} R_3$ (since $R_{opto} \ll R_3$).

where I_1 and I_{opto} are currents through R_2 and R_3 , respectively. By solving these equations, we can get I_{opto} as:

$$I_{opto} = I_C R_2 / (R_2 + R_3) = 281.2 \text{ }\mu\text{A}$$

Thus, the current through optocoupler in case of a segment short will be $\sim 281.2 \text{ }\mu\text{A}$. However, the optocoupler can handle a load current up to $\sim 90 \text{ mA}$.

D) Test with ^{55}Fe in lab The chamber was tested with ^{55}Fe source using $\text{Ar}/\text{CO}_2(70/30)$ gas mixture. The detector readout consists of a projective pad with varying sizes from $\sim 3.2 \text{ mm}$ to $\sim 17 \text{ mm}$. A 5V low voltage power supply is needed to operate the optocouplers. The resistive divider circuit provides a high voltage to the two detector halves. The data acquisition consisted of a pre-amplifier, amplifier, and MCA (multichannel analyzer). The ^{55}Fe spectrum obtained from the detector at a summed $\Delta V_{GEM} \sim 1110\text{V}$ is shown in Figure 5.38 (left). The variation of photo-peak ADC with GEM voltage is shown in Figure 5.38 (right).

The uniformity of the detector in terms of gain (in ADC units) has been measured by measuring the detector gain at the various position of the detector. The schematic of the position number on the detector module is shown in Figure 5.39 (left), and the variation of gain at a different position is shown in the right panel of the same figure. We observed a gain variation of 25-30% throughout

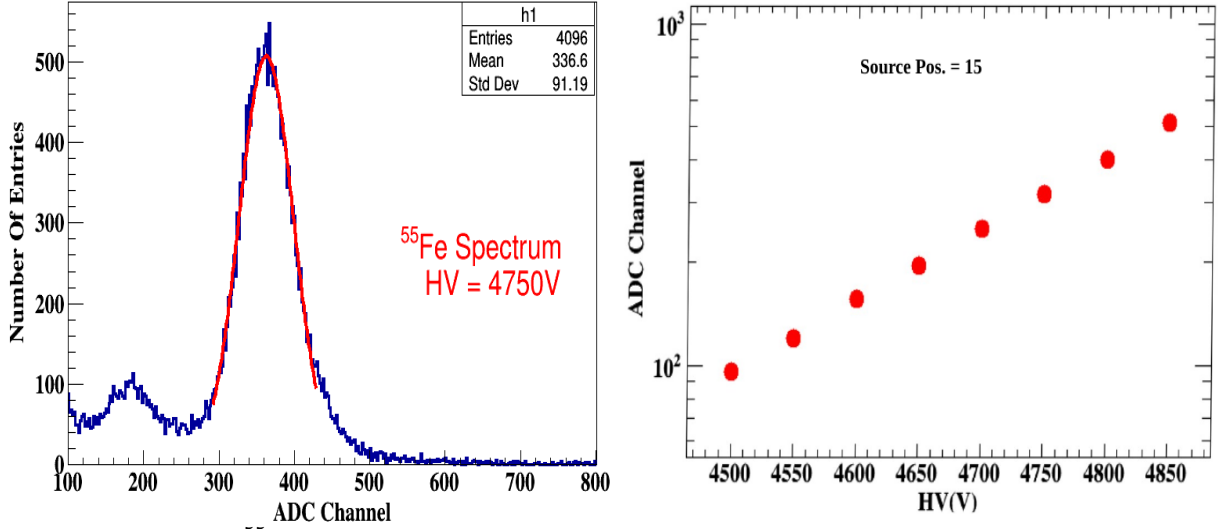


Figure 5.38: Left: ^{55}Fe pulse height spectrum from Mv2 module. Right: Variation of phot-peak ADC channel with HV. Statistical error bars are within the marker size.

the full active area of the detector.

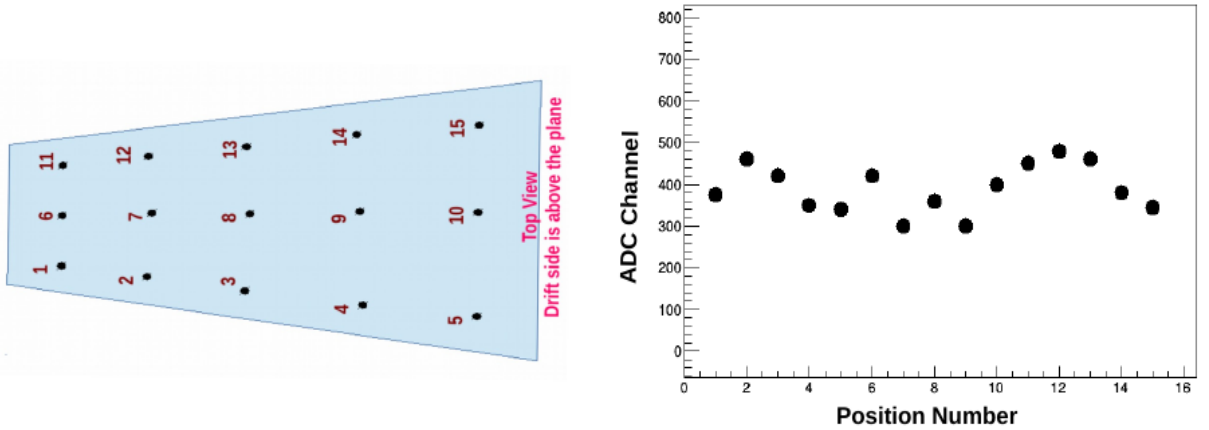


Figure 5.39: Left: Schematic of chamber showing position numbers. Right: Photo-peak ADC at different regions of the detector. (without T/P corrected). Statistical error bars are within the marker size.

5.3.2 Testing large size detector in mCBM experiment

These detectors have been tested with an X-ray source in the lab. We need to test this detector in the CBM like environment for its performance in the main CBM experiment. So we have installed and tested these detectors with nuclear collisions with a beam energy of 1-2 AGeV in the ongoing experiment at SIS18 accelerator facility GSI, called the mini-CBM experiment.

5.4 Summary

The design and assembly of real-size triple GEM detectors have been discussed in detail. Two versions of the real-size modules have been assembled, namely “Mv1” and “Mv2”. The real-size modules were tested with radioactive sources in the lab. Also, these were tested with high rate single-particle beams and the Pb+Pb collisions at CERN-SPS. The preliminary results in terms of spill structure, time correction, event building by taking diamond as reference detector have been discussed. A large area triple GEM prototype, “Mv2”, the chamber for station-1 of CBM-MuCh, was designed and fabricated at VECC, having a novel optocoupler-based HV biasing scheme. The robustness of the optocoupler devices has been studied in terms of radiation hardness and stability towards sparks in the GEM, satisfying the essential functional characteristics of GEM-MuCh. Pulse height characteristics of the chamber with and without optocouplers remain unchanged. Such a biasing approach would be very cost-effective, and one can also isolate the faulty segments, during data taking, with only minimum acceptance loss. Two such trapezoidal detector modules have been commissioned in the ongoing mini-CBM experiment at GSI for tests with nuclear collisions. The preliminary results show a good response from these detectors. A more detailed study on the effect of such a biasing scheme has been discussed in the next chapter of this thesis.

Chapter 6

Commissioning and testing of real-size GEM modules in mCBM experiment

A detailed description of the MuCh detector system and its layout is given in chapter 2. A GEM-based detector technology will be used for the first two stations of MuCh. As already mentioned that, two versions of real-size modules, namely, “Mv1” and “Mv2” were built and tested. The design and assembly of these prototypes have been discussed in chapter 5. In this chapter, installation, commissioning and testing two real-size (“Mv2”) modules in the mCBM experiment are discussed in detail. These modules were first tested in the lab with the source and then installed in the mCBM experiment for testing it in A-A collisions. The mCBM (mini-CBM) experiment is designed to test all the detector subsystems of CBM along with the final DAQ. The details about this experiment is given section 6.1. The mMuCh detectors were first installed in December 2018. Data were acquired with only one FEB due to the unavailability of electronics and limitation of DAQ. However, data with almost full FEB coverage were acquired in March 2019 and December 2019 beamtimes. STS/MuCh-XYTER ASIC was used for reading the signal from the detector (see section 6.4.1). The ASIC version used in December 2018 and March 2019 beamtimes were v2.0. This is summarized in table 6.1. The reason for using two versions is described in section 6.2 in details.

6.1 mCBM experiment

As it has been discussed, all detector subsystems of CBM will have to cope with very high interaction rate. The signals from them will be read out using self-triggered electronics, enabling one to collect data at this high rate, whereby each signal above a set threshold is recorded along with the timestamp of these hits. Events are then reconstructed offline by grouping such hits in time. It, therefore, becomes essential to study an integrated response of the detectors through a series of beam tests in which one studies in detail the performance of all the detector subsystems of CBM prior to the actual experiment. In this regard, a precursor experiment of CBM consisting of all CBM detector subsystems has been set up at the SIS18 facility of GSI called mCBM [137] (“mini-CBM”), as a part of the FAIR Phase 0 program. The mCBM experiment aims as a CBM full-system test and enables tests of real-size modules of each detector subsystem under realistic experimental conditions in high-rate nucleus-nucleus collisions. Major tasks are studying and optimizing the DAQ and data transport to a computer farm, in particular the timing-stability and data consistency of the subsystem data streams, investigating issues related to the operation of detectors in a high-rate environment, and developing and optimizing the software for online/offline data analysis, along with the reconstruction of rare events like Λ Hyperon production in nucleus-nucleus collisions at SIS18 energies.

A conceptual sketch of mCBM setup is shown in Figure 6.1. The detector axis is positioned at an angle of about 25° with respect to beam axis. The geometry implemented in the ROOT environment of mCBM setup at SIS18 facility of GSI is shown in Figure 3.1.

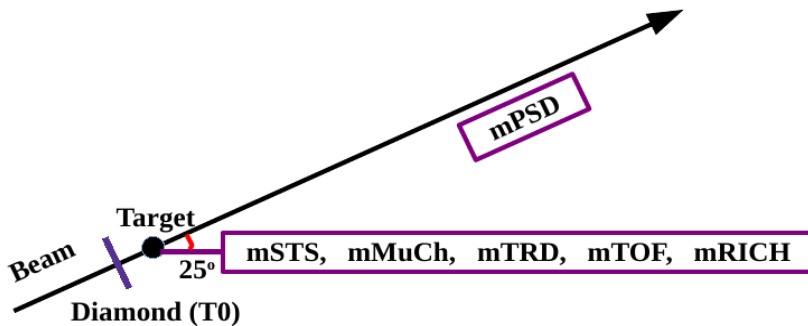


Figure 6.1: Conceptual sketch of the mCBM test setup. The detector subsystems are approximately positioned at 25° from the primary beam.

Table 6.1: Information about the beam in different beamtimes

Beamtime	Projectile	Kinetic Energy	STS/MuCh-XYTER Version
December 2018	^{108}Ag	1.20 AGeV	v2.0
March 2019	^{108}Ag	1.58 AGeV	v2.0
December 2019	^{40}Ar	1.70 AGeV	v2.1

6.2 mMuCh modules

Two real-size triple GEM detectors corresponding to the module sizes of station-1 of MuCh were installed and commissioned in the mCBM experiment. Ar/CO₂ (70/30) gas mixture has been the fill gas for all our tests. Tests of real-size detectors with proton beam and with Pb+Pb collisions have been reported in [173, 174] and in chapter 5. However, in these tests single-particle proton beams were used which were confined at a specific location on the detector. At mCBM, a multitude of particles originating from the nucleus+nucleus collisions would pass through the entire module. In this scenario, the goal is to study the simultaneous response from different regions of the detector, as well as in conjunction with those from other sub-systems. Once, such attempt was carried out at CERN-SPS [174], however, the real-size modules used were of different gap-configurations. The modules in mCBM have been specifically designed for first station of MuCh system. In addition to that, they were operated with different electronics. For mMuCh modules in mCBM, the first version of STS/MuCh-XYTER [141, 175] electronics have been used for the test. This has been specifically designed and developed for use by STS/MuCh sub-systems in CBM. Moreover, the data have been taken using the upgraded CBM DAQ [14].

The modules were installed in December 2018 beamtime, and the first set of data was acquired with one working FEB due to DAQ and electronics constraints. Tests with relatively greater number of active FEBs, thereby, covering wide acceptance on the detector, were performed in March 2019 and December 2019 beamtimes. The modules were read out using the first version of the STS/MuCh-XYTER chip (v2.0) in December 2018 and March 2019 beamtimes. During the test, it was discovered that the chip had a logic error. This error comes when a certain number of channels are fired within some time window. Particularly, this happens when at least seven channels are in coincidence. Due to this error either some channels give extra hits (hit copies) or they never give a signal (hit losses). The data were corrected by filtering out these hit copies. From simulations it has been observed that the bug is expected to affect only a small fraction (about 0.1%) of the high multiplicity events [176]. The bug was taken care of in the subsequent

version (v2.1) of the chip. The electronics were replaced in December 2019 and next beamtimes with v2.1. Data taken with v2.1 in December 2019 have been analyzed in detail. The results from the two electronic versions are discussed in section 6.5. The schematics of experimental and DAQ setup is given in section 6.3 and section 6.4, respectively.

6.3 Test setup at SIS18 facility of GSI (mCBM)

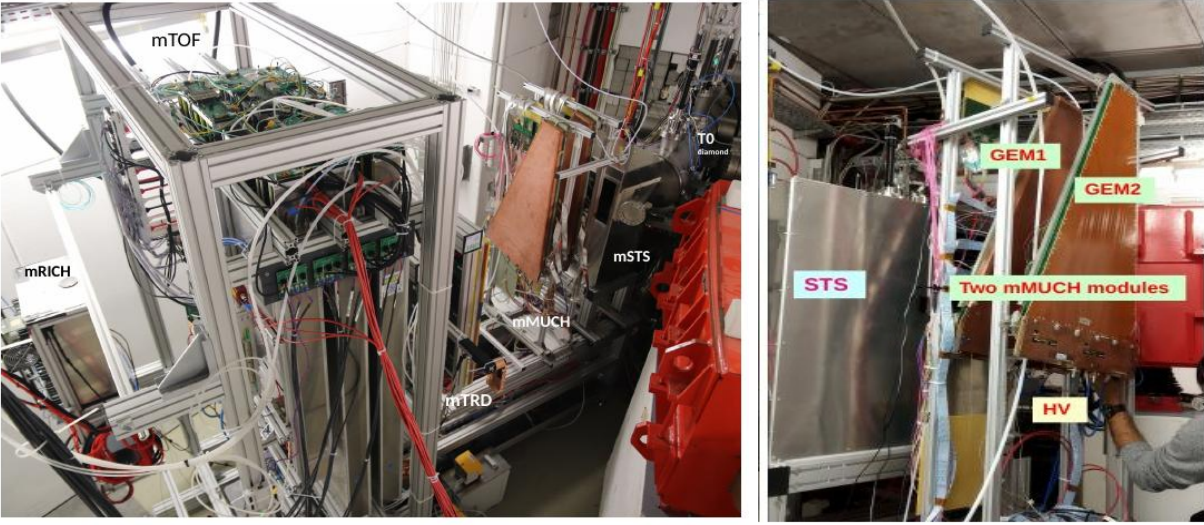


Figure 6.2: Left: Photograph of the experimental setup as of November 2019 showing the installed detector subsystems inside the mCBM cave at the SIS18 facility of GSI. Right: Closeup picture of two installed mMuCh modules.

A photograph of the two GEM modules as of November 2019, installed along with other detector subsystems inside the mCBM cave located at the SIS18 facility of GSI, is shown in Figure 6.2 (left). The subsystems were placed along the detector axis (25° line from beam direction) at different distances from the target, the position of which is taken as the origin (0,0,0). The height of the detector axis is approximately 2m from the ground and $\sim 25^\circ$ from the beam axis. Both mMuCh modules were mounted on an Al-plate of about 12 mm thickness. Each plate consists of ~ 6 mm Al-pipe winding inside the plate for carrying chilled water, thus providing the cooling of the front-end boards (FEBs) [177]. The schematic picture of Al-based cooling system is shown in Figure 6.3. A total of 18 FEB's (front-end-boards) are needed to populate one full chamber of station-1, with each FEB dissipating ~ 2.5 W of heat. In December 2019 beamtime, the number of working FEBs on the GEM1 plane was ~ 16 , and that on GEM2 was ~ 9 . For the ease of installation, the dimensions of the Al-plates used for mCBM were made slightly different than the

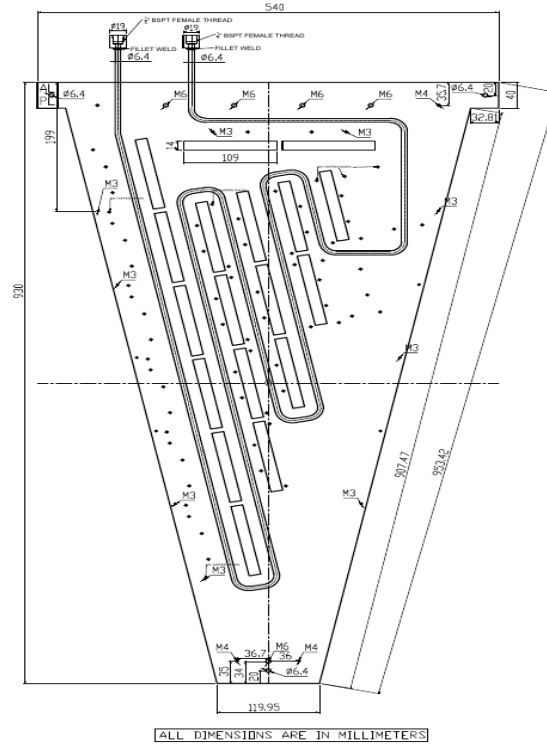


Figure 6.3: Schematic picture of cooling plate. Circular drill for fitting copper tube. Water flows inside the copper tube.

actual design for the CBM experiment. The full mMuCh system was then installed on the beam table, as shown in Figure 6.2 (right). A closeup picture of the GEM detectors along with the other components, like CROB¹, FEB², LVDB³ board, are shown in Figure 6.4. A brief description of these components are discussed in section 6.4.2. In absence of a dedicated alignment mechanism, relative positions of the modules with respect to the detector axis were measured using a meter scale. Using these values, the ROOT geometry was created for the mCBM setup. A schematic of the mCBM setup is shown in Figure 6.5, typical distances of the detector subsystems are as shown. The diamond detector (T0) was placed inside the target chamber. The dimension of the T0 detector is approximately 20 mm x 20 mm and placed roughly 20 cm upstream to the target. The mMuCh detectors were positioned with the readout side facing the target and oriented such that the long trapezoidal side was along the vertical axis, as shown in the figures. The detector axis (25° line from beam axis) intersected the modules at a distance of about 20 cm from the bottom edge of the trapezoid. Signals from the readout pads of the mMuCh modules were sent via the readout connectors to the corresponding FEBs fixed on the Al-cooling plate, using 10 cm

¹Common Readout Board

²Front End Board

³Low Voltage Distribution Board

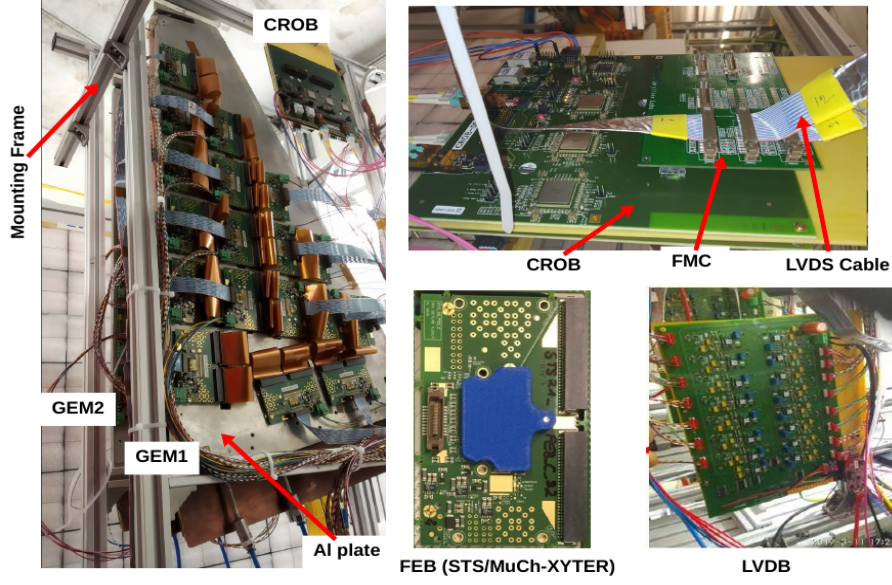


Figure 6.4: Closeup photograph of the mMuCh setup along with other components. CROB, FEBs, LVDB is also shown.

long flexible Kapton cables. Figure 6.4 shows the closeup view of these cables.

6.4 STS/MuCh-XYTER and Data Acquisition System (DAQ)

6.4.1 STS/MuCh-XYTER

The STS/MuCh-XYTER is a self-triggered readout electronics, which measures the time and amplitude of the signal [141, 142, 143]. The block diagram of the chip is shown in Figure 6.6, taken from [13]. The main specification of this chip is given below:

- it provides both timing and amplitude (ADC) information
- it is a self-triggered electronics
- 128 channels + 2 test channels
- can handle average hit rate 250 kHz/channel
- it has a 5-bit Flash ADC
- 14-bit for time measurement
- dynamic range = 100 fC, and it can be changed
- slow shaper time can be changed from 80 ns to 270 ns.
- fast shaper has a rise time of 30 ns
- timing resolution $\sim 4\text{-}5$ ns, time stamp resolution 1 ns

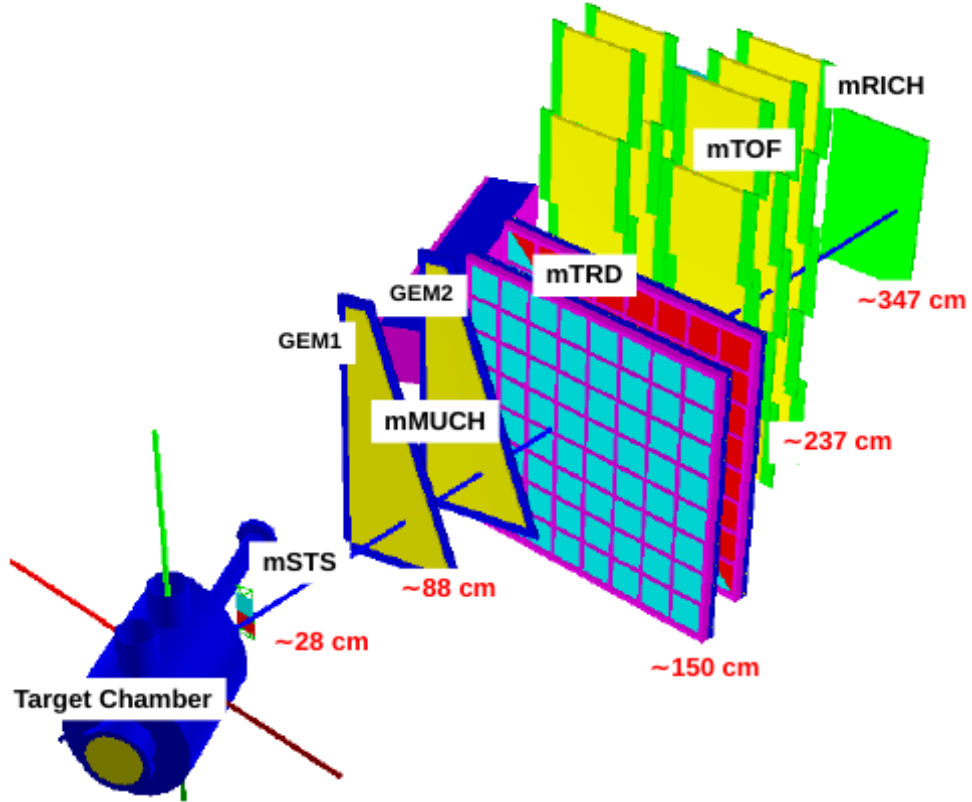


Figure 6.5: Schematic setup of mCBM experiment as of November 2019 as per the realistic mCBM geometry implemented in ROOT. Detectors are placed at $\sim 25^\circ$ from the beam axis. The diamond detector (T0) is placed inside the target chamber. mSTS - mini-Silicon Tracking System, mMuCh - mini-Muon Chamber System, mTRD - mini-Transition Radiation Detector, mTOF - mini-Time Of Flight, mRICH - mini-Ring Imaging Cherenkov.

- heat generated = $\sim 2\text{-}3$ W / FEB

6.4.2 Data Acquisition System (DAQ)

The block diagram of the data acquisition system for the mCBM experiment is shown in Figure 6.7 [14]. The data from the FEBs are first collected at the CROB, which is placed in close proximity on the detector mounting frames, via LVDS⁴ cable, and then data from all the CROB's were transported to the DPB⁵, placed in the DAQ room (outside the cave, about 50 m away), via the optical cable. The data from all the subsystems were further transported to the Green Cube (Computing Node of FAIR-GSI) [178], which is about 310 m from the DAQ room. The data in mCBM have been acquired in a free-streaming mode, as the case would be in CBM. The block

⁴Low Voltage Differential Signal

⁵Data Processing Board

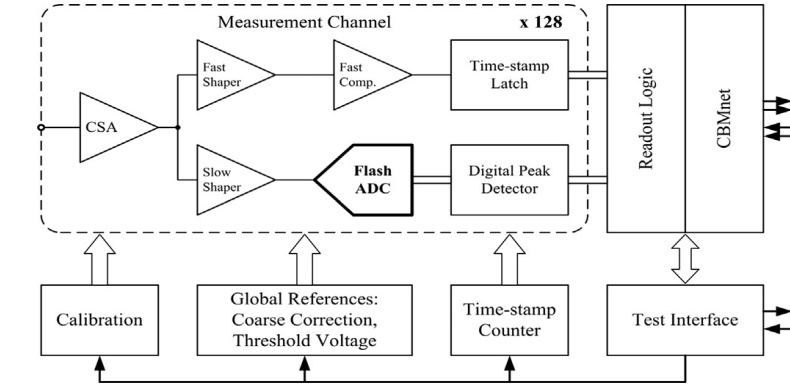


Figure 6.6: The block diagram of STS/MuCh-XYTER chip [13].

diagram of mMuCh readout chain is shown in Figure 6.8.

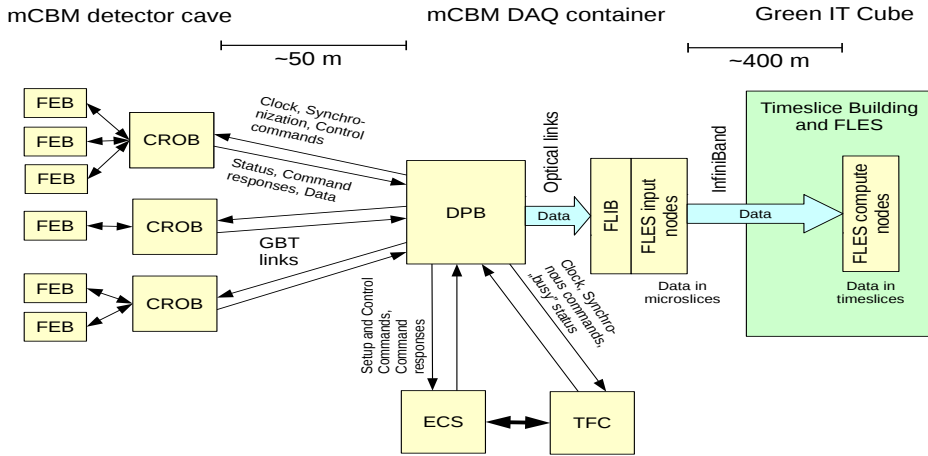


Figure 6.7: Schematic setup of the Data Acquisition System (DAQ) of the mCBM experiment [14].

In a free-streaming mode, signals from every electronic channel, if higher than a set threshold, are recorded along with their timestamps. The digitized signal from any electronic channel is referred to as Digi. The readout ASIC has 128 analog channels. Each channel uses a 5-bit Flash ADC, which was calibrated with a step size of 2.5 fC. For calibration of the chip, a known charge was injected in each channel of ASIC using an external pulse generator and a known value of capacitance. While readying the detector for data taking, suitable thresholds were set to control the noise such that the data rate remain within the usable bandwidth. Some channels in both the modules had exceptionally high noise and were masked before starting the data-run. The chip has a provision to set different thresholds to different channels. However, as a general procedure, a common threshold was implemented to all the channels. Implementing channel by channel thresholds is a bit complicated task which involves in-situ unplugging the FEBs in the cave and

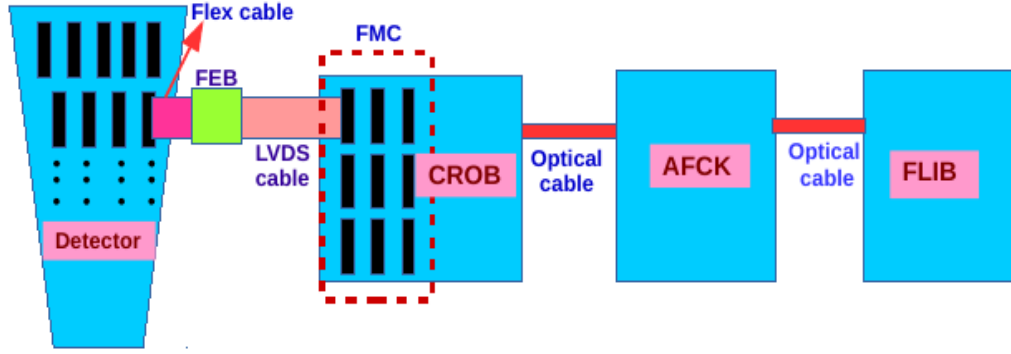


Figure 6.8: Schematic setup of the Data Acquisition System (DAQ) of the mCBM experiment.

re-calibrating the concerned channels. Based on the observed noise behavior of the chambers, the thresholds of the FEE boards were set to 6 fC, so that the noise rate stayed within the acceptable range of the usable bandwidth of the FEE boards. However, for a few boards in GEM2, a higher threshold had to be chosen.

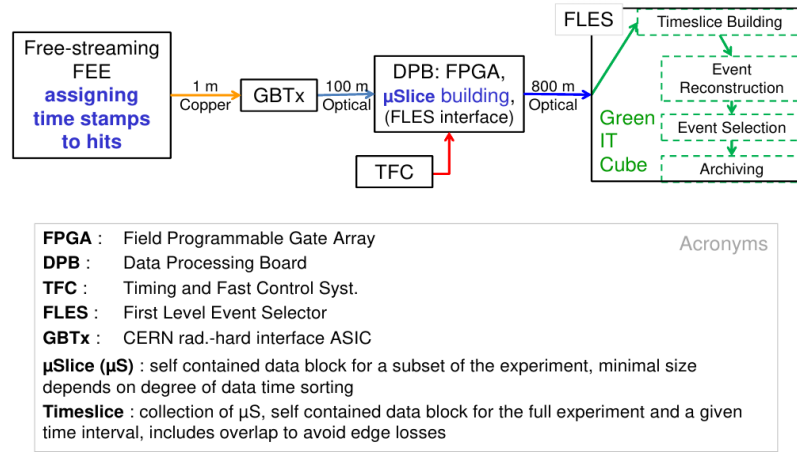


Figure 6.9: Schematic of data transport for CBM [15]

As per the CBM DAQ design, the digis from all the detectors were grouped in time within an interval of about 100 μ s at DPB. Each such time group is called a micro-slice (MS). The MS's from each DPB are then transferred to the FLIB⁶ PC where they are combined to build a time slice (TS) in the FLES⁷. The size of each TS is ~ 10 ms. The block diagram of data readout chain is shown in Figure 6.9. Raw data then are unpacked to the ROOT format as per the CBMROOT framework [179]. Every entry in the ROOT tree corresponds to 1 TS, and the entries inside each branch constitute the digitized signals from the individual subsystems.

⁶First Level Interface Board

⁷First Level Event Selector

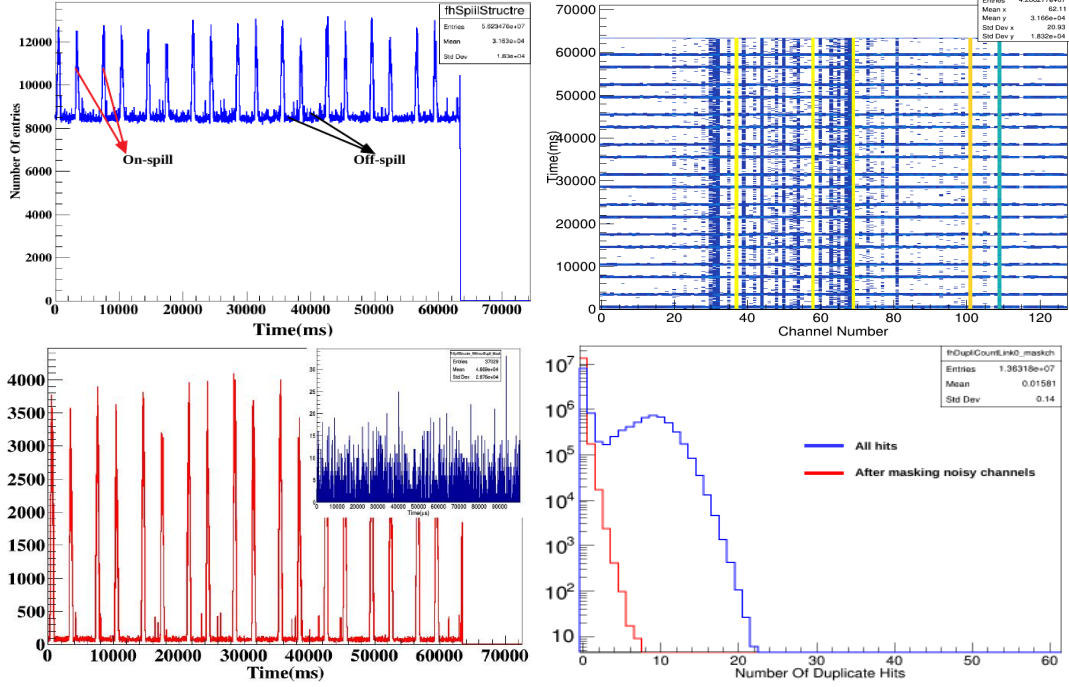


Figure 6.10: Top Left: Spill structure plot for all hits from one FEB (in 10 ms bins). Top Right: Variation of duplicate hits time with the channel number. Bottom Left: Spill structure after removing duplicate hits and noisy channels and the inset is for $1\mu\text{s}$ bin size. Bottom Right: Distribution of consecutive duplicate hits

6.5 Results from the mCBM test

6.5.1 Results using STS/MuCh-XYTER v2.0:

As discussed, in December 2018, the GEM detector took data with only one working FEB, which consists of 128 channels and covered an area of $\sim 42\text{ cm}^2$. Data were acquired for different HV settings. An ^{45+}Ag beam with varying intensity (10^5 sec^{-1} to 10^8 sec^{-1}) was incident on Au targets of thicknesses 2.5 mm and 0.25 mm. Data have been analyzed for a couple of runs. The spill structure or the distribution of hits with time (10 ms bin size), is shown in Figure 6.10 (top left). From the figure, we observe a spill length of $\sim 700\text{ ms}$ while two consecutive spills are separated by $\sim 2300\text{ ms}$ or $\sim 3400\text{ ms}$ as can be gathered from the figure. The spill structure seen to be riding on a constant background of ~ 8500 counts. A large number of hits or hit copies, bearing identical time-stamps and channel numbers were observed in the data due to a logic error in STS/MuCh-XYTER chip, as explained in section 6.2. A 2D plot of the hit time vs the channel number of these duplicates is shown in Figure 6.10 (top right). We observe that a few of the channels (mainly channel number 37, 58, 69, 101, 109) are highly noisy, while others give signal mainly during on-spill, as can be understood from the horizontal line. The hit rate in the spill

structure is high due to these noisy channels. With the help of off-spill data, such noisy channels were identified and were accordingly masked for further analysis. The duplicate hits come in groups and in each group there can be many of them. The distribution of these duplicate hits per group is shown in Figure 6.10 (bottom right). The blue histogram represents all hits, while the red one is after removing the noisy channels. These 5 noisy channels were the main source of duplicate hits as can be observed from the figure. The spill structure in 10 ms bin size, after filtering the duplicate hits and noisy channels, is shown in Figure 6.10 (bottom left). In the inset of this figure, a spill structure with a finer time-bin ($1\mu\text{s}$) is shown, which reveals the sub-structure in the beam.

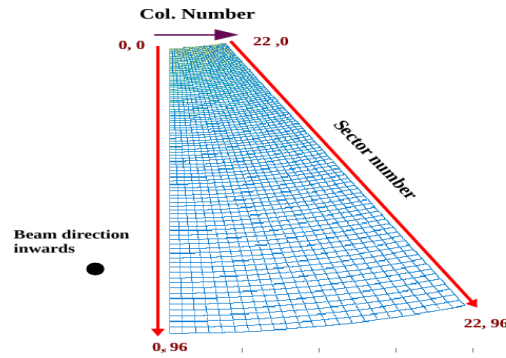


Figure 6.11: Schematic of detectors showing pads row and col. numbers

The schematic picture of the detector pads with row columns is shown in Figure 6.11. The sector number varies from 0 to 96 and column number varies from 0 to 22. A consecutive hit time distribution for many channels of GEM and fitted to an exponential function, as shown in Figure 6.12, gives an estimate of the incident particle rate on the detector. The average value thus calculated for all channels of the detector is shown in Figure 6.13. The rate values are normalized with the pad area. We have compared rates for the detector regions near and away from beam pipe, and also for two target thicknesses. The left column of the figure shows the variation of rate with sector number for 0.25 mm and 2.5 mm target thickness, respectively. We can observe that the rates with 2.5 mm target thickness are a factor of ~ 2.5 higher than with 0.25 mm. The right column of the figure shows the same variation for the near side (Col. 1) and away side (Col. 22) columns with respect to the beam axis. The rates are observed to be higher for the near-side case as expected.

The average particle rate was also calculated using the distribution of number of Digi/TS as shown in the left panel of Figure 6.14. The two peaks observed in the plots correspond to off-spill and on-spill data as indicated. The fitted mean values of these two peaks were extracted for all

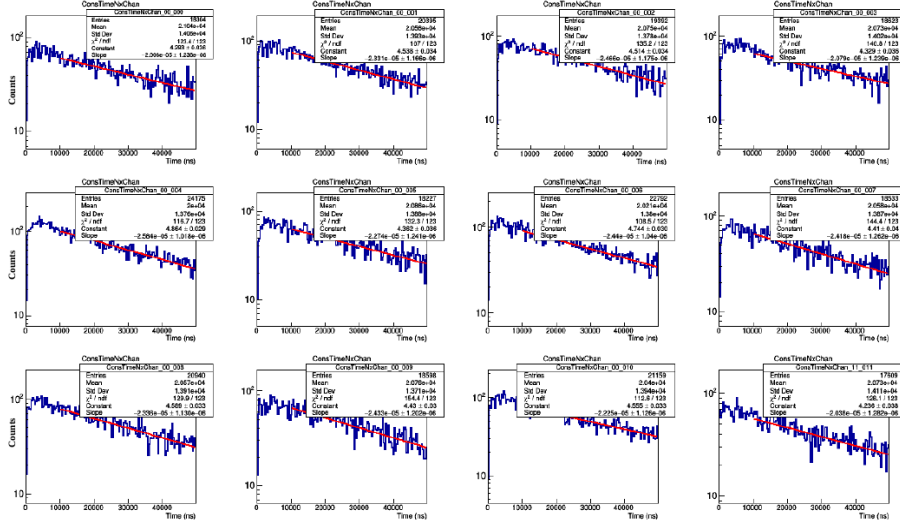


Figure 6.12: Consecutive time difference spectra for several channels of GEM1. It is fitted with exponential function to extract the slope and finally the average rate.

cases. After subtracting the background, estimated from the off-spill data, the average rate was thus calculated.

The effect of the beam intensity on the particle rate is summarized in the Table 6.2. We expect that the particle rate should be correlated with the beam intensity (or interaction rate). The masked noisy channels affect the detector acceptance and in turn affect the measured rates. The FEB configurations for the runs considered were identical. About 90% of the noisy channels identified for each runs were same. The ratio of measured rates matches closely to the ratio of beam intensities. This indicates the proportional response. 1-D distribution of the number of Digi/TS for run numbers 162, 163, 165 and 166 are shown in Figure 6.15.

Table 6.2: Effect of beam intensity on average hit rate.

Run No.	HV(V)	Target Thickness (mm)	Beam Intensity (ions/sec)	Intensity Ratio	Average Rate (kHz)	Rate Ratio
162	4700	0.25	7×10^6	~ 4.29	377.4	~ 4.43
165	4700	0.25	30×10^6		1673.5	
163	4700	2.5	7×10^6	~ 4.29	1438.5	~ 4.17
166	4700	2.5	30×10^6		5964.3	

The effect of target thickness on particle rate was also studied, which is summarized in Table 6.3. For a given beam intensity, the change in rates is observed to be a factor of about 3.8. FLUKA simulation was performed [17] (refer to Figure D.1) and the average particle rate ratio was calculated, which matches closely with the data. Ideally, we expect a factor 10 increase in

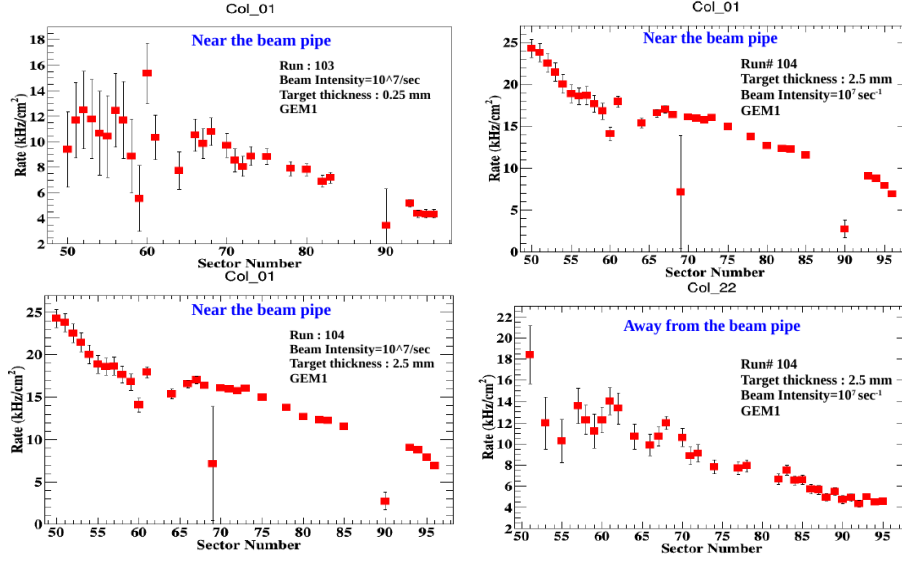


Figure 6.13: Left: Variation of signal rate per unit area with sector number of pads for near (top-left) the beam pipe and away (bottom-left) from the beam pipe. Right: Variation of signal rate per unit area with sector number of pads for 0.25 mm (top-right) and 2.5 mm (top-right) target thickness.

particle rate if target thickness is changed from 0.25 mm to 2.5 mm. The dominating factor for this observed number (factor of 3.8) is due to the absorption of produced delta rays in 2.5 mm target.

Table 6.3: Effect of target thickness on average hit rate

Run No.	HV(V)	Target Thickness (mm)	Beam Intensity (ions/sec)	Average Rate (kHz)	Rate Ratio
159	4800	0.25	2×10^5	31.2	~ 3.87
160	4800	2.5	2×10^5	120.5	
162	4700	0.25	7×10^6	377.4	~ 3.81
163	4700	2.5	7×10^6	1438.5	
165	4700	0.25	3×10^7	1673.5	~ 3.56
166	4700	2.5	3×10^7	5964.3	

The data from different subsystems are grouped in TS as explained above. The number of Digi in a TS from one detector subsystem should be correlated with others. This correlation between GEM1 & T0 and between GEM1 & GEM2 for beam intensity of 2×10^5 is shown in top panel of Figure 6.16. We observe a nice correlation as expected. However, for higher beam intensity, this correlation can be affected due to high particle rates falling on the detector. The Digi correlation at high intensity (3×10^7) is shown at the bottom panel of Figure 6.16. We can observe from the

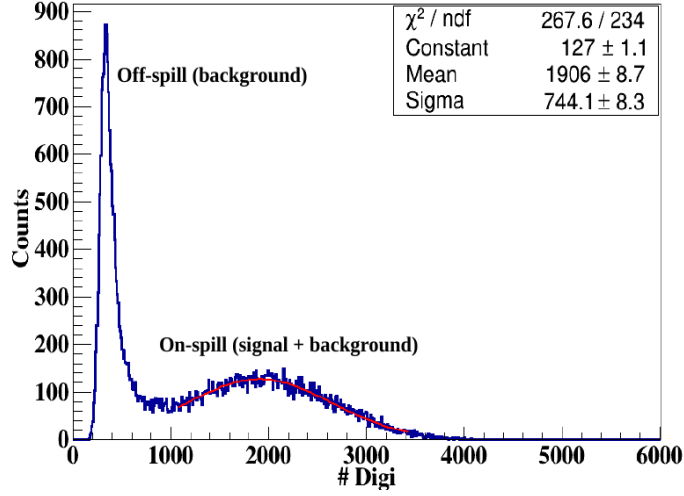


Figure 6.14: Distribution of number of digis/TS for GEM1. Average signal and noise rate are calculated using this.

bottom-left figure that, the T0 detector lost linearity and starts to saturate after a certain number of digis (about 170×10^3). But, the linearity in GEM1 and GEM2 correlation is not affected by this high intensity. This demonstrates the good operation of the GEM detector at high beam intensity. The interaction rates will be of the order of few tens of MHz for these high intensity data, which is larger than the expected interaction rate in the final CBM experiment. However, the beam energy is lower in case of mCBM as compared to main CBM.

6.5.2 Results using STS/MuCh-XYTER, v2.1

We report here results from the data taken in November and December 2019 with ^{40}Ar beam colliding on an Au-target of 2.5 mm thickness at an intensity of $\sim 5 \times 10^6$ per spill. The data were taken with the latest version of STS/MuCh-XYTER, i.e., v2.1. A preliminary CBM data analysis chain based on the CbmRoot software framework [179] has been applied to the data comprising unpacking, including individual time-offset corrections for the detector subsystems (digis), a event building by a timestamp cluster search for the first time and hit reconstruction for the detector subsystems. Using the digis as well as the hits, a dedicated analysis procedure was used to extract the mMuCh performance. This includes correlation study with other detectors. The results discussed in this section correspond mainly to a detector gain of $\sim 3.1 \times 10^3$. The schematics of the experimental setup are described in section 6.3.

The typical distribution of signal counts from the GEM1 detector in time-bins (10 ms), is shown in the left panel of Figure 6.17. The first hit time has been taken to be zero for reference. The

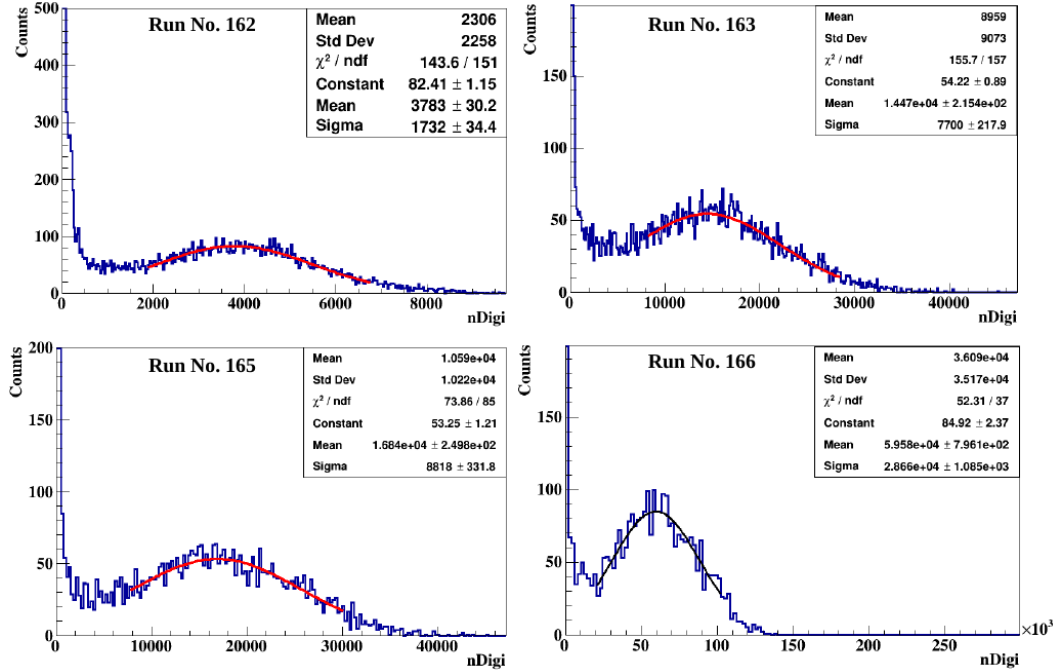


Figure 6.15: Distribution of number of Digi per TS for run numbers 162, 163, 165 and 166.

incident beam is in the form of spills, as displayed by the distribution of T0 counts. The raw counts from GEM1 are shown in the green histogram. One notices that this distribution does not display a proper spill structure. This is because of the significant noise contribution, which is dominant in both on-spill as well as off-spill regions as can be seen in the figure. An offline investigation of the off-spill data revealed that a few channels in some of the FEBs produced high noise, as can be seen from the count rate distribution for one FEB of GEM1 in Figure 6.17 (right). With the help of off-spill data, such noisy channels were identified in all ASICs (FEBs) and were accordingly masked for further analysis as per general procedure. The signal-count distribution for GEM1 (red), GEM2 (blue), after removing noisy channels, reveals the spill structure. They are now observed to be well correlated with those of T0, as expected. The residual count still remaining in the off-spill region is indicative of the noise rate and is observed to vary from one FEB to another FEB. Also, a higher noise level for GEM2 was observed as compared to that of GEM1. However, these are of much lower counts than the counts in the on-spill region. The extracted spill length of the beam is about ~ 7 s, with off-spill lengths of ~ 7 s and ~ 12 s, (due to parallel user operation at SIS18 beam-line) as can be noticed in Figure 6.17, left side.

Variation of ADC for the different electronic channels in the off-spill (left) and on-spill (right) case is shown in Figure 6.18 for the same number of TS (1100). In the off-spill case, we only see a few populations of digis, but in the case of on-spill, we observe a full ADC range filled with digis

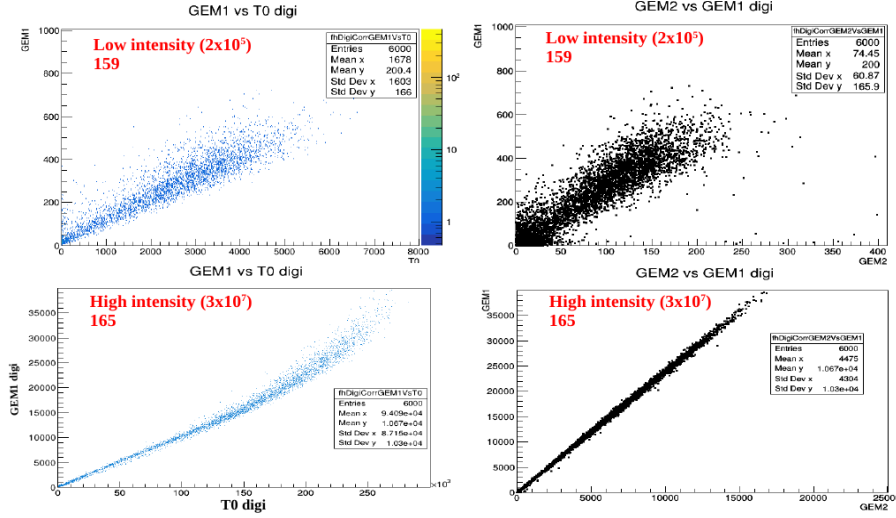


Figure 6.16: Digi correlation in time slice between T0 digi and GEM1 digi in a time slice. Top left panel is between GEM1 and T0 for low intensity, while bottom left is for high intensity. Top right panel is between GEM1 and GEM2 for low intensity, while bottom right is for high intensity

due to particles produced by the collisions. This display plots are useful during online monitoring of data quality.

Table 6.4: Table for noise for different detector slot numbers

Detector Slot Number	Noise Rate (Hz)	Detector Slot Number	Noise Rate (Hz)
0	0.5	10	70.6
1	0.8	11	41.3
2	1.8	12	17.2
3	1.9	13	70.8
4	3.5	14	16.4
5	2.3	15	65.2
7	9.1	16	21.7
8	5.8	17	10.7
9	50.5		

Noise Rate

The noise rate of each FEBs were measured using off-spill data. The total number of signals are counted for about 8000 TS. The schematic of FEB numbering for Mv2 module is shown in the left panel of Figure 6.19. Noise rate (Hz) with detector slot number is shown the right panel of same figure, and also given in Table 6.4. It is observed that for larger pad size, the noise rate is high but it is within 100 Hz.

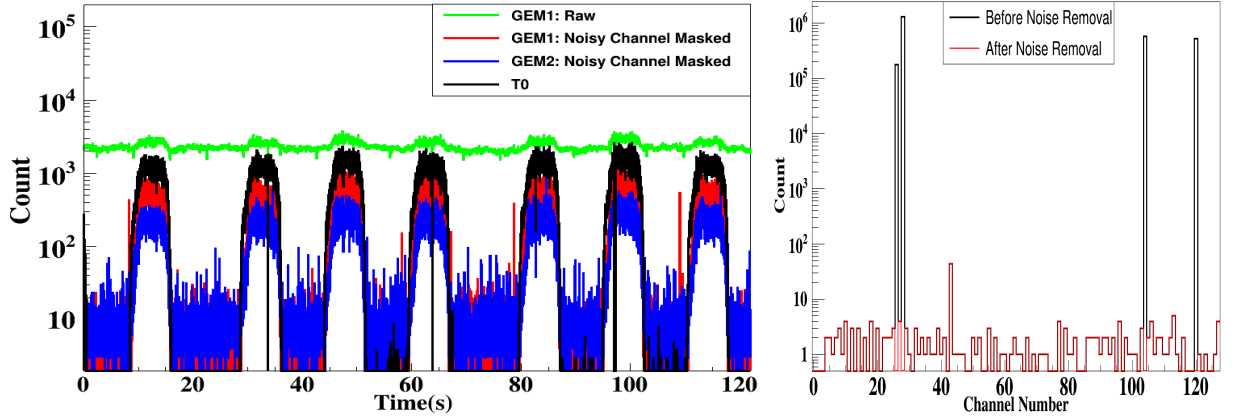


Figure 6.17: Left: Variation of digi counts with time, spill structure, for GEM1-raw (green), GEM1/GEM2 - noise subtracted and T0. Right: Channel hit distribution for one of the FEB's in beam-off condition. Black corresponds to the raw channel count, and red is after masking noisy channels. Only a few channels are found to be noisy.

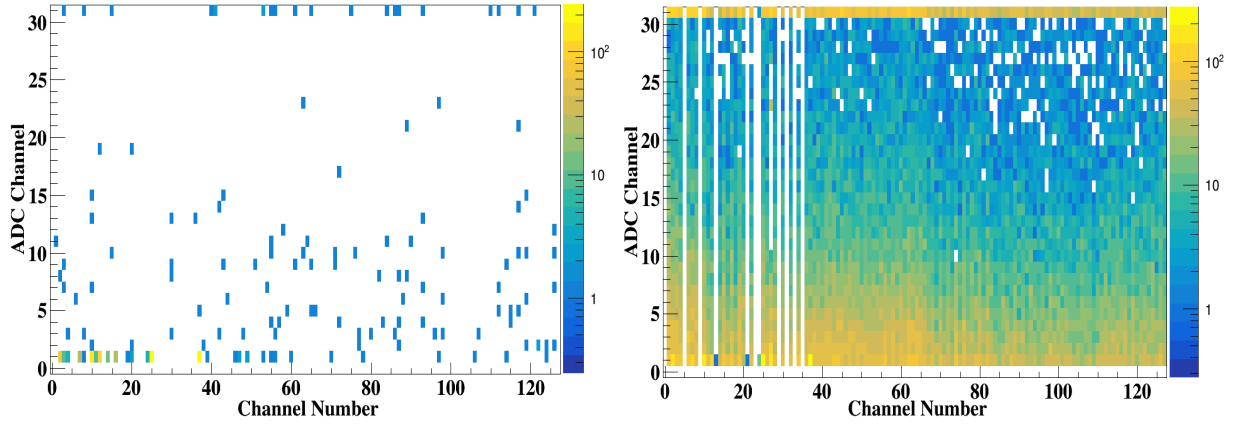


Figure 6.18: Variation of ADC with the channel, off-spill (left) and on-spill (right), for GEM1 for 1100 time slices.

As it is mentioned, the data were collected in 10 ms Time-Slice (TS) intervals. The distribution of the number of digis per TS for the two GEM modules and T0 is shown in Figure 6.20 (left). This includes counts in the off-spill region as well, which being relatively much lower, show-up in the form of a peak at values around 10-30 Digi/TS for the GEM modules, while the peaks on the higher side of the spectra are due to signals from the on-spill data. A difference between these two peaks provides the average number of digis/TS for any detector, corresponding to the particular operating conditions at which the data were taken. The on-spill peak for GEM2 is lower than that of GEM1 because of its lower acceptance owing to the smaller number of working FEBs. The correlations in terms of the number of digis per TS between T0 & GEM1 and between GEM1 & GEM2 are shown in the middle panel of the same figure.

Each collision occurs at a particular time, hence the digis from different detector subsystems

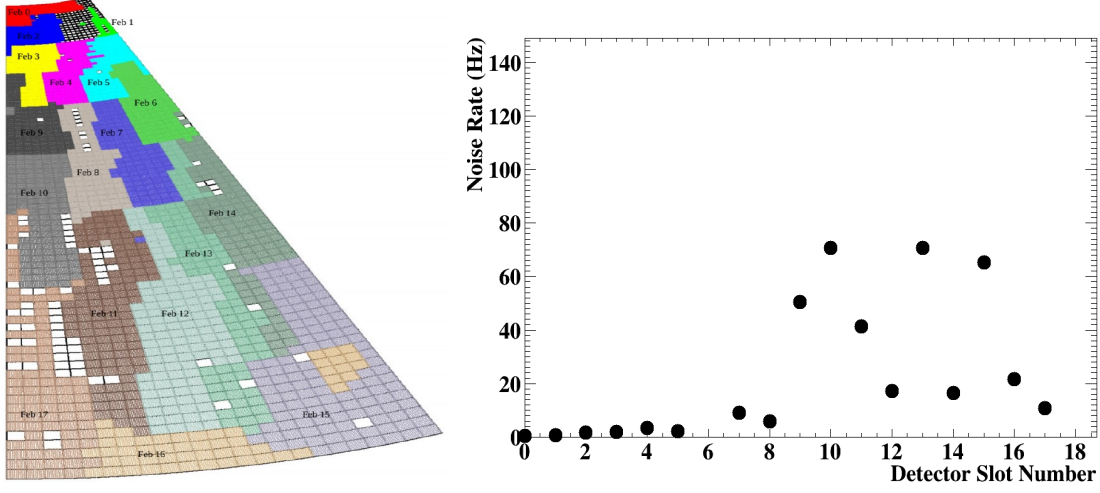


Figure 6.19: Left: Schematic of FEB numbering (detector slot number) for Mv2 module. Right: Variation of noise rate with detector slot number.

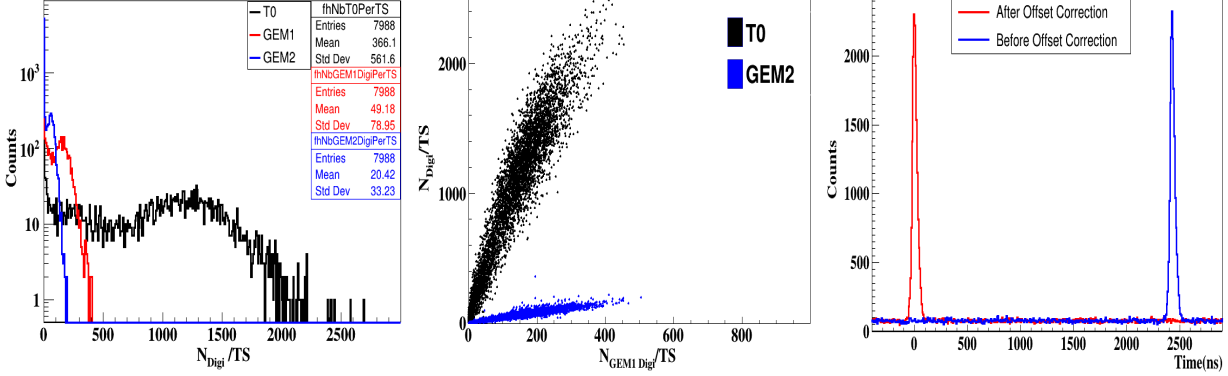


Figure 6.20: Left: Distribution of the number of digis per time-slice (Digi/TS) for GEM1 (red), GEM2 (blue) and T0 (black). Middle: Variation of the number of T0 Digi/TS with GEM1 Digi/TS (red) and the number of GEM2 Digi/TS with GEM1 Digi (blue). Right: Time difference distribution between one FEB of GEM1 with T0 before (blue) and after (red) offset correction (see text).

should be correlated in time. This is revealed from the time difference spectra shown in Figure 6.20 (right, blue) where, within every TS interval, the time difference distribution between the digis from a FEB of GEM1 and that of T0 has been plotted. This histogram represents a typical time-correlation spectra. The mean position of this distribution (~ 2500 ns) represents the offset for the particular FEB, which varies from one FEB to another. Synchronizing all the hits from different FEBs becomes thus crucial for a proper data analysis. In this direction, all time-offsets corrections need to be appropriately determined. The offset-value is subtracted from the timestamps of each digi for the corresponding FEB, such that the resulting time-corrected distribution now peaks at zero, as per construction (represented by the red curve in Figure 6.20). Such offset corrections

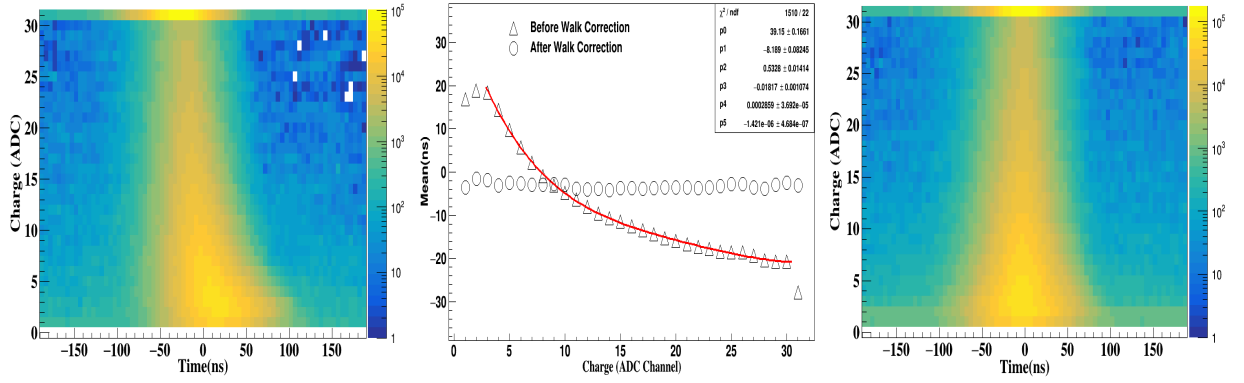


Figure 6.21: Left: Variation of the time difference between signals in GEM1 and one of the TOF modules (super module 0) with pulse height (in ADC unit) of GEM1. Middle: Variation of the mean (ns) of the time difference spectra with ADC before (upper triangle) and after (open circle) time-walk correction. The raw values are parameterized using a polynomial fit. Right: Variation of the time difference between GEM1 and one of TOF counter for different ADC values after time-walk correction.

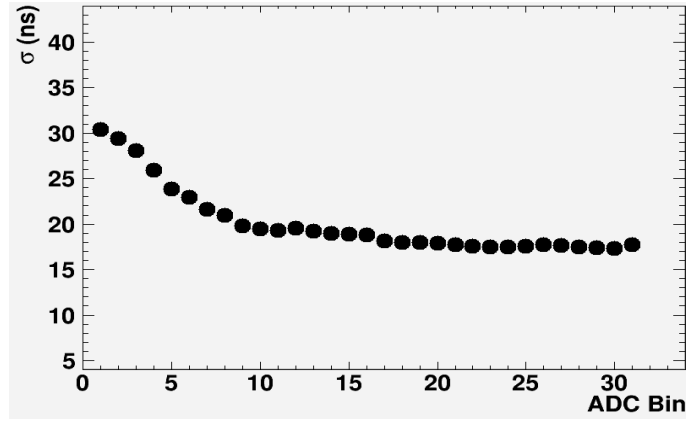


Figure 6.22: Variation of σ with ADC bin. σ improves for higher charge signal as expected.

were applied for all subsystems separately.

The time correlation spectra for all the FEBs were individually obtained. The mean position, which represents the time offset, was extracted using Gaussian fit. The time stamp for all channels of all the FEBs were accordingly corrected. By implementing these FEB-to-FEB corrections on the entire data set, we have made an effort to bring all the digis in synchronization with those from T0 for further analysis. However, there could still be time-walk effects [141] on the signal timing due to varying signal strength, as can be seen from the time difference vs. ADC plot for GEM1 in Figure 6.21 (left). The variation of the time difference peak position (ns) for the corresponding ADC bin is shown in Figure 6.21 (middle). It has been fitted with a polynomial to find a parametric equation for the time-walk correction. The resulting variation of the time-difference with time-walk corrected ADC values is shown in Figure 6.21 (right). Variation of σ for

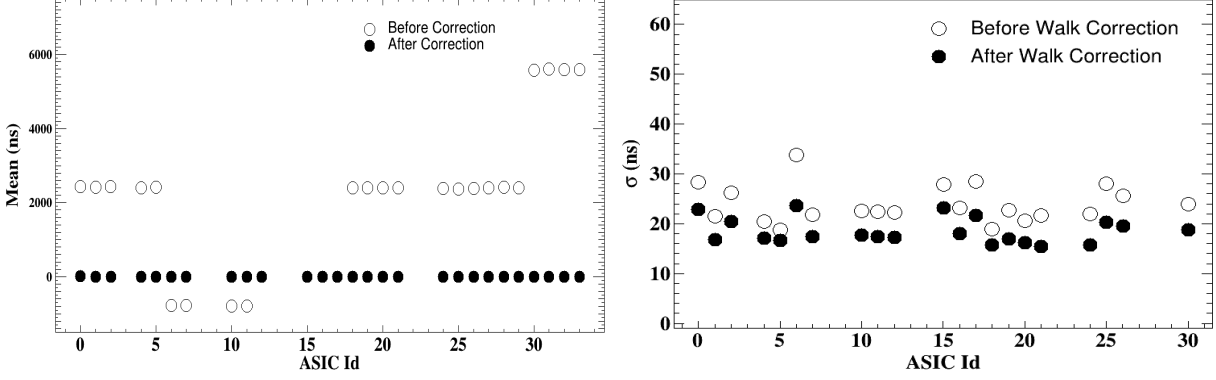


Figure 6.23: Left: Variation of the mean position (nano seconds) of time difference spectra for each ASIC before (open circle) and after (close circle) offset correction. Mean positions for a few ASICs are not shown here due to large offset value (which is in several μs). Right: The variation of σ with ASIC number before (open circle) and after (close circle) time-walk correction. The ASIC Id for GEM1 is from 0 to 23, while those beyond belong to GEM2.

different ADC values is shown in Figure 6.22. It is observed that the σ improves for high charge signal as expected.

The mean offset values for every FEB are now well peaked at around zero, by construction, as depicted in Figure 6.23 (left). The offset-values for different FEBs (represented by ASIC Id on the X-axis) are denoted by open circles. For a few FEBs, these offsets were very high (in several μs) and exceeded the scale of the plot. Eventually, all these offsets could be corrected (full circles). The width of the time difference spectra provides the time resolution of the detector. The sigma (σ) of this distribution for both before and after the time-walk correction is shown in Figure 6.23 (right). Accordingly, the time-walk correction improves the time resolution by about 6-7 ns.

A deeper look at the detector uniformity has been carried out at the level of individual pads/channels. The time mean and sigma of roughly 3000 channels (including GEM1 and GEM2) was measured from the data and the variation of this is shown in Figure 6.24. The 2-D plot displays graphically the time resolutions (after time-walk correction) of about 1400 channels of GEM1 in Figure 6.25 (left). The variation in time resolution is of the order of ~ 4 -5 ns from the mean value, which can be seen from the width of the 1-D distribution of σ (right panel of Figure 6.25).

The 2-D scatter plot of the mean ADC channel for those many channels is shown in Figure 6.26 (left). This tells about the variation of the gain at different regions of the detector. The 1-D projection of the mean ADC is shown the right panel of the same figure. From the scanned set of about 1400 channels, we observe a maximum variation in gain over full active area of about 14%.

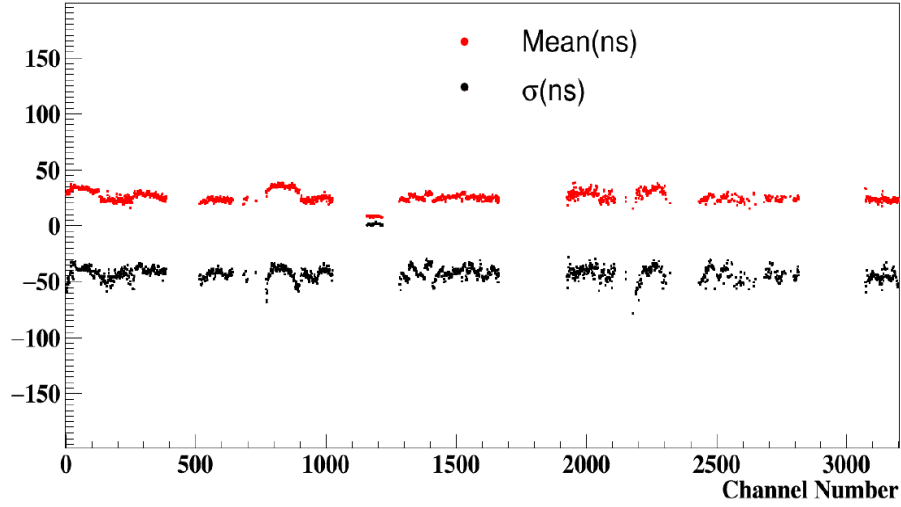


Figure 6.24: Mean and sigma of time correlation spectra of roughly 3000 channels measured from data.

6.6 Event building

We used December 2019 data for this analysis. In a self-triggered system, event reconstruction is a challenging task. Using the timestamps of the signals from the readout, there can be several algorithms of building events by suitably grouping together the recorded digis in time. A schematic of event building algorithm is shown in the left panel of Figure 6.27. The raw data contains digis from every subsystem in a time slice (TS). All the digis from different detectors are combined together as shown in the figure. As a first attempt in this direction, we have used a time window of 200 ns to group the digis together along with a condition of having a minimum of one T0 and six TOF counts in this time window. The typical time resolutions of the detector and the low beam rate guided the choice of this rather large time window of 200 ns. All the MuCh digis inside this time window along with the T0 and TOF hits, are clubbed together to form an event. Then the following time window of 200 ns and satisfying the same hits-criteria forms the second event, and so on. The optimization of event window was studied and is shown in Figure 6.27 (right panel). We can observe that for the time window of about 100 ns and greater than that, the number of reconstructed event is almost same. We have chosen a time window of 200 ns for our analysis.

The top and middle panel of Figure 6.29 depicts the variation of the number of T0 digi and the number of event reconstructed as a function of TS number, respectively. As expected, no events are reconstructed in the off-spill region, clearly due to criteria of minimum number of T0 and TOF counts. The number of incident beam particles varies from spill to spill, correspondingly changing

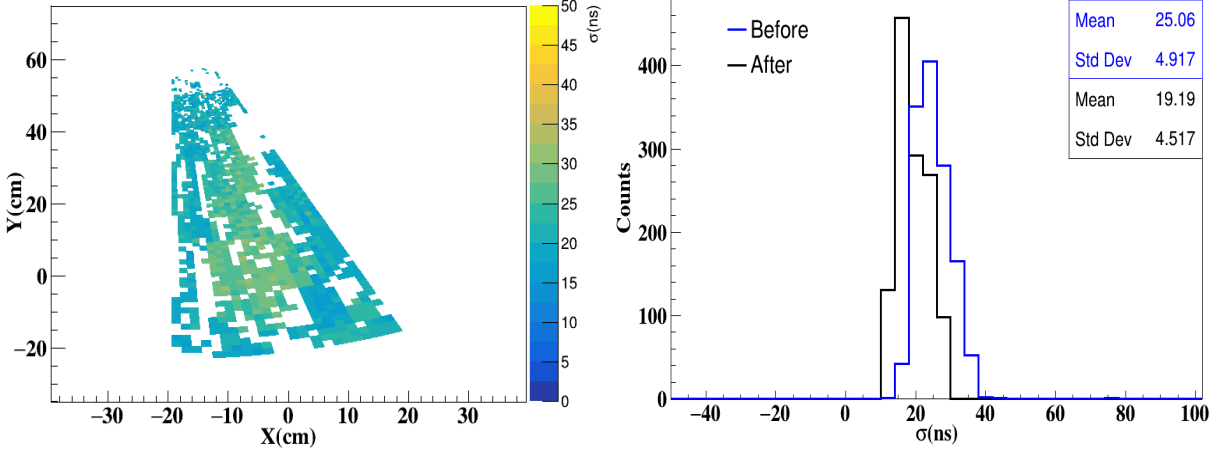


Figure 6.25: Left: Time resolution map on GEM1 plane. The z-axis is the σ (ns) of each pad. Right: 1-D distribution of time resolution for all the pads before (Blue) and after (Black) time-walk correction.

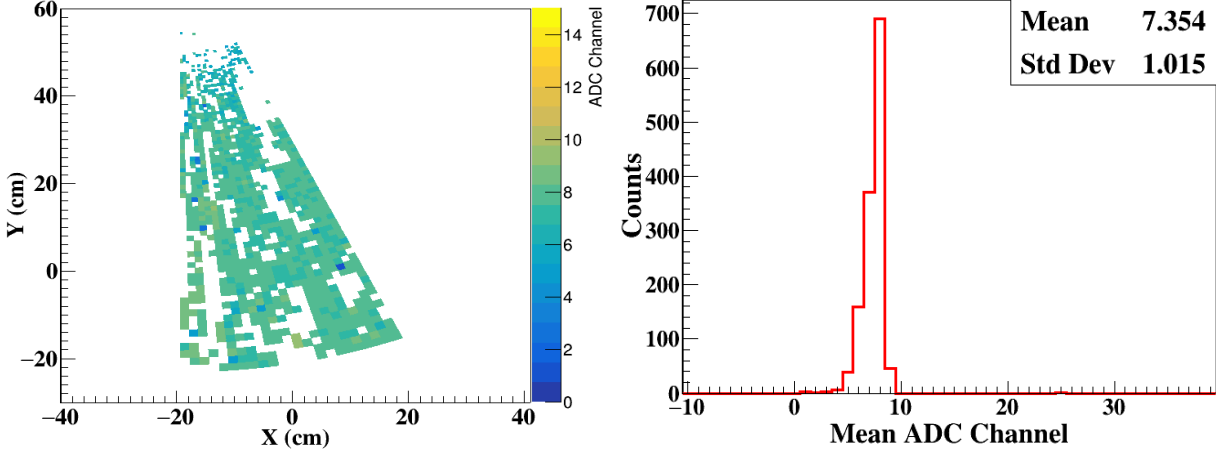


Figure 6.26: Left: 2D scatter plot of mean ADC for each channels. The third axis is the ADC channel. Right: 1-D projection of mean ADC channel.

the number of events reconstructed, as can be gathered from this plot. The ratio of number of events to the number of digi in a TS with TS number is shown in the bottom panel of same figure. Since there are hardly any events reconstructed in the off-spill region, the ratio plot in this region shows no entry. In addition to this, for this ratio plot, to avoid large statistical fluctuations at the spill boundaries, we have considered only those TS's in which the $N_{T0Digi}/TS \geq 10$. A projected 1-D histogram of this ratio is shown in the left panel of Figure 6.29, which conveys an average value of this ratio to be around 0.07, indicating a 7% interaction rate. This is in very good agreement (within 1%) with what one obtains by simple rate calculations using the given beam parameters, the target type, its thickness, and its interaction cross-section. The distribution of number of events reconstructed in each TS is shown in the right panel of same figure. On an average 96

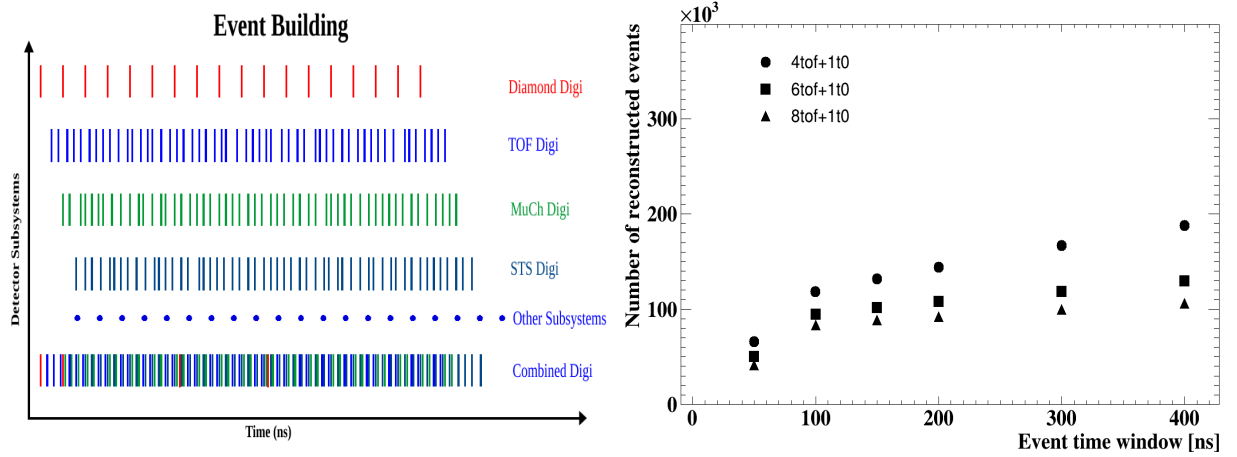


Figure 6.27: Left: Schematic of event reconstruction algorithm. Right: Variation of number of event reconstructed with the event time window at different selection condition.

events are reconstructed in a TS of size 10 ms. This tells that the event rate for this case is of the order of about 10 kHz.

The number of digis within a reconstructed event referred to as event size, varies event by event. The distribution of the total number of digis per event is shown in Figure 6.30, the average of which depends upon the number of subsystems, its configuration, active number of channels, their setting parameters, and the event time-window, among other things. If one looks at the time difference spectra between the first and the last digis, within every reconstructed event, we get distribution as shown in Figure 6.30 (right). The small rise at the tail is purely an artifact of the reconstruction using the time-window technique, whereby in some cases, a noise just before the real event may trigger the start of the time window, and a small portion of the event may sneak in close to the window-boundary. This would lead to a rise in the number of digis at the time-window boundaries.

As mentioned, the algorithm of event reconstruction is still evolving. One of the most straightforward quality checks for any algorithm would be to study the T0 distribution event by event. Since each time window satisfying the hit-criteria ideally should represent one collision, the number of T0 digis per event should also be typically average around “1”. This is revealed in Figure 6.31 (left), where the average number of T0 digis per reconstructed event comes out to be about 1.1, thus deviating from expected average by only 10%.

Event reconstruction was followed by cluster finding and hit reconstruction in the MuCh modules. Each particle track that produces a signal in the detector may affect one or more pads (digis), forming a cluster. The nearest neighbour algorithm was used to club together the digis in an event

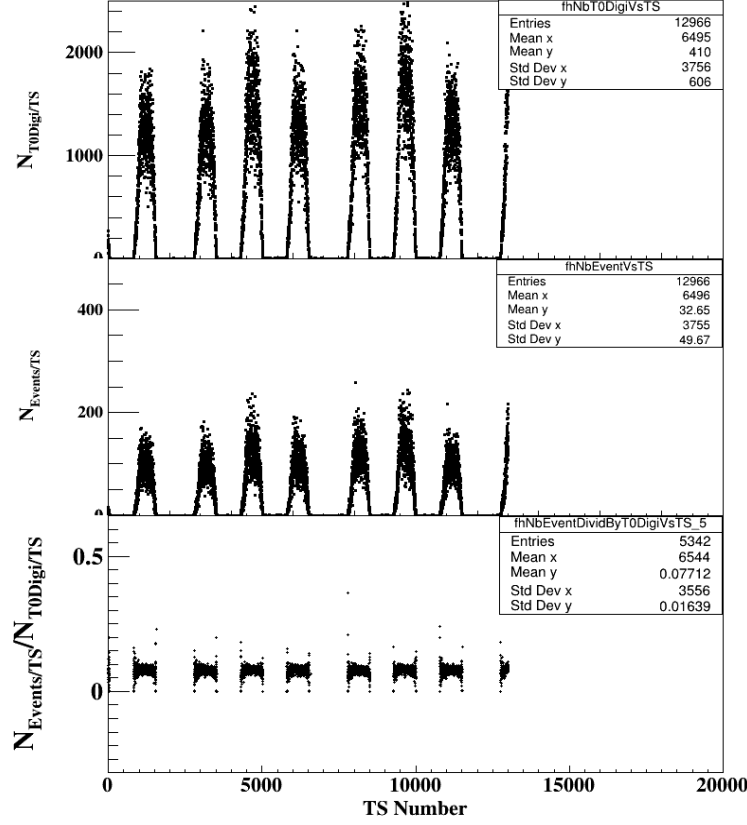


Figure 6.28: Variation of the number of T0 digi (top) and number of events reconstructed (middle) with TS number. The variation of the ratio of the number of reconstructed events to the number of T0 Digi/TS with TS (bottom).

forming a cluster. Large contiguous clusters were later split further based on the local maxima found within the clusters, thus forming “Hits”. The middle part of the figure systematically shows the distributions of the number of digis per event, the number of clusters per event, and finally, the number of “Hits” per event for GEM1. The average hit of about 1.4 is observed, which is lower than that observed in simulation (refer section 3.1). This could be because of the selection criteria of TOF and T0 digis used in event building. An average hit of about 2 is observed for event selection condition of 1 T0 and 8 TOF digis within time window of 200 ns. Large clusters are found at $\sim 1\%$ level, and as a result of this cluster splitting, the distribution of “Hits” is observed to be marginally wider than that for clusters. The time correlation of the GEM1 “Hits” with T0 digis within an event is shown in Figure 6.32 (left) and that for GEM2 is shown in the right panel of same figure. During “Hit” reconstruction, the algorithm chooses the smallest time of the digi within the cluster. Hence the width of this time-correlation spectra is slightly smaller than that in Figure 6.25 (right). The measured time resolution values at mCBM are quite close to what has been measured using single-particle beams in [173]. The width of the time correlation spectra

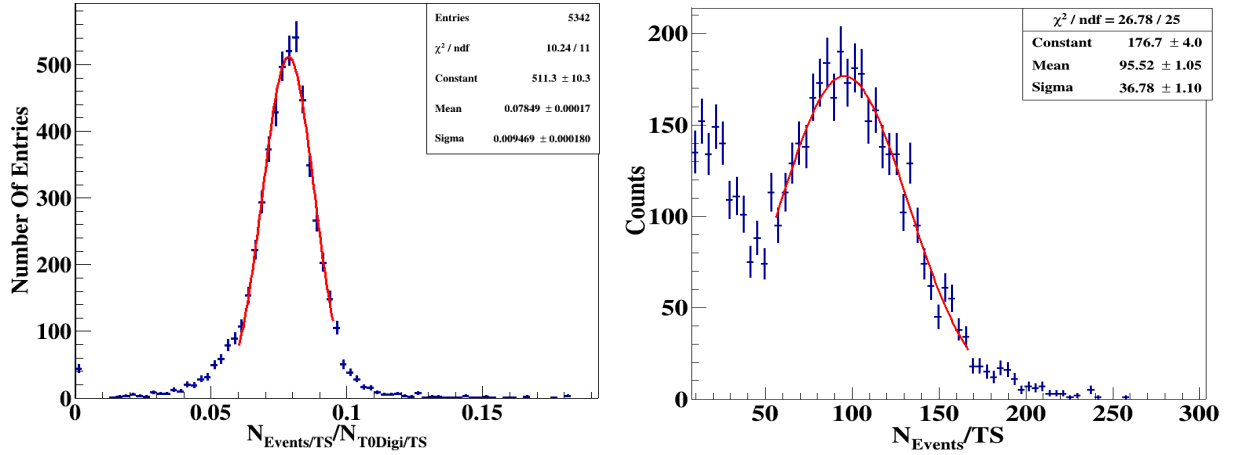


Figure 6.29: Left: 1-D distribution of the ratio of the number of reconstructed events to the number of T0 Digi/TS. Right: Distribution of the number events reconstructed per TS.

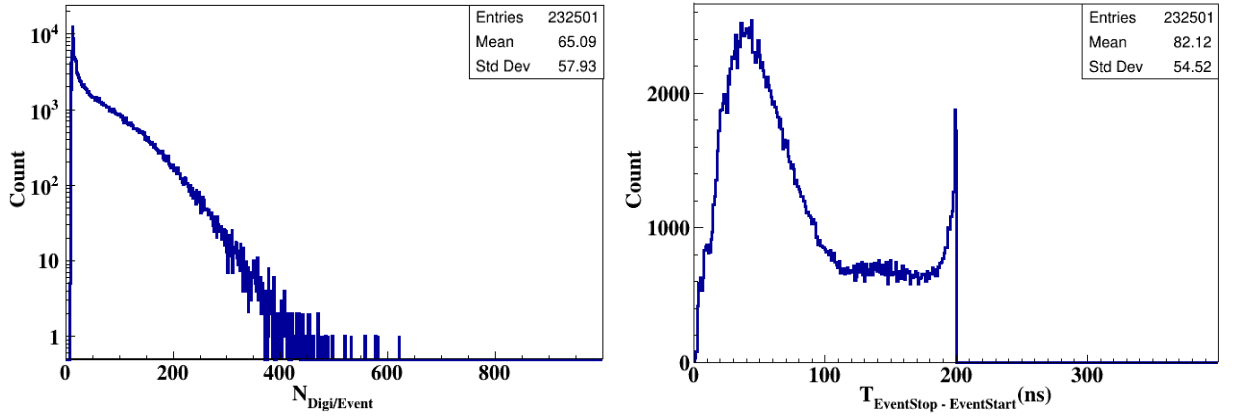


Figure 6.30: Distribution of the event-size (number of Digi/event) (left) and time separation between the last Digi to the first Digi in the event (right).

would play a crucial role in determining the time window of the event reconstruction algorithm, particularly when operating at high rates.

The X (cm) - Y (cm) distribution of hits for GEM1 (left) and GEM2 (right) are shown in Figure 6.33, revealing the detector acceptance. The blank spaces mostly correspond to the dead areas mainly due to non-working FEBs and also due to the masked noisy pads in the detector.

Figure 6.34 describes the cluster characteristics for the hits in GEM1. The left panel shows the typical cluster size distribution for GEM1 at an operating GEM voltage of $\Delta V_{\text{GEM}}(\text{sum}) \sim 1072 \text{ V}$. The corresponding distribution of the cluster charge (fC) for the entire GEM1 cluster is shown in the middle panel. Since we have used 5-bit ADCs, considerable charge falls in the overflow bin (31 ADC channel), hence we see a spike at $\sim 82 \text{ fC}$. Similar nature of the cluster charge (fC) distribution has also been seen in response simulations (GEANT). The cluster charge spectra are

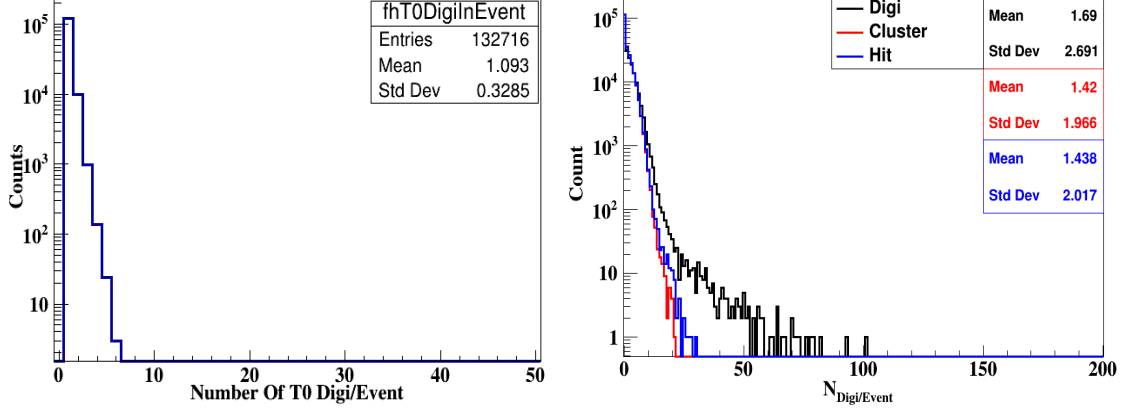


Figure 6.31: Left: Distribution of the number of T0 Digi / event. Middle: Distribution of the number of Digi (black), Cluster (red) and Hits (blue) per event. Right: Time difference distribution between the hits of GEM1 with that of T0 digi in the event.

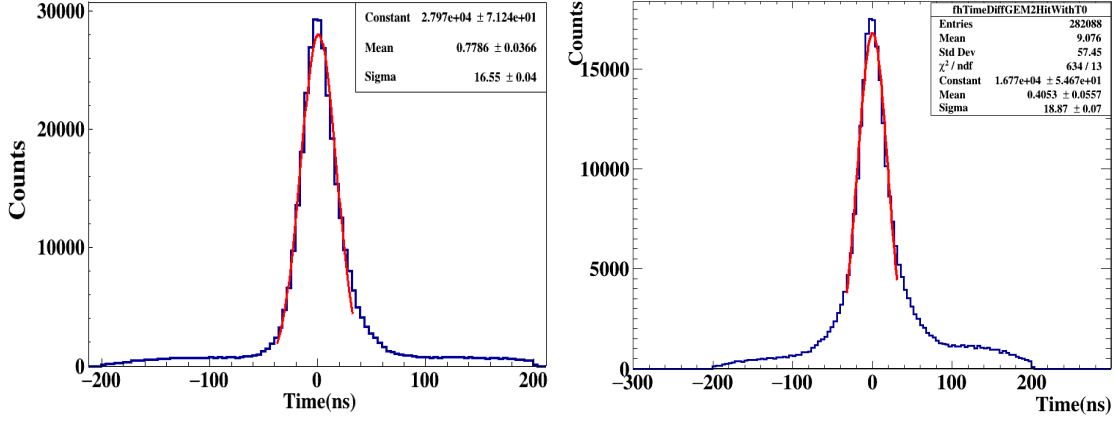


Figure 6.32: Time difference distribution between the hits of GEM1 with that of T0 digi (left panel) and between the hits of GEM2 with that of T0 digi (right panel) in the event.

fitted with a Landau distribution, thus giving an MPV of ~ 15 fC. The gain of the detector has been calculated using this MPV value. The gain at a summed GEM voltage ~ 1072 V is estimated to be about 3.1×10^3 . The gain of small size prototype ($10 \text{ cm} \times 10 \text{ cm}$) using the same electronics and similar setting parameters was measured using with cosmic muons in the lab. The detector gain in the lab and in the mCBM matches closely with variation of about 5%.

Within a reconstructed cluster, the distribution of the time-difference of all the digis with respect to the first digi in time is shown in Figure 6.34 (right). The RMS of this plot gives an idea about the time-spread between the digis of a MuCh cluster. It is observed that in more than 90% of times, the separation is located within 50 ns. This information will be used for optimizing the time separation between clusters related to the 4D tracking in CBM. The distribution of cluster charge (in ADC unit) for the clusters with single digi (right panel) and with all digis (left panel) is shown Figure 6.35. The MPV for single digi cluster is lower compared to that of all clusters, as

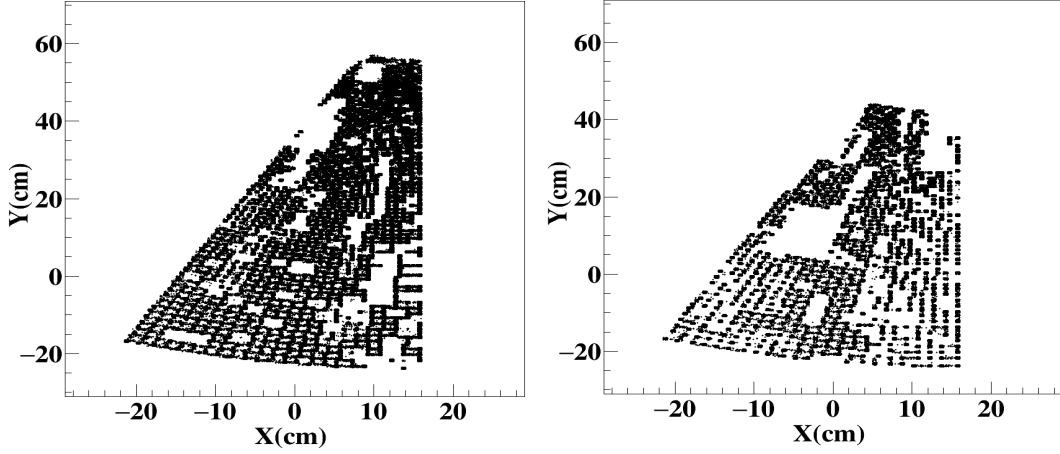


Figure 6.33: X (cm)-Y (cm) distribution of hits for GEM1 (left) and GEM2 (right) after hit reconstruction

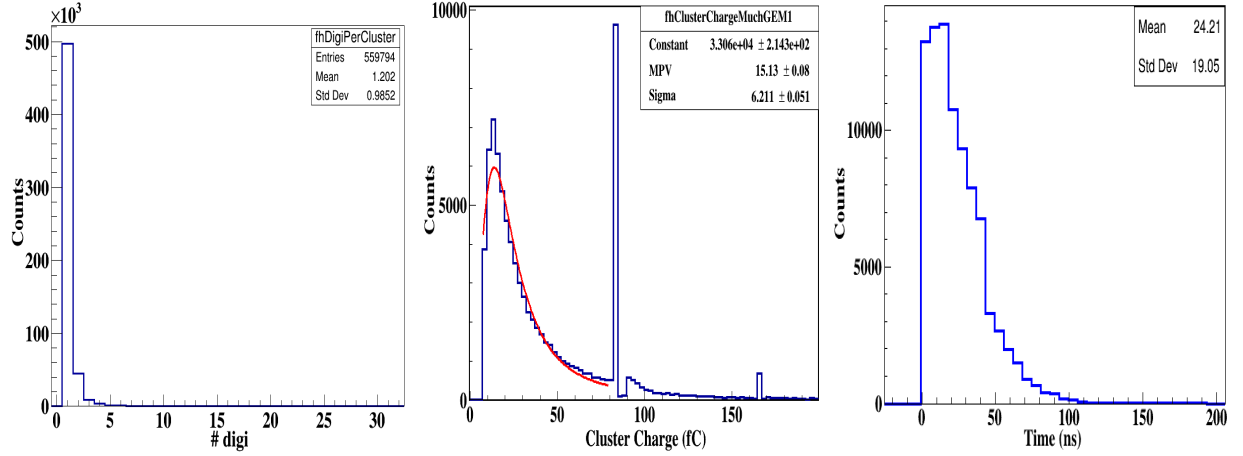


Figure 6.34: Left: Cluster size distribution for the entire GEM1 plane. Middle: Cluster charge (ADC) distribution for GEM1. The distribution is fitted with a Landau distribution. Right: Time separation of digis within clusters. The standard deviation yields to ~ 19 ns.

it is expected.

The relative gain of the detector was measured at various positions on the detector plane, as shown in Figure 6.36 (left). Each position number represents a specific zone in the detector, which is displayed in the right panel of the same figure. The gain distribution is observed to be uniform at the level of $\sim 15\%$. The readout plane has pads of varying granularity. We have also measured the cluster size distribution for different regions of the detector. The variation of the average cluster size for different granularity zones is shown in Figure 6.37. Statistical errors are included and they are within the marker size. Further contributions due to noise, thresholds, fluctuations in gain, etc., are not taken into account. The different regions are indicated by numerals, and the adjoining table in the middle indicates the corresponding granularity. The right panel of same figures shows

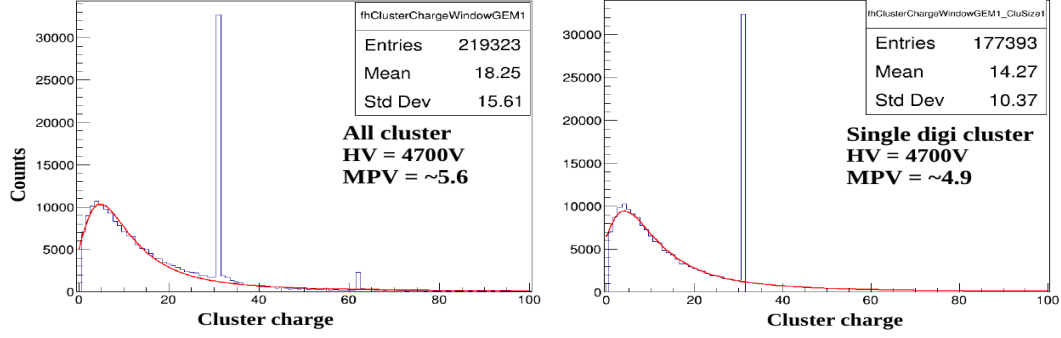


Figure 6.35: Cluster charge (ADC unit) distribution for all clusters (left panel) and for the cluster with single digi (right panel).

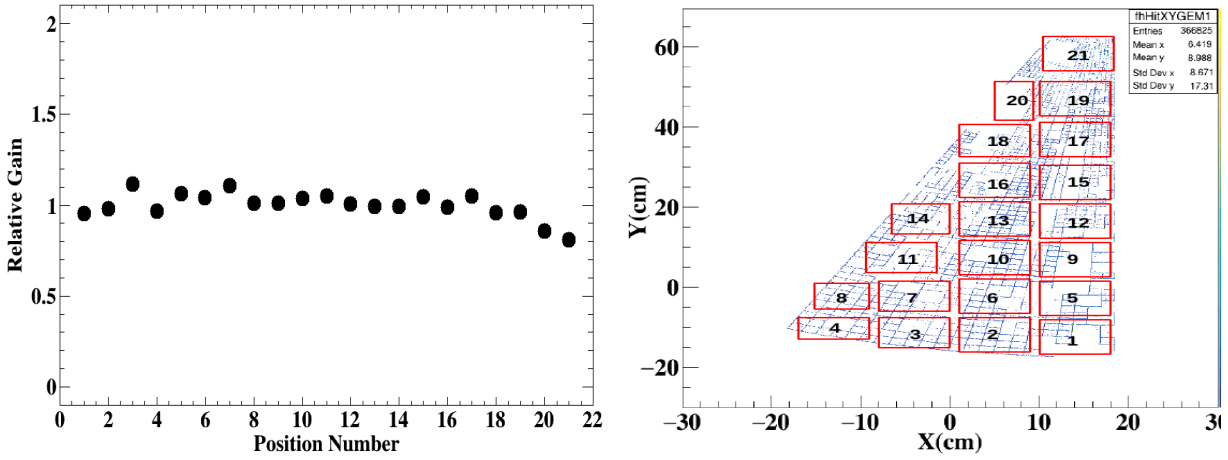


Figure 6.36: Left: Variation of relative regions of detector. Statistical error bars are within the marker size. Right: The schematic of different regions.

the zone numbering schematic. The corresponding values obtained from GEANT simulations using the mCBM environment and realistic GEM module configurations are also overlaid, and the two values are found to match closely within 10%. However, a time based simulation, which is underway, will compare the results in a more realistic way.

Detector characteristics have been studied as a function of the applied GEM voltages. The first among these is the variation of detector gain with the GEM voltage. As shown in Figure 6.38, the gain increases exponentially with increasing voltage, as expected. The variation of time resolution with voltage is shown in the right panel of same figure. It is observed to saturate around ~ 15 ns. The errors (statistical) on the data points in both the panels are within the marker size. The variation of the cluster size with voltage is shown in Figure 6.39 (left). The slight increase, which is also observed in simulation, is due to the increase of gain at higher voltages. The variation of the average number of hits per event is shown in Figure 6.39 (right). The curve shows a rising trend, indicative of the effect due to increased efficiency at higher GEM voltages.

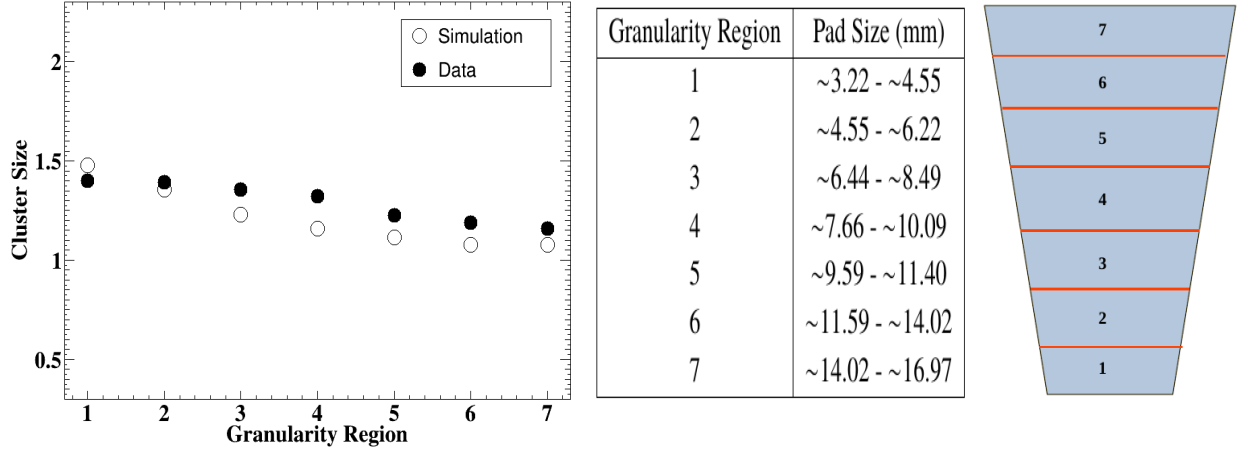


Figure 6.37: Left: Variation of cluster size at different granularity regions. Statistical error bars are within the marker size. Right: Table for granularity regions and their respective pad sizes.

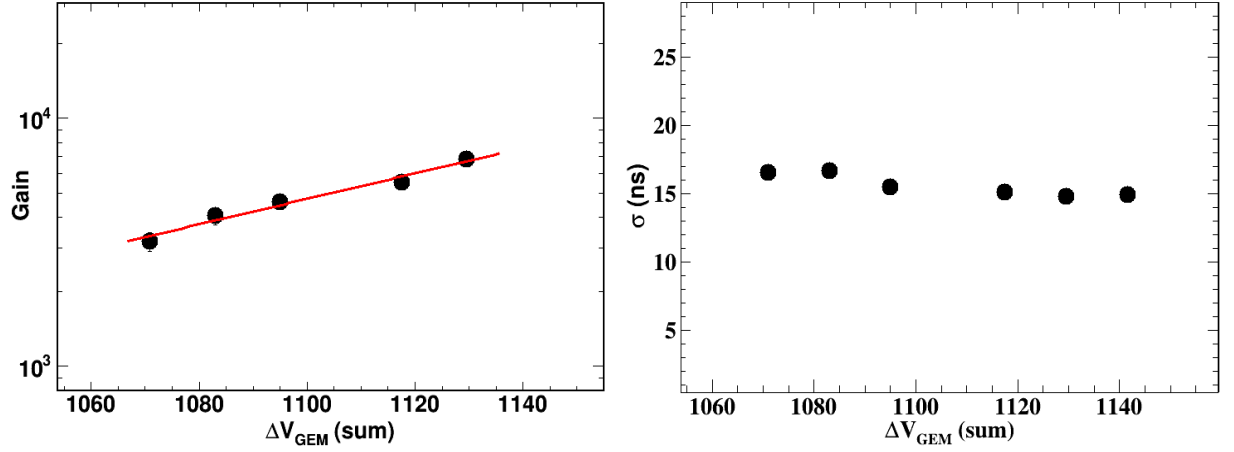


Figure 6.38: Variation of cluster size with voltage (left). Variation of average Hit/event with GEM voltage. Statistical error bars are within the marker size.

6.7 Spatial correlation and track reconstruction

Using the hits registered on the different detector planes within the events reconstructed as per procedure described in the above section, we try to investigate the spatial correlation and track reconstruction.

Figure 6.40 displays the spatial correlation in X and Y between GEM1 and GEM2. The extent of the correlation line observed in both X and Y matches with the observations of the 2D-Hits plot of Figure 6.33. A clear correlation is also seen between GEM1 and TOF, as shown in Figure 6.41. It must be stated here that it is only after event reconstruction that the correlation lines are clearly visible, otherwise at the TS level in a time interval of 10 ms, it gets smeared due to cross-correlation between events. While conveying an effective event reconstruction, these

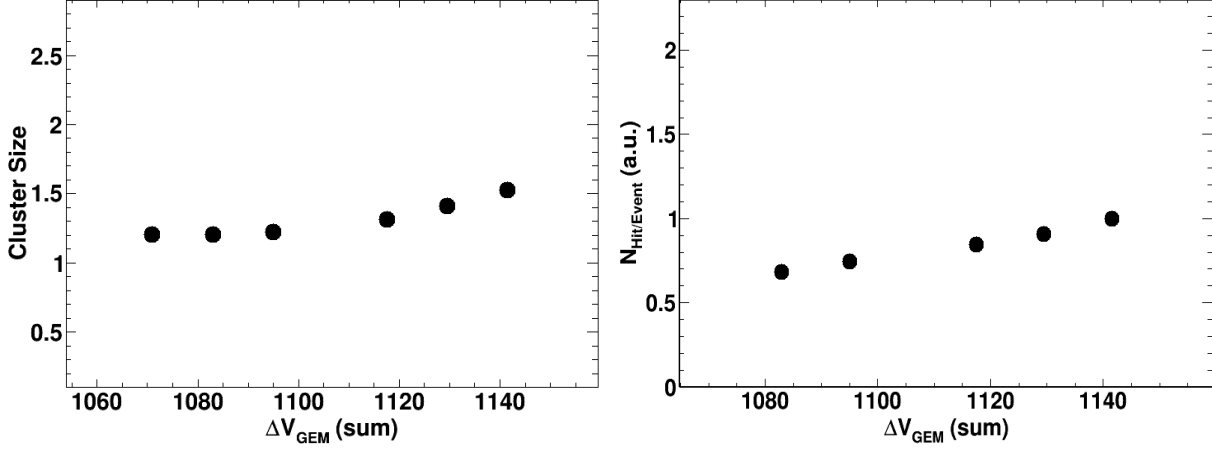


Figure 6.39: The variation of gain (left) and time resolution (right) of the detector with the GEM voltages. Statistical error bars are within the marker size.

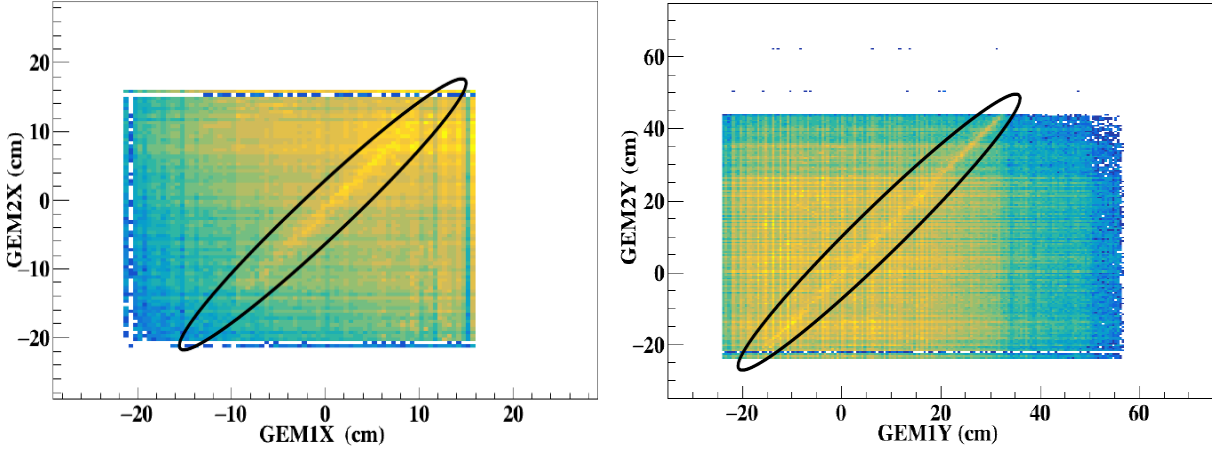


Figure 6.40: Spatial correlation in X (cm) and Y (cm) between GEM1 and GEM2 hits

spatial correlation plots also clearly demonstrate the time-synchronous behavior of two different detectors, or, for that matter, even two different subsystems employing entirely different detector technologies and readout electronics. The region of common acceptance is highlighted in the elliptical ring. This represents the first such observed spatial correlation between the two GEM modules & also between the GEM and TOF detectors in mCBM data. The spatial correlation was also studied in simulation by implementing identical detector configuration in CBMROOT and we observed nice correlations between GEM modules and between GEM and TOF modules.

Track reconstruction A straight line track-fitting has been carried out using hits on the TOF planes and on the GEM detectors. An event display showing track passing through different detector layers is shown in Figure 6.42. The parametric equation of line in 3-D is given by:

$$x = a + b \times z \quad (6.1)$$

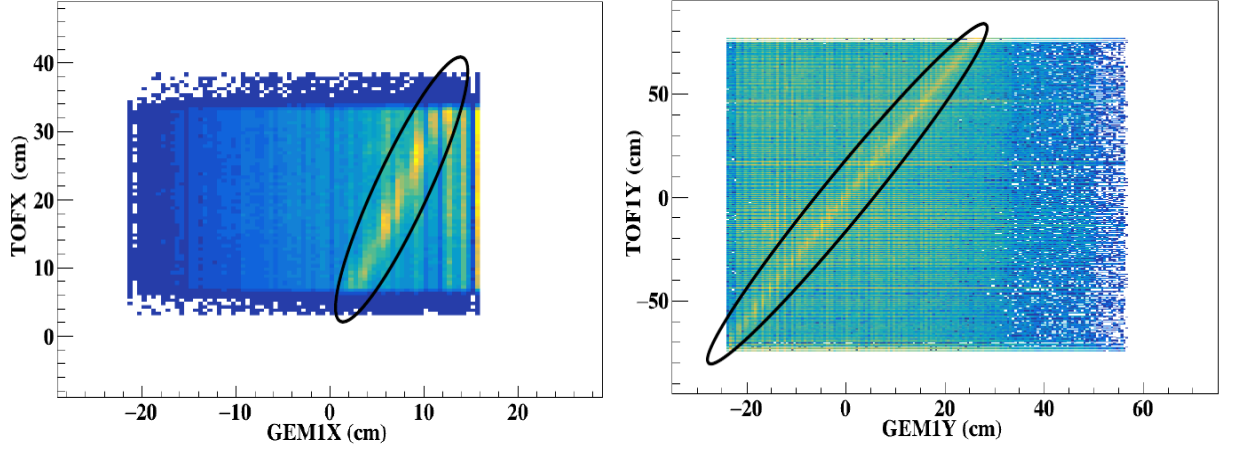


Figure 6.41: Spatial correlation in X (cm) and Y (cm) between GEM1 and TOF hits.

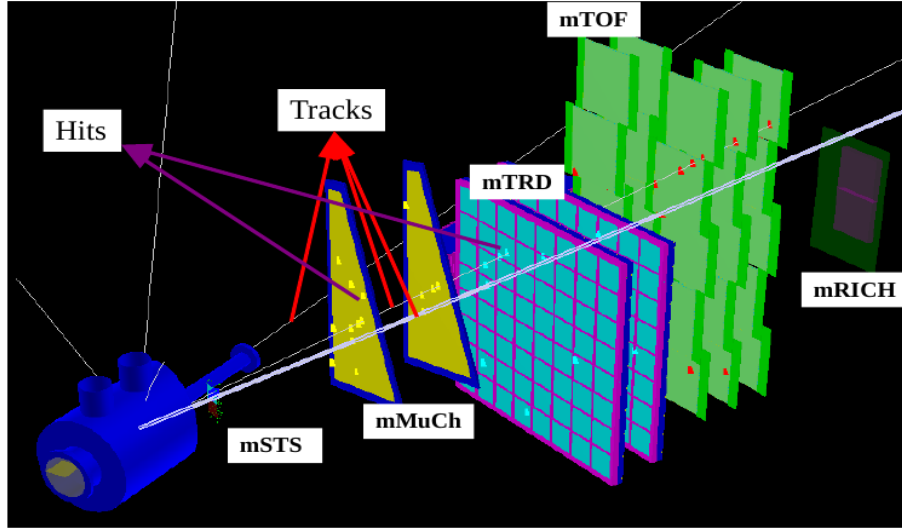


Figure 6.42: Schematic picture of track fitting

$$y = c + d \times z \quad (6.2)$$

where a , b , c , d are fit parameters. These parameters are calculated by minimizing χ^2 as:

$$\chi^2 = \sum_{i=0}^N \frac{(x_i - a - b \times z_i)^2}{\sigma_{x_i}^2} + \frac{(y_i - c - d \times z_i)^2}{\sigma_{y_i}^2} \quad (6.3)$$

where N is the number of detector stations. σ_{x_i} and σ_{y_i} are the measurement errors in x and y , respectively. x_i , y_i and z_i are the position coordinates of the hits.

To start with, we first construct a track using hits in the three planes of TOF and extrapolate it to the $z=0$ plane. The distribution of the extrapolated coordinates in X and Y at the origin showed shifts from $(0,0)$, indicating misalignment of the detectors. A shift of ~ 8 cm in X and ~ 1.5 cm

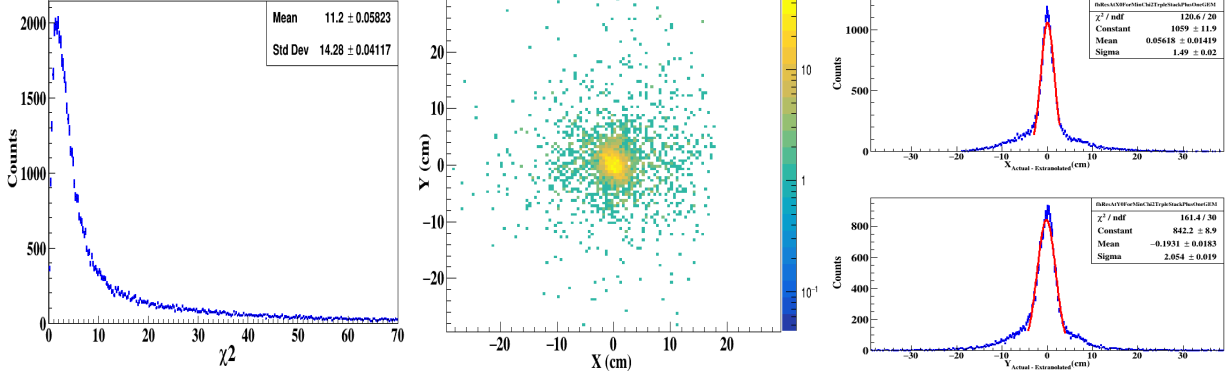


Figure 6.43: Left: χ^2 distribution of track reconstructed using 3 TOF plane and GEM1 plane. Middle: The extrapolated Y (cm) vs X (cm) of the tracks at $z=0$ plane. Right: Residuals in X (cm) and Y (cm) at vertex ($z=0$).

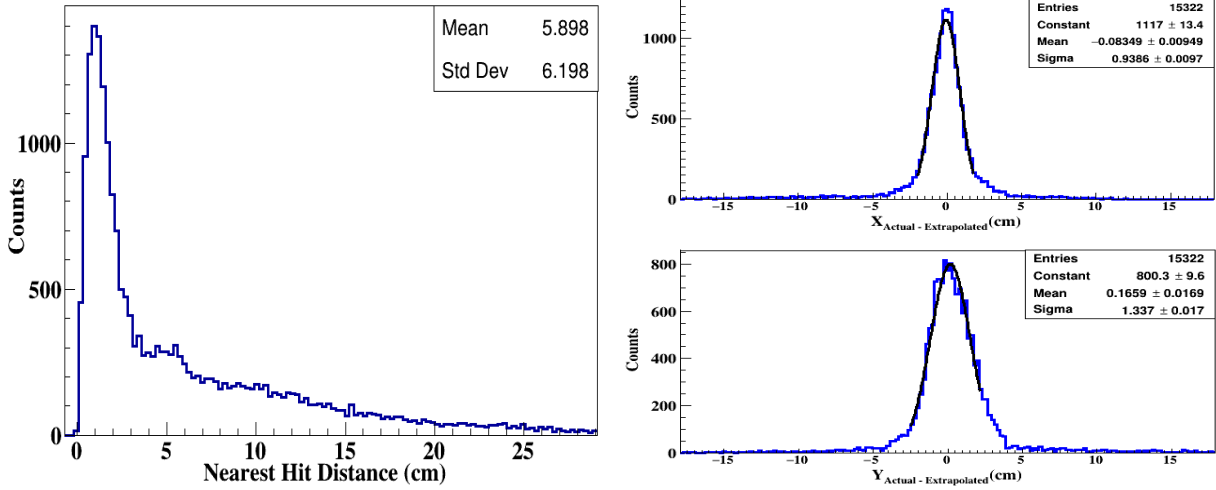
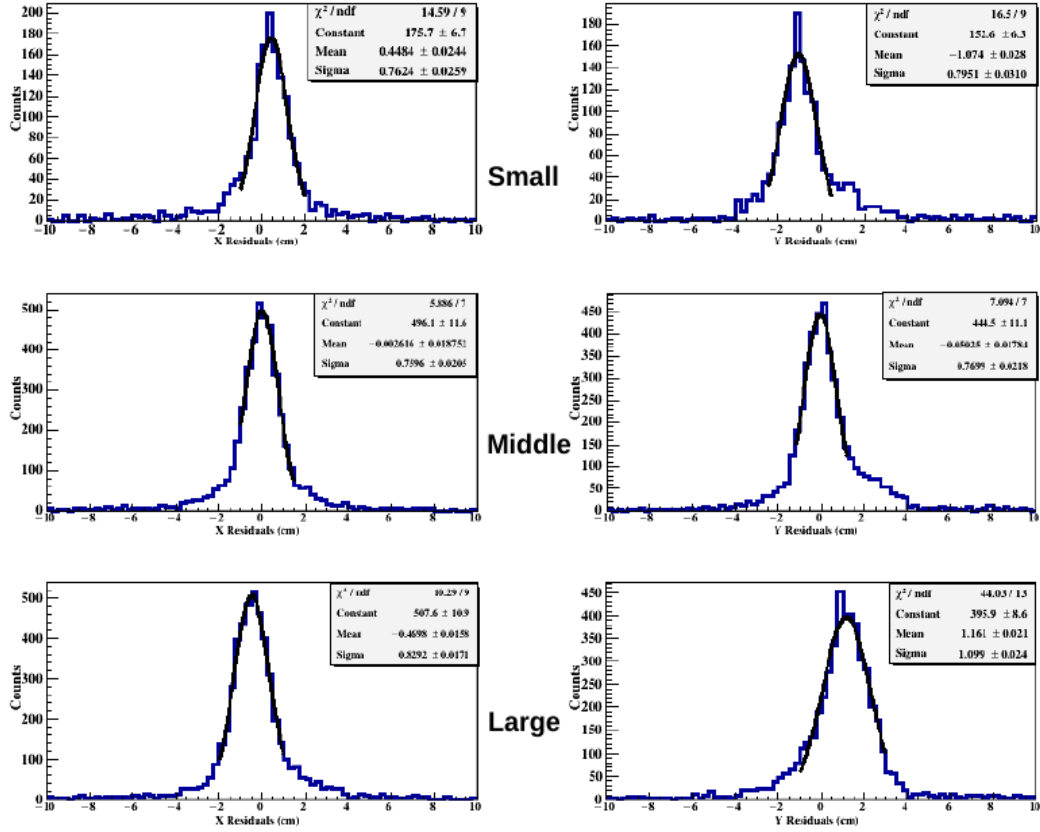


Figure 6.44: Track reconstructed using hits from 3 TOF planes and vertex ($z=0$). The distance between the nearest hit to the extrapolated track on GEM1 plane (left). Right: Residuals in X (cm) and Y (cm) at GEM1 plane with ~ 4 cm cut on distance.

in Y were observed. Similarly, we reconstructed tracks using the three TOF planes and the origin and extrapolated them to the GEM planes. We observed a shift of ~ 2.9 cm in X and ~ 6 cm in Y for the GEM detectors. Plugging in these spatial offset values, we implement corresponding translations in TOF and GEM hit coordinates and redo the tracking. The χ^2 distribution of the tracks using TOF and GEM1 after misalignment implementation is shown in Figure 6.43 (left) and the extrapolated X-Y distribution at $z=0$ plane, on the (middle) panel, centering at (0,0), thus validating the offset correction procedure. The residuals in X (cm) and Y (cm) at $z=0$ plane with $\sigma_x \sim 1.5$ cm and $\sigma_y \sim 2$ cm are shown in Figure 6.43 (right).

After this misalignment correction exercise, the tracks were then constructed using the TOF planes and the vertex ($z=0$) to measure the track resolution at the GEM plane. The distance



Small --> ~9.9 mm to ~12.9 mm, Middle --> ~13.2 mm to ~15.3 mm, Large --> ~15.5 mm to ~17.0 mm

Figure 6.45: Residual distribution at different granularities of GEM detector.

between extrapolated hits with the nearest hits on the GEM plane is calculated, and the distribution is shown in Figure 6.44 (left). Most of the hits are separated by less than ~5 cm. The residuals or the distribution of the difference between the extrapolated coordinates and the actual hit-coordinates in X (cm) and Y (cm) on the GEM1 plane is shown in Figure 6.44 (right). The distribution peaks around zero as expected and have a sigma of 0.92 cm and 1.3 cm in X and Y, respectively, thus giving us an estimate of the overall average spatial resolution of the detector. These numbers are slightly lower than that observed in simulation (refer section 3.1.3). As the granularity changes from small to large, we divided the entire area into three different regions, indicated as “small” (pad size ~9.9 mm to ~12.9 mm), “medium” (pad size ~12.9 mm to ~15.3 mm) and “large” (pad size ~15.0 mm to ~17.0 mm), and measured the track residuals for each region. This is shown in Figure 6.45. From the residual distributions we observe a sigma of 0.8 cm, 0.78 cm, 0.98 cm, in X and 0.86 cm, 0.81 cm, 1.5 cm in Y, for small, medium and large regions, respectively.

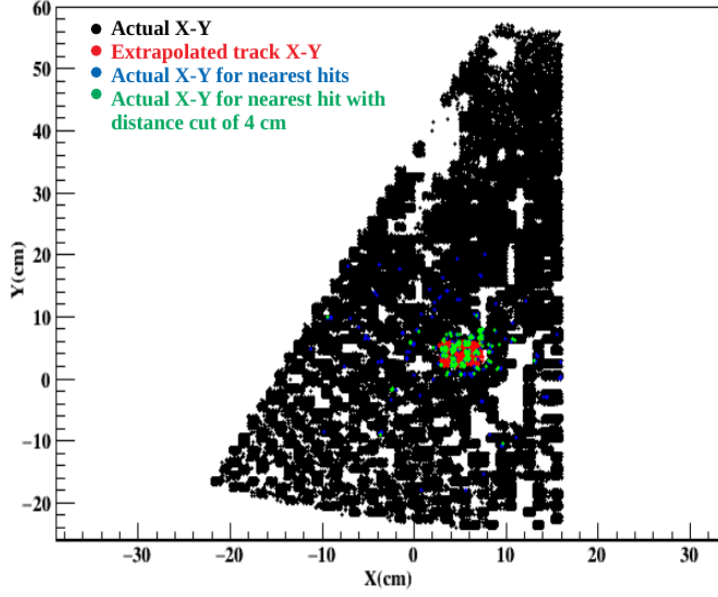


Figure 6.46: Hit coordinates of GEM detector for efficiency measurement. Black point represents the actual hit coordinate, red is for the extrapolated tracks, blue is for the hits nearest to the extrapolated track and green is for the nearest hit with 4 cm cut.

The efficiency of the detector was measured by extrapolating the tracks from TOF detector to GEM planes. Figure 6.46 represents the coordinates of hits. The different colors are as described in the legend. Number of GEM hits which lies within the 4 cm of the incident track are taken in the efficiency calculation, and the number of incident track is taken as the trigger. Only a small portion of the detector was chosen for this calculation. The efficiency of the detector was found to be about 74%. To get the proper efficiency number, we need to correct the acceptance of the detector. After acceptance correction, we found efficiency of the order of about 84%. Though, this number is slightly lower as compared to the results from the COSY test (discussed in chapter 5). At similar voltage in lab with small prototype detector, we observed efficiency about 88% using cosmic muons. More investigation is undergoing.

Further studies related to extracting multiplicity distributions, and performance at high intensities are expected to be carried out in the upcoming mCBM campaign.

6.8 Summary

We have commissioned two large-size trapezoidal GEM modules in the ongoing mCBM experiment at GSI and have tested them with nucleus-nucleus collisions. Test results with Ar+Au collisions at a beam energy of 1.7 AGeV have been reported. Noisy channels were identified using the off-spill

part of the data. Appropriate time-offset corrections were implemented to enable a time-based event reconstruction. The number of events reconstructed per T0 is observed to match with those obtained from simple calculations using the beam intensity parameters and target interaction properties, thus indicating the effectiveness of the event-reconstruction algorithm. Clustering and local hit reconstruction have been performed for the first time on the MuCh modules in the free streaming data set of mCBM. The cluster-size and cluster charge characteristics in different zones of the detector have been studied. The gain of the detector has been calculated using the cluster charge of the reconstructed Hits and its variation with GEM voltages studied. An average time resolution of ~ 16 ns was measured for the GEM module. Uniformity of the detector response has been studied in terms of the relative gain using MPV of the cluster charge distribution zone-wise and also in terms of the time resolutions measured for a large number of pads throughout the detector area. At 2σ level, a spread of about 8 ns was observed for this distribution. The average dispersion of the digis in time within a cluster has been studied. After event reconstruction, a nice spatial correlation is observed not only between GEM1 and GEM2 modules but also between GEM1 and TOF. Thus a synchronous response of the subsystems at mCBM has been observed for the first time, where two different subsystems employing different self-triggered electronics were involved. Finally, straight-line tracks were reconstructed using TOF and GEM Hits, and residuals at different regions of GEM planes have been estimated.

Chapter 7

Summary

CBM is a fixed target heavy-ion experiment at the FAIR facility of GSI Darmstadt Germany, and it is expected to begin the operation in the year 2025/2026. This experiment aims to study the QCD matter at high net-baryon densities and moderate temperature by colliding heavy-ion beams in the energy range of 2-14 AGeV (for Au nucleus) at the SIS100 setup. The main physics goal of the CBM is to study the equation of state at high net-baryon densities and measure the rare diagnostic probes such as multi-strange hyperons, charmed particles, and vector mesons decaying into lepton pairs with unprecedented precision and statistics. The di-lepton physics is the central part of the CBM experiment as they are sensitive diagnostic probes for the condition inside the fireball. Charmonium (J/ψ) and low mass vector mesons (ρ , ω , ϕ) are examples of di-leptons. Measurements of these will provide information on the temperature and lifetime of the fireball, chiral symmetry restoration, and in-medium properties of the vector mesons. However, the production cross-section of these particles is very small at FAIR energies and is termed as rare probes. The unique feature of CBM is that it will be operated at an unprecedented interaction rate of up to 10 MHz. This will open the possibility to measure these rare probes with high statistics.

The di-lepton measurements at CBM will be carried out in two modes of the detector setup, namely, di-muon and di-electron mode. For the di-muon measurements, a Muon Chamber (MuCh) chamber system will be used while for di-electrons a RICH detector system will be employed. The MuCh detector system of CBM consists of alternating layers of segmented absorbers and detector stations. This novel scheme of using segmented absorbers allows the detection of muon tracks in a broad momentum range. The particle rates and radiation doses (neutrons and Gamma) for the first two stations of MuCh will be very high. The maximum expected particle density for the first

station of MuCh is about 400 kHz/cm² (inner region) as calculated from simulation for minimum bias Au+Au collisions at 10 AGeV beam energy. Fast and high rate detectors which can work in such harsh environments and can cope up with high interaction rates are needed. A gaseous detector based on GEM technology will be used for the first two stations. GEM detectors have been used/chosen for charged particle detection in many experiments. Likewise, the large area GEM detectors of MuCh at CBM will carry out charged particle tracking for muon identification. The work in this thesis is dedicated to building and studying the performance of real-size triple GEM prototypes.

The performance of MuCh detectors in simulation has been studied by varying digitization parameters, such as mean gas gain and spot radius of the avalanche. The effect of these parameters on the reconstruction efficiency of ω meson was studied systematically for central Au+Au collisions at 8 AGeV beam energy. The main observation from this exercise is that the reconstruction efficiency saturates at a mean gas gain of about 3.5 k and remains unaffected by the change in spot radius. Other parameters, like residuals, signal (S) to background (B) ratio, significance ($S/\sqrt{S+B}$), etc., were also studied. All these results have been discussed in detail in chapter 3.

During the R & D phase, several triple GEM prototypes detectors (100 cm² to 1900 cm²) were built and tested with radioactive sources (X-rays and β -rays) in the laboratory and with particle beams at different accelerator facilities. In all these tests, two types of readout chains were used namely, conventional (NIM-based) and self-triggered (n-XYTER and STS/MuCh-XYTER). In a self-triggered system, all detector signals, which cross the set threshold are stored along with the time stamp. Basic characteristic measurements in terms of efficiency, cluster size, time resolution, gain, etc. for small size prototype detectors have been carried out in the laboratory using β & X-ray source and n-XYTER chip. The efficiency at the plateau region, obtained from self-triggered readout, is observed to be $\sim 95\%$. It varies within 5% throughout the active region of the detector. The maximum variation in time resolution is observed to vary within 2-3 ns over the full active region. Using a 5.9 keV X-ray source, the variation of relative gain due to changes in drift field, transfer field, induction field, and GEM voltages has been studied. The gain is observed to vary within 10% for E_{drift} of 1.6-3.0 kV/cm and $E_{transfer}$ of 2-4 kV/cm for a particular GEM voltage setting. All these results have been discussed in chapter 4.

A detailed description of the assembly and testing of real-size triple GEM modules is given in chapter 5. Two versions of real-size chambers were built at VECC, namely “Mv1” and “Mv2”. The main difference between these two modules is the gap configuration and HV biasing scheme.

“Mv2” has a gap configuration of 3/2/2/2 and a novel optocoupler-based HV biasing, which has been accepted as the final design while “Mv1” was operated with a gap configuration of 3/1/1/1.5. The design layout and test results are described in chapter 5. Trapezoidal-shaped single mask GEM foils were used for the real-size prototypes. The top surface of each foil is segmented into 24 divisions. These were stretched using the no-glue or “NS-2” technique. The readout consists of trapezoidal-shaped pads with progressively increasing size from ~ 4 mm to ~ 17 mm. The active area of each of the trapezoidal detectors is about 1900 cm^2 . Rigorous Quality Assurance (QA) of foils and other components were done before the detector assembly. All these modules were tested with an X-ray source in the laboratory to ascertain the overall proper functioning of the detectors. Variation of detector gain with ΔV_{GEM} has been studied. The effects of the environmental parameters such as Temperature and Pressure on normalized detector gain with time were observed to be within 5%. The real-size module was also tested with proton beams of momentum $2.36 \text{ GeV}/c$ at the COSY accelerator facility in Jülich. Using n-XYTER chip as readout electronics, a charged particle detection efficiency higher than $\sim 95\%$ was observed. The variation in efficiency with the incoming particle rate (with the maximum rate reaching up to $2.8 \text{ MHz}/\text{cm}^2$) was found to be about 2%.

Real-size prototype detectors were tested with a spray of particles from nucleus+nucleus collisions, as the case would be in the actual CBM experiment, for the first time at CERN-SPS, and more rigorously in mCBM (mini-CBM) experiment at GSI. Test results from Pb+Pb collisions at beam momenta of $150 \text{ AGeV}/c$ have been described in chapter 5. Time resolution measured in the multi-particle environment was observed to match well with that measured with single-particle beams. The mCBM experiment has been set up at the SIS18 facility of GSI to test the simultaneous response from different detector regions of any subsystems and also a correlated response between different subsystems in the nucleus+nucleus environment. Two “Mv2” detectors, corresponding to the module sizes of station-1, were commissioned in mCBM as part of the mMuCh system. The data at mCBM have been acquired using the actual CBM DAQ and realistic STS/MuCh-XYTER electronics, which is designed specifically for MuCh and STS detector systems. The detector characteristics such as gain, time resolution, cluster size, etc., have been studied with varying GEM voltages. The detector gain, as calculated using MPV of the cluster charge, was found to be about 3.1 k at $\Delta V_{GEM(sum)}$ of $\sim 1072 \text{ V}$ which matched within 15% with the gain value measured in the lab using 5.9 keV X-ray source. Zone-wise relative gain of the detector module was measured and it is observed to vary within 15% over the full active area of the detector. Time-walk correction

was applied on data and an improvement of 6-7 ns in time resolution (σ) of the detector was observed. Thus a time resolution of about 15 ns was observed for the GEM module. The uniformity as measured from the time resolution map involving large number of pads/channels over entire detector area was observed to vary within 4-5 ns. In free-streaming data, for the first time using different detectors in mCBM, event building was performed offline by grouping time stamps of the detector hits. Clustering and local hit reconstruction of mMuCh data have been performed, and the cluster characteristics have been studied. An average cluster size of about 1.2 was observed. The cluster size for different granularity regions was also measured and it matches closely with those obtained from simulations. The average dispersion of the digis in time for multi-digi clusters has been studied and it is observed that about 90% of digis are within 50 ns.

From the reconstructed events of the free-streaming data, a clear spatial correlation between GEM1 & GEM2 and between GEM & TOF modules have been observed, conveying an effective event reconstruction. This clearly demonstrates the time-synchronous behavior of two different detectors or, for that matter, even two different subsystems employing entirely different detector technologies and readout electronics. A straight line track fitting has been carried out using TOF detectors and GEM detectors event-by-event. Track residuals have been measured at the different granularity regions of the GEM modules. A σ of about 0.9 cm in X and 1.3 cm in Y was observed. Using reconstructed tracks, the efficiency of the detector was estimated. Average particle rates were measured for two target thicknesses (0.25 mm and 2.5 mm) and various beam intensities. A linear increase in average rate was observed with beam intensity. A factor of about 3.8 increase in the average rate was found on changing the target thickness from 0.25 mm to 2.5 mm, which is similar to that observed in the simulations. All these results have been discussed in chapter 6.

Based on the performance and test results of the detector modules discussed in this thesis, we expect that GEM-based detectors of MuCh should be able to carry out the intended measurements in CBM.

Appendix A

Systematic study of effect of setting parameters of n-XYTER self triggered electronics for CBM MuCh

Introduction Triple-GEM detectors will be used for muon tracking in the CBM experiment at FAIR. It will be positioned in the first two stations of MuCh, where the particle rate is very high. For the operation of CBM-MuCh at high interaction rates, self-triggered fast readout electronics are required. For the beam-test of GEM detector prototypes, n-XYTER ASIC was used for reading out the signal. It has several registers via which one can set the optimum values for operating the ASIC. Parameters such as V_{biasS} , V_{th} , V_{bfb} are some of the main ones which directly affect the signal amplitude or the noise characteristics of the detector. V_{th} is the global threshold voltage for the comparators, i.e., it defines the pulse strength that is necessary to trigger the comparator. V_{biasS} is the bias voltage for the first stage of the slow shaper of n-XYTER and sets the baseline. It does not affect the shape of the pulse and shifts the DC-offsets. The DC-level is temperature-dependent, so we need to maintain the temperature of the chip. Otherwise, the baseline value will shift. V_{bfb} sets the discharge time for pre-amplifier by controlling the resistance of the transistor used in pre-amplifier of n-XYTER, and its setting governs the behavior of the response at high rates. If it is set too low, then the large output signal produced by a large input charge might be cut through. Nevertheless, the discharge resistance decreases by increasing V_{bfb} , which results in huge noise and undershoot. In this report, we discuss the variation of signal and baseline with varying FEB parameters. In this chapter, we discuss the variation of signals with varying ASIC

parameters. The goal is to study the characteristics of the ASIC parameters and to have a better understanding of the test beam data already acquired. We present here a detailed and systematic study of these parameters.

The threshold calibration of the chip is shown in Figure A.1. The plot is taken from [16] (page number 33). The V_{th} of 50 corresponds to charge of ~ 1.9 fC.

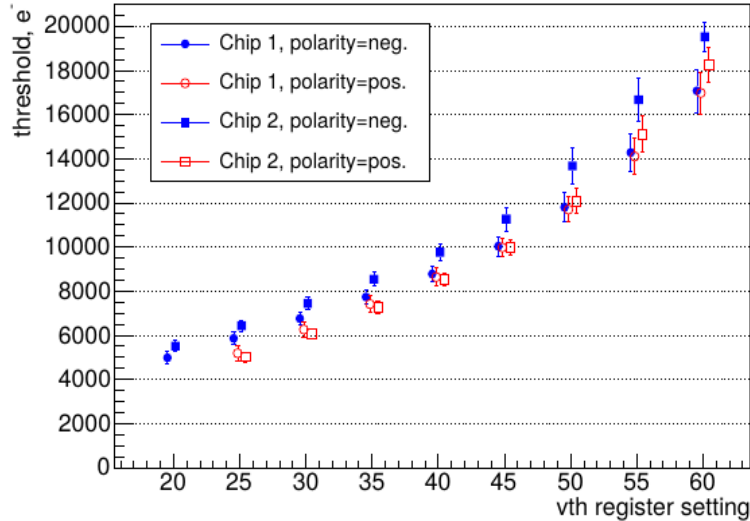


Figure A.1: Threshold calibration of n-XYTER chip. Taken from [16]

Experimental Setup The tests have been carried out using a triple GEM detector of $10\text{ cm} \times 10\text{ cm}$ and ^{55}Fe source. The picture of the setup is shown in the left panel of Figure A.2. The readout plane consists of 512 pads, each of $3\text{ mm} \times 3\text{ mm}$ in size, and read out using two n-XYTER FEBs. These FEBs are connected to ROC. The description of the n-XYTER FEBs are discussed in the chapter 4. ^{55}Fe source was placed at a fixed position of the detector such that the same pad was hit most of the times. Only one setting parameter was changed at any given time and data were acquired using DABC software [161, 162] developed at GSI. For all the measurements we have kept the FEB temperature fixed. We have allowed only a small variation of temperature by 1°C .

Results and discussion The baseline of the n-XYTER is fixed around ~ 2000 ADC for negative signal and due to this, the pulse height spectra is inverted implying lower amplitude signal occurring at higher ADC and vice-versa. The pulse height spectra obtained from the source or beam particles need to be subtracted from the baseline to have a meaningful picture of the ADC. The accuracy in baseline determination is thus an important issue and can directly affect the amplitude estimation of the signal. Figures A.2 (middle panel) and A.2 (right panel) show the raw and baseline corrected pulse height spectra of ^{55}Fe , respectively. The accuracy in baseline

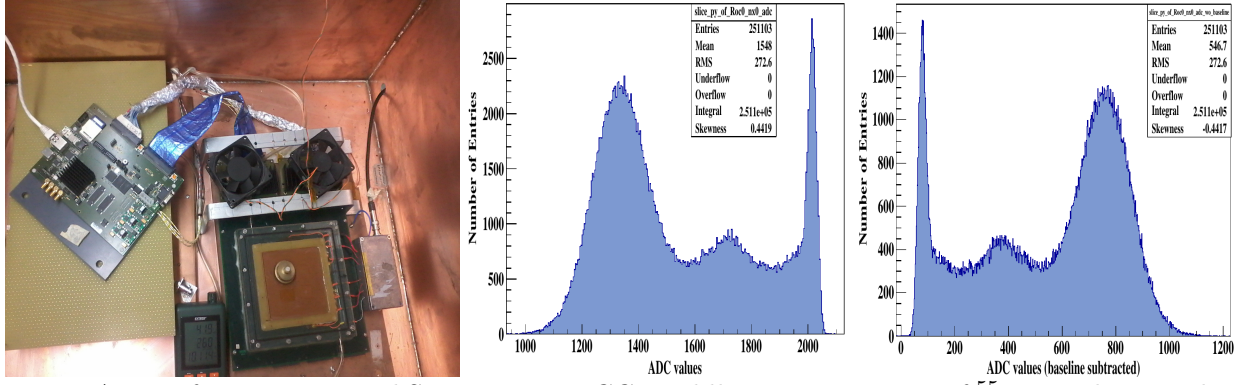


Figure A.2: Left: Experimental Setup in at VECC. Middle: Raw spectrum of ^{55}Fe . Right: Baseline corrected spectrum of ^{55}Fe .

determination is an important issue and can directly affect the amplitude estimation of the signal. The left and right panel of Figure A.3 shows the variation of baseline with V_{th} at different V_{fb} settings. Negligible effect of V_{th} is seen on the baseline values. There is a systematic change, but at an insignificant level ($<0.5\%$), in the baseline with increase in V_{fb} parameter.

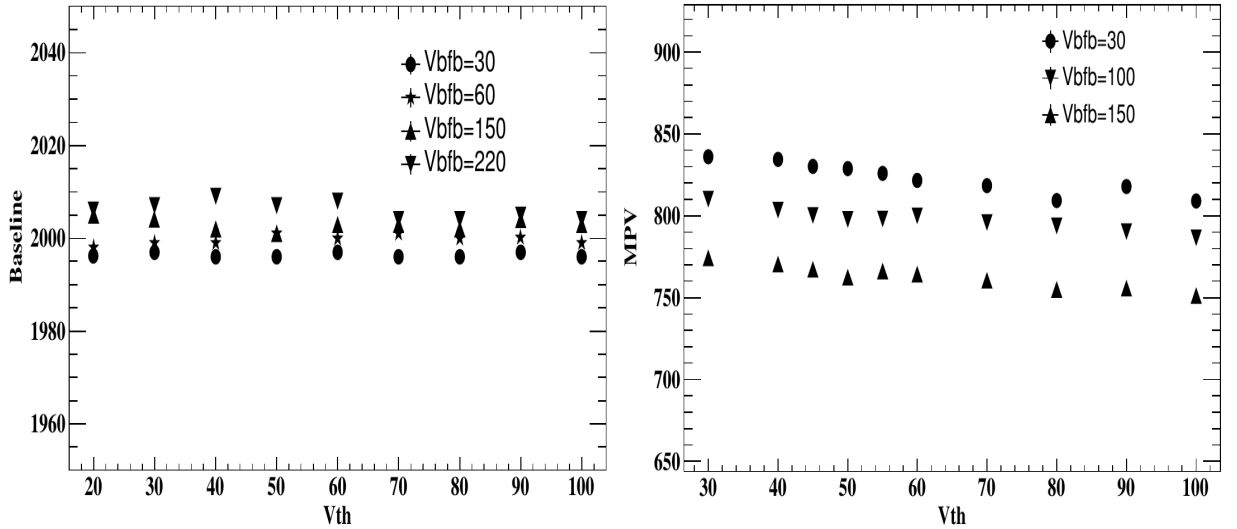


Figure A.3: Left: Variation of baseline with V_{th} at different V_{fb} . Right: Variation of MPV of the pulse height spectra with V_{th} .

The noise in the detector can be controlled by increasing the value of V_{th} , which if set too high can cut the signal. At any given V_{fb} , how the change in V_{th} affects the signal amplitude is shown in Figure A.3 (right panel). These pulse heights are normalized at $T/P = 0.2980$ K/hPa. It is seen that the peak pulse height gets affected only slightly (less than 3%) if the V_{th} value changes from 30 to 100. At the same time, on varying the V_{fb} value from 30 to 150 at a fixed V_{th} (say 50) a decrease in pulse height of about 9% is observed. This can also be gathered from Figure A.5. This

decrease in ADC channel by increasing V_{bfb} can be understood by the faster dissipation of charges on the readout pads. Figure A.4 (left panel) shows the variation of baseline with V_{biasS} for two different FEBs. The baseline increases linearly with V_{biasS} and gets saturated above certain V_{biasS} setting, because of the reference level of n-XYTER. Saturation value of baseline is fixed but the settings of V_{biasS} parameter will vary from one FEB to another FEB. The “auto V_{biasS} ” command in DABC sets the average baseline around 2000 ADC channel. The temperature variations in FEB also affects the baseline of the n-XYTER. We have allowed only a small variation of temperature by $\sim 1^\circ\text{C}$.

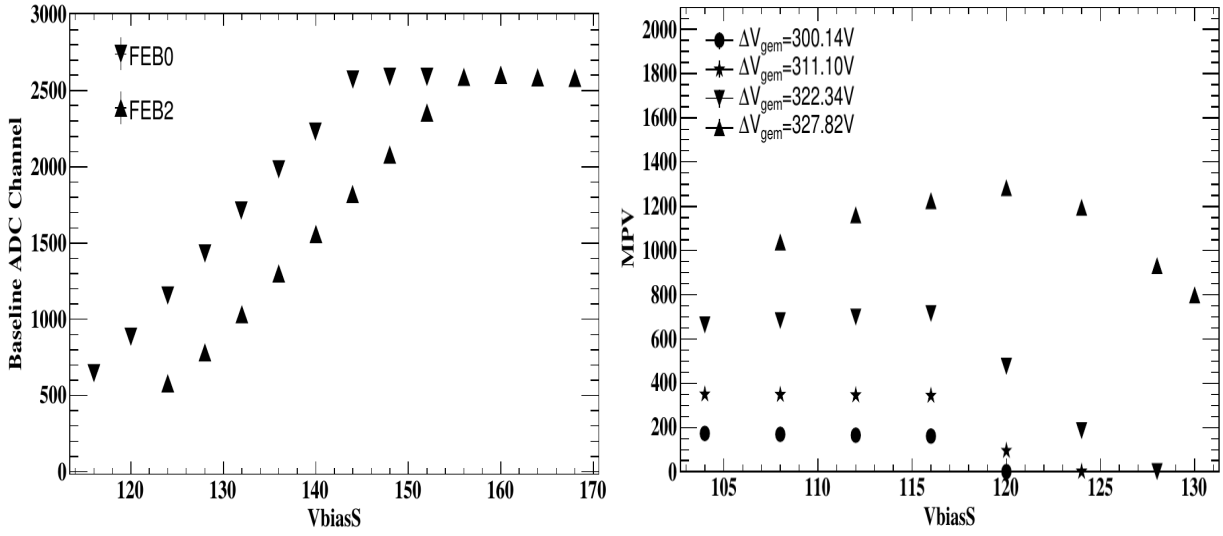


Figure A.4: Left: Variation of baseline with V_{biasS} . Right: Variation of peak pulse height with V_{biasS} at different ΔV_{gem} .

The right panel of Figure A.4 shows the variation of peak pulse height (the Most Probable Value, MPV) with V_{biasS} at different ΔV_{gem} . It remains flat with V_{biasS} for lower ΔV_{gem} up to a particular value, beyond which it decreases to zero. But for high amplitude signals (higher ΔV_{gem}), the MPV values are lower at lower V_{biasS} as compared to intermediate ones in the figure, and then starts to decrease after a particular value, as before. V_{biasS} sets the DC reference level for each channel. If the level goes below the output low of slow shapers, then the signal is clipped from the lower side and we get no output at low input signal. If the DC level is set to very high, then high input signal is saturated. This observation is in line with the expected behavior of electronics. This study indicates the range of V_{biasS} values within which one can expect a stable signal. While the decrease in amplitude is understood from the simple understanding of the reference level, the reason for the increase at higher gains could be due to the improvement in energy resolution.

For a stable operation of the detector at high rates in test beams, V_{bfb} parameter had to be

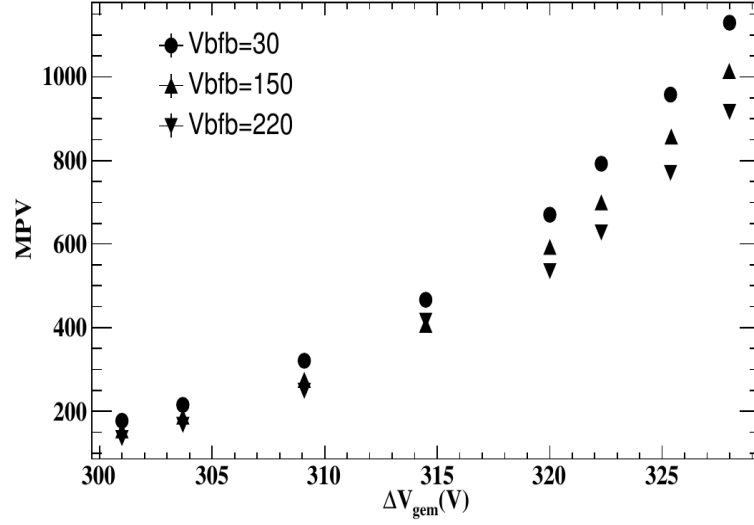


Figure A.5: Variation of peak pulse height with ΔV_{gem}

set at a high value of about ~ 150 , to avoid pre-amp saturation. However, high values of V_{bfb} may result into some amplitude loss, owing to faster dissipation of charge from the pads as discussed before. This effect of the varying V_{bfb} values on signal amplitude has been systematically studied. The variation of peak pulse height with ΔV_{gem} at three different V_{bfb} settings (30, 150, 220) is shown in Figure A.5. These pulse heights are normalized at $T/P=0.2980$ K/hPa. As observed from the figure, the gain reduction is at the level of about 10% in the MPV at $\Delta V_{gem} = 328$ V, when going from $V_{bfb} = 30$ to 150.

The baseline of the n-XYTER does not depend on the V_{th} , but it depends on the V_{biasS} settings. The peak pulse height is affected by only about 3% on varying the V_{th} in the range of our study. A high value of V_{bfb} affects the peak pulse height slightly. A decrease of 10% in signal amplitude as seen from the MPV values from the ^{55}Fe tests is observed when changing V_{bfb} settings from 30 to 150.

Appendix B

Effect of n-XYTER parameter (V_{th} , V_{bfb}) on detector characteristics

Introduction The basic study of n-XYTER parameters and their effect on gain and noise has been studied in appendix A. However, these parameters can also affect the efficiency, cluster size, etc. Hence, in this appendix, we show the effect of these parameters on the efficiency and cluster size of the triple GEM detector. The description of setup used for this is given in section 4.5.2 of chapter 4. Analysis of the data has been done using CBMROOT.

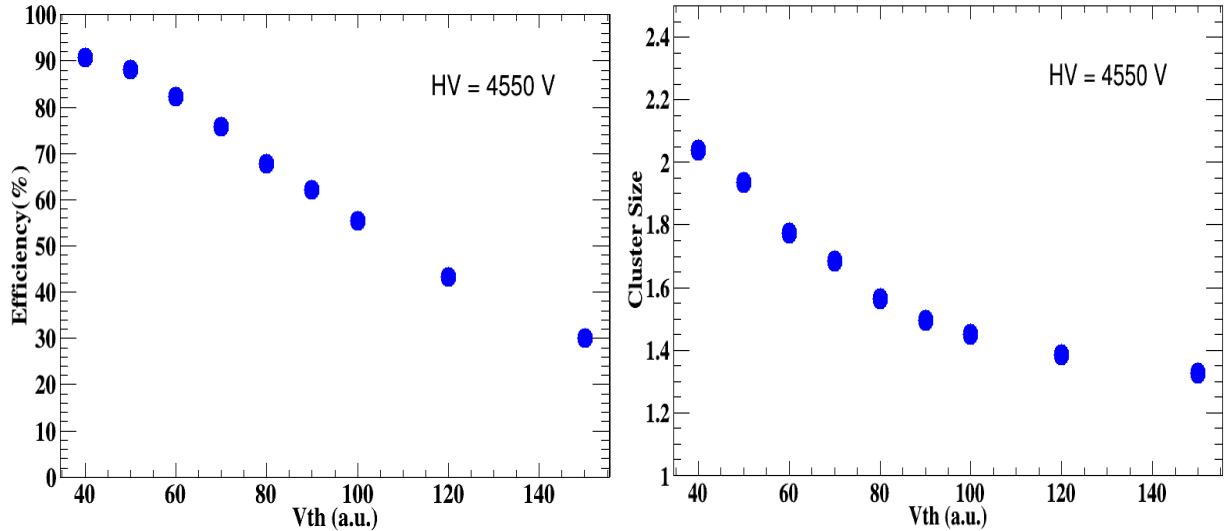


Figure B.1: Left: Variation of detector efficiency with V_{th} . Middle: Variation of average cluster size with V_{th} .

Results The variation of the efficiency and average cluster size with V_{th} is shown in Figure B.1. Higher V_{th} implies we are cutting signals, and we expect that the efficiency and cluster size should

decrease by increasing V_{th} value. The same effect is shown in the figure. We have used V_{th} of 50 for most cases in the lab and test beams. However, it is increased to a higher value for suppressing noise.

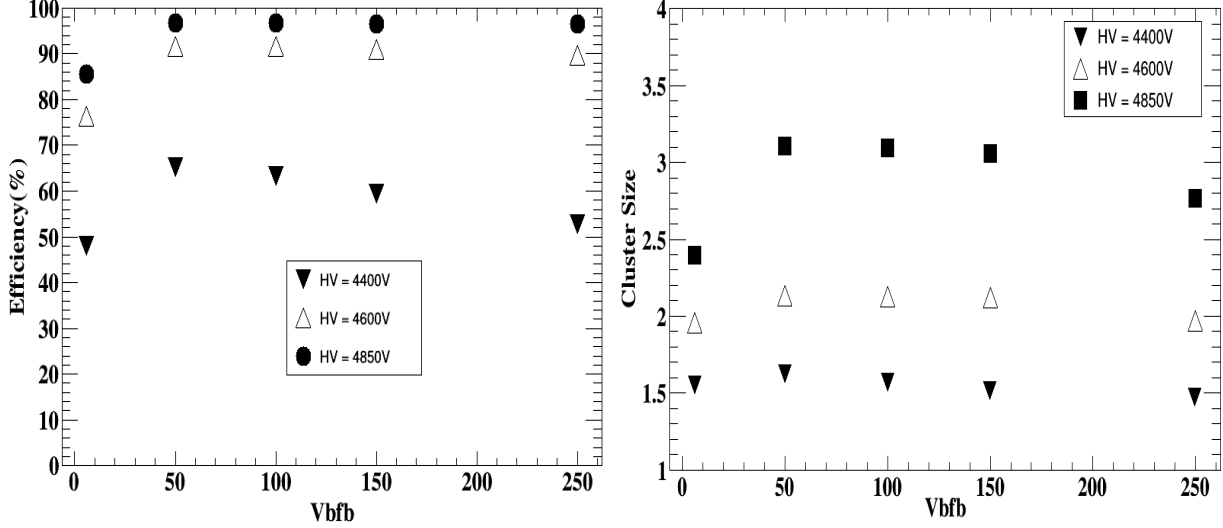


Figure B.2: Left: Variation of detector efficiency with V_{bfb} . Middle: Variation of average cluster size with V_{bfb} .

The exact measurement was done by increasing another parameter called V_{bfb} . The variation of efficiency and average cluster size with V_{th} is shown in Figure B.2. As discussed in appendix A, lower V_{bfb} can cut the signals, and if it is increased to a high value, then it results in greater noise and pulse undershoot. These effects can be observed in Figure B.2. In the lab and test beams, we have used V_{bfb} of 150.

Study of the effect of n-XYTER parameters (namely, V_{bfb} and V_{th}) is described in this appendix. The default value we used for V_{th} is 50 and 150 for V_{bfb} .

Appendix C

Gain Comparison Between MCA and n-XYTER data

Introduction As already mentioned, we have used MCA and n-XYTER based readout chains for the detector tests. It is necessary to compare the results obtained from both the readout chain. In this appendix, the comparison between MCA/NIM and n-XYTER based chain has been performed. The details about the readout chain is described in section 4.4 of chapter 4. A triple GEM detector and ^{55}Fe source were used for this test.

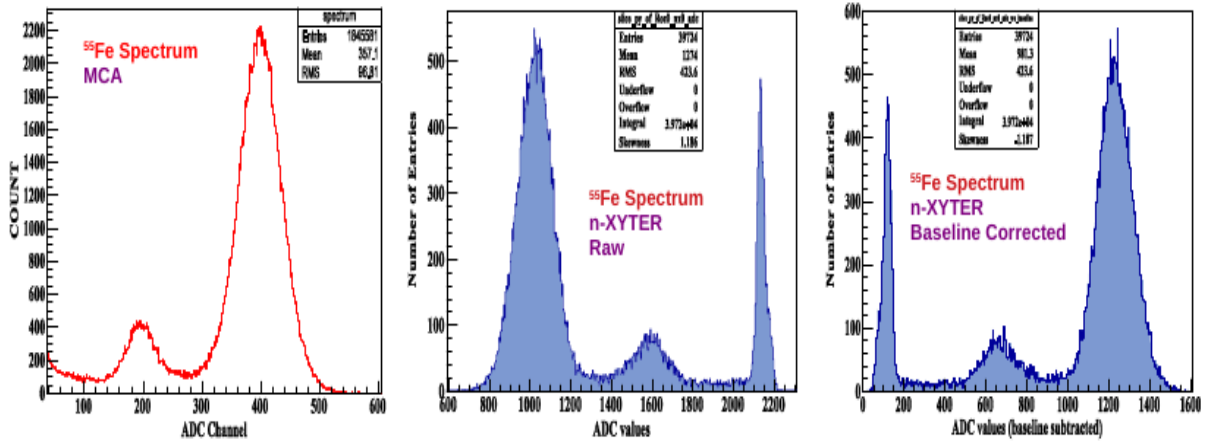


Figure C.1: ^{55}Fe spectrum from MCA and n-XYTER

Results The typical energy spectrum of the ^{55}Fe source using MCA/NIM (left panel) and n-XYTER (middle and right panel) is shown in Figure C.1. As discussed, the raw signal from n-XYTER is inverted, and we need to correct it from baseline. Both the spectrum is shown in Figure C.1.

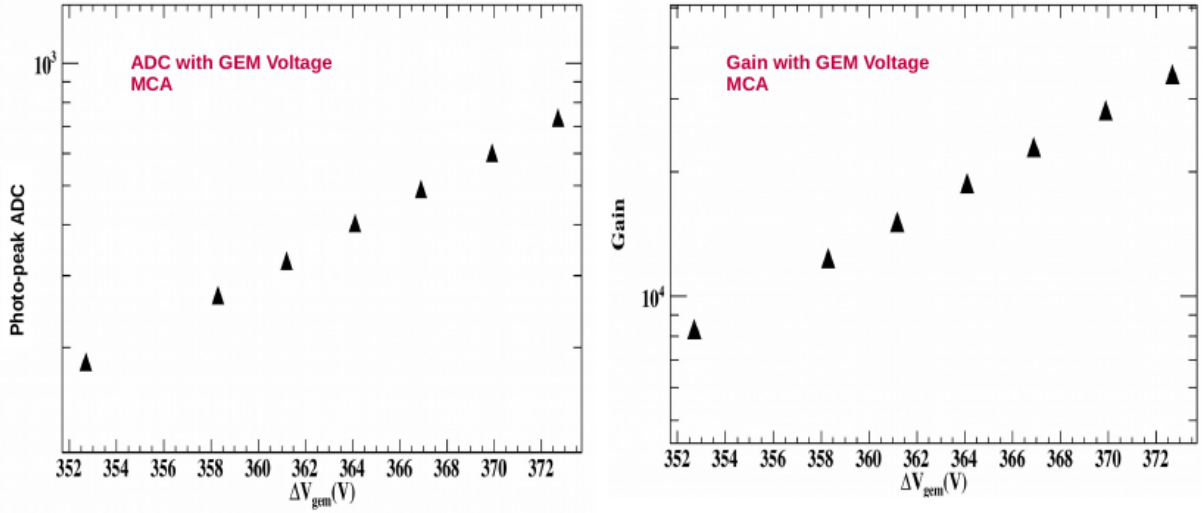


Figure C.2: ADC and Gain variation with GEM voltage from MCA

The peak-ADC channels of ^{55}Fe spectrum obtained from GEM detectors using discussed read-out chains are analyzed for different high voltage settings. The ADC values are then converted to gain using calibration equation (see section 4.4 of chapter 4) for both the cases.

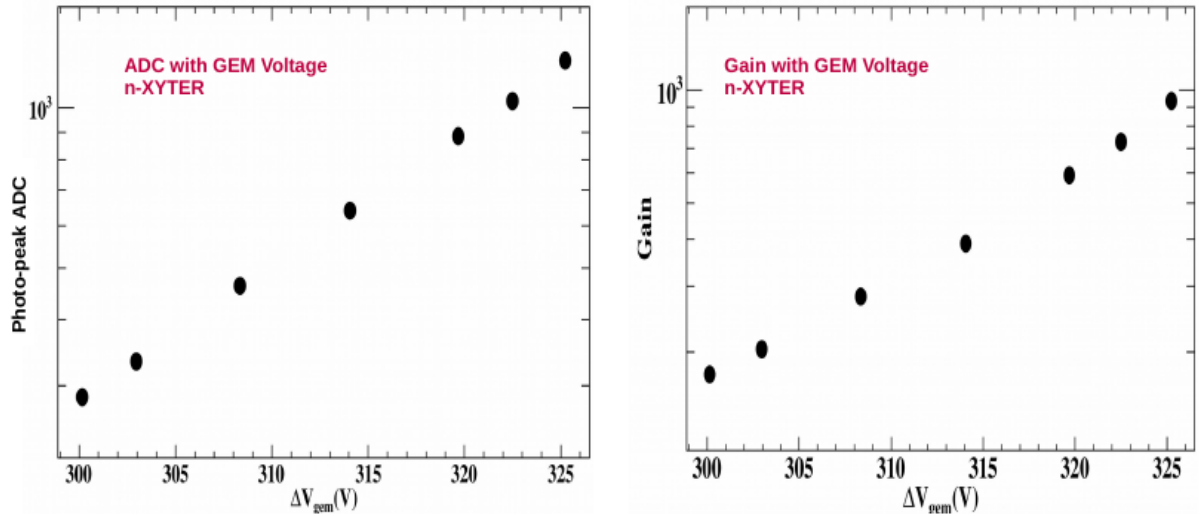


Figure C.3: ADC and Gain variation with GEM voltage from n-XYTER

The variation of peak-ADC channel and gain for the case of MCA is shown in the left and right panel of Figure C.2, respectively. Similarly, the variation of peak-ADC channel and gain for n-XYTER is shown in Figure C.3. The range of voltage settings in these two cases is different. This is because, with n-XYTER, we can not go to higher gains due to signal saturation. However, we can extrapolate the n-XYTER data to the MCA data. After extrapolation, we found that the gain value at similar voltage matches within $\sim 5\%$.

Appendix D

Simulation result

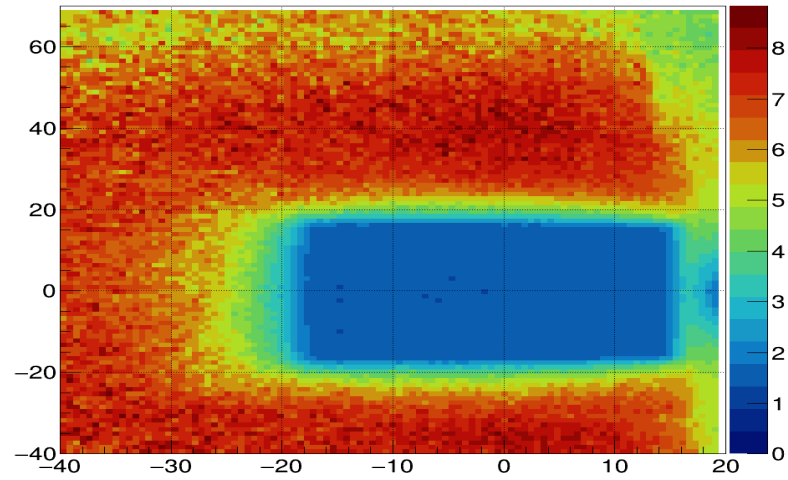


Figure D.1: Ratio of average particle rate on mMuCh in FLUKA simulation [[17](#)]

Bibliography

- [1] Kenji Fukushima and Tetsuo Hatsuda. *Reports on Progress in Physics*, 74:014001, 2010.
- [2] A. Sorin et al. *PoS, CPOD 042*, 2014.
- [3] C. Montag. *PoS, CPOD 041*, 2014.
- [4] Jan Michel et al. *IEEE Transactions on Nuclear Science*, 58:1745 – 1750, 2011.
- [5] A. Andronic et al. *Nuclear Physics A*, 772(3):167–199, 2006.
- [6] The CBM Report 2012-01. <http://www.gsi.de/documents/DOC-2011-Aug-29-1.pdf>.
- [7] The FAIR experiment. <https://fair-center.eu/>.
- [8] F. Sauli. Principle of operation of multiwire proportional and drift chambers. <https://cds.cern.ch/record/117989/files/CERN-77-09.pdf>.
- [9] J. Merlin. Ph.d. thesis. <https://cds.cern.ch/record/2155685/files/CERN-THESIS-2016-041.pdf>.
- [10] Passage of particles through matter. <https://pdg.lbl.gov/2020/reviews/rpp2020-rev-passage-particles-matter.pdf>.
- [11] Energy loss in argon. <http://pdg.lbl.gov>.
- [12] *Nucl. Inst. and Meth. A*, 714:136–140, 2013.
- [13] P. Otfinowski et al. *Nucl. Instrum. Meth. A*, 780:114–118, 2015.
- [14] mCBM@SIS18, A CBM full system test-setup for high-rate nucleus-nucleus collisions at GSI / FAIR, The CBM Collaboration. Technical report, 2017. <http://dx.doi.org/10.15120/GSI-2019-00977>.

- [15] C. Sturm. Goals and Perspectives of the CBM Experiment. <https://indico.gsi.de/event/9356/contributions/40577/attachments/29116/36240/20190928-CBM-PreMeeting-Guwahati-CBM-CSturm-v17nb.pdf>.
- [16] CBM Progress Report 2013. Technical report, Darmstadt, 2014.
- [17] Anna Senger. FLUKA simulation: delta electrons in mCBM. <https://indico.gsi.de/event/9063/contributions/39344/attachments/28293/35322/PartRateRatioFLUKA.pdf>.
- [18] W. Heisenberg. *Z. Phys.*, 101:533, 1936.
- [19] W. Heisenberg. *Z. Phys.*, 113:61, 1939.
- [20] E. Fermi. *Progress of Theoretical Physics*, 5:570, 1950.
- [21] I. Ya. POMERANCHUK. *Doklady Akad. Nauk. SSSR*, 78:889, 1951.
- [22] L. D. Landau. *Izv. Akad. Nauk SSSr*, 17:51, 1953.
- [23] R. Hagedorn. *Nuovo Cim. Suppl.*, 3:147, 1965.
- [24] R. Hagedorn. *Nuovo Cim.*, 56A:1027, 1968.
- [25] H. Fritzsche et al. *Physics Letters B*, 47:365–368, 1973.
- [26] Yoichiro Nambu. *Phys. Rev. Lett.*, 4:380–382, Apr 1960.
- [27] O. W. Greenberg. *Phys. Rev. Lett.*, 13:598–602, Nov 1964.
- [28] David J. Gross and Frank Wilczek. *Phys. Rev. Lett.*, 30:1343–1346, Jun 1973.
- [29] H. David Politzer. *Phys. Rev. Lett.*, 30:1346–1349, Jun 1973.
- [30] A. Bazavov et al. *Phys. Rev. D*, 85:054503, Mar 2012.
- [31] S. Borsanyi et al. *J. High Energ. Phys.*, 73:1009, 2010.
- [32] Y. Aoki et al. *Nature*, 443:675–678, 2006.
- [33] Z Fodor and S.D Katz. *Journal of High Energy Physics*, 2004(04):050–050, 2004.
- [34] A. Andronic et al. *Nuclear Physics A*, 837:65–86, 2010.

-
- [35] Mauro Anselmino et al. *Rev. Mod. Phys.*, 65:1199–1233, Oct 1993.
- [36] Massimo Mannarelli et al. *Phys. Rev. Lett.*, 101:241101, 2008.
- [37] The ALICE Collaboration, K Aamodt, et al. *Journal of Instrumentation*, 3(08):S08002–S08002, 2008.
- [38] W. A. Zajc. *Nuclear Physics A*, 805:283c–294c, 2008. INPC 2007.
- [39] J. M. Lattimer and M. Prakash. *The Astrophysical Journal*, 550(1):426–442, mar 2001.
- [40] Fridolin Weber. *Journal of Physics G: Nuclear and Particle Physics*, 27(3):465–474, feb 2001.
- [41] J.W. Harris et al. *Nuclear Physics A*, 566:277–285, 1994.
- [42] D.P. Morrison et al. *Nuclear Physics A*, 638:565c–569c, 1998. Quark Matter '97.
- [43] Marek Gazdzicki et al. *Journal of Physics G: Nuclear and Particle Physics*, 38:124024, 2011.
- [44] The NICA experiment at JINR. <http://nica.jinr.ru>.
- [45] Guenther Rosner. Future facility: Fair at gsi. *Nuclear Physics B - Proceedings Supplements*, 167:77–81, 2007.
- [46] Bengt Friman et al., editors. *The CBM physics book: Compressed baryonic matter in laboratory experiments*, volume 814. 2011.
- [47] The cbm experiment. <https://www.cbm.gsi.de/>.
- [48] T. Ablyazimov et al. *Eur. Phys. J. A*, 53(3):60, 2017. <https://doi.org/10.1140/epja/i2017-12248-y>.
- [49] The Facility for Antiproton and Ion Rsearch FAIR. <https://fair-center.eu/>.
- [50] K Kajantie and L McLerran. *Annual Review of Nuclear and Particle Science*, 37:293–323, 1987.
- [51] B Muller. *Reports on Progress in Physics*, 58(6):611–636, jun 1995.
- [52] John W. Harris and Berndt Müller. *Annual Review of Nuclear and Particle Science*, 46:71–107, 1996.

- [53] S A Bass et al. *Journal of Physics G: Nuclear and Particle Physics*, 25(3):R1–R57, jan 1999.
- [54] C. Y. Wong, editor. *Introduction to high energy heavy ion collisions*. World Scientific, Singapore, 1994.
- [55] Ramona Vogt, editor. *Ultrarelativistic Heavy-Ion Collisions*. Elsevier, 2007.
- [56] B. Müller, editor. *The Physics of Quark Gluon Plasma*. Springer, Heidelberg, 1985.
- [57] H. Satz S. Sarkar and B. Sinha, editors. *The Physics of the Quark-Gluon Plasma: Introductory Lectures, Lect. Notes Phys. 785*. Springer, Heidelberg, 2010.
- [58] Johann Rafelski and Berndt Müller. *Phys. Rev. Lett.*, 48:1066–1069, Apr 1982.
- [59] P Koch et al. *Physics Reports*, 142(4):167–262, 1986.
- [60] B Tomášik et al. *Eur. Phys. J. A*, 52(4):251, 2016.
- [61] Marek Gazdzicki and Mark I. Gorenstein. *Acta Phys.Polon. B*, 30:2705, 1999.
- [62] A. Andronic et al. *Nuclear Physics A*, 834(1):237c–240c, 2010.
- [63] P. Chung et al. *Phys. Rev. Lett.*, 91:202301, Nov 2003.
- [64] P. Braun-Munzinger et al. *Physics Letters B*, 596(1):61–69, 2004.
- [65] V. N. Gribov and L. N. Lipatov. *Sov. J. Nucl. Phys.*, 15:438–438, 1972.
- [66] V. N. Gribov and L. N. Lipatov. *Yad. Fiz.*, 15:781–781, 1972.
- [67] G. Altarelli and G. Parisi. *Nucl. Phys. B*, 126:298–298, 1977.
- [68] Y. L. Dokshitzer. *Sov. Phys. JTEP*, 46:641, 1977.
- [69] Y. L. Dokshitzer. *Zh. Eksp. Teor. Fiz.*, 73:1216, 1977.
- [70] Y. Akiba et al. *Nucl. Phys. A*, 774:403, 2006.
- [71] S.S. Adler et al. *Phys. Rev. C*, 76:034904, 2007.
- [72] Jean-Yves Ollitrault. *Phys. Rev. D*, 46:229–245, Jul 1992.
- [73] Y. Zhang S. Voloshin. *Phys. C*, 70:665, 1996.

-
- [74] R. Snellings. *New J. Phys.*, 13:055008, 2011.
- [75] B.B. Back et al. *Nuclear Physics A*, 757(1):28–101, 2005. First Three Years of Operation of RHIC.
- [76] I. Arsene et al. *Nuclear Physics A*, 757:1–27, 2005. First Three Years of Operation of RHIC.
- [77] Berndt Müller and James L. Nagle. Results from the relativistic heavy ion collider. *Annual Review of Nuclear and Particle Science*, 56:93–135, 2006.
- [78] Henning Heiselberg. *Physics Reports*, 351:161–194, 2001.
- [79] S. Jeon and V. Koch. *Phys. Rev. Lett.*, 83:5435–5438, Dec 1999.
- [80] S. Jeon and V. Koch. *Phys. Rev. Lett.*, 85:2076–2079, 2000.
- [81] Sean Gavin and Claude Pruneau. *Phys. Rev. C*, 61:044901, 2000.
- [82] J. Adams et al. *Phys. Rev. C*, 68:044905, 2003.
- [83] J. Adams et al. *Phys. Rev. C*, 71:064906, 2005.
- [84] H. Appelshäuser et al. *Physics Letters B*, 459:679–686, 1999.
- [85] L. D. McLerran and T. Toimela. *Phys. Rev. D*, 31:545–563, Feb 1985.
- [86] H. Arthur Weldon. *Phys. Rev. D*, 42:2384–2387, Oct 1990.
- [87] Rupa Chatterjee and Dinesh K. Srivastava. *Phys. Rev. C*, 79:021901, 2009.
- [88] R. Rapp and J. Wambach. *Eur. Phys. J. A*, 6(4):415–420, 1999.
- [89] Heng-Tong Ding et al. *Phys. Rev. D*, 94:034504, Aug 2016.
- [90] M. Herrmann et al. *Nuclear Physics A*, 560(1):411–436, 1993.
- [91] G. Chanfray and P. Schuck. *Nuclear Physics A*, 555(1):329–353, 1993.
- [92] W. Peters et al. *Nuclear Physics A*, 632:109–127, 1998.
- [93] G. Chanfray et al. *Phys. Rev. Lett.*, 76:368–371, Jan 1996.
- [94] D. Cabrera et al. *Nuclear Physics A*, 705(1):90–118, 2002.

- [95] Paul M. Hohler and Ralf Rapp. *Physics Letters B*, 731:103–109, 2014.
- [96] Ralf Rapp and Hendrik van Hees. *Physics Letters B*, 753:586–590, 2016.
- [97] Helmut Satz. Colour deconfinement and quarkonium binding. *Journal of Physics G: Nuclear and Particle Physics*, 32:R25–R69, 2006.
- [98] Helmut Satz. *Nuclear Physics A*, 783:249–260, 2007.
- [99] Louis Kluberg and Helmut Satz. arXiv:0901.3831.
- [100] T. Matsui and H. Satz. *Physics Letters B*, 178:416–422, 1986.
- [101] S. Digal et al. *Phys. Rev. D*, 64:094015, 2001.
- [102] P. P. Bhaduri. CHARMONIUM PRODUCTION AND DETECTION IN HIGH ENERGY NUCLEAR COLLISIONS AT FAIR, PhD Thesis, November, 2014.
- [103] W. Cassing et al. *Nuclear Physics A*, 691:753–778, 2001.
- [104] Alexander Malakhov and Alexey Shabunov, editors. *Technical Design Report for the CBM Superconducting Dipole Magnet*. GSI, Darmstadt, 2013.
- [105] Peter Senger and Volker Friese. CBM Progress Report 2020. Technical Report 2021-00421, 2021.
- [106] CBM Progress Report 2019. Technical Report CBM-PR-2019, 2020.
- [107] CBM Progress Report 2018. Technical Report CBM Progress Report 2018, 2019.
- [108] CBM Progress Report 2017. Technical Report CBM Progress Report 2017, 2018.
- [109] Ilya Selyuzhenkov and Alberica Toia, editors. *CBM Progress Report 2016*. GSI, 2017.
- [110] Johann Heuser et al., editors. *[GSI Report 2013-4] Technical Design Report for the CBM Silicon Tracking System (STS)*. GSI, Darmstadt, 2013.
- [111] Technical Design Report for the CBM Ring Imaging Cherenkov Detector. Technical report, 2013.
- [112] S. Chattopadhyay et al., editors. *The Muon Chamber of the CBM Experiment at FAIR : Technical Design Report for the CBM Muon Chamber (MuCh)*. GSI, 2015. <https://repository.gsi.de/record/161297>.

-
- [113] The Transition Radiation Detector of the CBM Experiment at FAIR : Technical Design Report for the CBM Transition Radiation Detector (TRD). Technical report, Darmstadt, 2018.
- [114] Norbert Herrmann, editor. *Technical Design Report for the CBM Time-of-Flight System (TOF)*. GSI, Darmstadt, 2014.
- [115] Fedor Guber and Ilya Selyuzhenkov, editors. *Technical Design Report for the CBM Projectile Spectator Detector (PSD)*. GSI, Darmstadt, 2015.
- [116] R. Arnaldi et al. *Phys. Rev. Lett.*, 96:162302, 2006.
- [117] R. Arnaldi et al. *Eur. Phys. J. C*, 61:711, 2009.
- [118] R. Rapp et al. Elementary Particles, Nuclei and Atoms · volume 23: “Relativistic Heavy Ion Physics” in Springer Materials (https://doi.org/10.1007/978-3-642-01539-7_6). Copyright 2010 Springer-Verlag Berlin Heidelberg.
- [119] Chihiro Sasaki. *Physics Letters B*, 801:135172, 2020.
- [120] R. Arnaldi et al. *Nucl. Phys. A*, 830:345c, 2009.
- [121] A.D. Frawley et al. *Physics Reports*, 462:125–175, 2008.
- [122] R. Arnaldi et al. *Phys. Rev. Lett.*, 100:022302, 2008.
- [123] N. Xu. PARTONIC EQUATION OF STATE IN HIGH-ENERGY NUCLEAR COLLISIONS, 2007.
- [124] Helena de Santos. PhD Thesis, 2004.
- [125] The UrQMD event generator. <https://urqmd.org/>.
- [126] The Geant transport engin. <https://geant4.web.cern.ch/>.
- [127] S. Ahmad et al. *Nucl. Inst. and Meth. A*, 775:139–147, 2015.
- [128] I.B. Smirnov. *Nucl. Inst. and Meth. A*, 554:474–493, 2005.
- [129] I. Kisel. *Nucl. Inst. and Meth. A*, 566:85–88, 2006.
- [130] R. E. Kalman. *Journal of Basic Engineering*, 82(1):35–45, 1960.

- [131] R. Fröhlich. *Nucl. Inst. and Meth. A*, 262:444–450, 1987.
- [132] C. Amsler et al. Review of particle physics. *Physics Letters B*, 667(1):1–6, 2008. Review of Particle Physics.
- [133] W. H. Press et al., editors. *Numerical Recipes: The Art of Scientific Computing*. Cambridge Univ Press, 2007.
- [134] R. Frühwirth et al., editors. *Data Analysis Techniques for High-Energy Physics*. Cambridge Univ Press, 2000.
- [135] A. Lebedev and G. Ososkov, editors. *LIT track propagation for CBM*. CBM Note, 2008.
- [136] S.A. Bass et al. *Progress in Particle and Nuclear Physics*, 41:255–369, 1998.
- [137] The mCBM experiment, to be published, see experiment proposal: <http://dx.doi.org/10.15120/GSI-2019-00977>.
- [138] The Pluto event generator. <https://www-hades.gsi.de/pluto>.
- [139] [Neutron Interactions with Matter](#).
- [140] J. R. Dunning et al. Interaction of neutrons with matter. *Phys. Rev.*, 48:265–280, 1935.
- [141] K. Kasinski et al. *Nucl. Instrum. Meth. A*, 908:225 – 235, 2018. <https://doi.org/10.1016/j.nima.2018.08.076>.
- [142] K. Kasinski et al. *Journal of Instrumentation*, 12(03):C03023–C03023, 2017.
- [143] K. Kasinski et al. *Journal of Instrumentation*, 11(11):C11018–C11018, 2016.
- [144] The n-XYTER manual. <https://cbm-wiki.gsi.de/pub/Public/PublicNxyter/nXYTER.pdf>.
- [145] A. S. Brogna et al. *Nucl. Inst. and Meth. A*, 568:301 – 308, 2006.
- [146] F. Sauli. *Nucl. Inst. and Meth. A*, 386:531–534, 1997.
- [147] A. F. Buzulutskov. *Instrum Exp Tech*, 50:287–310, 2007.
- [148] Eraldo Oliveri. *The forward inelastic telescope T2 for the TOTEM experiment at the LHC*. PhD thesis, 2010. Presented on 2010.

-
- [149] P. Abbon et al. The compass experiment at cern. *Nucl. Inst. and Meth. A*, 577(3):455–518, 2007.
- [150] Alessandro Cardini et al. The operational experience of the triple-gem detectors of the lhcb muon system: Summary of 2 years of data taking. Technical report, CERN, Geneva, Nov 2012.
- [151] Marinov, Andrey. *Feasibility study of a GEM based muon system for the CMS detector at the Large Hadron Collider*. PhD thesis, Ghent University, 2012.
- [152] A. Colaleo et al. Cms technical design report for the muon endcap gem upgrade. Technical report, 2015.
- [153] Technical Report CERN-LHCC-2017-012. CMS-TDR-016, CERN, Geneva, Sep 2017. <https://cds.cern.ch/record/2283189>.
- [154] Technical Report CERN-LHCC-2013-020. ALICE-TDR-016, CERN, Oct 2013. <https://cds.cern.ch/record/1622286>.
- [155] J. Adolfsson et al. The upgrade of the ALICE TPC with GEMs and continuous readout. *Journal of Instrumentation*, 16(03):P03022, mar 2021.
- [156] W. Anderson et al. *Nucl. Instrum. Meth. A*, 646:35 – 58, 2011. <https://doi.org/10.1016/j.nima.2011.04.015>.
- [157] 16/14 channel 1-1.3kv (1 - 3 ma) individual floating channel dual range boards for quadruple and triple gem detectors. <https://www.caen.it/products/a1515b/>.
- [158] 14/16 stacked channel multipin radiall to shv connector adapter for a1515tg/a1515qg. <https://www.caen.it/products/a1015g/>.
- [159] Laura Franconi Andrey Marinov. Status of no-stretch no-spacer GEM assembly, the ns2 technique method and experiment result. 2012. <https://indico.cern.ch/event/176664/contributions/1442160/>.
- [160] Extech sd700:pressure/humidity/temperature data logger. <http://www.extech.com/products/SD700>.

- [161] The DABC DAQ. https://www.gsi.de/en/work/research/experiment_electronics/data_processing/data_acquisition/dabc.
- [162] J. Adamczewski-Musch et al. *IEEE Transactions on Nuclear Science*, 55:251–255, 2008.
- [163] S. Franchino et al. Effects of high charge densities in multi-gem detectors. In *2015 IEEE Nuclear Science Symposium and Medical Imaging Conference*, 12 2015.
- [164] P. Everaerts. Rate capability and ion feedback ingem-detectors. https://libstore.ugent.be/fulltxt/RUG01/001/311/812/RUG01-001311812_2010_0001_AC.pdf.
- [165] M. Alfonsi et al. *Nucl. Inst. and Meth. A*, 535:319–323, 2004.
- [166] R. P. Adak et al. *Nucl. Inst. and Meth. A*, 846:29–35, 2017. <https://doi.org/10.1016/j.nima.2016.12.004>.
- [167] A.K. Dubey et al. *Nucl. Instrum. Meth. A*, 718:418 – 420, 2013. <https://doi.org/10.1016/j.nima.2012.10.043>.
- [168] A.K. Dubey et al. *Nucl. Instrum. Meth. A*, 755:62 – 68, 2014. <https://doi.org/10.1016/j.nima.2014.04.027>.
- [169] D. Nag et al. Design and fabrication of a controlled water based cooling system for cbm muon chamber. *Springer Proc. Phys.*, 203:893–895, 2018.
- [170] W.M. Zabolotny et al. Versatile prototyping platform for data processing boards for CBM experiment. *Journal of Instrumentation*, 11(02):C02031–C02031, 2016.
- [171] Swagata Mandal et al. Integration of gbtx emulator with much-xyter and data processing board for cbm experiment. In *2016 IEEE Nuclear Science Symposium and Medical Imaging Conference*, 10 2016.
- [172] Optocoupler data sheet. <http://www.ixysic.com/home/pdfs.nsf/www/CPC1393.pdf>.
- [173] Rama Prasad Adak et al. *Nucl. Instrum. Meth. A*, 846:29 – 35, 2017. <https://doi.org/10.1016/j.nima.2016.12.004>.
- [174] Ajit Kumar et al. *DAE Symp. Nucl. Phys.*, 62:1006–1007, 2017. <https://cds.cern.ch/record/2674709>.

- [175] Rafal Kleczek. *Journal of Instrumentation*, 12:C01053–C01053, 2017.
<https://doi.org/10.1088/1748-0221/12/01/C01053>.
- [176] P.-A. Loizeaua and M. Barej. Characterization of a logic error in the STS/MUCH-XYTERv2.0 ASIC.
<https://indico.gsi.de/event/5863/session/16/contribution/18/material/slides/0.pdf>.
- [177] S. K. Kundu et al. *CBM Progress Report*, pages 102–103, 2020.
https://repository.gsi.de/record/228172/files/cbm_pr2019_final.pdf.
- [178] The Green IT Cube. <https://ttsp-hwp.de/projects/green-it-cube/>.
- [179] The CbmRoot Framework. <http://computing.gitpages.cbm.gsi.de/cbmroot/>.